INFORMATION TO USERS

Study of Reactive Intermediates Within Non-Acidic Zeolites: β-Heterolysis & Radical Reactivity

by

Wendy Ortiz Ojeda

Submitted in partial fulfillment of the requirements

for the degree of Doctor of Philosophy

at

Dalhousie University

Halifax, Nova Scotia

May 2001

The author has granted a non-exclusive licence allowing the National Library of Canada to reproduce, loan, distribute or sell copies of this thesis in microform, paper or electronic formats.

The author retains ownership of the copyright in this thesis. Neither the thesis nor substantial extracts from it may be printed or otherwise reproduced without the author's permission.

L'auteur a accordé une licence non exclusive permettant à la Bibliothèque nationale du Canada de reproduire, prêter, distribuer ou vendre des copies de cette thèse sous la forme de microfiche/film, de reproduction sur papier ou sur format électronique.

L'auteur conserve la propriété du droit d'auteur qui protège cette thèse. Ni la thèse ni des extraits substantiels de celle-ci ne doivent être imprimés ou autrement reproduits sans son autorisation.

0-612-66654-9

Canada

DALHOUSIE UNIVERSITY

FACULTY OF GRADUATE STUDIES

The undersigned hereby certify that they have read and recommend to the Faculty of

Graduate Studies for acceptance a thesis entitled "Study of Reactive Intermediates

Within Non-Acidic Zeolites: β-Heterolysis & Radical Reactivity"

by   Wendy Ortiz Ojeda

in partial fulfillment of the requirements for the degree of Doctor of Philosophy.

Dated: May 24, 2001

External Examiner

Research Supervisor

Examining Committee

ii
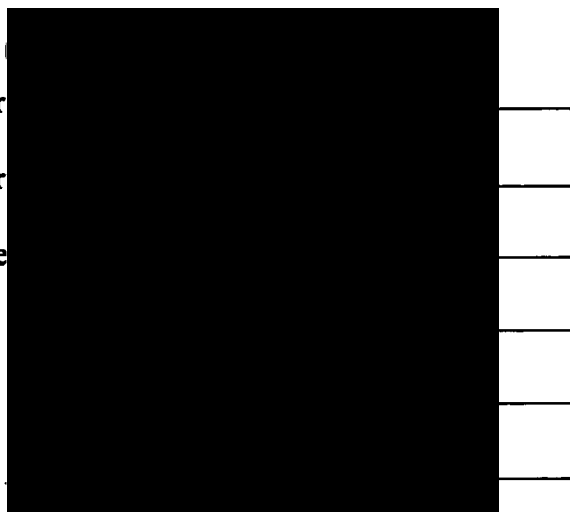
DALHOUSIE UNIVERSITY

DATE: May 28, 2001

AUTHOR: Wendy Ortiz Ojeda

TITLE: Study of Reactive Intermediates Within Non-Acidic Zeolites:

β-Heterolysis & Radical Reactivity

DEPARTMENT OR SCHOOL: Department of Chemistry

DEGREE: Doctorate   CONVOCATION: October   YEAR: 2001

Table of Contents

vi

List of Figures

xiii

List of Tables

Abstract

Zeolites are microporous materials capable of hosting organic molecules within their internal voids. Although considerable research has been directed towards understanding chemical transformations that occur within these structures, the fundamental role played by zeolites in promoting or controlling these transformations is still not well understood. The present doctoral project has involved the study of reactive intermediates within the internal voids of zeolites in order to enhance our understanding of such supramolecular systems and their effect on the reactivity of transient intermediates. Time-resolved nanosecond diffuse reflectance has been employed to systematically study the effect of zeolite composition on the dynamics of organic radical reactions.

The effect of zeolite environment on ionization reactions was examined to determine and quantify the internal ionizing power of various zeolites. In particular, the investigation focused on studying the kinetics of heterolysis reactions of organic radicals containing a leaving group at the β-position within alkali-metal exchanged Y-zeolites. The kinetic probe molecule, 2-halo-1-(4-methoxyphenylethyl radical was generated within zeolite supercages upon laser photolysis of a precursor arylethyl acetate. As the rate constant for the cleavage of the carbon-leaving group bond is highly sensitive to the environment of the media, this reaction was well-suited to probe the ionizing power of zeolites. Results show the ionizing power of Y zeolites depends strongly on the nature of the counterion and increases upon going from CsY to LiY (largest to smallest cation). However, the polar environment of zeolites was found to be less ionizing than aqueous conditions but reaction rate constants were similar to values obtained in water/methanol mixtures containing from 30% to 70% water. Interestingly, a significant reduction in the absolute ionizing ability of the zeolite was found when the suprastructure was hydrated. In addition, substrate structure was observed to have a significant role on the reactivity of the β-substituted radical within zeolites. These results demonstrate the active role played by the zeolite framework in encouraging heterolytic reactions to occur.

The reactivity of benzylic radicals generated by laser excitation of arylacetic acids within the cavities of zeolites was also examined. This project resulted in the first direct detection of the benzyl radical and the benzyl anion within cation-exchanged Y zeolites. Absolute rate constants for the reactivity of these types of radicals were obtained and it has been found that the reactivity is highly dependent on the structure of the radical and nature of the zeolite. The investigation revealed radical mobility and steric crowding are important factors in the radical decay mechanism. For example, the cumyl radical is less mobile within the zeolite framework than the smaller benzyl radical. As a result, it is less able to move and decays slower than the benzyl radical. Furthermore, each of these two similar radicals decay *via* different decay mechanisms in zeolites.

List of Abbreviations

\<S\>	loading level (moles of compound per moles of zeolite cavities)
AcN	acetonitrile
AcO	acetoxy group
AcOBrAn	2-bromo-1-(4-methoxyphenyl)propyl acetate
AcOBrVA	2-bromo-1-(4-methoxyphenyl)ethyl acetate
AcOClAn	2-chloro-1-(4-methoxyphenyl)propyl acetate
AcOCldiMeSty	2-chloro-1-(2,4-dimethylphenyl)ethyl acetate
AcOClMeSty	2-chloro-1-(4-methylphenyl)ethyl acetate
AcOClVA	2-chloro-1-(4-methoxyphenyl)ethyl acetate
AcOTFAAn	2-trifluoroacetoxy-1-(4-methoxyphenyl)propyl acetate
AcOTFAVA	2-trifluoroacetoxy-1-(4-methoxyphenyl)ethyl acetate
An	anisole group (or belonging to the 4-anethole substrate)
aq.	aqueous solution
CsY	cesium cation exchanged faujasite Y zeolite
CumCOOH	cumylcarboxylic acid
d	diameter
D	diffusion coefficient
E_a	activation energy, activation barrier
ESM	exponential series method
ε	extinction coefficient
HFIP	1,1,1,3,3,3-hexafluoroisopropanol
ISC	intersystem crossing
k	rate constant
kJ	kilojoule
KY	potassium cation exchanged faujasite Y zeolite
τ	lifetime

LiY	lithium cation exchanged faujasite Y zeolite
MeOH	methanol
MY	alkali-metal exchanged faujasite Y zeolites
NaY	sodium cation exchanged faujasite Y zeolite
nm	nanometer
ns	nanosecond
PhAcOH	phenylacetic acid
ps	picosecond
RbY	rubidium cation exchanged faujasite Y zeolite
Sty	styrene
TFA	trifluoroacetoxy group
TFE	2,2,2-trifluoroethanol
VA	vinylanisole, 4-methoxystyrene
λ	Wavelength
$\Delta J/J_o$	change in diffuse reflectance
$\Delta O.D.$	change in optical density
$\Delta G^{\ddagger}$	free energy of activation
$\Delta H^{\ddagger}$	enthalpy of activation
$\Delta S^{\ddagger}$	entropy of activation
μs	microsecond

Acknowledgments

The amount of encouragement and support that I have received over the past few years, particularly in the last few months has been immense. Family and friends have been a source of motivation and assistance that have allowed me to pass somewhat sane through these austere times .

It goes without saying that I am eternally grateful to my supervisor, Dr. Fran Cozens, for her guidance, encouragement, support and unlimited patience. Her continuous expressions of "that doesn't make any sense" and "why is that?" have guided me throughout my studies and have provided the foundation for the knowledge that I have acquired. Although her role in my scientific development is vital, equally important has been her confidence in me; even though sometimes such counsel went through my deaf ears. The opportunities that I now have available before me are in no small part due to Dr. Cozens, and for that I am also grateful.

I would also like to express my sincere appreciation to Dr. Norm Schepp for all the tutelage and advice he continuously distributed to a pestering student. His unlimited supply of wisdom and interest in research has been encouraging. In addition, his selfless attitude and patience towards helping students in-need has been outstanding.

Most people that know me are aware that writing this thesis has been the most excruciatingly painful experience of my relatively non-eventful life. Although people say that it was just in my head, my family, Mom, Dad, Edwin, Odin, Krista and babies, have stood behind me every single day. Their endless love, support and encouragement have shown me how fortunate I am to have them. In addition, the person that had the unlucky position to live with me during these months, 24 hrs a day and 7 days a week, deserves a great reward. Unfortunately, Trevor just gets to continue being married to me.☺ Thank you Trev for being the person that you are.

There are many members of the department that have assisted and befriended me during my undergraduate and graduate studies here at Dalhousie. I'd like to thank them all. In particular, Dr. Arnold and Dr. Pincock, who have been extremely kind in allowing

me to walk through their research facilities everyday, borrow several laboratory items (I will return them) and mostly for their advice and insight. Rick, Ross, Brian, and Jüergen have been crucial in allowing me to conduct many of the experiments discussed in this thesis, thank you. In addition to technical advice, Jüergen has been a friend, his wise advice about life and finances will be fondly remembered.

I'd also like to thank every single member of our research group for their support, patience, and entertainment. I am very fortunate to have met such wonderful people that selflessly aid others in distress and offer their superb friendship. From now on, 'tea breaks' will have a special significance. Thank you, Elaine, Suzanne, Roumiana, Alex, Mariluz, Sandy, Karen, Jen, Amy, Monica, Elizabeth, Aviva, Leslie, Jeff, Dave and Melanie.

Melanie has been a special person in my life. Her 'unusual ways' have often made me smile and I am very lucky to have her as a friend. Her constant optimism and encouragement have been a source of strength during the past few years. I would like to thank her for her willingness to help and for her friendship. See you in Patagonia!

This thesis is dedicated to my grandmother
Te extraño Praxita

Chapter 1. Zeolites

Control of the chemical behaviour of organic molecules in terms of medium has been an important subject in organic chemistry. Originally, most of the research in this area focussed on the effect that properties like polarity and ion-solvating ability of homogeneous solvents have on the reactions and reactivity of organic compounds. More recently, the effects of various organized assemblies, including micelles, microemulsions, vesicles, and several inclusion compounds such as cyclodextrins, calixarenes, and zeolites have been examined.[1-6] Reactions in organized and constrained media have attracted growing research interest aimed at understanding peculiar chemical behaviour influenced by the system topology and ultimately finding ways to control the kinetics by suitably manipulating the microscopic environment.[3,4,7]

Zeolites are one of the various types of organized assemblies that have been and continue to be extensively studied. Over the past couple of decades, zeolites have been shown to be valuable host materials in both industry and research laboratories.[8-15] They have met wide-scale industrial applications due to their unique physical and chemical properties, such as strong acidity, large internal surface area, high thermal stability and shape selectivity. In addition, zeolites can host a wide variety of organic molecules in their cavities and channels, and such inclusion complexes have often been shown to modify the normal chemistry observed in homogeneous solution.[16-18]

Despite the fascinating features of zeolites as solid reaction media, large gaps remain in our understanding of how zeolites influence the reactions of included guest molecules. As a result, considerable research has been directed to establish a correlation between mechanistic aspects of chemical processes in zeolite-adsorbed systems and the specificity and selectivity of reactions.[19] Better understanding of these reaction mechanisms can extend and/or improve the present utility of these materials or even create novel applications. With this in mind, the main focus of this thesis was the study of how the internal properties of zeolites influence two particular reactions, one being the

ionization of leaving groups as observed in an S_N1-like process, and the other the radical-radical combination of benzyl radicals.

1.1. Introduction to supramolecular structure of zeolites

Commercially, zeolites are widely used as water softeners in detergents, adsorbents or desiccants, ion exchangers, catalysts, and microreactors for a variety of organic and inorganic transformations. Many petrochemical processes, including cracking, selective toluene alkylation, and xylene isomerization, take advantage of the high activity of the acidic form of these microporous environments.[14,20,21] Furthermore, the application of zeolites to the generation of fine chemicals is growing rapidly.[22,23] Zeolites are also being explored as vessels for the synthesis of chiral molecules[11,24-27] and investigations of organic-functionalized molecular sieves (OFMSs) are also being reported.[28]

Zeolites have also been used extensively as prototypical organizing media for a variety of chemical reactions since zeolites can compartmentalize the entrapped molecules within their rigid openings and provide stabilization to reactive species.[2,10,29] Several types of zeolites are frequently employed in chemical research, the most common ones being the faujasites (zeolites X and Y), zeolite A, mordenite, zeolite L, and ZSM-5.

Much of the special ability of zeolites to modify organic reactions arises from their unique structural features. Structural characterization of these solid materials is made available by means of various instrumental techniques such as solid state NMR and ESR, X-ray photoelectron spectroscopy (XPS), and both neutron- and synchrotron-based diffraction.[30-37] Some of the findings about zeolites are summarized below.

1.1.1. Zeolite topology and composition

Zeolites are microporous crystalline aluminosilicates with a fully cross-linked open structure made up of corner-sharing $[SiO_4]^{4-}$ and $[AlO_4]^{5-}$ tetrahedra.[2,8,9,38-40] These fundamental building blocks are connected via shared oxygen atoms to create

three-dimensional networks of channels, cavities and pores of discrete size and shape, Figure 1-1. While each silicon atom within the framework has no charge, each aluminum center bears a negative charge that must be balanced with a charge-balancing cation. In addition, the electrostatic forces generated by the presence of charges within the zeolite result in a hygroscopic environment. This arrangement leads to the following general formula where n represents the cation valence:

$$M^{n+}_{x/n}[(AlO_2)_x(SiO_2)_y] \cdot mH_2O$$
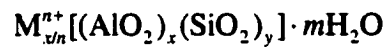
Numerous framework topologies of zeolites are possible which differ in their chemical composition as well as the size and shape of their internal voids. The large variation in framework topology leads to various systems of channels and cavities which allow for one-, two- or three-dimensional diffusion of included guest molecules. There are two main types of structural design: one provides a three-dimensional arrangement of cavities interconnected by channels and the second consists of only interconnected channels. The faujasites are examples of the former class where the framework consists of large supercages interconnected by three channels. The pentasils are examples of the latter class, Figure 1-2.

AlO_4^{5-} and SiO_4^+
fundamental building blocks

Tetrahedra linked together

Zeolite X & Y
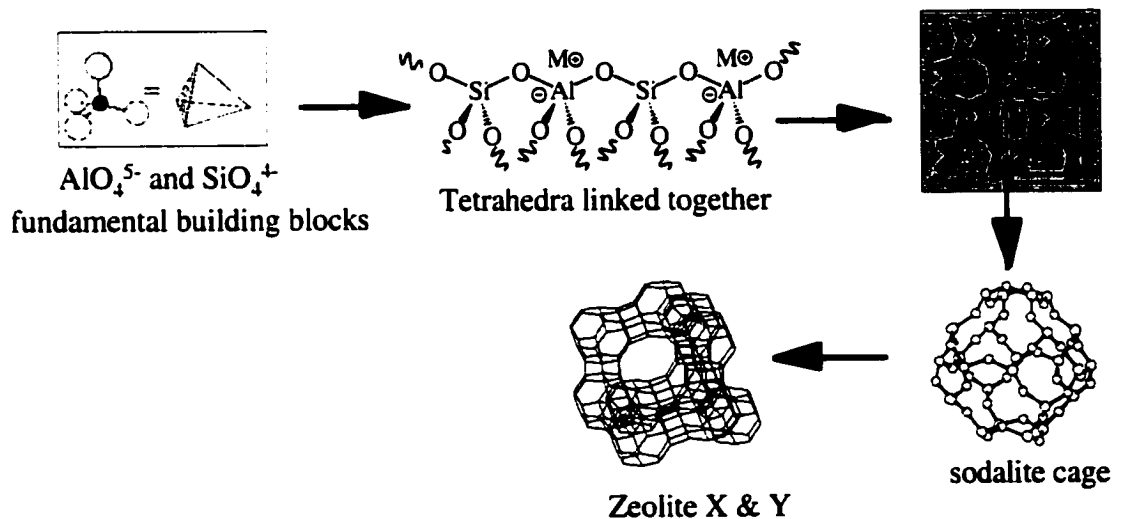
sodalite cage

Figure 1-1. Schematic of the structural development of faujasite zeolites from the primary tetrahedra, AlO_4^{5-} and SiO_4^+, building blocks.
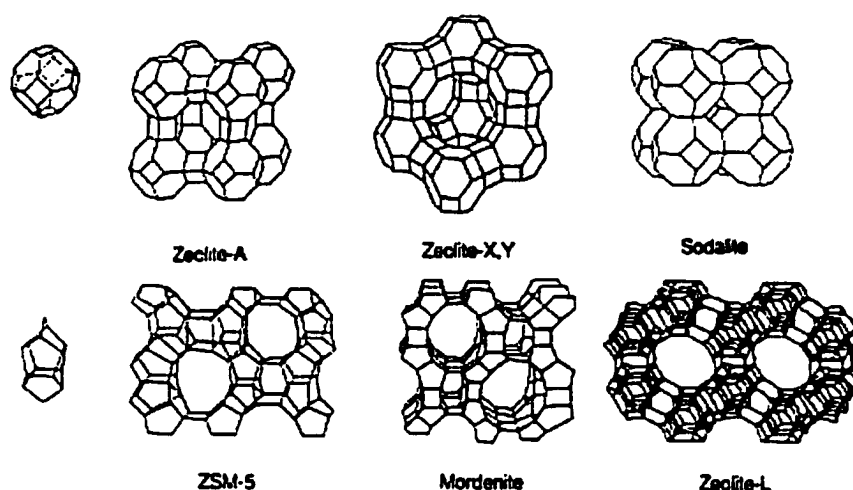
Figure 1-2. Some common supercage structures generated from sodalite cages (top) and pentasil cages (bottom) for several zeolites.

The structure of faujasite zeolites (Zeolites X and Y) is cubic and built from sodalite cages connected via a double six-membered oxygen window. Sodalite cages or β-cages are 6.6 Å in diameter with an entry aperture of 2.1 Å. Zeolite X and Y have different framework Si/Al ratios (1.0-1.5 for zeolite X and 1.5-3 for zeolite Y). They form a three-dimensional network of nearly spherical supercages of about 13 Å in diameter connected tetrahedrally through 7.4 Å windows.

Zeolite A is a synthetic aluminosilicate material composed of the sodalite cages similar to faujasite but connected through double four-membered oxygen rings of $[SiO_4]^+$ and $[AlO_4]^{5-}$. By this connection three cages are present: cubic (D4R), sodalite cage, and α cage (11 Å in diameter with 4.1 Å opening). The structure of zeolite A is also cubic, having a Si/Al ratio of 1.0, with alternating Si and Al atoms in the framework. Aromatic guest species are not readily adsorbed inside α cages because of the size restriction and only external surfaces are available for their adsorption in small quantity. Hence, the chemistry of organic guest molecules within zeolite A is limited.

When pentasil (five-membered ring) units are present as the fundamental building blocks instead of sodalite units, channel-type zeolites such as ZSM-5 and mordenite are formed. ZSM-5 has a structure consisting of two intersecting channel systems, with the vertical channels being elliptical (5.7 x 5.1 Å), and the horizontal channels having nearly circular 5.4 x 5.6 Å openings. On the other hand, the channel system in mordenite is a one-dimensional 12-membered ring system with an opening of 6.5 x 7.0 Å. Zeolite L has a unidimensional channel system as in the mordenite case. The 12-membered ring opening of the zeolite L is 7.1 Å, slightly larger than that in mordenite.

One method of zeolite classification is based on their pore size. The pore dimension determines the size of molecules that can be readily adsorbed into the microporous structure; i.e. it controls access to the channels and cavities and the diffusion of the molecules. The pore size is typically defined by the number of oxygens found within the ring of atoms that forms the pore. The range in pore size is illustrated in Table 1-1 for a variety of zeolites. The number of oxygen atoms found in the rings forming the pores may also be used to classify the pores as small (8 oxygens), medium (10 oxygens) or large (12 oxygens). Additionally, the pore size can be modified by the framework composition, ion exchange, framework flexibility, sorbents, and external surface modification.

Table 1-1. Size of pore openings and dimensionality of the pore system for selected zeolites. The number in parenthesis corresponds to the smaller pore.

Zeolite	Pore Size (Å)	Channel/Cage type
Stilbite	4.9 x 6.1 and (2.7 x 5.6)	Two interconnected channels
ZSM - 11	5.3 x 5.4	Two interconnected channels
ZSM - 5	5.3 x 5.6 and 5.1 x 5.5	Two interconnected channels
Linde Type L	7.1	Single channel with a lobe (da = 7.5 Å)
Mordenite (M)	6.5 x 7.0 and (2.6 x 5.7)	Two interconnected channels
Offretite	6.7 and (3.6 x 4.9)	Two interconnected channels
Beta (_)	7.5 x 5.7 and 6.5 x 5.6	Three dimensional channel
Faujasite (X and Y)	7.4	Three dimensional channel with a cage (db = 12 Å)
Sodalite (S)	2.3	Three dimensional channel with a cage (db = 6.6 Å)
Zeolite A	4.2	Three dimensional channel with a cage (db = 11.4 Å)
Mazzite (()	7.4 and 5.6 x 3.4	Single channel

a d = diameter of lobe. b d = diameter of cage

1.1.2. Counterions and silicon to aluminum ratio

The number of silicon atoms relative to the number of aluminum atoms, or the Si/Al ratio, can vary significantly upon going from one kind of zeolite to another. Silicalite lies at one extreme in that no aluminum atoms are present within the framework. Aluminum can replace up to about 50% of the silicon atoms, but the thermal stability of the zeolite decreases as the aluminum content increases. This is a direct result of the difference between the Si-O and Al-O bond lengths; the longer and weaker Al-O bonds weaken the structural framework. In addition, the energetically unfavorable environment of having two adjacent negative aluminum sites limits the Si/Al ratio to a minimum of one.[41]

Si/Al ratios for some common zeolites are summarized in Table 1-2. The exact value for the Si/Al ratio varies slightly with preparation method and commercial source, so only typical ratios are listed. While most of the zeolites in Table 1-2 have considerably different topologies along with different Si/Al ratios, changes to the Si/Al ratio do not necessarily result in structural changes to the zeolite. For example, the framework structures of zeolite X and Y are identical, but they have different Si/Al ratios. The ratio ranges for zeolite X and zeolite Y are 1 to 1.5 and 1.5 to 3, respectively.

Table 1-2. Typical Silicon to Aluminum ratios for various zeolites.

Zeolite	Si/Al ratio
Na Fau	27.5
NaY (Fau)	2.4
NaX (Fau)	1.2
Mordenite	6.5
Na ZSM-5	25
Na β	18

In aluminum-containing zeolites, negative charges are generated in the framework due to the presence of the tetra-coordinate $[AlO_4]^{5-}$ tetrahedra. As a result of the charge imbalance, zeolites with low Si/Al ratios (high aluminum content) have strongly polar anionic frameworks. The negative charge in the framework must be balanced by charge-compensating cations, with the Si/Al ratio determining the total number of cation sites. These cations contribute to large local electrostatic fields which may interact strongly with water and other guest molecules present within the zeolite.[7,42-46] In addition, the reactivity and selectivity of zeolites as catalysts is directly related to the active sites generated by the inclusion of aluminum into the zeolite framework; the more aluminum present the greater the number of anionic centers which are thought to be the catalytic sites.

The charge-balancing cations found within zeolites are typically protons, alkali or alkaline earth metal cations. These cations are not covalently bound to the zeolite framework; therefore, they can be readily exchanged by a variety of other cations through simple cation exchange procedures without producing any alteration in the crystalline structure of the solid. In this manner Brønsted acid sites can be easily introduced into the framework by exchanging the Na^+ cations with protons. These acidic solids have been the most extensively studied systems due to their high catalytic ability.[47] In addition, the relatively easy ion-exchange properties of zeolites are responsible for their high usage in detergents (for Mg^{2+} absorption), waste-water treatment, and contaminants clean-up.

Research into zeolites has revealed that the position, size and number of cations can significantly alter the properties of the zeolite.[48,49] Hence, the positions of the cations within the faujasite framework of X and Y have been well characterized.[44] The typical unit cell composition, which consists of eight cavities for these zeolite systems are:

$$X \text{ type}: M_{86}(AlO_2)_{86}(SiO_2)_{106} \cdot 264H_2O$$

$$Y \text{ type}: M_{56}(AlO_2)_{56}(SiO_2)_{136} \cdot 253H_2O$$
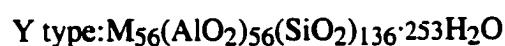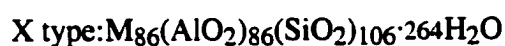
where M is a monovalent cation. In these zeolites, the charge-compensating cations are commonly found in three different locations, Figure 1-3. Cations located on the hexagonal prism faces between the sodalite cages are designated as type I cations, and there are 16 present in every unit cell. There are 32 type II cations per unit cell located in the open hexagonal faces of the sodalite cages facing into the supercage. Type III cations, with 38 per unit cell for zeolite X and 8 per unit cell for zeolite Y, are located on the walls of the supercage cavity as illustrated in Figure 1-3. Only cations at sites II and III are accessible to adsorbed organic compound within a supercage as the windows into the small sodalite cage (site I) are too small for a typical organic molecule.

The size of the cation also contributes to the modification of the effective size of the pore opening, with larger cations like Cs^+ causing the pore to be significantly narrower than smaller cations like Li^+, Figure 1-4. In addition, as shown in Table 1-3, the

free volume available for guest molecules within the supercage is dependent on the nature and number of the charge-balancing cations. However, even with the counterbalancing cations present in the cavities of zeolites, supercages of faujasites have been found to be quite large as shown by their average available volume capacity of 28 water, 5.4 benzene or 2.1 perfluorodimethylcyclohexane molecules per supercage.
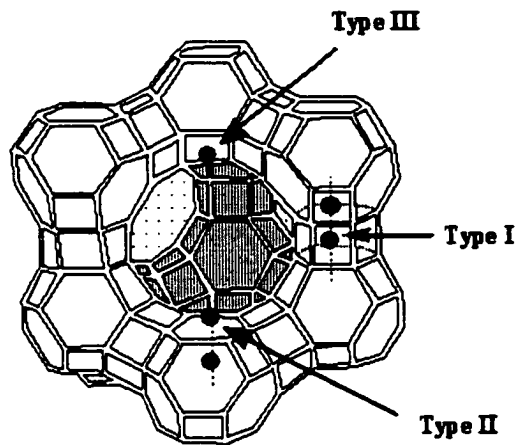
Figure 1-3. Cation location (I, II, III) within X and Y type zeolites.

The framework cages or channels are normally filled with cations and water. The cavity-filling water molecules are readily lost upon heating and regained reversibly without damage to the framework structure. When dehydrated, other guest molecules can occupy the void spaces as long as the interior spaces are large enough and the aperture sizes allow passage of the substrates. Typically, the aperture size of zeolite pores range from 3 to 8 Å, and the inner diameter of interior spaces from 5 to 13 Å.

Li⁺ Na⁺ K⁺ Rb⁺ Cs⁺

d= 1.52 Å   2.04 Å   2.76 Å   3.04 Å   3.34 Å
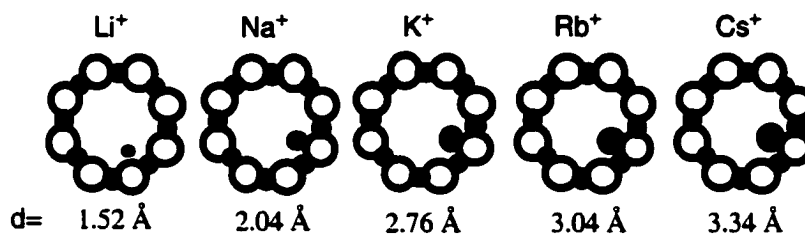
Figure 1-4. Schematic representation of the narrowing of the pore opening as a function of cation diameter.

Table 1-3. Effect of cation size on estimated supercage volume for faujasite zeolites.

M^+ Cation	Ionic Radius of Cation (Å)	Supercage Volume ($Å^3$)	
		Zeolite Y	Zeolite X
none	-	840	888
Li	0.76	834	873
Na	1.02	827	852
K	1.38	807	800
Rb	1.52	796	770
Cs	1.67	781	732

The supercages are considered as primary sites of occupancy by adsorbed guest species as the available external surface is much smaller (<1%) than the internal surfaces.[50] Another indication of the internal location of the molecules is the size-restriction associated with the incorporation of molecules.[2,51] Furthermore, the intentional destruction of the zeolite crystal structure results in the loss of the adsorption ability of the zeolites.[52]

1.2. Properties of zeolites

While a basic knowledge of the architecture and composition of zeolites is clearly important when studying these solid-state materials, it is the properties of the zeolites as defined by their topology and composition that determine their utility as media for reactions in organic chemistry. In the following section, several properties relevant to the present thesis such as hydrophilicity, acidity and basicity, and polarity are discussed, together with the effect of zeolite structure and composition on these properties.

(1) Hydrophilicity

Examination of physical and chemical properties characteristic of zeolites provides some insight into the active role played by the host. A very common characteristic associated with zeolites is their highly hygroscopic nature due to the strong polar environment within the internal framework. In fact, the name zeolite means 'to boil' due the boiling-like appearance when heated as the numerous water molecules escape.

Water molecules within zeolites can have a significant effect on the specific positions of exchangeable cations. Migrations of cations within the lattice are often observed in zeolitic materials upon adsorption or desorption of water.[53] The cations in hydrated zeolites are typically coordinated to both the oxygen atoms of the framework and the oxygen atom of the water molecules, thus maximizing the coordination around the cations. When the zeolite is dehydrated, the framework will either flex to accommodate the coordination requirements of the cation or the cation may move to a different position where it can obtain a higher coordination environment. Hence, the presence of water, or other co-adsorbents that can effectively coordinate with metal cations, can have a large impact on the arrangement of the balancing cations. Included water can therefore affect the organic guest-host interactions through modification of the internal environment experienced.

The ordering of residual water and alkali-metal cations in zeolites Y and X has been investigated by several research groups using various experimental techniques and modeling methods (X-ray diffraction, MAS NMR, and temperature-programmed desorption).[53-55] There are three general classes of zeolitic water according to their physicochemical properties: the first type describes water molecules that are strongly bound chemically or coordinated to metal cations residing preferentially in small cavities (e.g. sodalite cage). The second group encompasses water molecules that are physically bound or physisorbed on the framework oxide surface (e.g. supercage surface). Finally, the last group comprise highly mobile water molecules clustered near the center of large cavities that can be removed by gentle evacuation.[56] Thus, water has been observed to desorb from faujasite type zeolites in a stepwise manner, with the nature of the cation strongly influencing the course of desorption at higher temperatures. Study of the interactions of water in MNaY zeolites (M = alkali metal cations) revealed that mainly sodium cations participate in the interaction with the water molecules within the cavities of KNaY, RbNaY and CsNaY, by forming distinctive sodium-water aggregations.[54] However, the heavier alkali-metal ions do affect these structures in an indirect manner by blocking some of the cation positions available for the sodium ion.

Studies of the energetics of formation and hydration of alkali cation-exchanged Y zeolites revealed that the hydration enthalpy per mole of *zeolite* decreases in the order LiY > NaY > RbY > CsY. However, the hydration enthalpy per mole of *water* had little dependence on the nature of the exchanged cations. These results were explained by the fact that water molecules can be more efficiently packed in the smaller cation zeolites due to larger internal volume and stronger water-cation coordination.[57] In other words, the total energetic contribution by hydration decreases from LiY to CsY as the larger internal volume and stronger interactions lead to a higher water content in the smaller cation zeolites (H_2O per M^+ cation). As a result, greater changes in enthalpy due to water are detected in LiY and NaY but these enthalpy changes are relatively similar when the amount of water is taken into account.

The ubiquitous and often times unwanted presence of water caused by the high hydrophilicity of zeolites has important implications with respect to the behaviour of incorporated guest molecules, and with respect to results observed using spectroscopic techniques. A particularly illustrative example comes from results by Thomas and co-workers who, upon irradiation of aromatic molecules within NaY and NaX, observed the formation of the radical cations of aromatic molecules and trapped electrons in the form of Na_4^{3+} absorbing at 520 nm in NaY and 550 nm in NaX on laser excitation of the aromatics.[58,59] In contrast, Gessner and Scaiano failed to confirm the presence of Na_4^{3+} as a counterpart of the radical cations in a similar experiment.[60] This contradiction was later explained by the fact that the absorption spectra of trapped electrons are considerably affected by the presence of water within the zeolites. Their adsorption peak shifts to longer wavelengths in the presence of large quantities of co-adsorbed water that might be introduced in the sample preparation procedures.[61]

Other studies of aromatics reported that both fluorescence and triplet decay rates were significantly affected by the presence of water in zeolites.[42,62] Ramamurthy and co-workers reported that the fluorescence decay rate of pyrene adsorbed into NaY is smaller with increasing hydration level.[42] This effect was explained as a liberation of the guest molecules from the host zeolite by the action of water molecules which have a much stronger interaction with the zeolite and can lie preferentially on the zeolite walls.

Similarly, the long triplet lifetimes of aromatic species are altered dramatically at various hydration levels in the zeolites. In dehydrated NaY (< 0.4 wt % water content), an anthracene triplet decay constant of 60 s^{-1} was obtained; this value was comparable to that observed in a rigid plastic matrix, poly(methyl methacrylate). A plot of decay rate constants versus solvent amount yielded convex curves. For example, with increasing water content, the decay rate constant increased to a value about three orders of magnitude larger than the dehydrated value and then decreased when fully hydrated to a value similar to the original dry decay rate constant. The observation was rationalized on the basis of the different mobilities of anthracene within the supercage networks of the zeolite being strongly dependent on the water content, leading to self-quenching and

triplet-triplet annihilation. This study also revealed that solvents with strong affinity for zeolite frameworks (alcohols, acetonitrile, pyridine, etc) have a similar but less pronounced effect on the triplet lifetime of anthracene but those with weak interaction with the zeolite (n-hexane, benzene) have practically no effect. As a result, solvent molecules typically used for adsorption of aromatic species remaining in the sample after preparation due to insufficient evacuation treatment are hard to perceive experimentally even when present in samples.

Although water elimination from samples is necessary in order to study the naked internal environment of the zeolite and the effects on included organic guests, there are times when the presence of water may be advantageous.[63] For example, aggregation tendencies of relatively large molecules within zeolites can be controlled by the presence of co-adsorbed water or solvents.[64] Differences in product ratios may also be affected by co-incorporated water[63,65,66] as was observed for the photodimerization and photo-oxygenation of *p*-methoxystyrene by Kojima *et al.* Head-to-head *cis*- and *trans*-cyclobutane dimers were produced at the isomer ratio of 91/9 under vacuum and 38/62 under wet air. Similarly, the nature of the solvent was found to have a major influence on reaction kinetics and product selectivity during oxidation of olefins and alcohols on Ti-β zeolite.[67]

(2) Active sites: acid/base & electron donating/accepting properties

Zeolites have amphoteric properties and the existence of Lewis acid and Lewis base sites in non-acidic zeolites is well documented.[47,52,68-74] Charge compensating cations or tri-coordinated and extraframework aluminum atoms act as the Lewis acid, or electron acceptor, while the framework oxygens are often designated as the Lewis base, or electron donor. A large number of experimental[75-82] and theoretical studies[83] have been directed to determine the factors that govern the donor/acceptor properties of zeolites and to develop a systematic method to effectively monitor the properties.[68-71,84] In general, the overall Lewis acid strength of the zeolite increases with decreasing Si/Al ratio and with smaller alkali metal cations.[78,82] As the negatively charged framework

aluminum interacts with a balancing cation, the basicity of the oxygen is indirectly influenced by the cation. Thus, the stronger the Lewis acid (counterion), the weaker the conjugate base (oxygen bridge). For example, LiY is a better Lewis acid than CsY, while CsX is more basic than CsY. That is, with strongly acidic cations such as Li^+ and Na^+ the charge on the Si-O-Al oxygen bridge is low and the zeolite will behave as a Lewis acid. When the cation is less acidic or has low electronegativity, e.g. Rb^+ and Cs^+, the zeolite shows Lewis base behavior. Accordingly, the chemical properties of the zeolites can be fine-tuned in terms of composition, cations, and framework structure.[85,86]

Unlike proton-exchanged zeolites which are highly acidic from a Brønsted acid perspective, alkali metal ion-exchanged X and Y zeolites are expected to have little Brønsted acid activity. In fact, only negligible Brønsted acid sites could be detected from IR spectroscopic measurements and MAS NMR on NaY zeolites.[87] A more sensitive "indicator titration" method that measures differences in electronic absorption characteristics between protonated and unprotonated forms of conjugated dyes estimated about one acidic site for every 116 aluminums in NaY ($< 1\%$ H^+ impurity).[69] In contrast to zeolite Y, alkali metal exchanged X zeolites were found to lack acidic sites that could be detected by the sensitive probe used in the study. Although the degree of Brønsted acidity present in alkali-exchanged Y zeolites is minimal, there have been reports where this small population of acid sites has played a role in the photochemistry of adsorbed guests.[85,88-91] Interestingly, the number of Brønsted sites varied[29,69,87,92] with the commercial source of the zeolite. Presumably, slight variations in zeolite composition arise from differences in the synthesis and pre-treatment of the zeolite (e.g. during ion-exchange).

(3) Polarity of Zeolites

Another concept which represents an important property of zeolites is the electrostatic field generated by the charge-balancing cations present within the framework. The role of these electrostatic fields is crucial in assessing the physical properties and microenvironment of zeolites. The fields are believed to be created by the

cations facing the supercage where the cations are only partially shielded[93-95] (Type II and Type III sites) due to weak coordination to the lattice oxygen atoms. As a result, the micropolarity of zeolite supercages is a reflection of the electric field provided by the cations and is distance and direction dependent, thereby allowing the polarization of adsorbed molecules to a degree comparable to the magnitude of field generated by the framework cations. However, most techniques used to probe the polarity and electric field variation within the cages of zeolites measure the global (average) property of several locations and not the distinct microenvironments within a supercage.

Absorption spectroscopy, UV and IR, X-ray diffraction and Xe-NMR are some of the techniques which have been used to probe the micropolarity and electric field variation within the cages of zeolites.[30] Theoretical calculations of electric fields and electric field gradients have also been utilized to explore the environment within these suprastructures.[96,97] Earlier approaches have used ionic lattice approximation and three-dimensional descriptions of the field and potential inside the supercage of faujasite zeolites.[43,77,95,97] With improvements in computer power, more sophisticated methods have been employed to calculate electronic environments of the suprastructure of zeolites. For example quantum-chemical simulations were performed by Stich et al.[98] and a charge-transfer molecular dynamics analysis was developed by Martínez et al.[99] Detailed maps of the electrostatic potentials across the internal sections of the channels and cages have been deduced by applying ab initio quantum chemical methods to large clusters that emulate a reasonably large portion of the zeolite network. The conclusion drawn from zeolite ZSM-5 model calculations is that the strength of the internal fields increases as the number of framework Al increases, but important fields are experienced by a guest even in all-silicon clusters where the framework does not bear any negative charge (de-aluminated zeolite models).[51] In contrast, other calculations have shown that the average field increases with silicon/aluminum ratio; for example, cations in zeolite Y show higher electrostatic fields than in zeolite X.[100] As zeolites define a rigid environment, the strength of the field is at a maximum near the walls, decreasing progressively towards the center of cavity. As a result, the maximum stability for

positively charged species is achieved when there is a tight fit between the zeolite framework and the guest molecule.

The electric field strength experienced within the cavities of zeolites is dependent on the nature and size of the counterbalancing cation (local property). Similarly, the Si/Al ratio will also have an effect on this parameter as this ratio directly determines the number of balancing cations present (global property). For example, the small Li^+ ion induces a stronger field in its proximity than the larger Cs^+ ion, Table 1-4.[44] For a given cation, the *individual* calculated fields increase with silicon/aluminum ratio but in the case of NaY and NaX, the number of cations present in the zeolite contributes to the overall electric field experienced by the molecule.[100]

Table 1-4. Dependence of electrostatic parameters in Y Zeolites as a function of counterbalancing cation. Taken from reference 44.

Cation (M^+)	Ionic Radius of cation (Å)	Electrostatic Field (V/Å) within the cage	Electrostatic Potential (e/r) of the cation
Li	0.76	2.1	1.67
Na	1.02	1.3	1.05
K	1.38	1.0	0.75
Rb	1.52	0.8	0.67
Cs	1.67	0.6	0.59

The strong electrostatic fields existing in the cavities induce polarization of any polarizable guest molecule. In this medium, the zeolite will polarize the guest such that the negative end rearranges to face the cation and the positive end towards the anionic framework, similar to the reactant molecule being placed in a highly polar salt solution. With this in mind, the effect of the fields in terms of solvent polarity has been explored with a number of organic probes incorporated into zeolites.

The earliest such study was undertaken by Baretz and Turro and utilized pyrenealdehyde as the probe molecule.[101] Although this investigation was complicated

by excimer formation due to high loading levels, supercages were inferred to be polar. Yoon and Kochi concluded from studies of redox reactions of methyl viologen (MV^{2+}) in NaY (when compared to values obtained in solution) that the polarity of zeolite matrices could be likened to those in an aqueous medium (e.g. NaY ~ 50% aq. AcN).[102,103] Thomas and co-workers have also concluded, using pyrene as the probe, that the supercages of X and Y zeolites are polar.[104,105] Another report concluded that NaX zeolites are more polar than NaY zeolites and that the polarity of these two zeolites are similar to that of aqueous methanol mixtures.[106] Ramamurthy and co-workers also developed photophysical probes in the early 90's for monitoring the micropolarity within the faujasite supercage.[43] Three different organic probes were utilized to give qualitative information about the internal environment of the cages by measuring the emission band maxima for the probe molecules. In this study, the polarity of the supercage was found to decrease with cation size ($Li^+ > Na^+ > K^+ > Rb^+ > Cs^+$) and that the NaX supercage was more polar than in Y zeolites.[43]

More recently Ramamurthy and co-workers have carried out experiments using probe molecules for monitoring the micropolarity within the faujasite supercage.[107] Three different organic probe molecules, Nile red, coumarin-500 and pyrene-1-carboxaldehyde were utilized to give information about the internal environment of the cages by measuring the absorption and emission band maxima for the probe molecules. The study demonstrated that the micropolarity of a zeolite supercage is far higher than any organic solvent in which most organic molecules can be dissolved. As such, they characterized the zeolite supercage as "superpolar". The conclusions indicated that dry alkali cation exchanged X and Y zeolites are highly polar, and the extent of polarity is dependent on the cation size where the polarity of the supercage was found to significantly decrease with cation size ($Li^+ > Na^+ > K^+ > Rb^+ > Cs^+$). In particular, LiY and NaY zeolites were found to be more polar than any organic solvent. In addition, it was found that the polarity of alkali cation X zeolites was slightly *lower* than Y zeolites. Using the polarity parameter $E_T(30)$ they narrowed the polarity values for the cation-exchanged zeolites to be between 68 (Cs^+) and 78 (Li^+); the $E_T(30)$ value of water is 63.

The authors also found that when water is introduced into the zeolite, the polarity of the zeolite is diminished.

The hydration state of the zeolite was shown to strongly influence the interior polarity of the microenvironment. Upon the uptake of water into the zeolite framework the polarity as indicated by the probe molecules substantially decreased. In addition to a lowering of the overall polarity the effect of the cation on the polarity was also diminished. Thus the range of polarity obtained upon going from hydrated LiY to hydrated CsY was much smaller than under dry conditions. This is presumably because the water interacts strongly with the cation reducing the electrostatic field effects felt by the probe molecule.

Another early examination of the solvent-like nature of zeolites was based on a solvatochromic indicator that measured the α-value of faujasitic zeolites as a function of Si/Al ratio.[108,109] The α-value is a measure of the hydrogen bond donor ability of the solvent, with large α-values representing strong hydrogen bond donors. Results obtained showed the α-value of the zeolite increased with Si/Al ratio to a maximum value, followed by a decrease at higher Si/Al ratios.[110] In the Na^+ exchanged form of the faujasite zeolite, an α-value comparable to the strongest H bond donor solvents was obtained (polar hydroxylic solvents). On the other hand, a study on zeolite ZSM-5 using the Π^* parameter (measure of solvent ability to stabilize charge) yielded a relatively constant value for this parameter indicating that even with increasing aluminum content of ZSM-5, the zeolite's ability to solvate charges remained unchanged.[111]

Other attempts at understanding the "solid-state ionizing solvent' view of zeolites have made use of well-known ability of zeolites to stabilize ground state donor-acceptor charge complexes. Formation of charge-transfer complexes between oxygen and hydrocarbons,[112], aromatic donors and pyridinium acceptors,[102,103,113] and aromatics and tetracyanobenzene[114] are some examples of polarity studies in zeolites.

1.3. Zeolites as reaction vessels for molecular guests

The 'nanoscopic reaction vessel' model describes the influence of the supramolecular media on the behaviour of included organic guest molecules and classifies the possible interactions as 'passive' and 'active'. Size exclusion, mobility restrictions and reactant isolation (cavity size, shape, and flexibility parameters) are examples of 'passive' interactions where little to insignificant interactions between the guest and the host are present at various points along the internal walls of the host. Active interactions may involve weak van der Waals forces or strong hydrogen bonds, electrostatic forces between charged centers, and interactions between Brønsted and Lewis acid sites with the molecule. If we are to attempt to modify the chemical behaviour of a guest molecule and to tailor the use of zeolites as catalysts and reaction media, one must fully understand the relationship between the suprastructure and the guest molecule.

Location and motion of guest aromatic species is of importance in elucidating the interaction of guest species with the host zeolite as well as the reactivity of molecules within the zeolite. The distribution of guest molecules within passive reaction cavities is expected to follow a simple statistical distribution. An active reaction cavity, on the other hand, possesses active sites that can interact with the guest through weak forces (*e.g.* hydrogen bonding, cation-π interaction), and consequently leads to more complex patterns in the distribution of guest molecules. The supercages of faujasites have been suggested to be the primary sites of occupancy by adsorbed guest molecules. For example, small aromatic guest molecules such as benzene are suggested to be adsorbed primarily at site II (Lewis acid site), interacting with some of the charge-compensating cations, Na^+ ions, and secondarily at 12-membered ring windows interacting with framework oxygen (Lewis base site).[115-117] The nature of the interactions at these two sites differs with cation-π interactions playing a key role at the first site, and CH$\cdots$O interactions being the primary force that holds a guest molecule in the second position.

Xenon has been used as an efficient adsorbate for probing the probe structure and guest location and measuring the rates of intracrystalline self-diffusion within

zeolites.[42,118] In these studies the sensitivity of the nuclear shielding of the spin 1/2 ^{129}Xe to the environment is utilized as xenon perturbs the photophysical properties of the excited singlet state of aromatic guest molecules through the external heavy atom effect. The probe molecules were found not to be uniformly distributed within zeolites as indicated by their multiexponential decay of excited singlet states. Experiments showed that two different microenvironments were available to the aromatic guest molecule, one highly polar and the other moderately polar. The cationic site was found to be particularly sensitive to the presence of xenon due to favorable interaction between the guest and xenon thus permitting the heavy-atom effect to operate.

The adsorption and location of simple organic molecules (e.g. benzene, p-xylene and pyridine) on zeolites has been followed by several techniques including infrared spectroscopy, Raman spectroscopy, UV diffuse reflectance spectroscopy, NMR spectroscopy, neutron diffraction, X-ray diffraction, and theoretical calculations.[5,101,102,119-131] In addition, there have been photophysical studies which confirm the occasional tendencies of aromatic molecules to aggregate within cation exchanged Y zeolites.[19,121,122,129,132,133] This phenomenon of ground-state aggregation is traced to the presence of cation-aromatic π-interaction. The studies have also revealed that solvents can coordinate to the counterbalancing cation thereby eliminating the cation-aromatic interaction and promoting a monomeric distribution. The importance of these noncovalent forces is increasingly being recognized as a key factor in the molecular recognition process. The possibility that metal ions can promote π-stacking adds another dimension to the role that cations can play in supramolecular chemistry.

It has become clear through extensive investigations that the molecules are not stationary within the zeolite suprastructure. They undergo rotational motions at the site itself and also migrate between different sites in a cage as well as between neighboring cages.[128] Typically, intercage hopping assumes a relatively high activation barrier. For most organic molecules studied in zeolites, this is a slow process, allowing the guest molecules to probe all the adsorption sites within a given cage many times before they can finally move to a neighboring cage. The diffusion processes in zeolites have been

extensively studied and several terms such as mean residence time and mean jump length, have been developed to describe this process.[134] The mean residence time is the time spent at a site between two successive jumps, while the mean jump length is defined as the average distance of travel in one jump. These parameters depend on the type of zeolite (channel geometry and dimensions), the nature of the guest molecule (size, shape, planarity, and polarity), loading level, the counterbalancing cation, and the temperature. Similarly, the time-scale for such motions varies with the zeolite and the guest molecule.

Computer simulation techniques available for the study of the diffusion process of guest molecules in zeolites involve traditional molecular mechanics or molecular dynamics (MD),[119] in addition to techniques for slowly diffusing molecules such as kinetic Monte Carlo or "Bluemoon" simulations.[128,134-140] The activation energies for diffusion of benzene have been found to be about twice as large in NaY as they are in NaX (33.7 kJ/mol vs 17 kJ/mol at low loading). This is a result of the reduced number of sodium cations in NaY compared to the number in NaX.[141] In addition, the self-diffusion coefficient was found to decrease with increasing loading in both zeolites. A recent investigation employs a continuous time random walk model to explain the kinetics of pseudo-first-order long-range reactions in zeolites assisted by migration between the adsorption sites with good agreement to experimental data.[142,143] In a different study, solid-state exchange ^{13}C NMR was used to measure directly discrete intercage hopping of strongly adsorbed molecules on CaY zeolite.[144] Activation energies of 73 and 76 kJ/mol were measured for benzene intra- and intercage hopping, respectively. In addition, they obtained 10^{-19}-10^{-18} m^2/s for self-diffusion coefficients for the temperature range of 338 to 378 K. These are 'slow' diffusion coefficients for site-hopping processes.

Electron complexes in Zeolites

In 1966 it was reported by Kasai *et al.* that a bright color was observed upon exposing NaY to sodium vapor under vacuum.[95] ESR investigations attributed this to the formation of paramagnetic Na_4^{3+} centers consisting of an electron delocalized among four sodium cations. Similarly, the sodium zeolite X (NaX) was found to give a blue color on

exposure to sodium vapor which was interpreted as arising from Na_6^{5+} centers.[145] Subsequently, several other paramagnetic $M_n^{(n-1)+}$ species have been discovered by ESR and crystallography in zeolite X, Y, A and sodalite.[58,146-149] Crystallographic findings have led to an increased understanding of the diversity of alkali-metal clusters that can form within zeolites.[150-153] The most common cluster found is the Na_4^{3+} cationic alkali-metal cluster and the Na_5^{4+} and Na_6^{5+} clusters in zeolite NaX and NaY have also been identified.[153,154] Researchers identified the new alkali metal clusters Cs_4^{3+}, Cs_3^{2+} and Rb_6^{4+} and determined their structures and placement within zeolite A and faujasite X; K_4^{3+} and K_3^{2+} clusters have also been observed in zeolite A.[152,155-158]

Generation of trapped electrons can be achieved photochemically either through photoionization of adsorbed aromatic species[59,61,159] or by direct excitation of the zeolite itself using high energy radiation.[58,156,159-162] Due to the characteristic absorption bands of these clusters, it has been possible to study their nature and reactivity by the use of transient absorption spectroscopy. Some published optical characteristics of some common sodium clusters are given in Table 1-5. These absorption bands are typically quite broad and structureless.[40]
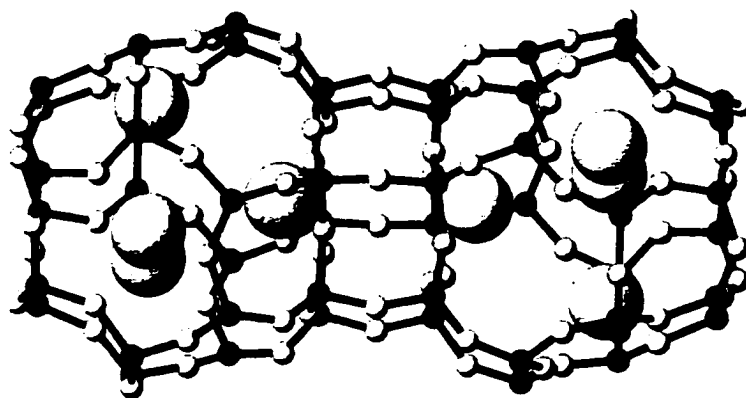
Figure 1-5. Two sodalite cages in NaY showing neighboring Na_4^{3+} centers, each composed of four site I' cations. Taken from reference 154.

Thomas's group and others have explored the phenomenon of electron trapping by particular sites within zeolites using high-energy radiation such as pulsed electrons, γ-rays, X-rays, and pulsed UV-laser light.[58,59,61,147,159-163] In dehydrated zeolites with Na^+ as the charge-compensating cation, three types of trapped electrons species in the form of sodium ion clusters, i.e. Na_4^{3+}, Na_3^{2+} and Na_2^+, were identified with ESR spectroscopy. Na_4^{3+} formed in NaY, Figure 1-5, has a distinctly long lifetime that is highly dependent on the hydration level (nanosecond to milliseconds).

Table 1-5. Optical absorption parameters of some alkali-metal ion clusters in various zeolites.[40]

Sodium cluster	Absorption Band λ_{max} / nm			
	NaA	NaSOD	NaX	NaY
Na_4^{3+}	550	560	550	520
Na_3^{2+}	640	660	650	
Na_2^+	>750			
K_4^{3+}			550	
K_3^{2+}			720	710

The thermal stability of the cluster ions in zeolites has been found to be in the order of Na_4^{3+} > Na_3^{2+} > Na_2^+. The stability appears to be related to the location of these clusters. An *ab initio* simulation study suggested that the cluster Na_3^{2+} is stable when formed within the sodalite cage as Na_4^{3+} but that the Na_2^+ is not stable. The cluster Na_2^+ is presumed to form at window sites in the supercage.[156,161,164]

As was mentioned in the 'hydration' section above, the absorption spectra and lifetimes of trapped electrons in zeolites are affected by the amount of water present, but not by other solvents such as methanol or *n*-pentane.[61,160,163] At a water content of less than 0.02 mL of water per gram of zeolite, a similar transient absorption (λ_{max} = 550 nm) to that in dehydrated NaX was obtained and assigned to Na_4^{3+}. On the other hand, with

increasing amounts of water present within the cavities of the zeolite, an additional broad absorption band with a peak at 880-900 nm appeared. This band was found to appear simultaneously with that of the Na_4^{3+} band. Upon additional amounts of water, the Na_4^{3+} absorption band eventually disappeared. Concomitantly, the peak position of the red absorption band exhibited a blue shift to 780-800 nm. Further shifting to the blue region was observed with increasing amount of co-adsorbed water. There is some debate as to the interpretation for this wavelength-shift. Thomas and co-workers attribute this band to hydrated electrons whereas Hashimoto and co-workers prefer to assign the bands to trapped electrons in the form of smaller cationic clusters, namely a combination of Na_3^{2+} and Na_2^+. It seems there remains uncertainty for the understanding of these bands but their association with complexed electrons is well established.

The faster decay with increasing water content is indicative of quenching of Na_4^{3+} by water molecules adsorbed in the zeolite. In the absence of water, the decay mechanism is believed to be back electron transfer with either the zeolite or the oxidized guest depending on the original ionized matter. However, the presence of other electron traps such as oxygen will have an influence on the observation and lifetime of trapped electrons. Oxygen increases the rate of decay by electron transfer by trapping the electron to form O_2^-.[156]

Complexed electrons in cationic clusters are often observed in transient spectra of organic aromatic species within zeolites, especially for Li^+, Na^+, and K^+ zeolites. Although cationic clusters from Rb^+ and Cs^+ cations are known, these clusters are not typically obtained in absorption spectroscopy which is representative of their reduced stability. As photoionization is a common reaction pathway for photoexcited aromatic molecules, trapped electrons are commonly encountered in transient diffuse reflectance spectra of organic molecules within zeolites.

1.4. Scope of thesis

Despite the considerable amount of information obtained in the past two decades and the central role presently played by zeolites in catalysis and organic reactions, there

are still many aspects of the guest-host behaviour that are poorly understood. Interactions between a guest molecule and a host material are important properties of supramolecular systems that need to be further addressed. Understanding the nature of supramolecular chemical systems involving zeolite-host materials and guest molecules will aid in the development of novel applications using zeolite host materials.

The methodology used by our research group to explore zeolites is to provide a quantitative model that describes the host-guest interactions and the chemistry observed within zeolites. This is achieved by quantifying the effect of the zeolite environment on the chemical reactivity of the incorporated organic guest species. Time-resolved laser flash photolysis studies of reactive intermediates generated within the cavities of zeolites has been utilized to investigate reaction dynamics in these molecular hosts. Specifically, the present report examines the effect of the zeolite environment on the dynamics of carbon-leaving group ionization reactions by examining the heterolysis of β-substituted carbon-centered radicals generated within zeolites. A second aspect of this thesis targets the reactivity of substituted benzyl radicals within the confined environment of non-acidic zeolites. Quantitative information on how the zeolite environment alters the kinetics for these chemical reactions compared to the same reactions in homogeneous solution can help in our understanding of the internal environment of the zeolite and to characterize the various zeolite environments.

Chapter 2. Ionization of β-substituted radicals in Zeolites

2.1. Introduction

The intrazeolite environment has been found to influence fundamental properties of incorporated guest molecules including mobility, photochemistry and thermal reactivity.[7,40,44] In particular, zeolites have been the host choice for many studies of organic cations and radical cations.[40,80,165-171] Presumably, zeolites provide stabilization due to their internal electrostatic fields in addition to providing a confined environment which protects the reactive intermediate from other reactive/quenching species.

Electron-deficient molecules like carbocations are readily generated thermally within zeolites by, for example, protonation of alkenes or ionization of leaving groups in alkyl halides.[172-174] Similarly, radical cations can be produced thermally by zeolite framework induced oxidation of aromatics or alkenes.[175-179] While the properties of these species once formed have been studied extensively, little is known about the dynamics of the chemical reactions taking place within zeolites that lead to carbocation or radical cation formation in zeolites. For example, no quantitative information is available about rate constants for reactions such as protonation or bond heterolysis two classic reactions in organic chemistry that lead to carbocation formation. Information about the kinetics of reactions in organic chemistry has played a central role in the development of principles that allow us to predict whether or not a particular set of conditions are suitable for a particular chemical reaction. The fact that this kind of information is lacking with respect to the formation of carbocations within zeolites, indicates that we lack the ability to predict what factors promote or discourage carbocation formation. As a result, it is difficult to rationally modify a zeolite by changing its composition so that the reaction of interest is promoted while unwanted side-reactions are reduced in importance.

Decades of research have resulted in a thorough understanding of the requirements for efficient carbocation formation via bond heterolysis of leaving groups as

observed in the first step of a S_N1 reactions. In particular, it is well-known that this kind of carbocation formation is strongly influenced by the ionizing ability of the solvent. Thus, water, which is a strongly ionizing solvent, promotes heterolysis of leaving groups, while acetonitrile, a less ionizing solvent, does not promote carbocation formation. One of the goals of the work described here is to determine the ionizing ability of the interior of zeolites relative to solvents like water, 1,1,1,3,3,3-hexafluoroisopropanol (HFIP) or methanol. For example, with respect to bond heterolysis reactions, knowing where the ionizing power of zeolites ranks on scales that are commonly used to represent the ionizing power of solvents and solvent mixtures, such as the Y scale, would be useful in the further development of zeolites as host materials for organic reactions. In addition, little is known about the effect of charge-balancing cations on the dynamics of this kind of reaction. The nature of the charge-balancing cation should have a significant effect on the rate constant for the ionization reactions, since the strength of the electrostatic fields, as shown in Table 1-4, are strongly dependent on the nature of the counterion.

Other variables such as the nature of the leaving group and the presence of electron-donating or electron-withdrawing groups near the reaction center also are known to influence carbocation formation by bond heterolysis in solution. While it is reasonable to assume that carbocation formation within zeolites may be influenced in the same way by these structural changes, no quantitative information about the effect of leaving group ability or substituents on the dynamics of carbocation formation within zeolites is known. Thus, a second goal or this research is to examine the dynamics of heterolysis reactions as a function of these variables.

2.1.1. Strategy for measuring dynamics of bond heterolysis

One of the main reasons for the lack of dynamic information about the formation of carbocations or radical cations is due to the fact that organic substrates are often adsorbed by zeolites more slowly than their subsequent conversion to the reactive carbocation. Thus, when a labile substrate like xanthenol is incorporated into an acidic zeolite like HY or HX, faint colour changes to the zeolite are observed immediately upon incorporation due to the formation of the xanthenyl cation as the substrate is adsorbed into the acidic host.[180] This colour change intensifies as more substrate is adsorbed and then stops once adsorption is complete. Under these circumstances, it is very difficult to study the dynamics of carbocation formation because adsorption of the substrate is likely to be the rate-determining step. Alternatively, it may be that the substrate is converted too slowly to the carbocation. For example, when xanthenol is incorporated into a non-acidic zeolites like NaY at room temperature, no colour change is observed, and no information about the conversion of the substrate to the carbocation can be obtained.

The strategy used in the present work allowed us to use laser flash photolysis techniques to overcome the difficulties outlined above. This strategy involves first incorporating a specially designed thermally stable precursor into a particular zeolite of interest. The precursor is not only required to be thermally stable, but also must be able to undergo a rapid photochemical conversion to a photoproduct, termed a probe molecule, that is sensitive to ionization of a leaving group. Using this strategy, we control when the ionization reaction is initiated, and thus remove any difficulties arising from slow incorporation of the precursor.

The probes chosen for this study are the β-substituted arylethyl radicals generated by photohomolysis of arylethyl acetates as shown in Scheme 2-1.

Scheme 2-1

$$R \text{—} \underset{X}{\text{(C}_6\text{H}_4\text{)}} \text{—CH—CH}_2\text{—LG} \xrightarrow{h\nu} R\text{—(C}_6\text{H}_4)\text{—}\overset{\bullet}{\text{C}}\text{H—CH}_2\text{—LG} \longrightarrow \left[R\text{—(C}_6\text{H}_4)\text{—CH=CH}_2 \right]^{+\bullet}$$
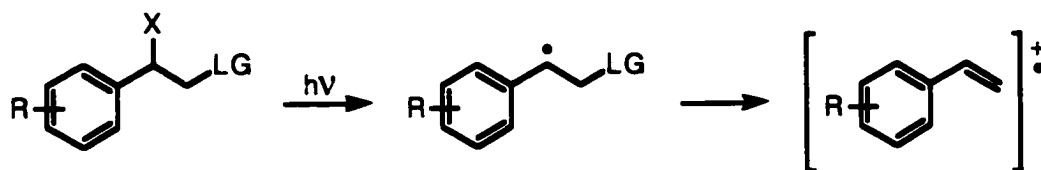
These radicals were chosen for a number of reasons. First and foremost is that these types of radicals are known to undergo fairly rapid ionization of the leaving group in a manner that is very similar to the ionization reaction of more common organic substrates. In particular, as outlined in more detail below, the kinetics for the ionization of the leaving group adjacent to the radical is sensitive to solvent ionizing ability, leaving group ability and electronic effects. Thus, by measuring absolute rate constants for the ionization reaction under different conditions, it is possible to determine and quantify the internal ionizing power of non-acidic zeolites as a function of zeolite structure and composition.

Another reason for having chosen these probes is that the β-substituted arylethyl radicals contain a benzyl radical moiety which have sufficiently characteristic UV spectra for them to be easily identified and observed. In addition, the size and the shape of the probe molecule is similar to that of many classes of aromatic compounds that are currently being investigated within the cavities of zeolites. The results from this work could therefore possibly be extended to other similar compounds. Finally, the ionization of the leaving group leads to the formation of substituted styrene radical cations. These radical cations have been well-studied both in solution and in zeolites.[92,181-186] Of particular importance to the present work is that substituted styrene radical cations have distinctive absorption spectra; hence their generation can be easily monitored using time-resolved diffuse reflectance spectroscopy. Styrene radical cations are also sufficiently long-lived to be easily observed using diffuse reflectance spectroscopy.

For the approach described above to work, the radical must have very specific kinetic properties. In particular, the heterolysis reaction must be relatively fast, but not so

fast that it cannot be resolved with the nanosecond laser system. Thus, the rate constant for the heterolysis cannot be greater than 5×10^7 s^{-1}. At the same time, if the rate constant is too slow, other reactions of the radical, in particular radical-radical coupling, will dominate and heterolysis will not be observed. Also, if the heterolysis reaction is too slow, the radical cation may decay more quickly than it is generated. Under these conditions, no radical cation will be observed, and it would be difficult to determine if ionization is taking place. Other requirements are that the transient spectra should be as free as possible from unexpected transient species. In the presence of such unwanted species, accurate determination of heterolysis rate constants would be made more difficult.

In order to find an appropriate probe that meets these criteria, the following compounds were investigated, Scheme 2-2. These substrates differ with respect to the leaving group and the substituent on the aromatic ring. In some cases, an additional methyl group is present at the β-position. The different structural features will greatly influence the dynamics of the heterolysis and would lead to the formation of a probe radical with appropriate kinetic properties. In addition, if more than one of these probes is suitable, some information concerning the effect of zeolite structure and composition on the effect of substituents on S_N1-like reactions can be obtained.

Scheme 2-2
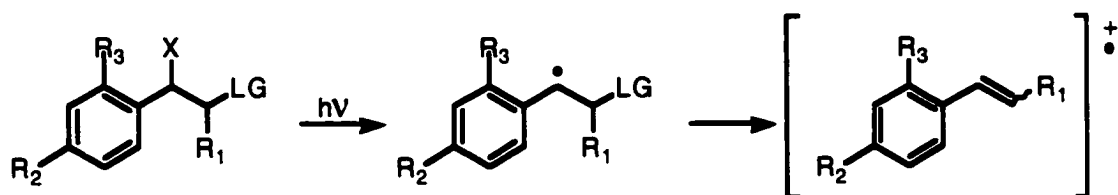
(a) $R_1 = H, R_2 = CH_3O, R_3 = H, LG = Cl$

(b) $R_1 = CH_3, R_2 = CH_3O, R_3 = H, LG = Cl$

(c) $R_1 = H, R_2 = CH_3O, R_3 = H, LG = Br$

(d) $R_1 = CH_3, R_2 = CH_3O, R_3 = H, LG = Br$

(e) $R_1 = H, R_2 = CH_3, R_3 = CH_3, LG = Cl$

(f) $R_1 = H, R_2 = CH_3, R_3 = H, LG = Cl$

(g) $R_1 = H, R_2 = CH_3O, R_3 = H, LG = OC(O)CF_3$

(h) $R_1 = CH_3, R_2 = CH_3O, R_3 = H, LG = OC(O)CF_3$

2.1.2. β-Radicals in solution

In order to understand the reactions of the photogenerated β-substituted radicals in the zeolite, some background information concerning their chemistry in solution must be described. β-Substituted radicals have long been established as reactive intermediates with synthetic and biological relevance.[187] For example, carbon-centred radicals with leaving groups such as hydroxy, ammonium, or phosphate groups attached to the carbon adjacent (β) to the radical are thought to be primary intermediates in some enzyme catalyzed reactions such as ribonucleotide reductase catalyzed conversion of ribonucleotides to deoxyribonucleotides.[188,189] These types of reactive species have also been proposed as intermediates in the mechanism of anaerobic, radical-induced DNA strand scission, eq. 2.1.[190-193] Heterolytic fragmentation of the C3'-O bond leads to formation of an alkene radical cation, which is subsequently trapped by solvent and reduced to form solvolysis products. This mechanism has been supported by

photocurrent measurements, CIDNP (Chemically Induced Dynamic Nuclear Polarization) experiments and by trapping of the radical cation intermediate with allylic alcohols, to name a few.

$$\text{DNA} \xrightarrow[-\text{RH}]{\text{R}\bullet} \quad \longrightarrow \quad 2.1$$
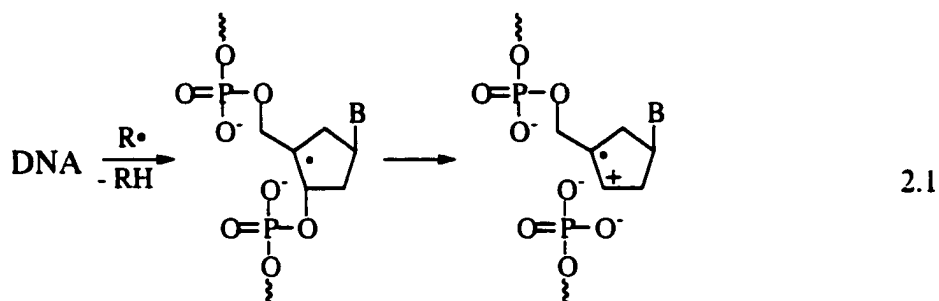
In addition, radicals possessing a β-acetate or phosphate group have also been implicated as intermediates in oxidative lipid damage.[194] Another chemical process where β-radicals have been observed include the photoyellowing of paper.[195]

An early observation made in studies of carbon-centred radicals containing leaving groups such as -Cl, -OSO$_3$R, or -OPO$_3$R$_2$ (R = alkyl) in the β position is that ionization of the leaving group can be very rapid under certain conditions. For example, alkyl β-substituted radicals are hydrolyzed in aqueous solution several orders of magnitude faster than alkyl compounds containing the same leaving-groups. Thus, the rate constant for the hydrolysis of 1-chloro-2-propyl radical, eq. 2.2, is 5.5 x 10^6-fold faster than the hydrolysis of tert-butyl chloride, eq. 2.3.[196,197]

$$\xrightarrow[-\text{H}^+]{\text{H}_2\text{O}} \qquad k_{hyd} = 3.5 \times 10^4 \text{ s}^{-1} \qquad 2.2$$

$$\xrightarrow[-\text{H}^+]{\text{H}_2\text{O}} \qquad k_{hyd} = 6.4 \times 10^{-3} \text{ s}^{-1} \qquad 2.3$$
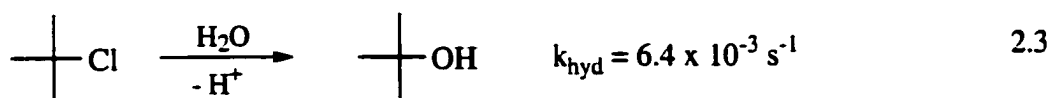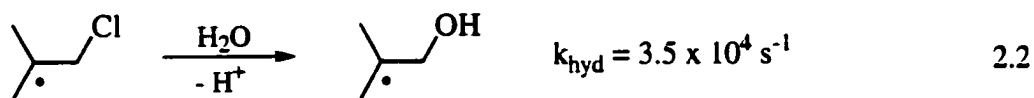
There is evidence from theoretical studies that nucleophilic substitution processes in radicals face much lower kinetic barriers than in closed shell systems. An estimate for

the increase in the speed of the carbon-chlorine bond heterolysis by the neighboring radical center can be obtained by comparing the activation energy for the hydrolysis of the 1-chloro-2-propyl radical (9 ± 1 kcal/mol) with that of *tert*-butyl chloride (22 kcal/mol). This barrier lowering is thought to result from a mixed homolytic/heterolytic character of the dissociation process in open shell systems.[196,198,199]

The importance of β-heterolysis as a reaction pathway of β-substituted radicals was recently examined in a detailed study of the dynamics of this ionization reaction in solution.[200] For example, the heterolytic cleavage of the 2-bromo-1-(4-methoxy-phenyl)propyl ($R_1=OCH_3$, $R_2=CH_3$, X=Br) radical in highly ionizing solvents such as water (H_2O) or 2,2,2-trifluoroethanol (TFE) was found to be very fast with rate constants, k_{-Br}, in the 10^6 to 10^8 s^{-1} range, eq. 2.4 and Table 2-1. Similar fast rate constants for heterolytic cleavage were obtained in LFP kinetic studies of α-methoxy-β-phosphatoxyalkyl radical reactions in 5% TFE/AcN mixtures.[201]

2.4
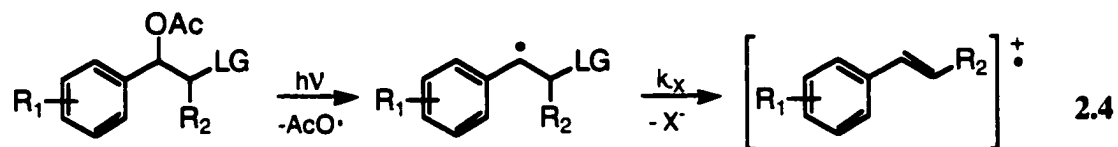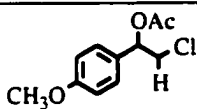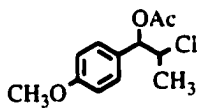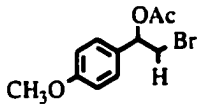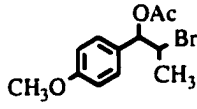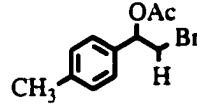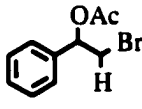
Table 2-1. Selected β-heterolysis rate constants for β-substituted radicals in various solvents.

Compound	$k_{het} / 10^6 \text{ s}^{-1}$					
	83% TFE/ AcN	50% TFE/AcN	83% HFIP/ AcN	50% HFIP/AcN	50% MeOH/H$_2$O	50% AcN/H$_2$O
	2.3	0.64	24	0.52	5.6	1.8
	17	6.4	36	6.6	15	11
	14	2.2	71	2.5	31	7.0
	64	37	98	47	25	52
	β-heterolysis not observed					
	β-heterolysis not observed					

The occurrence of the heterolysis reaction was demonstrated through direct observation of the initial heterolysis product, the substituted styrene radical cation. The reaction was found to be influenced in the same way as other S_N1 type ionization reactions with respect to the nature of the ionizing ability of the solvent, the leaving group, and electronic effects. For example, while heterolysis was typically rapid in highly ionizing solvents like water, no heterolysis was observed in a poorly ionizing solvent like acetonitrile. In this solvent, the radicals decayed in a second-order manner indicating that coupling of two radical-centres was the primary mode of radical decay. Furthermore, when chloride was used as the leaving group instead of bromide, the heterolysis reaction was distinctly slower. This trend is the same as that observed for more conventional S_N1 reactions. In addition, for the 2-bromo-1-phenylethyl (R_1=H, R_2=H, X=Br) and 2-bromo-1-(4-methylphenyl)ethyl (R_1=CH$_3$, R_2=H, X=Br) radicals, no heterolysis was observed even under strongly ionizing conditions. The rate constant for ionization was therefore shown to be strongly dependent on the electron-donating ability by the substituent on the phenyl ring. The results from this study exemplified the ability of the radical center to interact with the positive charge formed as the heterolysis process proceeds from the initial state to the transition state, Scheme 2-3.

Scheme 2-3
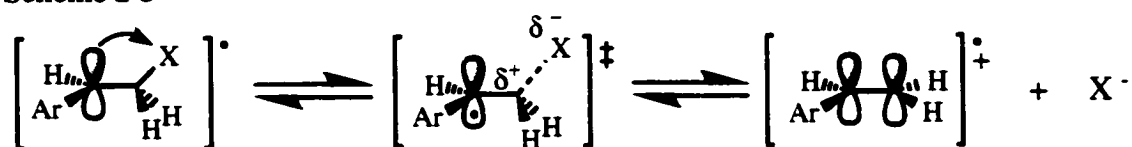
The rate constants for the formation of the radical cation product of the β-substituted radicals were measured in water/methanol mixtures and correlated to the solvent ionizing ability parameter, Y_{AdCl}. Plots of the rate constant versus Y values yielded linear plots with slopes that changed substantially depending on the nature of the

leaving group and the substitution at the β-position, R_2. In all cases, m values (slope of plot) less than 1 ($m = 0.54$-0.72) were obtained indicating a very early transition state and a corresponding decrease in the sensitivity to solvent ionizing power. Slope values less than one are typically observed for ionization reactions with substantial nucleophilic assistance or significant S_N2 character in the substitution reaction. However these possibilities were eliminated due to the direct detection of the radical cation as the product of the heterolysis.

Evidence for reversible nucleophile addition, eq. 2.5, has also been obtained for some of the substrates under the appropriate conditions, such as in polar, ionizing solvents and when the nucleophile was also a good leaving group. In these situations, formation of the β-substituted radical by nucleophilic addition to the radical cation and decomposition of the same radical by β-heterolysis were rapid processes that allowed an equilibrium state to be established in the presence of excess nucleophile. Equilibrium constants for the 2-halo-1-(4-methoxyphenyl)ethyl radical and radical cation equilibrium in 50% aqueous acetonitrile were 0.0023 and 0.0050 M^{-1}, for bromide and chloride ion, respectively. These values imply that the radical cation is the dominant species present at equilibrium with the nucleophile adduct being the less favored species.

$$2.5$$

Heterolysis of the leaving group is not the only reaction available to the β-substituted radicals. For example, β-bromo radicals generated in the photodecomposition of vicinal dibromides in acetonitrile solution undergo homolytic cleavage of the second bromine atom to generate an alkene, eq. 2.6. Using a nanosecond laser photolysis study, the researchers were only able to estimate a lower limit for the formation of the alkene (10^8 s^{-1}) attesting to the fast reactivity of these intermediates.[202,203]

$$\text{(2.6)}$$

In addition to heterolytic and homolytic cleavage of the carbon-leaving group bond, bond rearrangement of the leaving group to generate a more stable radical is another possible reaction of β-substituted radicals, eq. 2.7.

$$\text{(2.7)}$$

The rearrangement reaction is limited to β-(phosphatoxy)alkyl and β-(acyloxy)alkyl radicals. Extensive studies have demonstrated the existence of concerted or ionic mechanisms.[187,204-210] The concerted mechanisms involve either a 1,2-shift or a 2,3-shift depending on the substitution pattern and medium, suggesting that the nature of the transition state changes according to the solvent and substitution of the substrate. Results from these studies have led to the advancement of polarized three electron-three center and five electron-five center cyclic transition state resembling phosphate or carboxylate anions loosely bound to alkene radical cations. In the ionic mechanism, the phosphate or carboxylate anions exist as distinct intermediates ion-paired to the radical cation. Beckwith, Crich and co-authors summarized the available data to a continuum of mechanisms, Scheme 2-4, with the precise location being determined by the ability of the system to support charge separation.[187]

Scheme 2-4

"inert" ⟵——————— rearrangement ———————⟶ fragmentation

Increasing polarity and reaction rate
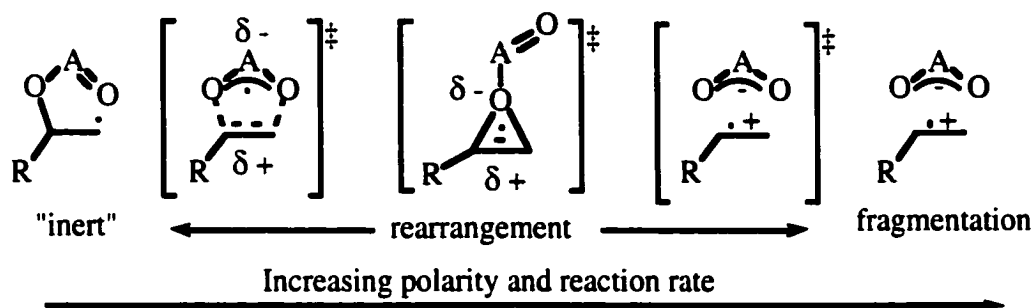
2.1.3. Solvent effects on S_N1 type reactions

A well-known concept in substitution and elimination reactions is the solvent dependence of the rates for these types of reactions. As β-heterolysis and other S_N1 (and also S_N2) reactions lead to the development of charge in the transition state for compounds containing a good leaving group (R-X) the polar environment around the molecule and the solvent ability to stabilize the charges are very important. There are many investigations on the kinetic effect of variations in solvent polarity for different substrates and mechanisms and thus the solvent ability to produce, eliminate or disperse charge in going from the initial state to the transition state. Several correlation equations between the solvent characteristics and their effect on the rates of a reaction have been developed. For example, Gutmann's donor (DN) and acceptor numbers (AN) attempt to measure the ability of solvent molecules to function as Lewis bases and Lewis acids.[211] Other studies use multiple parameter equations to identify various factors that may be important in a reaction such as nucleophilicity, polarization, electrophilic solvation, polarizability, etc. Similarly, developments have been made by Kamlet and Taft for the analyses of S_N1 reactions, eq. 2-8, where π* is a measure of solvent dipolarity/polarizability, α is a measure of solvent hydrogen bond donor acidity, and β is a measure of solvent hydrogen bond acceptor basicity.[212] The absorption maximum solvent-dependence or solvatochromism of zwitterionic betaine dyes has also been used to develop an $E_T(30)$ scale to quantify the solvent polarity.[213]

$$\log k = \log k_o + s\pi^* + a\alpha + b\beta \qquad \text{2-8}$$

However, the Grunwald-Winstein equation is the most commonly used correlation of solvent effects on the reactivity of substitution reactions, eq. 2-9.[211,214-218] This linear free-energy relation for solvent ionizing power is defined in terms of the solvolysis rate of t-butyl chloride, a system assumed to react without nucleophilic assistance with S_N1 reactivity; where k/k_o refers to solvolysis rates at 25 °C in any solvent (k) relative to 80% v/v ethanol/water (k_o),

$$\log\left(\frac{k}{k_o}\right)_{t-BuCl} = mY \qquad \text{2-9}$$

The Y value then represents the characteristic "ionizing power" property of the measured solvent. For t-butyl chloride solvolysis rates, the slope m, is defined as 1. For other reactions m measures the sensitivity of the particular system to solvent change; where a value less than one represents small sensitivity. Subsequent studies of solvolytic reactions in weakly nucleophilic, highly ionizing media such as HFIP and trifluoroacetic acid demonstrated that nucleophilic assistance on the relative rates of t-butyl chloride had been underestimated.[219] As a result, further refinements and additional ionizing scales have since been developed. In particular, solvolysis of 1- and 2-adamantyl substrates have played a central role in mechanistic aspects of solvolysis reactions. The relatively rigid, caged structure of the adamantyl skeleton allows a systematic study of both solvent and structural effects on organic reactivity. Backside nucleophilic attack on this substrate is inhibited sterically and a variety of solvent ionizing power scales for different leaving groups have been formulated.[215,217,220-223] Table 2-2 presents a selected list of solvents and their properties with respect to polarity.

Table 2-2. Solvent parameters typically used for quantifying solvent ability to create/stabilize charged species for selected solvents.[214,224]

Solvent	Y_{Ots}[a]	Y_{OTf}[b]	Y_{Br}	Y_{Cl}	Y^c	ε^d	π^*	$E_T(30)$ (kJ/mol)
EtOH	-1.96	-1.66	-2.4	-2.5	-2.03	24.3	0.54	217
80% aq. EtOH	0.0	0.0	0.0	0.0	0.0			
H₂O	4.1		4.44	4.57	3.49	80.4	1.09	264
MeOH	-0.92	-0.79	-1.12	-1.2	-1.09	32.7	0.60	232
80% aq. MeOH	0.47	0.52	0.70	0.67	0.38			
60% aq. MeOH	1.52	1.53	2.04	2.07	1.49			
40% aq. MeOH	2.43	2.51	3.14	3.25	2.39			
20% aq. MeOH	3.39		3.94	4.10	3.03			
50% aq. AcN	1.2							
25% aq. AcN	2.5							
10% aq. AcN	3.6							
TFE	1.77		2.53	1.0	1.15	26.5	0.73	249
85% aq. TFE	1.92							
70% aq. TFE	2.00	1.42	2.79	2.96	1.66			
HFIP	3.82					16.7	0.65	273
97% aq. HFIP	3.61		4.51	5.08	2.46			
AcN	-3.21					37.5	0.75	193

[a] 1- and 2-Adamantyl tosylate. [b] 2-Adamantyl triflate. [c] t-Butylchloride. [d] Dielectric constant.

2.2. Results

The following sections present results concerning diffuse reflectance laser flash photolysis of β-substituted arylalkyl acetates in alkali-metal zeolites. Unless otherwise stated, the excitation source was the fourth harmonic from a Nd:YAG laser (266 nm, <10 mJ/pulse, < 10 ns/pulse). Detailed explanation of the sample preparation and conditions under which the experiments were performed can be found in the experimental section. Thermal stability of the various compounds within the zeolites used in this study was verified by the incorporation of the compounds with subsequent removal from the zeolite cavities by continuous extraction. In each case, the extracted material consisted exclusively of the starting material, which suggests that the precursor molecules are thermally stable within the cavities of the zeolite over the time frame of a typical experiment. The only exception was 2-bromo-1-(4-methoxyphenyl) propyl acetate which decomposed in the Y zeolites. The average loading level is typically about one molecule in every ten zeolite cavities (<S> ~ 0.10). A slightly higher substrate loading level was used only when the transient absorption was too small to be easily detected; in those cases a loading of one molecule in every five zeolite cavities was used. The Figures described in the text can be found after each section.

2.2.1. Photolysis of 2-chloro-1-(4-methoxyphenyl)ethyl acetate in alkali-metal exchanged Y zeolites

The incorporation of ca. 4 mg of 2-chloro-1-(4-methoxyphenyl)ethyl acetate (AcOClVA) into ca. 315 mg NaY using hexanes as the carrier solvent led to 100 % incorporation of the organic compound into the zeolite. Assuming a random distribution the loading level corresponds to one molecule of AcOClVA in every ten supercages.

The time-resolved diffuse reflectance spectra generated upon 266 nm excitation of AcOClVA in NaY in an evacuated (10^{-4} torr), sealed sample cell are shown in Figure 2-1. The spectrum taken 360 ns after the laser pulse consists of two strong absorption bands located at 360 and 600 nm. The two bands showed the same decay profile which suggests that they belong to the same transient species (inset of Figure 2-1). The location

and shape of these two bands are identical to those of the 4-methoxystyrene radical generated previously from AcOClVA in solution,[200] and by photoionization of 4-methoxystyrene in solution[185,186] and in zeolites.[92] Thus, the transient generated upon irradiation of the AcOClVA in NaY can be readily identified as the 4-methoxystyrene radical cation, eq. 2.10.

2.10
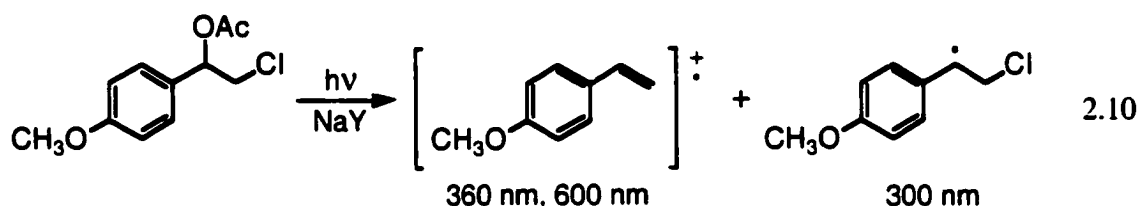
The possibility that these absorption bands at 360 and 600 nm belong to the 2-chloro-1-(4-methoxyphenyl)ethyl acetate radical cation generated by photoionization of an electron from the anisole group of AcOClVA can be ruled out since alkyl-substituted anisole radical cations typically have absorption maxima near 420 nm in solution and in zeolites.[165] However, in the 420 nm region of the transient spectrum shown in Figure 2-2, a weak absorption band is seen which is consistent with the formation of a small amount of 2-chloro-1-(4-methoxyphenyl)ethyl acetate radical cation via photoionization of AcOClVA. In agreement with the formation of a small yield of radical cation is the broad and structureless band that can be detected around 500 nm under vacuum conditions, Figure 2-1. This absorption band is typical for the trapped electron complex, Na_4^{3+}. Support for this assignment can be obtained from the observation that the 500 nm band is significantly quenched under a nitrous oxide environment, Figure 2-2.

The spectra in Figure 2-1 also show the presence of a short wavelength absorption band near 300 nm. The same band is observed upon irradiation of 2-chloro-1-(4-methoxyphenyl)ethyl acetate in acetonitrile and has been identified as the 2-chloro-1-(4-methoxyphenyl)ethyl radical. Thus, laser irradiation of AcOClVA in NaY leads to the formation of two identifiable transients, the 4-methoxystyrene radical cation and the 2-chloro-1-(4-methoxyphenyl)ethyl radical, eq. 2.10.

Purging the zeolite sample prior to photolysis with oxygen led to complete quenching of all absorption bands, Figure 2-3. Reactivity with oxygen is a common method of identifying radical species, and is consistent with the identification of the 300 nm band as the 2-chloro-1-(4-methoxyphenyl)ethyl radical. On the other hand, the 4-methoxystyrene radical cation has been shown to be unreactive toward oxygen.[225] Thus, the absence of the radical cation in the presence of oxygen is not due to a direct quenching reaction. Instead, the observation that oxygen completely inhibits the formation of the radical cation indicates that it is generated from an oxygen sensitive precursor. This is consistent with a mechanism for the formation of the 4-methoxystyrene radical cation upon photolysis of AcOClVA that involves rapid β-heterolysis of the photogenerated β-substituted arylethyl radical, eq. 2.11.

According to this mechanism, complete trapping of the radical by oxygen would lead to no radical cation formation, eq. 2-12.

The time-resolved growth of the 600 nm band due to formation of the 4-methoxystyrene radical cation in NaY is shown in Figure 2-4. The kinetic trace was analyzed with a double first-order expression, with one component of the fit corresponding to the first-order growth, and the second component corresponding to the initial decay of the radical cation. The data fit well to the rate expression, and gave a rate

constant for the growth of 3.9×10^7 s^{-1}. This value is close to, but slightly less than the maximum rate constant of 5×10^7 s^{-1} that can be measured with the diffuse reflectance laser system used for this investigation. Thus, since the radical cation is produced by loss of chloride from the initially formed 2-chloro-1-(4-methoxyphenyl)ethyl radical, the rate constant of 3.9×10^7 s^{-1} represents the rate constant, k_{het}, for the heterolysis reaction, eq. 2.11.

In order to study the effect of framework counterbalancing cation on the rate constant for β-heterolysis, substrate reactivity, AcOClVA was also incorporated into LiY, KY, RbY and CsY, using hexane as the carrier solvent. All samples, including NaY, were prepared in the same manner, on the same day and with loading levels of one molecule in every ten supercages. Thus, all experimental factors (*e.g.* volume of solvent used, solvent removal, evacuation time, climate conditions, etc.) are constant throughout the study and the only variable is the nature of the counterbalancing cation associated with the zeolite framework.

The diffuse reflectance spectra obtained upon 266 nm laser irradiation of AcOClVA in the LiY, KY, RbY and CsY zeolites under dry, evacuated (10^{-4} torr) and sealed conditions are shown in Figures 2-5 to 2-8. In each spectrum, a strong absorption band at 360 nm and a weaker band at 600 nm corresponding to the 4-methoxystyrene radical cation are readily observable. In each case, the decay of the two absorption bands was identical which supports an assignment of the bands to a single transient species, the 4-methoxystyrene radical cation. In RbY and CsY, a third absorption band is also clearly observable at 300 nm. Close examination of the spectra for LiY, NaY and KY reveals the presence of this 300 nm band, but to a much lesser extent.

In addition to the radical cation, the 2-chloro-1-(4-methoxyphenyl) ethyl radical is a necessary intermediate along the reaction pathway. As described earlier, this radical is known to have an absorption maximum near 300 nm. Assignment of an absorption band to a radical species is classically supported by the quenching of the band by the addition of oxygen. Indeed, the intensity of the 300 nm band decreased and the decay rate constant increased in the presence of oxygen. On the basis of these observations, the

absorption at 300 nm is assigned to the 2-chloro-1-(4-methoxyphenyl)ethyl radical produced by photohomolysis of 2-chloro-1-(4-methoxyphenyl)ethyl acetate, eq. 2.11.

The time-resolved kinetic traces at 600 nm due to the 4-methoxystyrene radical cation produced upon laser photolysis of ACOClVA under vacuum conditions in each of the cation-exchanged zeolites are shown in Figure 2-9. In LiY (Figure 2-9a), a significant increase in absorption due to the formation of the radical cation by β-heterolysis is observed, but this increase is complete within the 20 ns time resolution of the diffuse reflectance laser system. Thus, the rate constant for β-heterolysis of the chloride leaving group from 2-chloro-1-(4-methoxyphenyl)ethyl radical in LiY must be equal to or greater than 5×10^7 s^{-1}. The β-heterolysis reaction in LiY is therefore more rapid than the same reaction in NaY discussed above which occurred with a rate constant of 3.9×10^7 s^{-1}. It should be noted that a small growth following the very rapid rise in absorption at 600 nm in LiY is evident in Figure 2-9a. However, this growth was always very small compared to the rapid rise, and was too weak to be analyzed.

In KY, the growth in absorption at 600 nm was sufficiently slow to be analyzed. Fit of the growth using the double exponential rate expression led to a rate constant for heterolysis of 8.9×10^6 s^{-1} that is significantly slower than the heterolysis rate constant in both NaY and LiY. This trend whereby increasing the cation size decreases the rate constant continues in RbY and CsY. In both of these zeolites, the growth of the radical cation is clearly observed, and is distinctly slower than the growths in all of the other Y zeolites. In RbY, analysis of the growth trace led to a rate constant for β-heterolysis of 3.4×10^6 s^{-1} that is almost 3-fold slower than the rate constant in KY, while in CsY, the rate constant for heterolysis was measured to be a further 4-fold smaller at 1.0×10^6 s^{-1}. All of the rate constants for the formation of the 4-methoxystyrene radical cation by heterolysis are summarized in Table 2-3.

Table 2-3. First-order rate constants for the heterolysis of chloride from the 2-chloro-1-(4-methoxyphenyl)ethyl radical (22 ± 1°C) in dry alkali metal-cation exchanged Y zeolites.

Counterion	k_{het} / s^{-1}
Li^+	$> 50 \times 10^6$
Na^+	$(39 \pm 2) \times 10^6$
K^+	$(8.9 \pm 0.5) \times 10^6$
Rb^+	$(3.4 \pm 0.6) \times 10^6$
Cs^+	$(1.0 \pm 0.3) \times 10^6$

Since the radical cation is produced by heterolysis of the leaving group from the radical, the rate constant for the disappearance of the radical should match the rate constant for the growth of the radical cation. However, acquiring reliable data for the decay at 300 nm at short times after the laser pulse was not possible due to strong luminescence at this wavelength. This luminescence persisted for up to 300 ns after the laser pulse. Since radical cation formation in LiY, NaY and KY was essentially complete over this time scale, it is not surprising that the decay of the radical in these zeolites could not be observed. The growth of the radical cation in RbY and CsY was slower, and a small decay at 300 nm due to the disappearance of the radical was observed in these zeolites. The rate constant for the decay of the 300 nm band in this region was $(8 \pm 1) \times 10^5 s^{-1}$ for CsY; representative kinetic decay traces for the radical and radical cation bands are given in Figure 2-10.

2.2.2. Effect of oxygen on β-heterolysis

The presence of oxygen during laser irradiation of 2-chloro-1-(4-methoxyphenyl) ethyl acetate in the various alkali-metal exchanged zeolites (insets in Figures 2-5 to 2-8) had the same effect as described above for NaY, Figures 2-1 and 2-3. In each case, an oxygen environment completely suppressed the formation of the 4-methoxystyrene

radical cation by trapping the radical precursor prior to ionization of chloride.

In order to learn more about the effect of oxygen on the kinetics of the β-heterolysis reaction, samples were purged with varying mixtures of N_2 and O_2 ranging from 100% N_2 to 90% N_2:10% O_2 to 50% N_2:50% O_2, Figure 2-11. As shown in Figure 2-12, the radical cation was still observed in the samples purged with the 90% N_2:10% O_2 gas mixture. However, a significant reduction in the initial diffuse reflectance intensity of the radical was observed in all of the alkali-exchanged Y zeolites. The results shown in these spectra suggest partial quenching of the formation of the styrene radical cation (*i.e.* less β-heterolysis taking place) due to the competitive reaction of the β-chloro radical with molecular oxygen, eq. 2.12.

Figure 2-11 shows kinetic traces from experiments carried out in KY. These traces clearly show that the amount of oxygen significantly decreases the amount of 4-methoxystyrene radical cation formed. In addition, the rate constant for the formation of the radical cation increases as the oxygen content of the gas increases. Thus, in KY purged with the 10% O_2:90% N_2 mixture, the rate constant for the growth of the radical cation was almost twice the rate constant for the growth in KY purged with pure N_2. In the 50:50 mixture, the rate constant became too fast to measure. These results are also consistent with the reactions shown in eq. 2-12 whereby oxygen traps the radicals which also undergo β-heterolysis. Under these circumstances, the observed rate constant for the disappearance of the radical, and hence the growth of the radical cation, is the sum of the rate constants for heterolysis and addition of oxygen to the radical, eq. 2-13, and should increase with increasing O_2 content.

$$k_{growth} = k_{het} + k_{O_2}[O_2]$$
2.13

2.2.3. Effect of oxygen on decay of 4-methoxystyrene radical generated by β-heterolysis

While examining the effect of oxygen on the heterolysis reaction, it also became evident that the rate constants for the decay of the 4-methoxystyrene radical cation generated by β-heterolysis were in some cases strongly influenced by the presence of oxygen. The effect of oxygen on the decay of the radical cation in different alkali-metal Y zeolites is shown in Figure 2-13. These kinetic traces clearly show that in all of the zeolites except LiY, the presence of a 10% oxygen atmosphere increases the decay of the radical cation. The extent of this effect was found to be strongly dependent on the nature of the counterbalancing cation, with oxygen being a far more effective quencher of the radical cation as the size of the cation increases from Li^+ to Cs^+.

This effect could in principle be quantified by calculating the rate constants for the decay of 4-methoxystyrene radical cation in the Y zeolites under pure nitrogen and the 90% nitrogen:10% oxygen mixture (9:1). However, since in some cases, the radical cation does not completely decay over time-scales as long as 500 μs after the laser pulse, obtaining accurate rate constants is difficult. Under these circumstances, the traces were analyzed on the basis of the assumption that the radical cation decayed completely to zero. In addition, the traces clearly did not fit well to a first-order expression, but were found to fit well to a double first-order rate expression. The rate constants determined in this way for the radical cation decay under a pure N_2 atmosphere and an atmosphere of 10% O_2 : 90% N_2 are listed in Table 2-4. Not surprisingly, the rate constants associated with the slow component are highly variable due to the fact that only a small fraction of the slow decay is captured over the 500 μs of the experiment. However, the rate constants associated with the fast components clearly indicate that oxygen increases the rate constant for radical cation decay in the presence of oxygen and that the oxygen effect is strongest in CsY, and smallest in LiY, Table 2-5.

Table 2-4. Decay rate constants for the disappearance of 4-methoxystyrene radical cation from β-heterolysis under dry nitrogen and dry 90% nitrogen:10% oxygen conditions at 22 ± 1 °C.

MY	Nitrogen		90% Nitrogen:10% Oxygen	
	k_{decay} / $10^4 s^{-1}$ (fast)	k_{decay} / $10^2 s^{-1}$ (slow)	k_{decay} / $10^4 s^{-1}$ (fast)	k_{decay} / $10^2 s^{-1}$ (slow)
LiY	1.06 ± 0.10	4.76 ± 0.23	1.05 ± 0.18	5.28 ± 0.38
NaY	1.53 ± 0.10	9.71 ± 0.19	1.67 ± 0.14	12.5 ± 4.7
KY	0.66 ± 0.11	6.46 ± 0.54	1.82 ± 0.13	9.47 ± 0.29
RbY	0.81 ± 0.04	7.21 ± 0.37	5.40 ± 0.35	4.02 ± 0.46
CsY	0.96 ± 0.06	13.7 ± 0.9	8.37 ± 0.71	4.32 ± 0.40

Table 2-5. Ratio of decay rate constants for the fast component shown in Table 2-4 for the 4-methoxystyrene radical cation in the dry nitrogen and dry 90% nitrogen:10% oxygen conditions.

MY	Ratio 90% N_2:10% O_2/100% N_2 Fast decay
LiY	0.99
NaY	1.09
KY	2.75
RbY	6.66
CsY	8.75

The observation that oxygen increased the rate constant for the decay of the 4-methoxystyrene radical cation was very surprising since previous studies had shown that the decay of the same radical cation generated by photoionization of 4-methoxystyrene in solution and in zeolites was completely insensitive to the presence of oxygen.[92,185,186] One possible explanation for the increased decay rate constant observed in the present work is that a dynamic 4-methoxystyrene radical cation / 2-chloro-1-(4-methoxy-phenyl)ethyl radical equilibrium is generated within the zeolite cavity, eq. 2.14.

$$+ \quad Cl^- \qquad 2.14$$
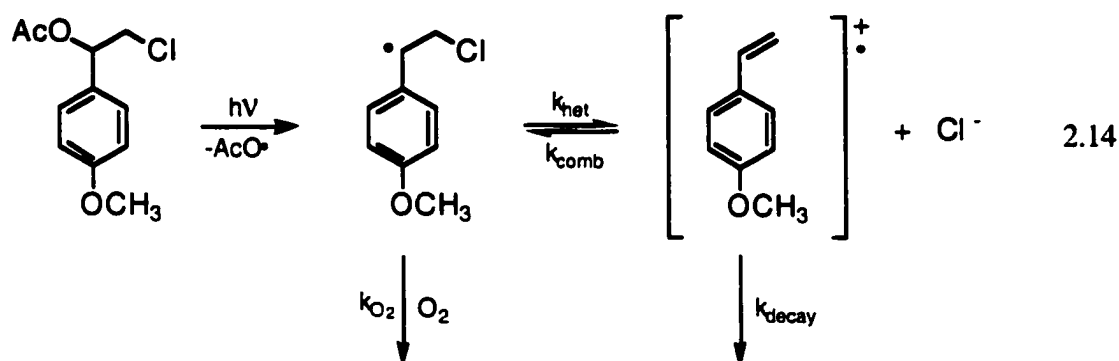
Under these conditions, the observed decay rate constant for the disappearance of 4-methoxystyrene radical cation is described by equation 2.15. According to this equation, the rate constant will increase in the presence of oxygen as a direct result of quenching of the β-chloro radical with oxygen.

$$k_{obs} = \frac{k_{decay} k_{het} + k_{O_2} k_{comb} [O_2][Cl^-]}{k_{het} + k_{comb} [Cl^-]} \qquad 2.15$$

Alternatively, if no equilibrium is present and radical cation formation is irreversible, eq. 2.16, the observed rate constant for the decay of the radical cation would be independent of the presence of oxygen, eq. 2.17.

$$+ \quad Cl^- \qquad 2.16$$
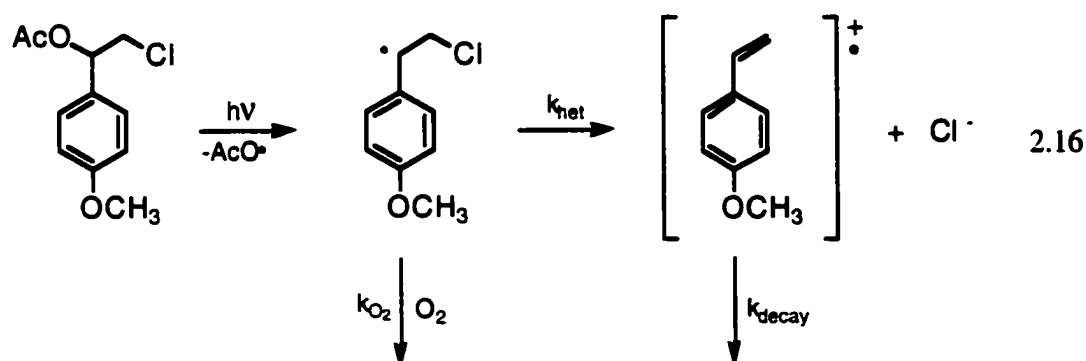
$$k_{obs} = k_{decay}$$

$$2.17$$

Attempts were made to obtain data that might be used to estimate a value of the equilibrium constant for the radical and the radical cation equilibrium. Since the values for the rate constants for heterolysis, k_{het}, were already measured in the present work, an equilibrium constant, $K_{eq}= k_{het}/k_{comb}$, could have been obtained by measuring the rate constant for addition of chloride to the radical cation, k_{comb}, using eq. 2.18.

$$2.18$$
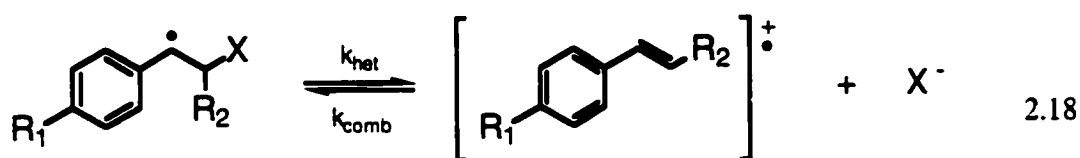
Obtaining a value for k_{comb} requires generating the 4-methoxystyrene radical cation by an alternative method, namely photoionization of 4-methoxystyrene. In addition, the decay of the radical cation generated in this way would have to be examined as a function of added chloride ion. The introduction of chloride salts into the selected cation-exchanged zeolites was attempted by stirring the zeolite powder in an aqueous concentrated solution of the corresponding metal chloride salt. Minimal washing of the zeolite slurry was performed in order to avoid removing the chloride ions from the zeolite.

Unfortunately, experiments with 4-methoxystyrene and AcOClVA in NaY and CsY containing chloride ions were quite uninformative. The spectra and kinetics obtained for NaY and NaY/NaCl and also CsY and CsY/CsCl complexes were virtually identical, indicating the added nucleophile was having little effect on the dynamics of the system. The kinetic traces obtained in the presence and absence of added chloride anion for 4-methoxystyrene in NaY and CsY are shown in Figures 2-14 and 2-15.

Other attempts were made to incorporate chloride ions within the cavities of zeolites using tetrabutylammonium chloride salt with hexanes as the carrier solvent, Figure 2-16. As above, the kinetics and spectra were fairly similar upon laser photolysis

of 4-methoxystyrene in both the zeolites with and without the addition of chloride. These results indicate that the salt must be strongly interacting with the zeolite framework, hence the chloride is unable to play a nucleophilic role. It is also likely that the precursor molecule resides in a completely different cavity than the chloride anion, which again would decrease the probability for an equilibrium to be established. UV/vis spectra obtained of the decanted zeolite slurries demonstrated much lower incorporation levels of the 4-methoxystyrene in the presence of tetrabutylammonium chloride salt. Presumably, the strong interaction between the salt and the interior polar zeolite framework on the outer surface of the zeolite prevents the incorporation of the 4-methoxystyrene. In this case, the salt would likely block the cavities from the incorporation of the 4-methoxystyrene.
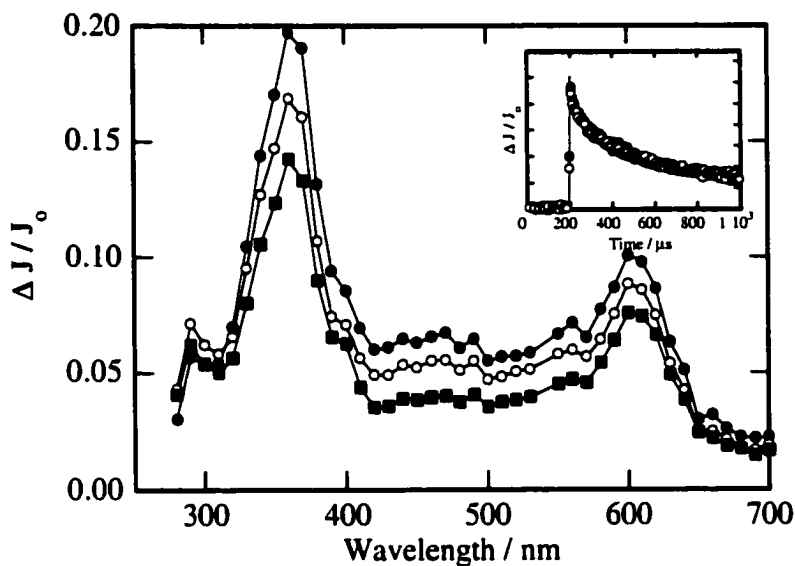
Figure 2-1. Transient diffuse reflectance spectra after 266 nm excitation of 2-chloro-1-(4-methoxyphenyl)ethyl acetate in NaY under vacuum (10^{-4} torr) conditions. Spectra were recorded (●) 0.36 μs, (O) 2.56 μs, and (■) 14.4 μs after the laser pulse. The inset shows the normalized time-resolved decays at 365 nm (●) and 600 nm (O) over 800 μs.
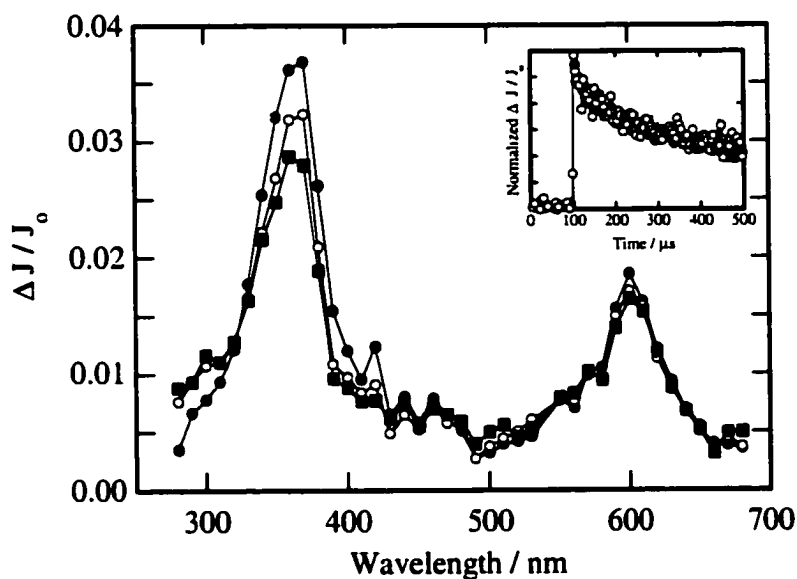
Figure 2-2. Transient diffuse reflectance spectra after 266 nm excitation of 2-chloro-1-(4-methoxyphenyl)ethyl acetate in NaY under a nitrous oxide environment. Spectra were recorded (●) 0.48 μs, (O) 4.48 μs, and (■) 12.8 μs after the laser pulse. The inset shows the normalized time-resolved decays at 365 nm (●) and 600 nm (O) over 400 μs.
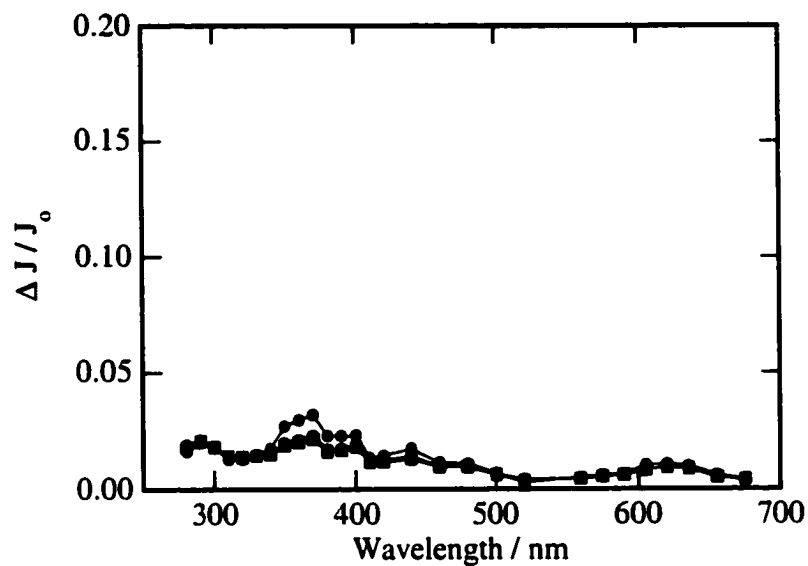
Figure 2-3. Transient diffuse reflectance spectra after 266 nm excitation of 2-chloro-1-(4-methoxyphenyl)ethyl acetate in NaY under an oxygen environment. Spectra were recorded (●) 0.48 μs, (○) 7.52 μs, and (■) 12.7 μs after the laser pulse.
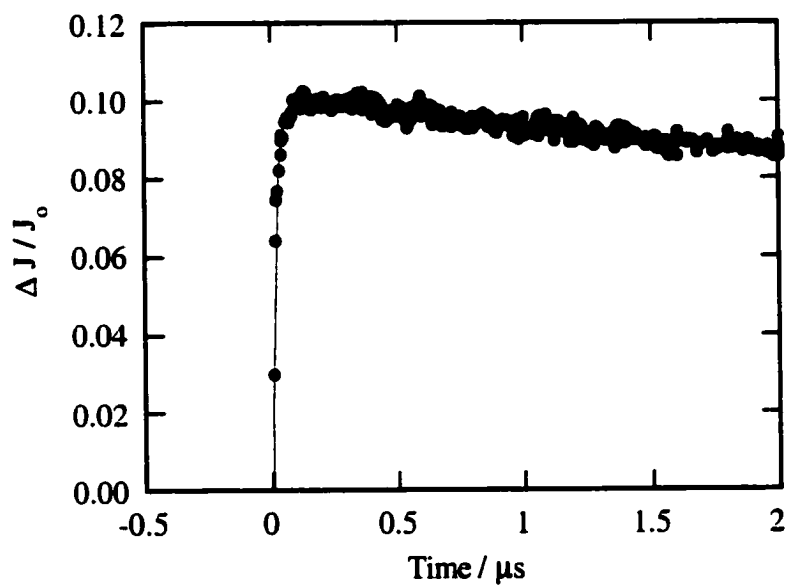
Figure 2-4. Time-resolved changes at 600 nm observed upon 266 nm laser irradiation of 2-chloro-1-(4-methoxyphenyl)ethyl acetate in NaY under vacuum (10^{-4} torr).
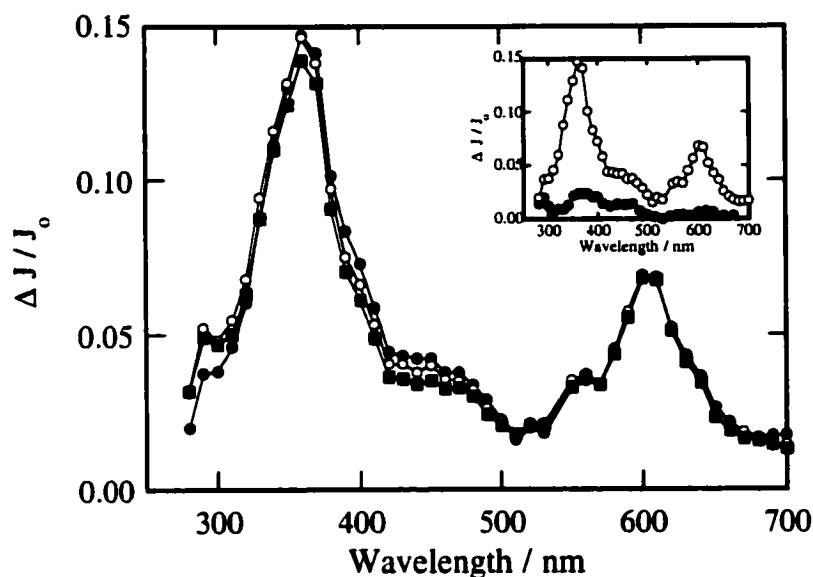
Figure 2-5. Transient diffuse reflectance spectra after 266 nm excitation of 2-chloro-1-(4-methoxyphenyl)ethyl acetate in dry LiY under vacuum conditions (10^{-4} torr). Spectra were recorded (●) 0.36 µs, (○) 1.16 µs, and (■) 2.56 µs after the laser pulse at 22 ± 1 °C. Inset compares the transient spectrum obtained 360 ns after photolysis in evacuated (●) and oxygen-saturated (○) NaY.
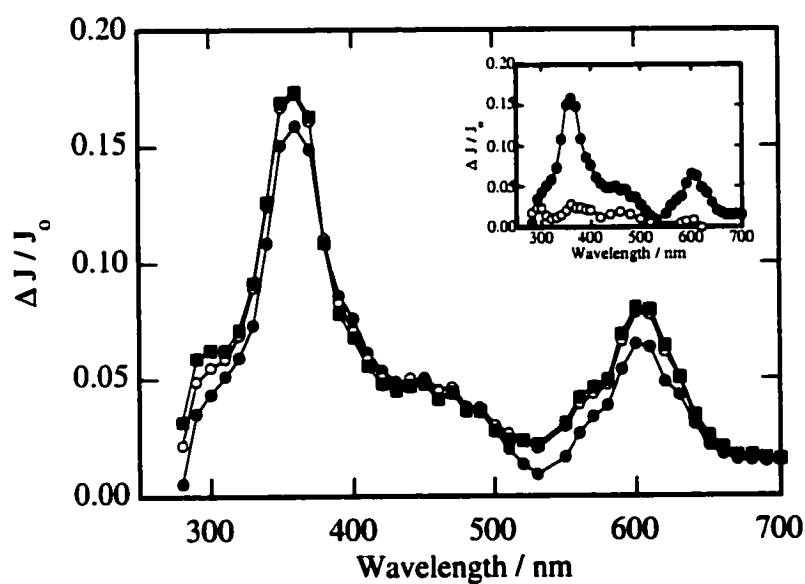
Figure 2-6. Transient diffuse reflectance spectra after 266 nm excitation of 2-chloro-1-(4-methoxyphenyl)ethyl acetate in dry KY under vacuum conditions (10^{-4} torr). Spectra were recorded (●) 0.16 µs, (○) 0.32 µs, and (■) 0.48 µs after the laser pulse at 22 ± 1 °C. Inset compares the transient spectrum obtained 160 ns after photolysis in evacuated (●) and oxygen-saturated (○) KY.
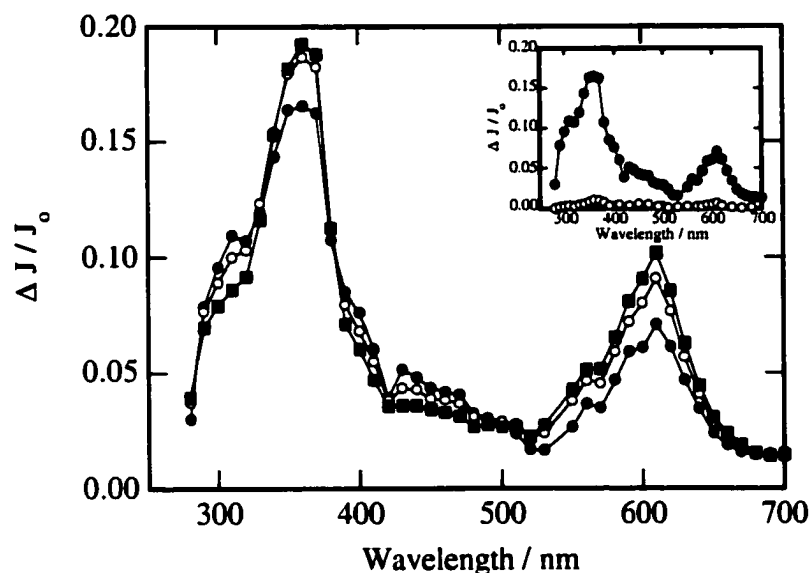
Figure 2-7. Transient diffuse reflectance spectra after 266 nm excitation of 2-chloro-1-(4-methoxyphenyl)ethyl acetate in dry RbY under vacuum conditions (10^{-4} torr). Spectra were recorded (●) 0.28 μs, (○) 0.60 μs, and (■) 1.48 μs after the laser pulse at 22 ± 1 °C. Inset compares the transient spectrum obtained 280 ns after photolysis in evacuated (●) and oxygen-saturated (○) RbY.
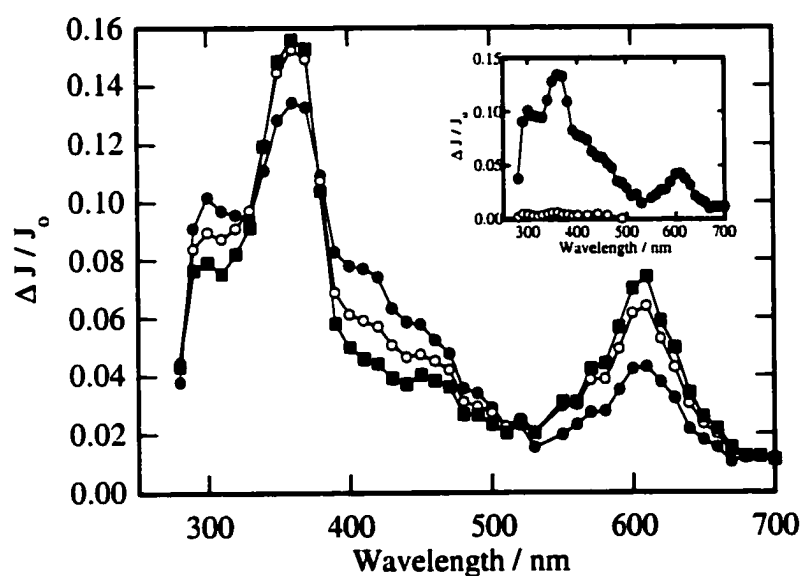
Figure 2-8. Transient diffuse reflectance spectra after 266 nm excitation of 2-chloro-1-(4-methoxyphenyl)ethyl acetate in dry CsY under vacuum conditions (10^{-4} torr). Spectra were recorded (●) 0.36 μs, (○) 1.16 μs, and (■) 2.56 μs after the laser pulse at 22 ± 1 °C. Inset compares the transient spectrum obtained 360 ns after photolysis in evacuated (●) and oxygen-saturated (○) CsY.
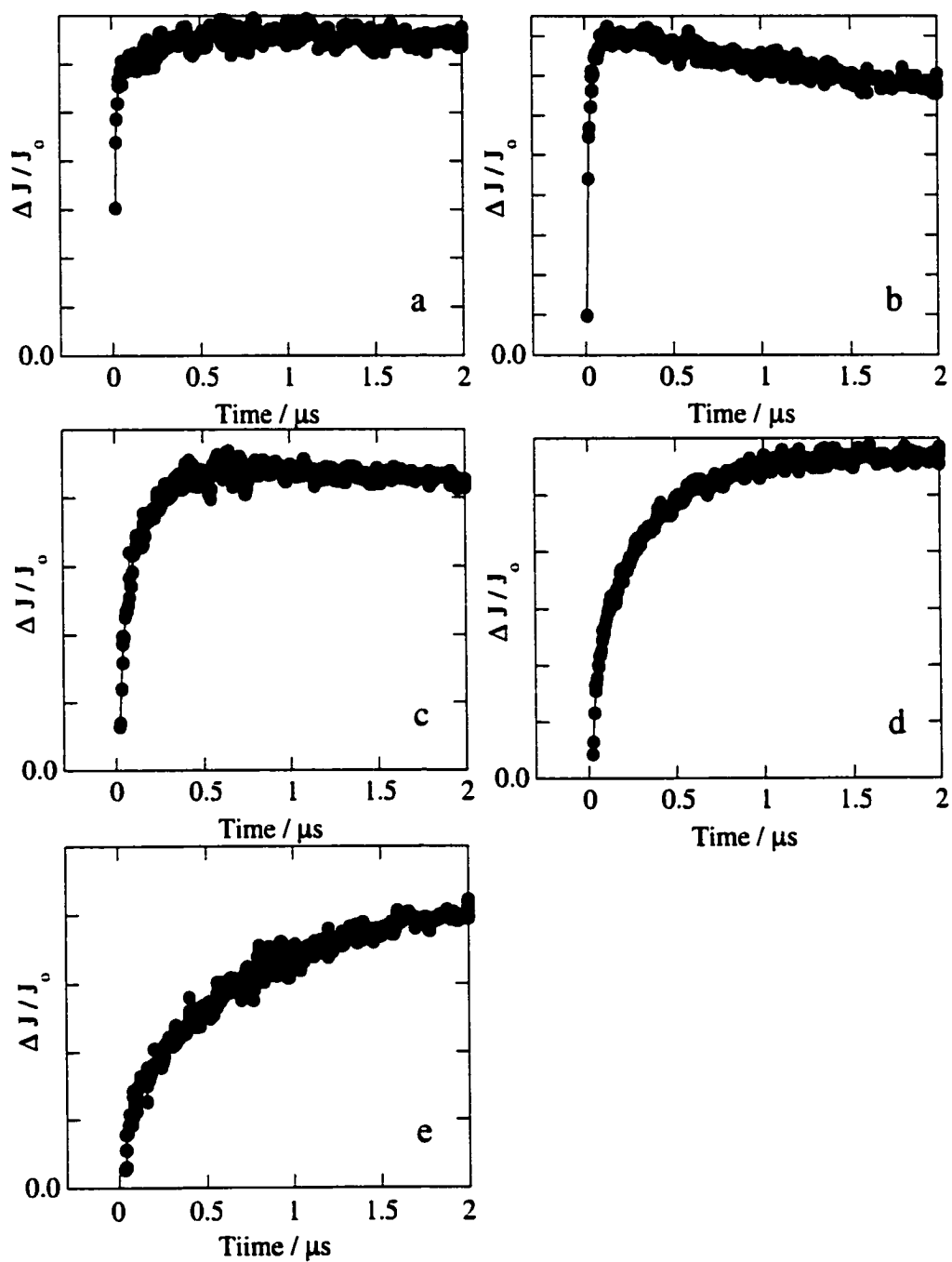
Figure 2-9. Time resolved growth traces generated upon 266 nm excitation of 2-chloro-1-(4-methoxyphenyl)ethyl acetate in dry (a) LiY,(b) NaY, (c) KY, (d) RbY and (e) CsY under vacuum and sealed (10^{-4} torr) conditions. Traces were monitored at 600 nm over 2 μs at 22 ± 1 °C.
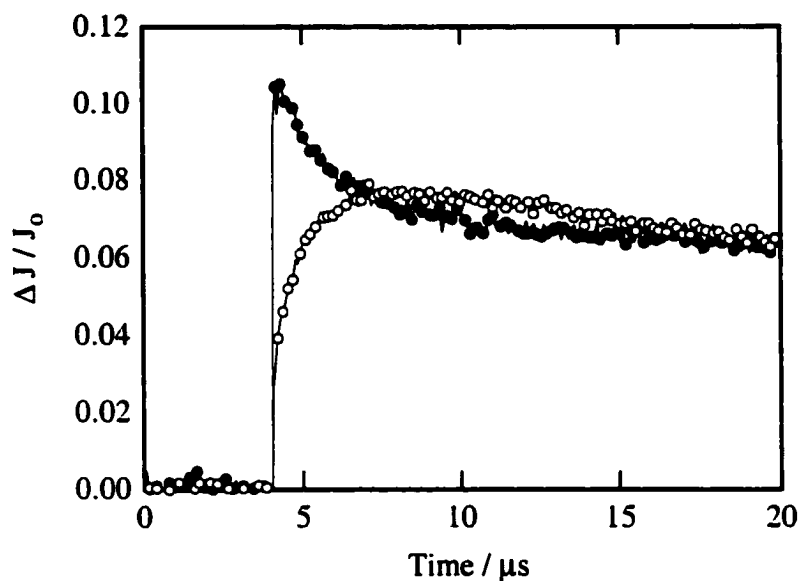
Figure 2-10. Time resolved kinetic traces generated upon 266 nm excitation of AcOClVA in CsY under vacuum (10^{-4} torr) at (●) 300 nm and (○) 600 nm.
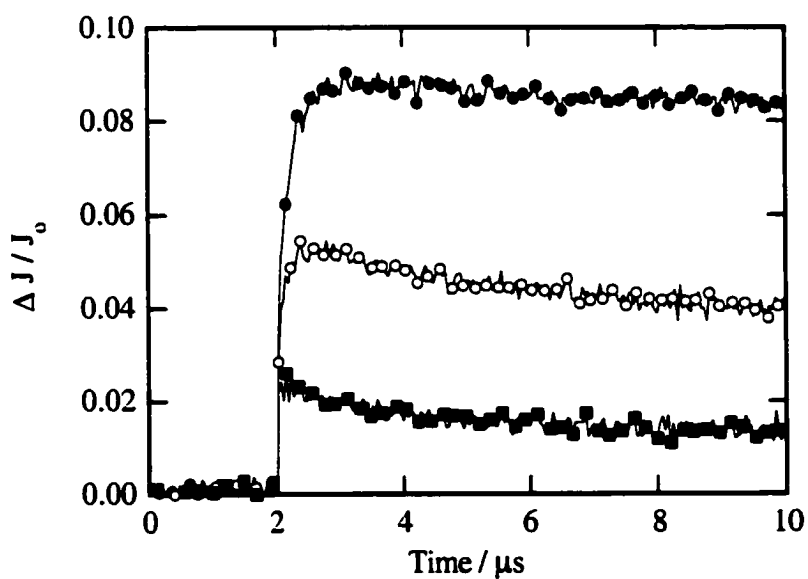
Figure 2-11. Time resolved growth traces generated upon 266 nm excitation of 2-chloro-1-(4-methoxyphenyl)ethyl acetate in KY under (●) 100% nitrogen, (○) 90% nitrogen:10% oxygen, and (■) 50% nitrogen:50% oxygen at 22 ± 1 °C. Traces were monitored at 600 nm.
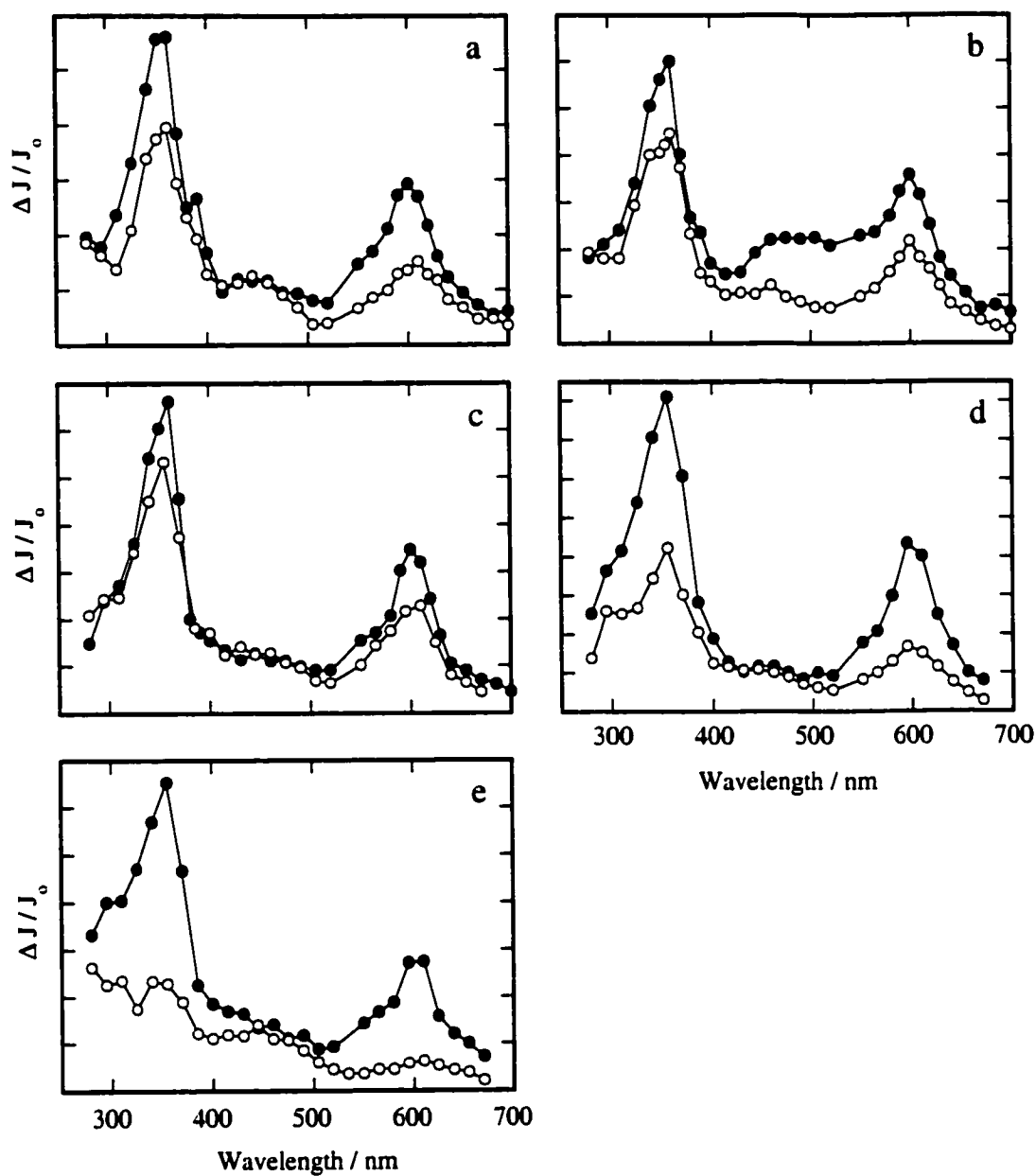
Figure 2-12. Transient diffuse reflectance spectra upon 266 nm excitation of 2-chloro-1-(4-methoxyphenyl)ethyl acetate in (a) LiY, (b) NaY, (c) KY, (d) RbY, and (e) CsY under dry-nitrogen (●) and nitrogen/oxygen mixture (9:1) (○) conditions. Spectra were recorded 5.72 μs after the laser pulse at 22 ± 1 °C.
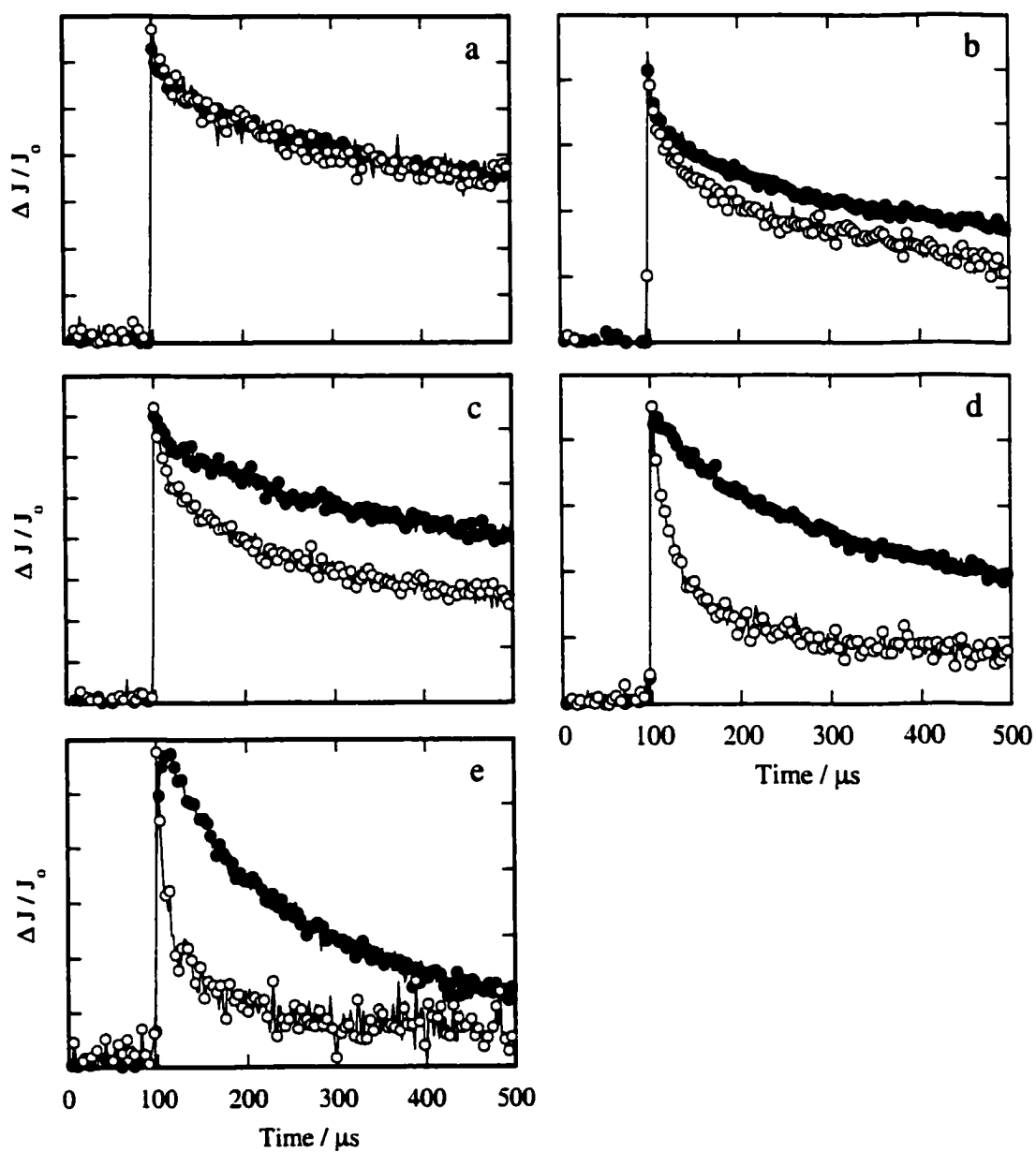
Figure 2-13. Normalized transient decay kinetics generated upon 266 nm excitation of 2-chloro-1-(4-methoxyphenyl)ethyl acetate in dry (a) LiY, (b) NaY, (c) KY, (d) RbY and (e) CsY under vacuum (●) and 10% oxygen in N_2 (O). Monitored at 600 nm over 400 μs at 22 ± 1 °C.
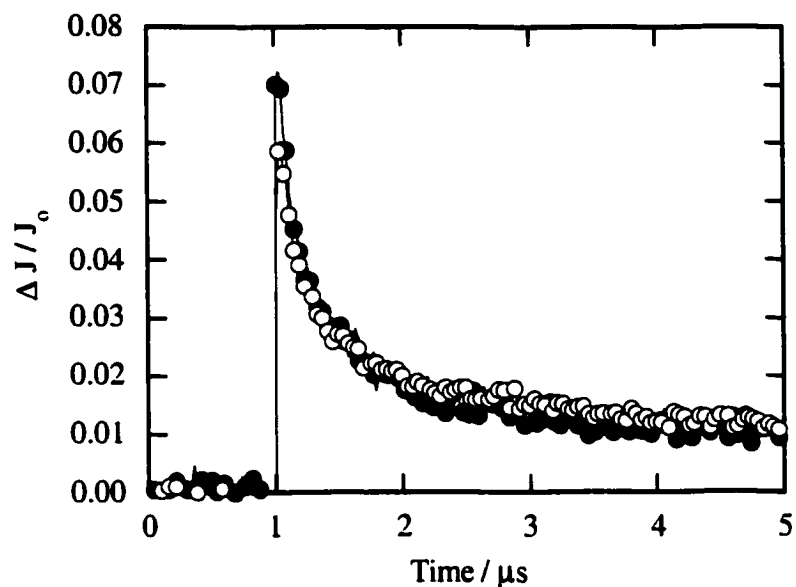
Figure 2-14. Time resolved decay at 600 nm observed upon 266 nm laser irradiation of 4-methoxystyrene in evacuated (10^{-3} torr) NaY with (●) and without (○) pre-incorporated NaCl.
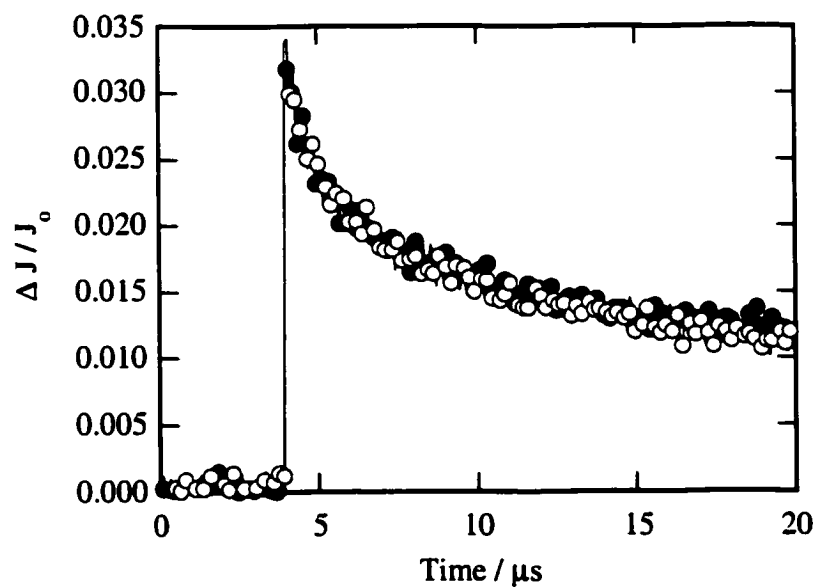
Figure 2-15. Time resolved decay at 600 nm observed upon 266 nm laser irradiation of 4-methoxystyrene in CsY under vacuum (10^{-3} torr) with (●) and without (○) pre-incorporated CsCl.
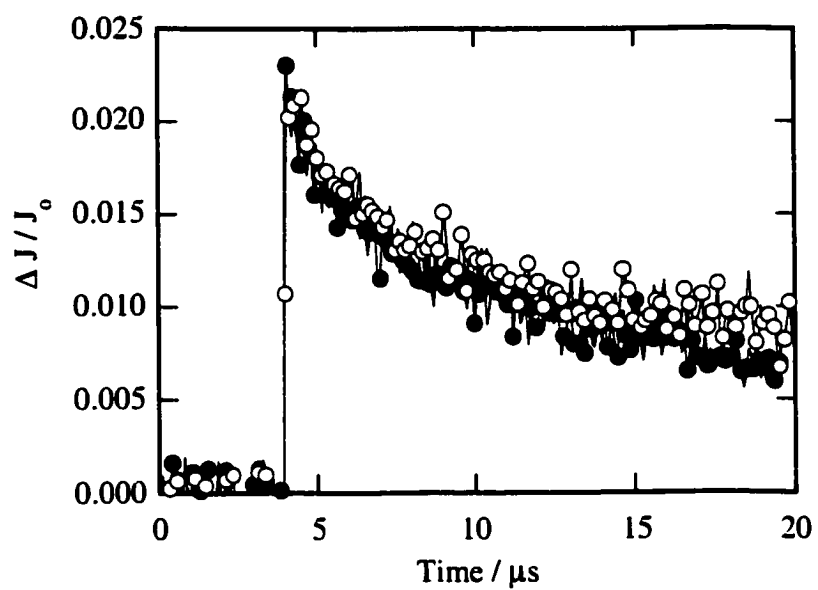
Figure 2-16. Time resolved decay at 600 nm observed upon 266 nm laser irradiation of 4-methoxystyrene in CsY under vacuum (10^{-3} torr) with (●) and without (○) pre-incorporated tetrabutylammonium chloride.

2.2.4. Dynamics of 2-chloro-1-(4-methoxyphenyl)ethyl acetate in alkali-exchanged Y zeolites with co-incorporated water

As described earlier, zeolites have a remarkable tendency to adsorb water. In the early stages of this doctoral research, it became obvious that preparation techniques and environmental conditions had significant effects on the results from the diffuse reflectance experiments, especially with respect to the dynamics of the heterolysis reaction. These effects were attributed to water being inadvertently adsorbed from the air into the zeolite cavities during incorporation of the substrate. As a result, a meticulous method for sample preparation was developed to ensure the dryness of the zeolite sample and reproducibility of the results.

The different behaviour observed with the hydrated samples became a source of interest for study, and experiments were carried out with samples that were purposely hydrated. To prepare the hydrated samples, freshly activated zeolites were allowed to cool slightly in air for 1 minute prior to being added to dry hexane containing the dissolved substrate. This procedure resulted in the co-incorporation of 2-4 wt % by weight water in the zeolite.

As shown in Figures 2-17 to 2-21, distinct absorption bands at 360 nm and 600 nm were clearly observed upon laser irradiation of AcOClVA in all of the hydrated zeolites. Thus, the radical cation of 4-methoxystyrene was generated under these hydrated conditions via β-heterolysis of chloride ion from the intermediate radical as observed in the dry zeolites described earlier. In addition, the 2-chloro-1-(4-methoxyphenyl)ethyl radical was also observed, especially in the RbY and CsY zeolites.

The time-resolved changes in diffuse reflectance at 600 nm generated upon 266 nm laser irradiation of AcOClVA are shown in Figure 2-22. The heterolysis reaction as represented by the increase in absorption due to the radical cation is clearly observed in all of the zeolites studied, even in LiY where under dry conditions the radical cation was formed promptly within the laser pulse. Analysis of the growths in all of the zeolites as a function of time led to the first-order rate constants for heterolysis listed in Table 2-6. Included in the table are the rate constants for heterolysis in the dry zeolites. Comparing

the two sets of data show that the rate constants for β-heterolysis are quite sensitive to the hydration state of the zeolite, with the ionization reaction in the slightly hydrated zeolites being 5- to 10-fold slower than in the corresponding dry zeolites. This phenomenon can be more clearly seen in the kinetic decay traces under dry and hydrated conditions shown in Figure 2-22.

Table 2-6. Rate constants for the heterolysis of chloride from the 2-chloro-1-(4-methoxyphenyl)ethyl radical (22 ± 1 °C) in dry and hydrated (2-4 wt-%) alkali-metal-cation-exchanged Y-zeolites under vacuum conditions.

Zeolite MY	k_{het} / s^{-1} (dry)	k_{het} / s^{-1} (hydrated)
LiY	$> 50 \times 10^6$	$(16 \pm 2) \times 10^6$
NaY	$(56 \pm 2) \times 10^6$	$(10 \pm 2) \times 10^6$
KY	$(8.9 \pm 0.5) \times 10^6$	$(0.9 \pm 0.2) \times 10^6$
RbY	$(3.4 \pm 0.6) \times 10^6$	$(0.20 \pm 0.05) \times 10^6$
CsY	$(1.0 \pm 0.6) \times 10^6$	$(0.20 \pm 0.01) \times 10^6$
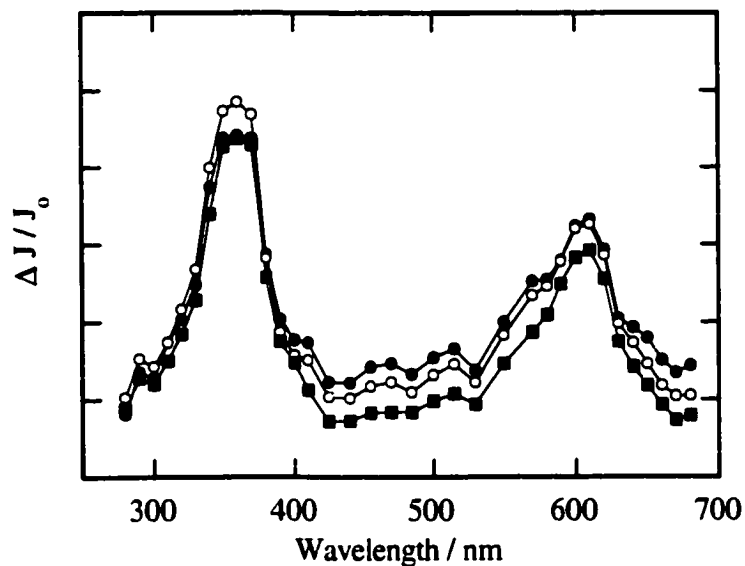
Figure 2-17. Diffuse reflectance spectrum obtained after 266 nm laser photolysis of 2-chloro-1-(4-methoxyphenyl)ethyl acetate in hydrated LiY under vacuum (10^{-4} Torr) conditions. Spectra were obtained (●) 0.52 μs, (O) 1.80 μs, and (■) 12.9 μs after the laser pulse.
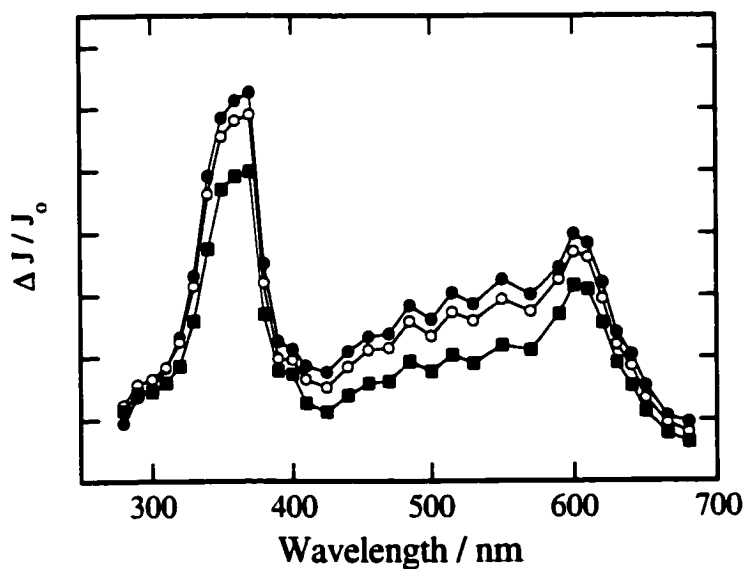
Figure 2-18. Diffuse reflectance spectrum obtained after 266 nm laser photolysis of 2-chloro-1-(4-methoxyphenyl)ethyl acetate in hydrated NaY under vacuum (10^{-4} Torr) conditions. Spectra were obtained (●) 0.52 μs, (O) 1.80 μs, and (■) 12.9 μs after the laser pulse.
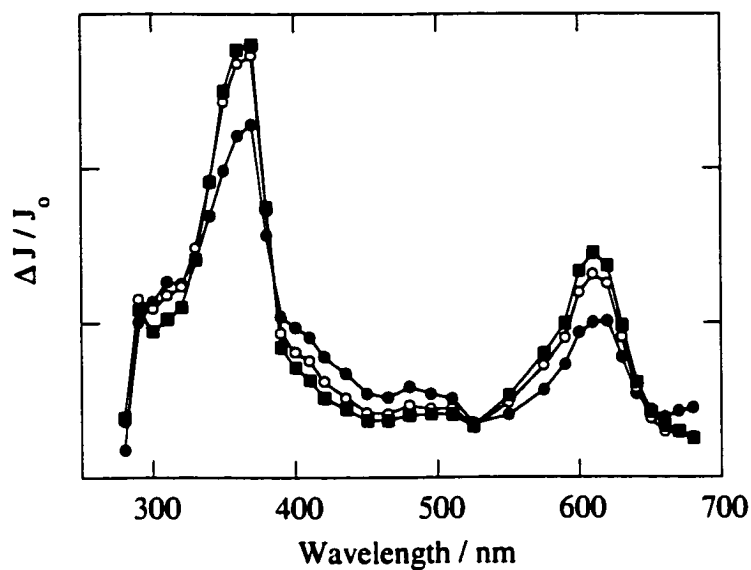
Figure 2-19. Diffuse reflectance spectrum obtained after 266 nm laser photolysis of 2-chloro-1-(4-methoxyphenyl)ethyl acetate in hydrated KY under vacuum (10^{-4} Torr) conditions. Spectra were obtained (●) 0.36 μs, (○) 1.08 μs, and (■) 2.44 μs after the laser pulse.
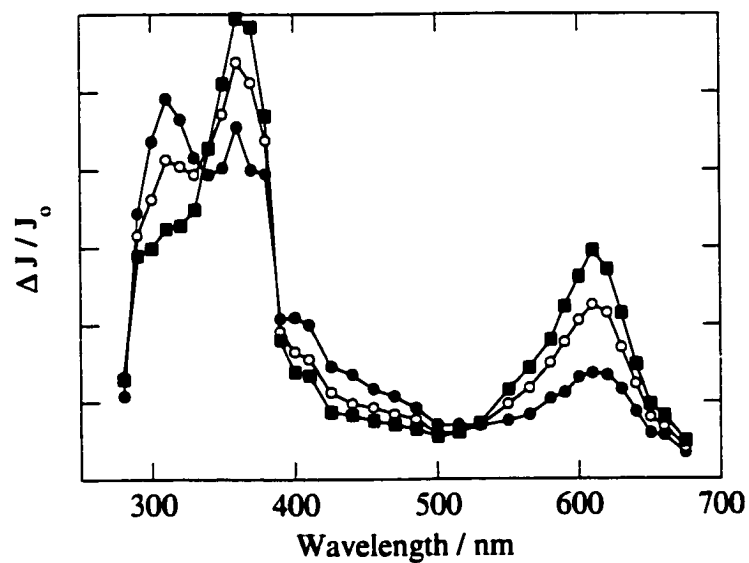
Figure 2-20. Transient diffuse reflectance spectra obtained after 266 nm laser photolysis of 2-chloro-1-(4-methoxyphenyl)ethyl acetate in hydrated RbY under vacuum (10^{-4} torr) conditions. Spectra were recorded (●) 0.52 μs, (○) 1.80 μs, and (■) 4.64 μs after the laser pulse at 22 ± 1 °C.
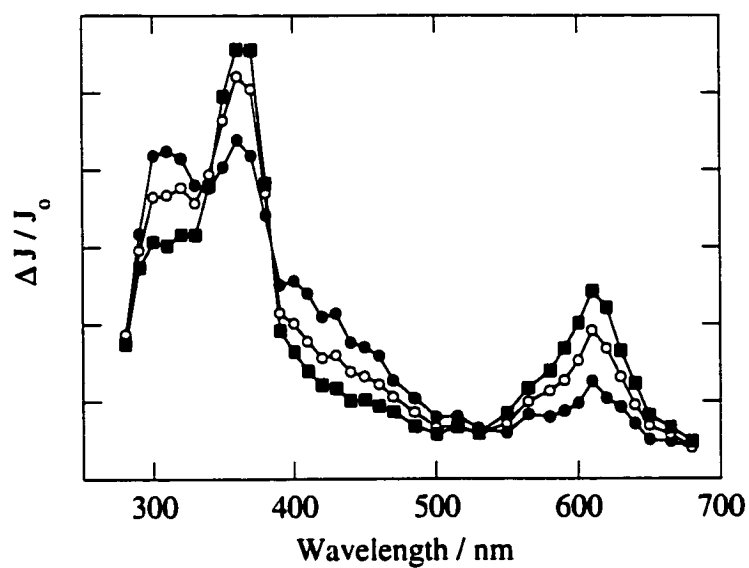
Figure 2-21. Diffuse reflectance spectrum obtained after 266 nm laser photolysis of 2-chloro-1-(4-methoxyphenyl)ethyl acetate in hydrated CsY under vacuum (10^{-4} Torr) conditions. Spectra were obtained (●) 0.52 μs, (O) 1.80 μs, and (■) 4.64 μs after the laser pulse.
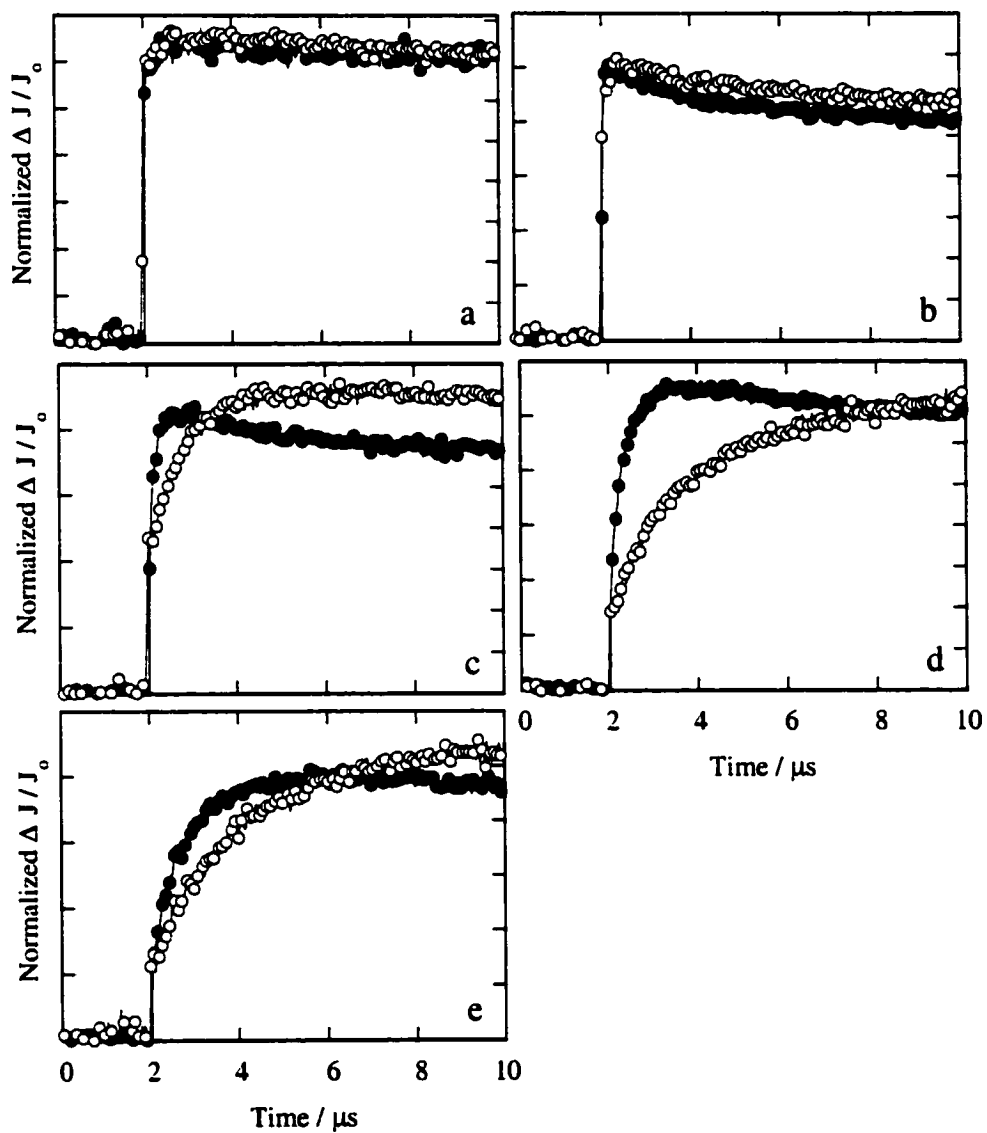
Figure 2-22. Normalized change in diffuse reflectance at 600 nm as a function of time upon 266 nm excitation photolysis of 2-chloro-1-(4-methoxyphenyl)ethyl acetate in (●) dry and (○) slightly hydrated (a) LiY, (b) NaY, (c) KY, (d) RbY and (e) CsY.

2.2.5. Effect of temperature on β-heterolysis

Activation parameters like enthalpy of activation and entropy of activation can often be interpreted to give useful insight into factors that control chemical reactivity. In particular, for typical S_N1 reactions in solution, changes in reactivity as a function of solvent are often strongly influenced by changes in entropy caused by differential solvation. As part of our efforts into understanding the factors that define S_N1-like reactions in zeolites, the effect of temperature on the β-heterolysis of chloride from the radical was measured, both in zeolites as a function of charge balancing cation, and in solution as a function of solvent ionizing ability.

2.2.5.1. Activation parameters in dry zeolites

Rate constants for the ionization of chloride from the 2-chloro-1-(4-methoxyphenyl)ethyl radical in the alkali metal cation-exchanged zeolites NaY, KY, RbY and CsY were measured in the same way as described earlier. The only exception was that the sample cell was placed in a specially designed cell holder connected to a constant temperature bath. With this apparatus, the zeolite samples could be maintained at a constant temperature over a temperature range from -10 °C to 50 °C. To ensure accurate temperature readings, the sample cells were equilibrated in the sample holder for at least one-half hour prior to carrying out the laser experiments.

To determine the activation parameters, rate constants for the growth of the radical cations by β-heterolysis in NaY, KY, RbY and CsY were measured at 10 different temperatures ranging from about -8 °C to 35 °C. Figures 2-23 to 2-26 are representative kinetic traces showing the effect of temperature on the rate constant for the formation of the 4-methoxystyrene radical cation upon heterolysis of chloride from the 2-chloro-1-(4-methoxyphenyl)ethyl radical in four alkali-exchanged Y zeolites. In NaY at 33 °C, the growth of the radical cation is almost too fast to resolve. However, as the temperature is dropped to -6 °C, the growth is easily resolved indicating that the β-heterolysis reaction is considerably slowed. Similar behaviour was observed in KY, RbY and CsY, but the

overall slower rate constants in these zeolites allows the temperature effect to be more easily seen.

Activation energies can be obtained from rate constants measured as a function of temperature using the Arrhenius equation, eq. 2.19. According to this equation, rate constants can be plotted as a function of the inverse of the temperature to give a slope that corresponds to the activation energy, E_a, and a y-intercept that corresponds to the pre-exponential factor A.

$$\ln k_{het} = \ln A - \frac{E_a}{RT} \qquad \qquad 2.19$$

The activation energy is of interest to chemists because it represents the energy barrier a molecule must overcome to react. The activation energy is defined as the difference between the energy of the starting material and the energy of the transition state structure. That is, the energy required for the development of the arrangement of atoms and electrons that is of highest energy along a reaction coordinate diagram that will lead to product(s). The pre-exponential term in the Arrhenius equation represents the probability factor for the reaction, that is, what proportion of the molecular collisions leads to product(s).

An Arrhenius plot for four alkali-exchanged Y zeolites under dry-vacuum conditions is shown in Figure 2-27. The plots were constructed by taking the average of several individual kinetic traces at each temperature. Arrhenius parameters obtained from these plots are summarized in Table 2-7. These values were obtained by averaging one to three different experiments per zeolite. The plots cover a temperature range varying from –10 °C to 35 °C.

Examination of the data presented in Table 2-7 indicates that the pre-exponential factor for the heterolysis reaction of 2-chloro-1-(4-methoxyphenyl)ethyl radical does not vary significantly as the alkali-metal cation is changed within the zeolites. In addition, there is no distinct trend in the activation energies upon going from NaY to RbY. The inability to establish a distinct trend is likely caused by the fact that the 10-fold decrease in rate constant upon going from NaY to RbY at ca. 25 °C only requires a small 5 kJ/mol

increase in the activation energy under conditions where the preexponential factor remains unchanged. A significantly higher activation energy of 55 kJ/mol was calculated for CsY. This result is consistent with the considerably smaller rate constant for heterolysis in CsY as compared to NaY.

Table 2-7. Arrhenius parameters for the β-heterolysis reaction of 2-chloro-1-(4-methoxyphenyl)ethyl radical in dry alkali-exchanged Y zeolites.

Zeolite	E_a (kJ/mol)	ln A
LiY	-	-
NaY	41 ± 2	33 ± 1
KY	45 ± 1	33 ± 1
RbY	43 ± 2	32 ± 1
CsY	55 ± 1	35 ± 1

Transition state theory and the Eyring equation, eq. 2.20, can also be used to obtain activation parameters from the rate constants of reactions at various temperatures. In this approach, the transition state is considered a chemical species and treated from the point of view of thermodynamics. Thus, an activation free-energy ($\Delta G^{\ddagger}$), activation enthalpy ($\Delta H^{\ddagger}$), and activation entropy ($\Delta S^{\ddagger}$), for the transformation from reactants to the transition state can be defined for this species, eq. 2.21.

$$k_{het} = \frac{kT}{h} e^{\Delta S^{\ddagger}/R} e^{-\Delta H^{\ddagger}/RT}$$

2.20

or

$$\ln\frac{k_{het}}{T} = -\frac{\Delta H^{\ddagger}}{RT} + \left(\ln\frac{k}{h} + \frac{\Delta S^{\ddagger}}{R}\right)$$

2.21

In the Eyring equation, $\Delta S^{\ddagger}$ and $\Delta H^{\ddagger}$ are the entropy of activation and enthalpy of activation, respectively; k is Boltzmann's constant and h is Planck's constant. The enthalpy of activation is the difference in bond energies, including strain, resonance, and solvation energies, between the starting compounds and the transition state. The

transition state of a reaction can have various degrees of bond-breakage and bond-forming with respect to starting materials, and the energy required is represented by the enthalpy of activation.

Entropy of activation is defined as the difference in entropy between the starting material and the transition state. $\Delta S^{\ddagger}$ is often important in bimolecular reactions as specific orientations of the molecules involved are required. In this scenario, the molecules must 'freeze' in a particular orientation in order to adopt the arrangement that leads to reaction. Thus, a considerable loss in entropy is involved, i.e. $\Delta S^{\ddagger}$ is negative. On the other hand, in unimolecular reactions where significant bond cleavage occurs before the transition state one would expect a greater degree of disorder to be present as fragmentation would have begun to occur. For example the pyrolytic conversion of cyclopropane to propene and the dissociation of di-t-butyl peroxide have positive activation entropies.[226,227]

Solvent molecules also contribute to the entropy and enthalpy of activation. Rearrangement of the solvent molecules around the transition state is very important where significant charge-separation in the transition state exists. As a result, the transition state may be required to have a more organized solvation shell with respect to the starting material thus decreasing the entropy at the activated complex.

Equation 2.21 is a more convenient form of the Eyring equation as a plot of $\ln(k_{het}/T)$ versus $1/T$ can give us the activation parameters directly when we obtain kinetic rate constants over various temperatures as given in Figure 2-28. The results from these plots are summarized in Table 2-8. The data in this table show a trend in which the $\Delta H^{\ddagger}$ values increase as the size of the cation is increased. A similar trend is observed for the change in $\Delta S^{\ddagger}$ values if the data for RbY is disregarded. Inclusion of RbY in the comparison ruins the trend as the $\Delta S^{\ddagger}$ value for the heterolysis reaction in this zeolite is lower than those observed in NaY and KY. Nonetheless, an important observation from the above data is that the entropy values are all positive. Thus, the data indicate an increase in entropy occurs within the cavities of zeolites as the transition state is achieved. This contrasts sharply with the negative activation entropies for ion forming

reactions such as S_N1 type ionizations typically observed in solution,[216,217,228-230] and suggests fundamental differences in the processes which control the ionization reaction in zeolites and in solution.

Table 2-8. Enthalpies, entropies and free energies (at 25 °C) of activation for β-heterolysis reaction of 2-chloro-1-(4-methoxyphenyl)ethyl radical in dry alkali-exchanged Y zeolites.

Zeolite	$\Delta H^{\ddagger}$ (kJ/mole)	$\Delta S^{\ddagger}$ (J/mol·K)	$\Delta G^{\ddagger}$ (kJ/mol)
LiY	-	-	-
NaY	39 ± 3	22 ± 1	32 ± 1
KY	42 ± 2	23 ± 1	35 ± 1
RbY	41 ± 2	14 ± 1	36 ± 1
CsY	52 ± 2	40 ± 1	40 ± 1
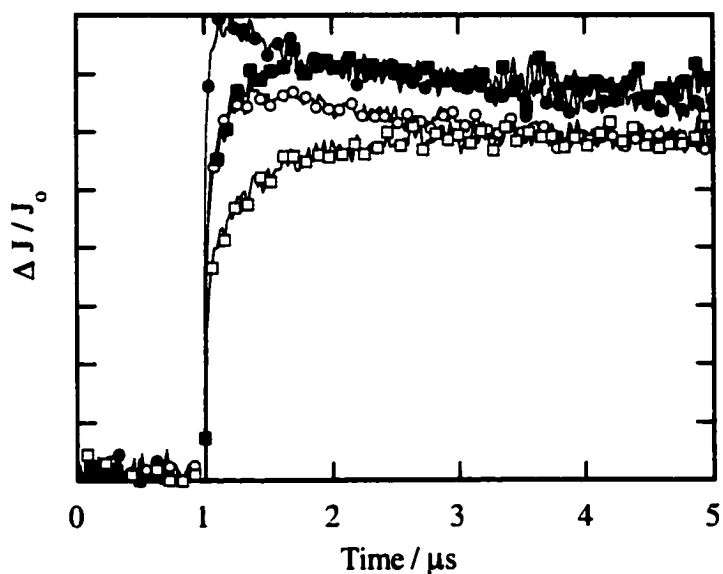
Figure 2-23. Change in reflectance at 600 nm as a function of time upon 266 nm laser photolysis of 2-chloro-1-(4-methoxyphenyl)ethyl acetate in dry NaY zeolites under vacuum (10^{-4} tor) and sealed conditions at (●) 33 °C, (○) 23 °C, (■) 8°C, and (□) -6°C (±1 °C).
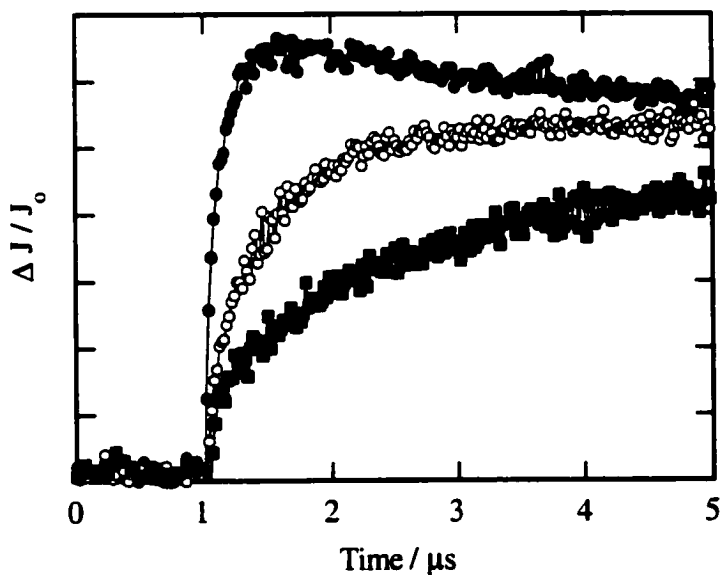
Figure 2-24. Change in reflectance at 600 nm as a function of time upon 266 nm laser photolysis of 2-chloro-1-(4-methoxyphenyl)ethyl acetate in dry KY zeolites under vacuum (10^{-4} tor) and sealed conditions at (●) 33 °C, (○) 11 °C, and (■) -6 °C (±1 °C).
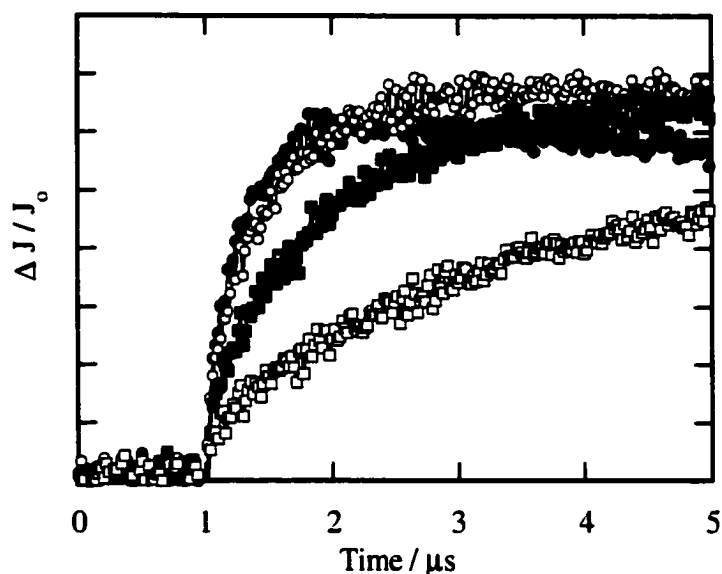
Figure 2-25. Change in reflectance at 600 nm as a function of time upon 266 nm laser photolysis of 2-chloro-1-(4-methoxyphenyl)ethyl acetate in dry RbY zeolites under vacuum (10^{-4} tor) and sealed conditions at (●) 31 °C, (○) 18 °C, (■) 7 °C, and (□) −6 °C (±1 °C).
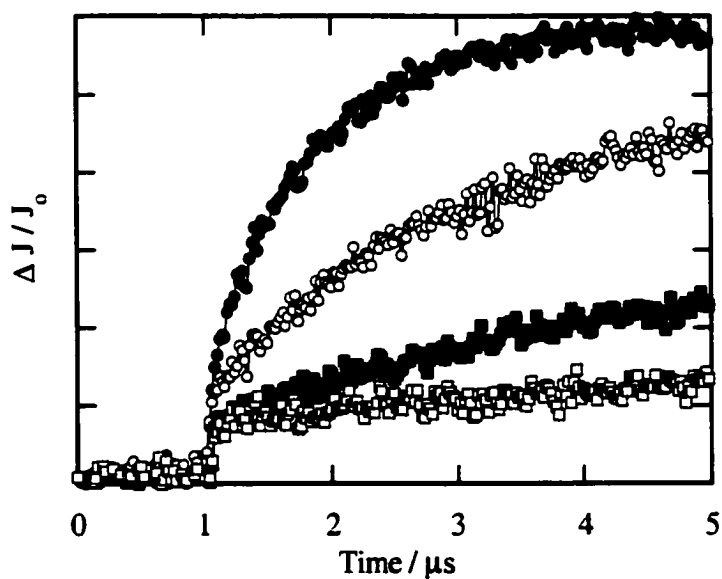
Figure 2-26. Change in reflectance at 600 nm as a function of time upon 266 nm laser photolysis of 2-chloro-1-(4-methoxyphenyl)ethyl acetate in dry CsY zeolites under vacuum (10^{-4} tor) and sealed conditions at (●) 34 °C, (○) 18 °C, (■) 10 °C, and (□) −5 °C (±1 °C).
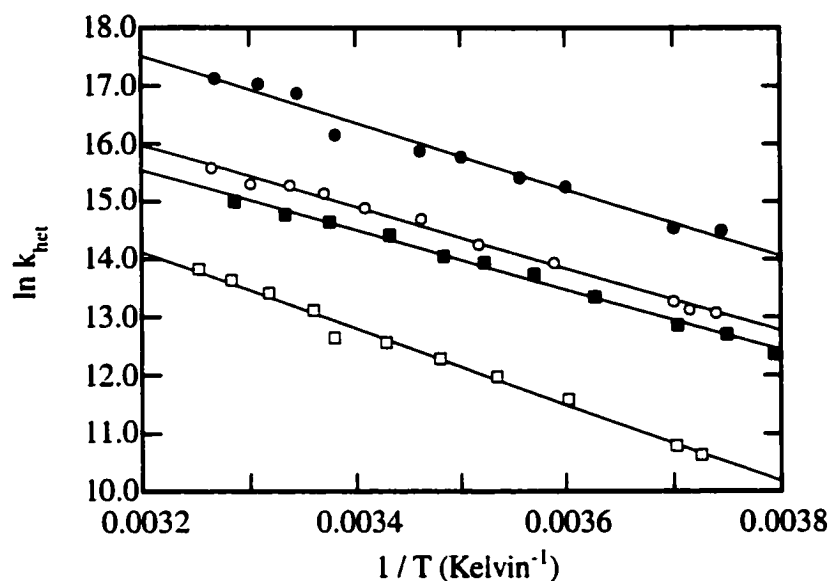
Figure 2-27. Arrhenius plot for the heterolytic cleavage of chloride from the 2-chloro-1-(4-methoxyphenyl)ethyl radical in dry alkali-metal-cation-exchanged Y zeolites in (●) NaY, (O) KY, (■) RbY, and (□) CsY.
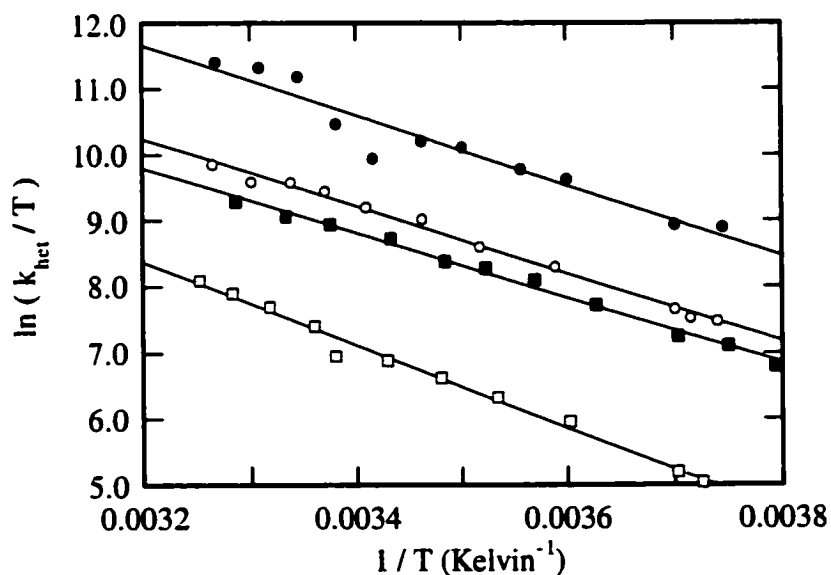
Figure 2-28. Eyring plot for the heterolytic cleavage of chloride from the 2-chloro-1-(4-methoxyphenyl)ethyl radical in dry alkali-metal-cation-exchanged Y zeolites in (●) NaY, (O) KY, (■) RbY, and (□) CsY.

2.2.5.2. Activation parameters in hydrated zeolites

Activation parameters were also determined in hydrated zeolites in an attempt to identify the source of the large decrease in the rate constant for heterolysis in the presence of co-incorporated water. Figures 2-29 to 2-33 show some representative traces of the effect of temperature on the β-heterolysis reaction in the five hydrated alkali-exchanged Y zeolites with incorporated AcOClVA. It is interesting to note that a fast growth for the formation of the 4-methoxystyrene radical cation can be detected in LiY.

An Arrhenius plot using the rate constants measured in the hydrated zeolites was constructed in the same way as that for the results in the dry zeolites, Figure 2-34. The activation energies calculated from the slopes and the pre-exponential factors are listed in Table 2-9.

Table 2-9. Arrhenius parameters for 2-chloro-1-(4-methoxyphenyl)ethyl radical in hydrated alkali-exchanged Y zeolites.

Zeolite	E_a (kJ/mole)	ln A
LiY	45 ± 3	33 ± 1
NaY	45 ± 3	32 ± 1
KY	53 ± 3	36 ± 1
RbY	60 ± 3	36 ± 1
CsY	66 ± 4	40 ± 2

In contrast to the values for the energy of activation obtained for dry samples of AcOClVA in MY, a distinct increase in the activation barrier as the size of the counterbalancing cation increases is observed. For example, in the smaller cation zeolites LiY and NaY where heterolysis is rapid, the energy of activation of 45 kJ/mol is considerably smaller than the activation energies of 53, to 60 and 66 kJ/mol in KY, RbY and CsY, respectively, where the heterolysis reactions are considerably slower. A similar trend is also observed for the pre-exponential factor which increases with changes in the charge balancing cation.

Eyring plots were also constructed from the rate constants for heterolysis measured in the hydrated zeolites, Figure 2-35. Activation parameters calculated from the slopes and intercepts of these plots and the free energy of activation at 25 °C are summaried in Table 2-10.

Table 2-10. Enthalpies, entropies and free energies (at 25 °C) of activation for β-heterolysis reaction of 2-chloro-1-(4-methoxyphenyl)ethyl radical in hydrated alkali-exchanged Y zeolites.

Zeolite	$\Delta H^{\ddagger}$ (kJ/mol)	$\Delta S^{\ddagger}$ (J/mol·K)	$\Delta G^{\ddagger}$ (J/mol·K)
LiY	43 ± 3	23 ± 1	36 ± 2
NaY	43 ± 3	35 ± 1	33 ± 2
KY	50 ± 2	42 ± 1	37 ± 1
RbY	58 ± 2	53 ± 1	42 ± 1
CsY	64 ± 2	73 ± 2	42 ± 2

While the enthalpies of activation for the reaction in the LiY and NaY zeolites are both 43 kJ/mol, the data clearly show that activation enthalpy increases as the size of the cation increases. A clear trend in which the entropy of activation also increases as the size of the cation increases also emerges from this data.
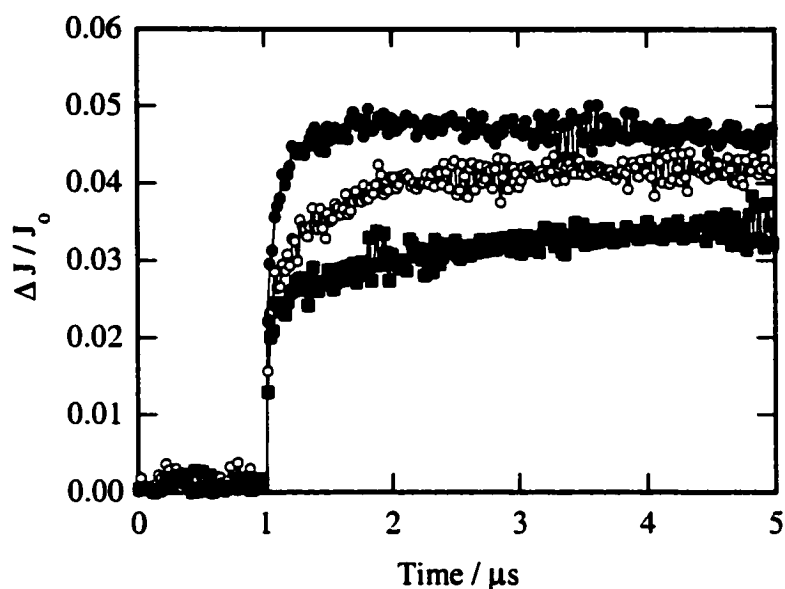
Figure 2-29. Change in reflectance at 600 nm as a function of time upon 266 nm laser photolysis of 2-chloro-1-(4-methoxyphenyl)ethyl acetate in hydrated LiY zeolites under vacuum (10^{-4} tor) and sealed conditions at (●) 32 °C, (O) 15 °C, and (■) -4 °C (±1 °C).
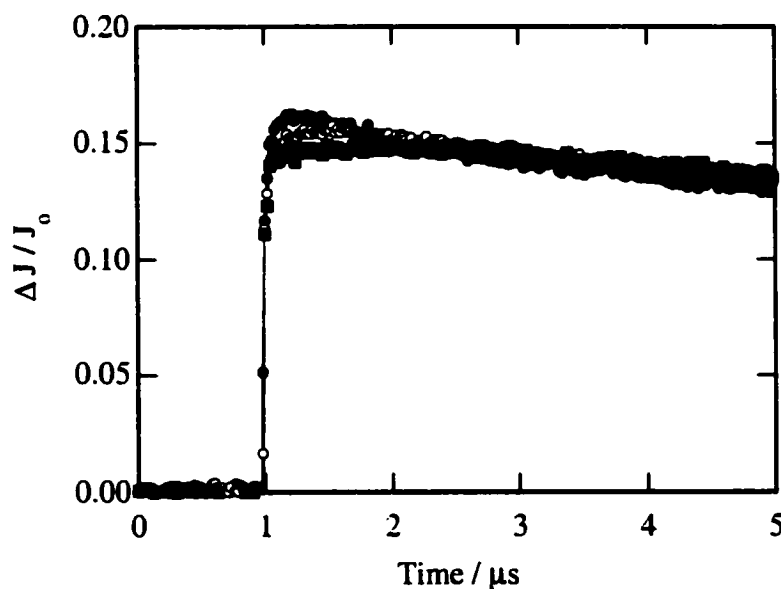
Figure 2-30. Change in reflectance at 600 nm as a function of time upon 266 nm laser photolysis of 2-chloro-1-(4-methoxyphenyl)ethyl acetate in hydrated NaY zeolites under vacuum (10^{-4} tor) and sealed conditions at (●) 30 °C, (O) 15 °C, and (■) 5°C (±1 °C).
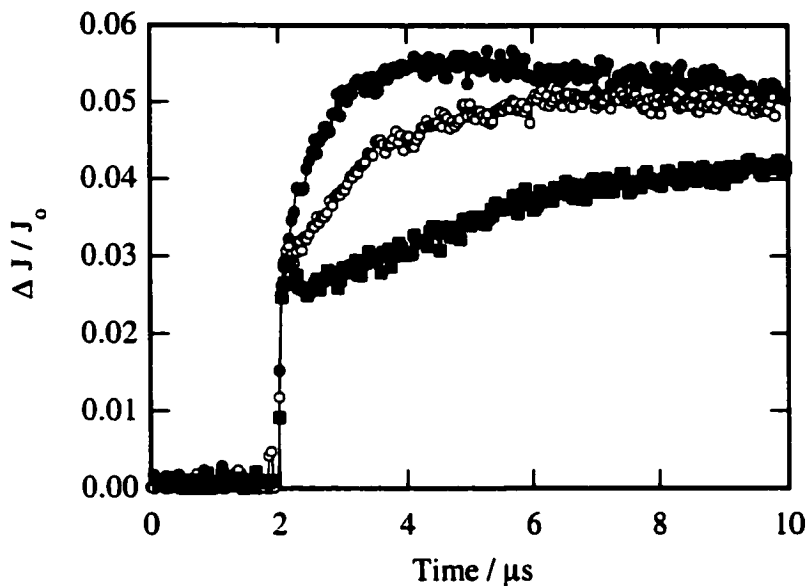
Figure 2-31. Change in reflectance at 600 nm as a function of time upon 266 nm laser photolysis of 2-chloro-1-(4-methoxyphenyl)ethyl acetate in hydrated KY zeolites under vacuum (10^{-4} tor) and sealed conditions at (●) 30 °C, (○) 18 °C, and (■) 4 °C (±1 °C).
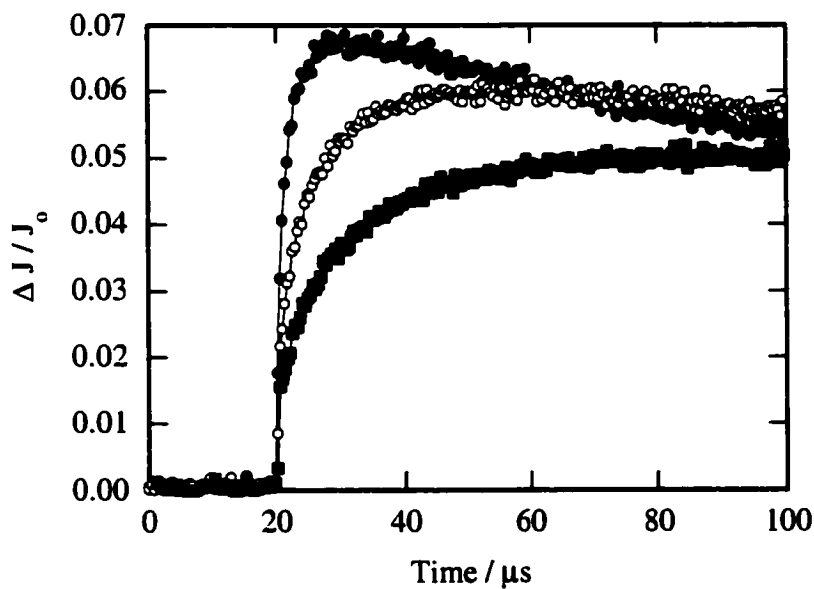
Figure 2-32. Change in reflectance at 600 nm as a function of time upon 266 nm laser photolysis of 2-chloro-1-(4-methoxyphenyl)ethyl acetate in hydrated RbY zeolites under vacuum (10^{-4} tor) and sealed conditions at (●) 30 °C, (○) 16 °C, and (■) 6 °C (±1 °C).
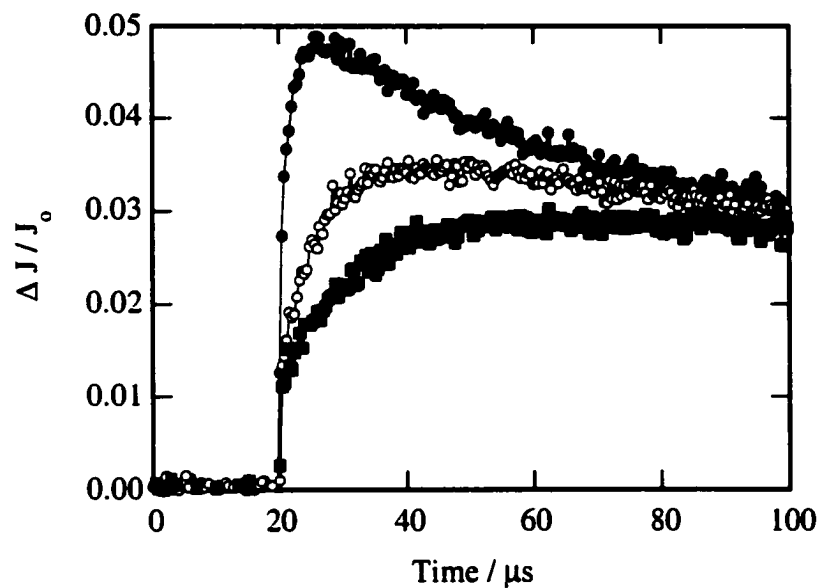
Figure 2-33. Change in reflectance at 600 nm as a function of time upon 266 nm laser photolysis of 2-chloro-1-(4-methoxyphenyl)ethyl acetate in hydrated CsY zeolites under vacuum (10^{-4} tor) and sealed conditions at (●) 30 °C, (○) 14 °C, and (■) 2 °C (±1 °C).
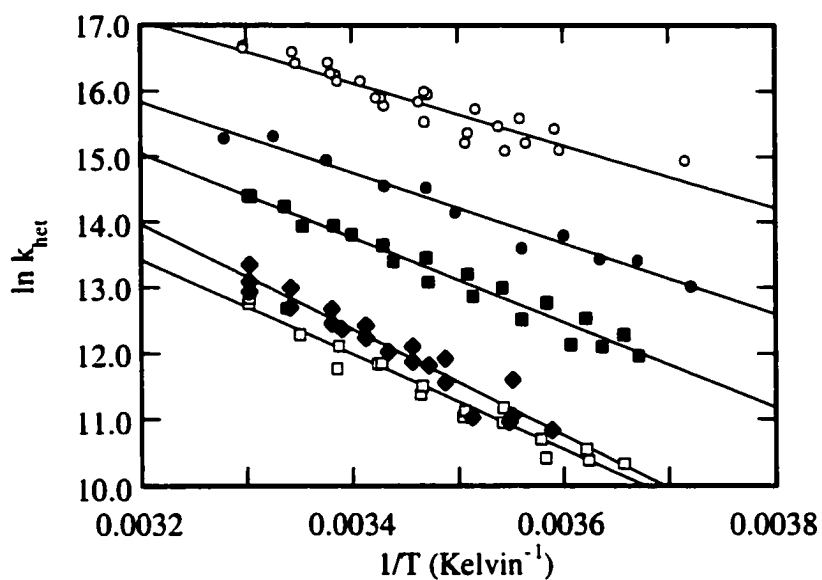
Figure 2-34. Arrhenius plot for the heterolytic cleavage of chloride from the 2-chloro-1-(4-methoxyphenyl)ethyl radical in partially hydrated alkali-metal-cation-exchanged Y zeolites in (●) LiY, (○) NaY, (■) KY, (□) RbY, and (◆) CsY.
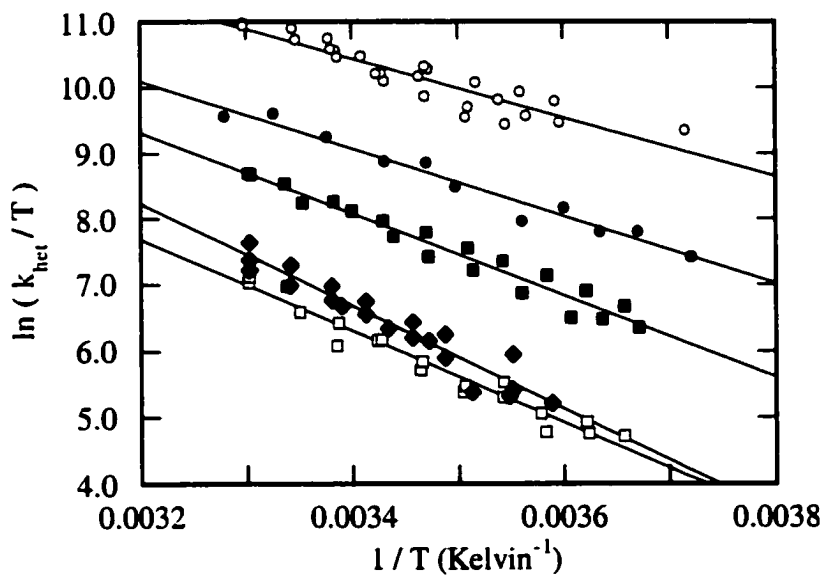
Figure 2-35. Eyring plot for the heterolytic cleavage of chloride from the 2-chloro-1-(4-methoxyphenyl)ethyl radical in partially hydrated alkali-metal-cation-exchanged Y zeolites in (●) LiY, (○) NaY, (■) KY, (□) RbY, and (◆) CsY.

2.2.5.3. Activation Parameters in Solution

In an attempt to better understand the activation parameters obtained for the β-heterolysis reaction within zeolites, the reactivity of the probe molecule with varying temperature was also examined in solution. The solvents chosen were TFE/AcN, HFIP/AcN and MeOH/H$_2$O mixtures in which the 2-chloro-1-(4-methoxyphenyl)ethyl radical undergoes efficient β-heterolysis.[200] In these solvent mixtures, the rate constant for heterolysis at a given temperature always increased as the fraction of the more ionizing solvent increased. Thus, in TFE/AcN solutions, the rate constant was greater in the solution containing 100% TFE than the rate constant in the solution containing 80% TFE:20% AcN. Similarly, the rate constants in 80% HFIP:20% AcN were greater than those in the solution with only 60% HFIP. In the methanol:water mixtures, the rate constants always increased at each temperature as the water content increased.

The reaction was examined at various temperatures ranging from 30 to –5 °C. As expected, the rate constants for radical cation formation increased as a function of increasing temperature. A set of representative time-resolved kinetic traces for the formation of the 4-methoxystyrene radical cation by β-heterolysis of the 2-chloro-1-(4-methoxyphenyl)ethyl radical at various temperatures is shown in Figures 2-36 and 2-37. The rate constants calculated from these traces were then plotted versus 1/T to create the Arrhenius and Eyring plots shown in Figures 2-38 to 2-43. The thermodynamic information calculated from these plots is summarised in Table 2-11.

Several trends emerge from the data summarised in Table 2-11. In the methanol/water mixtures, values for E_a and $\Delta H^{\ddagger}$ become progressively larger as the water content in the mixtures becomes smaller. Since the rate constants for heterolysis decrease with decreasing water content, it can also be said that E_a and $\Delta H^{\ddagger}$ increase as the rate constants decrease. On the other hand, $\Delta S^{\ddagger}$ values show an unusual dependence such that they initially increase upon going from 70% to 50% aqueous methanol, and then decrease upon going to 30% aqueous methanol. The activation entropy value is negative in all cases.

Somewhat different results are observed for the reaction in fluorinated solvents. In TFE/AcN and HFIP/AcN solvent mixtures, the activation energy tends to decrease as the reaction slows down in the less ionizing-solvents containing smaller amounts of the fluorinated solvents. To illustrate, the rate constant for β-heterolysis for the 2-chloro-1-(4-methoxyphenyl)ethyl radical in 100 and 60% TFE/AcN mixtures decreases from 10^7 s^{-1} to 10^6 s^{-1} while the activation energy decreases from 26 kJ/mol to 21 kJ/mol. The data in Table 2-11 also show that the entropy of activation becomes more negative as the fluorinated alcohol content decreases. Thus, the entropy of activation decreases as the rate constant for ionization decreases.

Table 2-11. Thermodynamic data for the heterolysis reaction of 2-chloro-1-(4-methoxyphenyl)ethyl radical in various solvents.

Solvent	E_a (kJ/mol)	ln A	$\Delta H^\ddagger$ (kJ/mol)	$\Delta S^\ddagger$ (J/mol·K)
	(±2)	(±1)	(±2)	(±3)
70% aq. MeOH	20	25	18	-45
60% aq. MeOH	27	27	25	-26
50% aq. MeOH	30	28	27	-21
40% aq. MeOH	30	27	27	-29
30% aq. MeOH	30	27	28	-32
100% TFE	26	27	24	-28
80% TFE in AcN	23	24	21	-54
60% TFE in AcN	21	22	19	-69
80% HFIP in AcN	28	28	25	-19
70% HFIP in AcN	24	25	21	-46
60% HFIP in AcN	26	25	24	-47
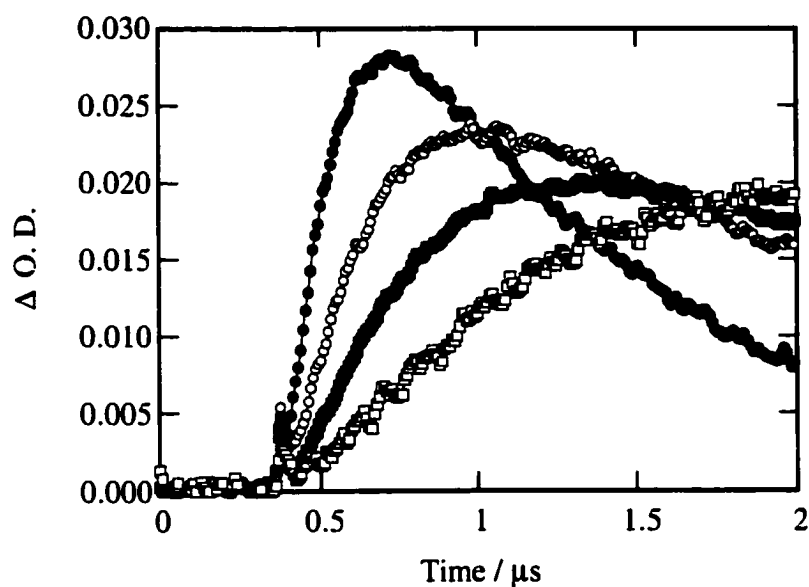
Figure 2-36. Time resolved growth at 600 nm observed upon 266 nm laser irradiation of 2-chloro-1-(4-methoxyphenyl)ethyl acetate in nitrogen-saturated 60% aqueous methanol mixture at (●) 35 °C, (○) 18 °C, (■) 6 °C, and (□) -1 °C (± 1 °C).
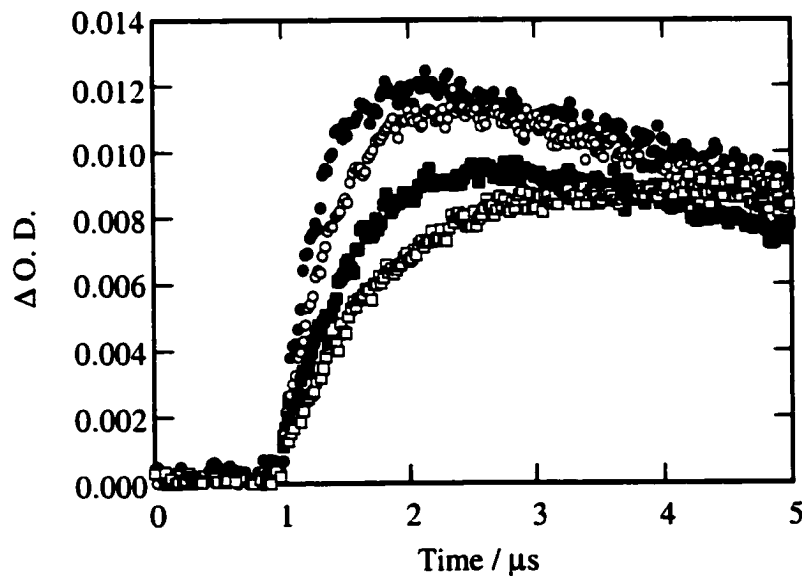
Figure 2-37. Time resolved growth at 600 nm observed upon 266 nm laser irradiation of 2-chloro-1-(4-methoxyphenyl)ethyl acetate in nitrogen-saturated 80% TFE in AcN mixture at (●) 37 °C, (○) 22 °C, (■) 14 °C and (□) 2 °C (± 1 °C).
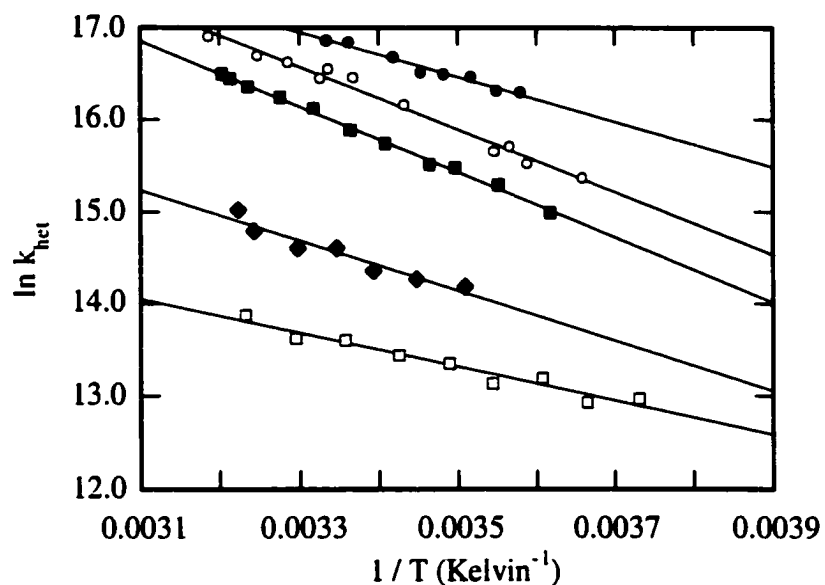
Figure 2-38. Arrhenius plot for the heterolytic cleavage of chloride from the 2-chloro-1-(4-methoxyphenyl)ethyl radical in (●) 30% aq. MeOH, (○) 40% aq. MeOH, (■) 50% aq. MeOH, (□) 60% aq. MeOH and (◆) 70% aq. MeOH mixtures.
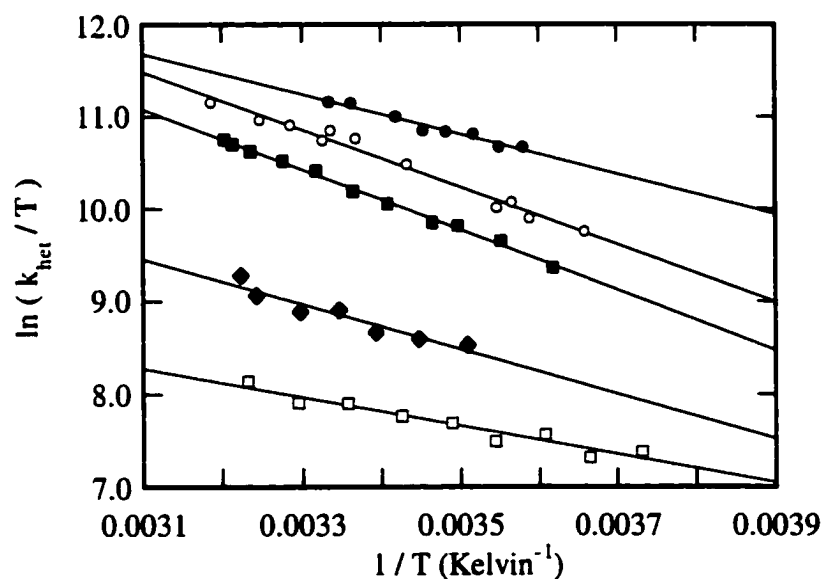
Figure 2-39. Eyring plot for the heterolytic cleavage of chloride from the 2-chloro-1-(4-methoxyphenyl)ethyl radical in (●) 30% aq. MeOH, (○) 40% aq. MeOH, (■) 50% aq. MeOH, (□) 60% aq. MeOH and (◆) 70% aq. MeOH mixtures.
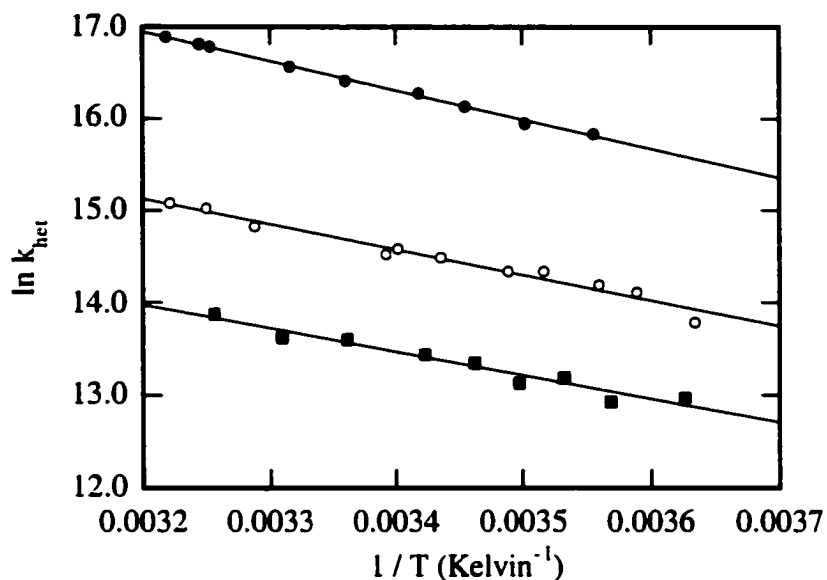
Figure 2-40. Arrhenius plot for the heterolytic cleavage of chloride from the 2-chloro-1-(4-methoxyphenyl)ethyl radical in (●) 100% TFE, (O) 80% TFE in AcN, and (■) 60% TFE in AcN mixtures.
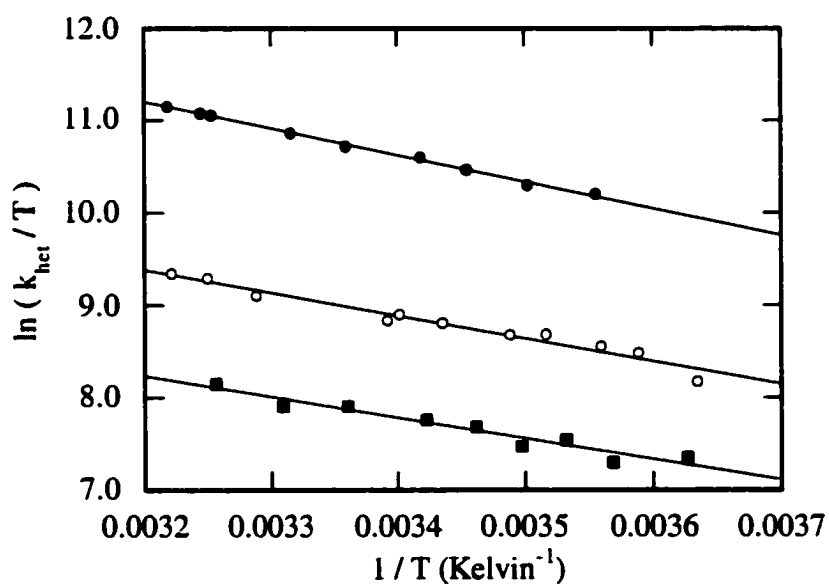
Figure 2-41. Eyring plot for the heterolytic cleavage of chloride from the 2-chloro-1-(4-methoxyphenyl)ethyl radical in (●) 100% TFE, (O) 80% TFE in AcN, and (■) 60% TFE in AcN mixtures.
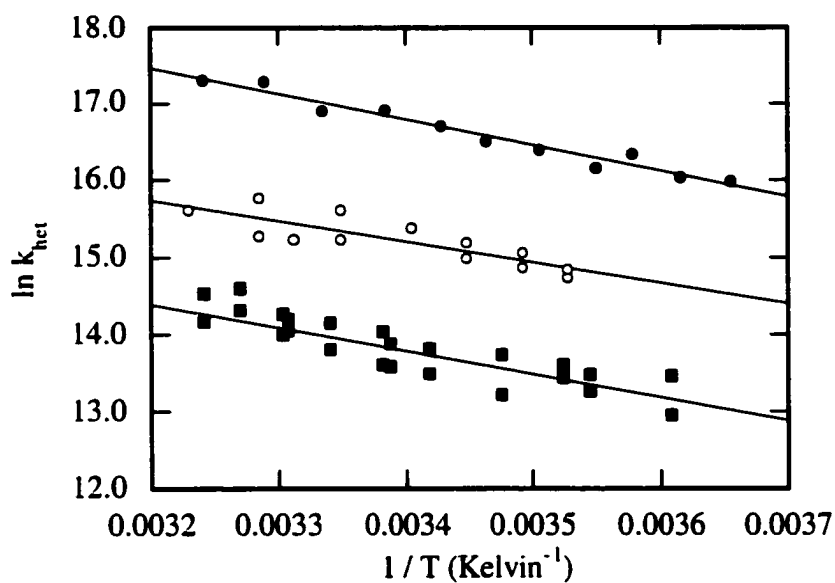
Figure 2-42. Arrhenius plot for the heterolytic cleavage of chloride from the 2-chloro-1-(4-methoxyphenyl)ethyl radical in (●) 80% HFIP in AcN, (○) 70% TFE in AcN, and (■) 60% TFE in AcN mixtures.
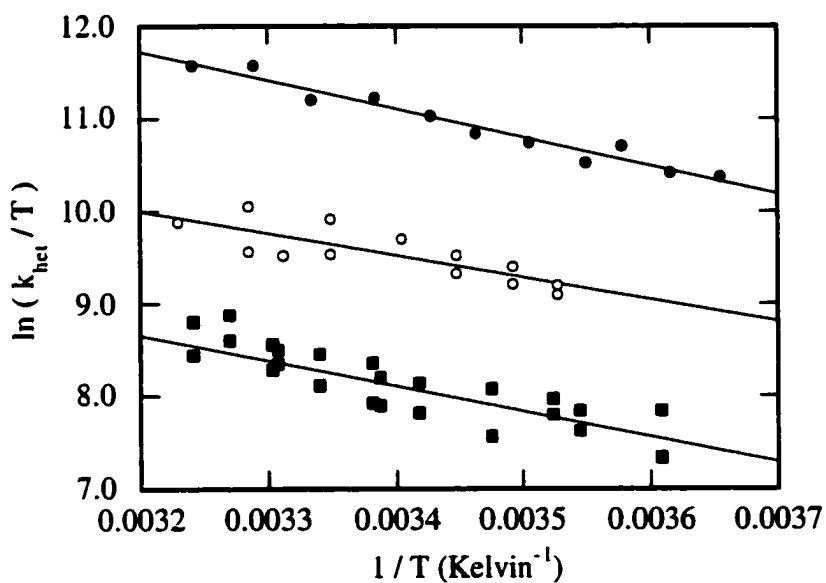
Figure 2-43. Eyring plot for the heterolytic cleavage of chloride from the 2-chloro-1-(4-methoxyphenyl)ethyl radical in (●) 80% HFIP in AcN, (○) 70% TFE in AcN, and (■) 60% TFE in AcN mixtures.

2.2.6. β-Heterolysis of other substrates.

As mentioned in the introduction, specific criteria were needed in order for a photogenerated arylalkyl radical to be a suitable probe for the ionization reaction. While the 2-chloro-1-(4-methoxyphenyl)ethyl radical satisfied those criteria, all of the other substrates investigated were not suitable. In some cases, the spectra were contaminated with unknown transients that made analysis of the data too unreliable to make conclusions concerning the effect of zeolite environment on the dynamics of leaving group ionization. Alternatively, heterolysis could be monitored, but only in two or three cation exchanged zeolites. In other cases, the heterolysis was too rapid to observe, so no useful dynamic information could be obtained.

As a result of these difficulties, the probe molecules discussed in this section were not investigated in as much detail as the 2-chloro-1-(4-methoxyphenyl)ethyl radical described above. Nonetheless, a description of the results obtained with these compounds is useful to provide additional information concerning the effect of leaving group and structure on the ionization reaction in zeolites.

2.2.6.1. 2-Chloro-1-(4-methoxyphenyl)propyl acetate

Laser photolysis of 2-chloro-1-(4-methoxyphenyl)propyl acetate (AcOClAn) incorporated using hexanes within NaY under dry and vacuum (10^{-4} torr) conditions led to the transient diffuse reflectance spectra shown in Figure 2-44. The spectra show characteristic absorption bands at 390 and 610 nm that correspond to the 1-(4-methoxy-phenyl)-1-propene (or anethole) radical cation generated via β-heterolysis of the 2-chloro-1-(4-methoxyphenyl)propyl radical, eq. 2.22.

2.22
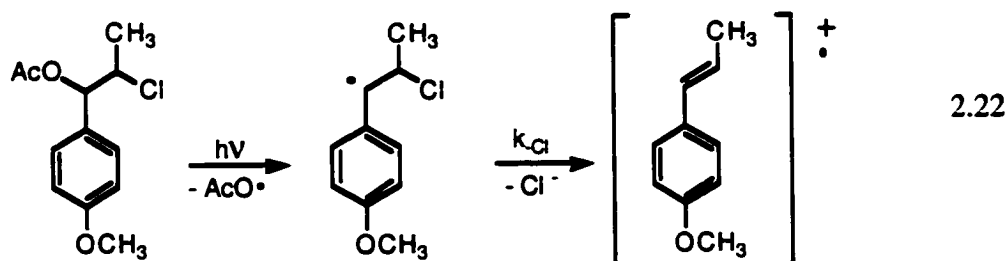
Additional absorption not due to the presence of the anethole radical cation is observed in the 400-600 nm region. This absorption is quenched in the presence of N_2O, Figure 2-45, and is therefore likely due to the presence of a trapped electron complex, presumably Na_4^{3+}. As expected, the formation and decay of the anethole radical cation is not affected by addition of N_2O.

Similar spectra were observed upon 266 nm laser irradiation of AcOClAn in each of the alkali-metal exchanged Y zeolites (i.e. LiY, NaY, KY, RbY and CsY) under evacuated conditions, Figure 2-46. In each case, the spectrum is dominated by the presence of the anethole radical cation.

Time-resolved changes at 610 nm due to the formation of the anethole cation are given in the insets of Figure 2-46. In each case, except LiY, the kinetic traces consist of two distinct components. One component is a very fast increase in absorption that takes place promptly within the laser pulse. This prompt increase is substantial and accounts for between 50% to 80% of the maximum absorption eventually observed. The second component is a growth that is sufficiently slow to be resolved. The kinetic traces therefore indicate that a significant fraction of the 2-chloro-1-(4-methoxyphenyl)-1-propyl radicals undergo rapid heterolysis to give the anethole radical cation over a time-scale too short to be resolved with the nanosecond laser system. The rate constant for this process is therefore $> 5 \times 10^7$ s^{-1}. The rest of the radicals undergo a slower heterolysis that can be resolved. Analysis of the slower process gave the rate constants listed in Table 2-12.

The spectra in Figure 2-46 also show little evidence for the presence of the 2-chloro-1-(4-methoxyphenyl)propyl radical in the 300 nm region. The only exception is the spectrum for CsY, which does show a small absorption near 300 nm. The inability to detect the radical is consistent with the conclusion made above that a significant fraction of the radicals undergoes very rapid heterolysis to the radical cation.

In a manner similar to that described earlier for the 2-chloro-1-(4-methoxy-phenyl)ethyl acetate system, laser irradiation of 2-chloro-1-(4-methoxyphenyl)propyl

acetate in the presence of oxygen led to a considerable reduction of the maximum absorption of the radical cation at both 390 and 610 nm as compared to the maximum absorption under vacuum conditions. This reduced intensity is likely due to trapping of the 2-chloro-1-(4-methoxyphenyl)propyl radical before conversion to the anethole radical cation. However, unlike the 2-chloro-1-(4-methoxyphenyl)ethyl radical which was completely trapped by oxygen and no longer underwent β-heterolysis to the 4-methoxystyrene radical cation, the 2-chloro-1-(4-methoxyphenyl)propyl radical is not completely quenched by oxygen as shown by the lingering absorption by the anethole radical cation, Figure 2-47. Presumably, some fraction of the 2-chloro-1-(4-methoxyphenyl)propyl radicals is undergoing the β-heterolysis reaction too quickly to be trapped by oxygen. This is consistent with the observation that β-heterolysis from some of the radicals are taking place with rate constants too fast to be measured, $k > 5 \times 10^7$ s^{-1}.

The complicated and fast kinetics for the radical cation formation upon irradiation of 2-chloro-1-(4-methoxyphenyl)propyl acetate made it unsuitable as a reliable probe to investigate the effect of the zeolite interior on the ionization reaction. Nonetheless, the results do suggest that the β-heterolysis of chloride from the 2-chloro-1-(4-methoxyphenyl)propyl radical is more rapid than the same reaction from the 2-chloro-1-(4-methoxyphenyl)ethyl radical. This is consistent with results obtained in solution showing that the addition a β-methyl group stabilizes the radical cation and increases the rate constants for β-heterolysis.

Table 2-12. Rate constants for the slow heterolysis of chloride from the 2-chloro-1-(4-methoxyphenyl)propyl radical (22 ± 1°C) in dry alkali-metal-cation-exchanged Y zeolites.

Counterion	k_{growth} / s^{-1} (slow)
Li$^+$	$> 50 \times 10^6$
Na$^+$	$(5.8 \pm 0.6) \times 10^6$
K$^+$	$(1.5 \pm 0.2) \times 10^6$
Rb$^+$	$(1.2 \pm 0.1) \times 10^6$
Cs$^+$	$(0.3 \pm 0.1) \times 10^6$
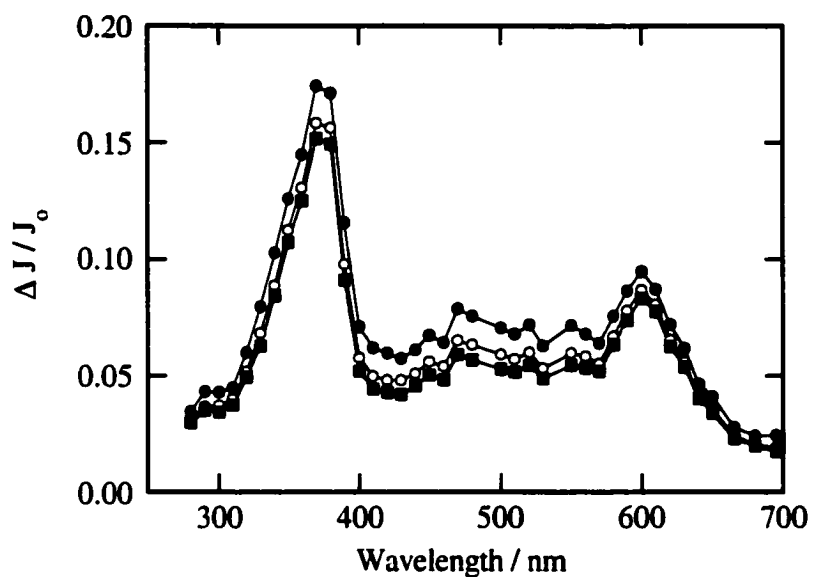
Figure 2-44. Transient diffuse reflectance spectra generated upon 266 nm excitation of 2-chloro-1-(4-methoxyphenyl)propyl acetate in NaY under dry vacuum conditions. Spectra were recorded (●) 1.88 μs, (○) 4.40 μs, and (■) 12.9 μs, after the laser pulse.
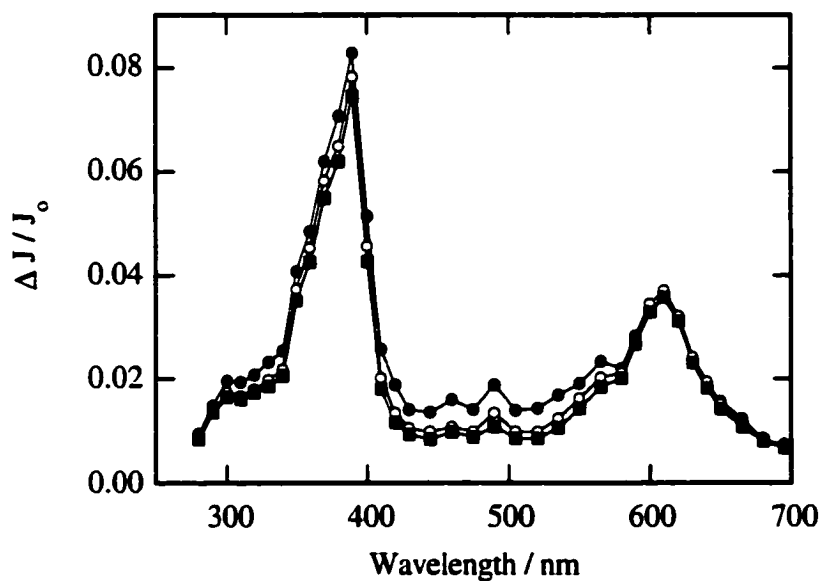
Figure 2-45. Transient diffuse reflectance spectra generated upon 266 nm excitation of 2-chloro-1-(4-methoxyphenyl)propyl acetate in NaY purged with N_2O. Spectra were recorded (●) 1.40 μs, (○) 7.60 μs, and (■) 12.8 μs, after the laser pulse.
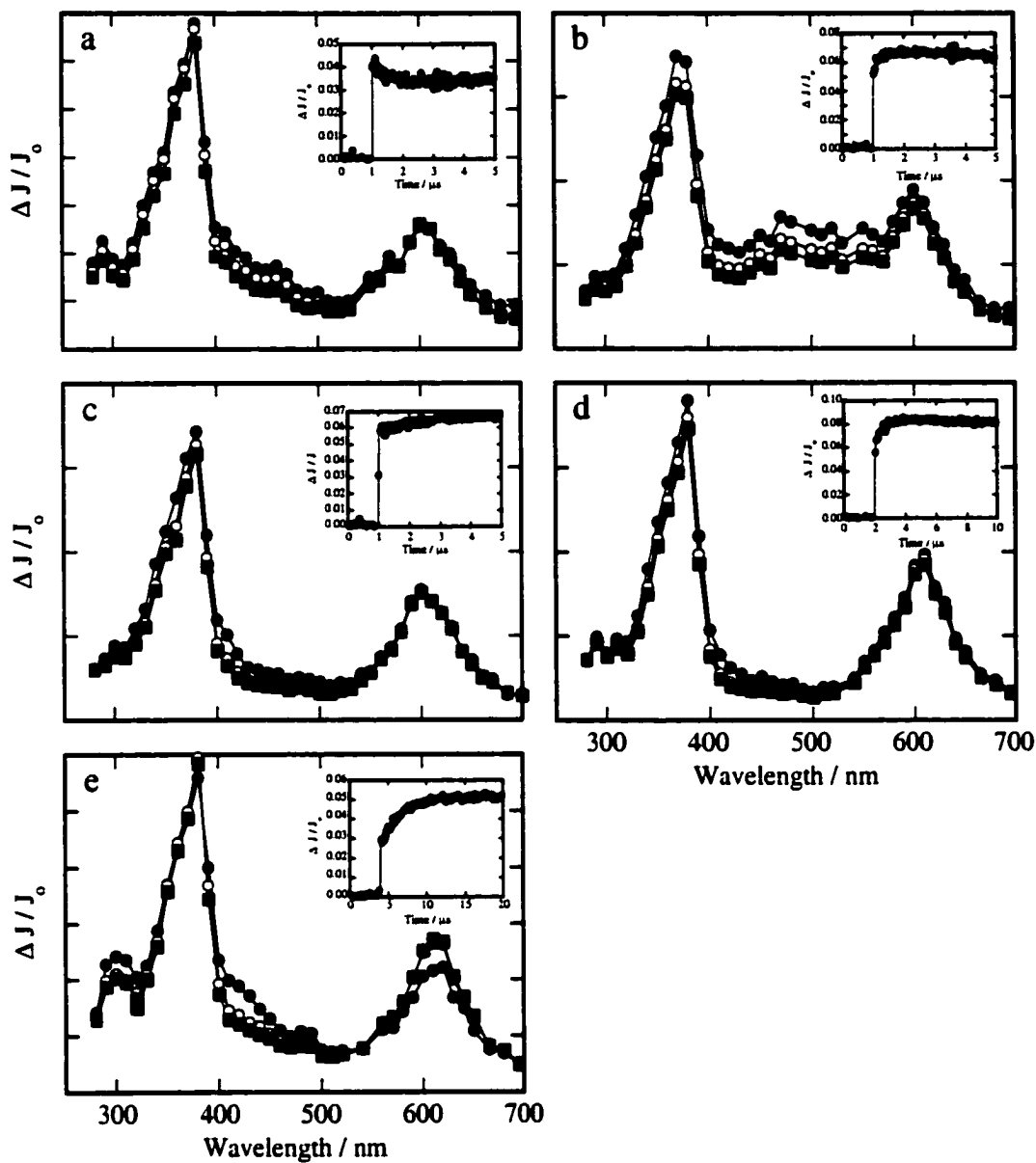
Figure 2-46. Transient diffuse reflectance spectra generated upon 266 nm excitation of 2-chloro-1-(4-methoxyphenyl)propyl acetate in (a) LiY, (b) NaY, (c) KY, (d) RbY and (e) CsY under dry and vacuum conditions after 266 nm excitation. Spectra were recorded (●) 1.88 µs, (○) 4.40 µs, and (■) 12.9 µs, after the laser pulse. The insets show the time-resolved growth trace at 610 nm at 22 ± 1 °C.
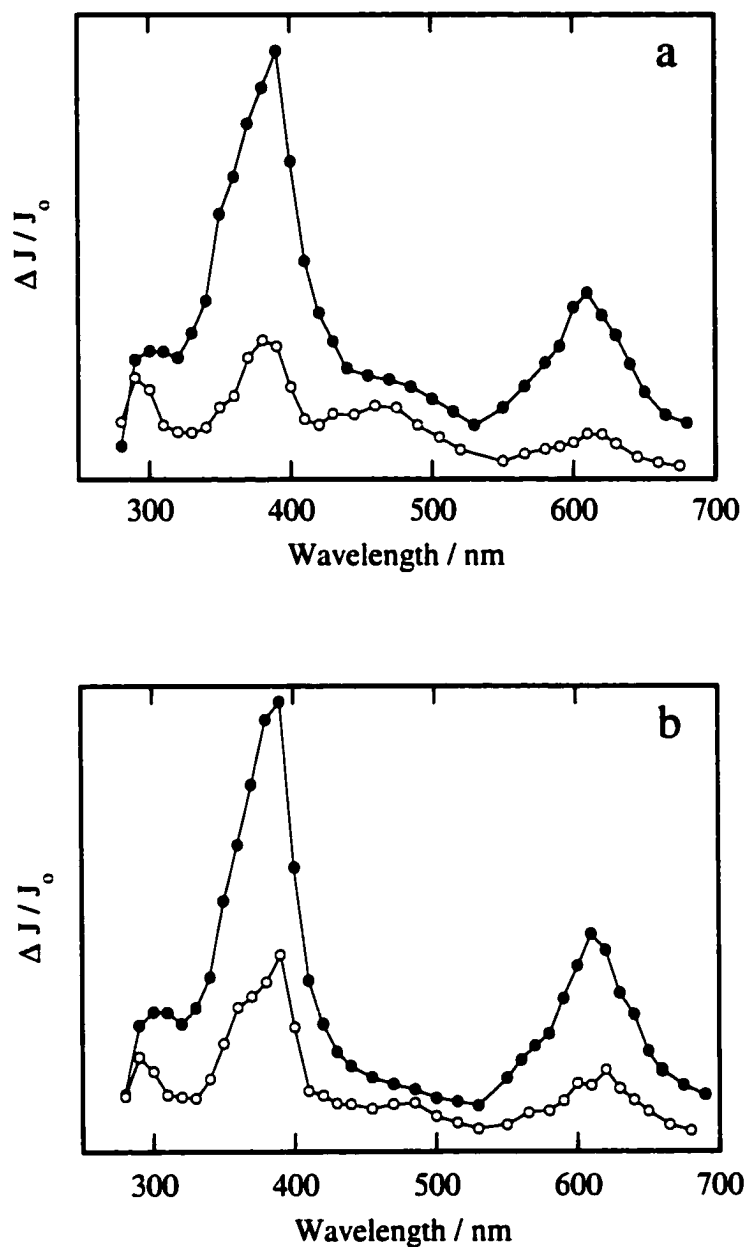
Figure 2-47. Transient diffuse reflectance spectra upon 266 nm excitation of 2-chloro-1-(4-methoxyphenyl)propyl acetate in (a) KY, (b) RbY under nitrogen (●) and oxygen (○) conditions. Spectra were recorded 0.50 μs after the laser pulse at 22 ± 1 °C.

2.2.6.2. 2-Trifluoroacetoxy-1-(4-methoxyphenyl)ethyl acetate

Figure 2-48 shows the transient diffuse reflectance spectrum obtained immediately following 266 nm laser photolysis of 2-trifluoroacetoxy-1-(4-methoxy-phenyl)ethyl acetate (AcOTFAVA) in evacuated (10^{-4} torr) LiY (<S> = 0.2).[231] The spectra consist of the characteristic absorption bands of the 4-methoxystyrene radical cation at 365 and 600 nm and a much weaker band at 300 nm that might correspond to the 2-trifluoroacetoxy-1-(4-methoxyphenyl)ethyl radical. The time-resolved trace obtained at 600 nm shows the growth corresponding to the formation of the 4-methoxystyrene radical cation with a rate constant of 3.8 x 10^5 s^{-1} (inset Figure 2-48).

Results obtained upon laser irradiation of a second precursor, 3-oxo-2-(4-methoxyphenyl)-1-butyl trifluoroacetate which gives the 2-trifluoroacetoxy-1-(4-methoxyphenyl)ethyl radical by a Norrish Type I photoreaction, eq. 2-23, were similar to those described above. The transient spectrum generated upon 266 nm photolysis of this precursor compound under evacuated conditions is given in Figure 2-49 and shows the same 365 and 600 nm bands. The complete quenching of the radical cation bands in the presence of oxygen supports their generation occurs via β-heterolysis, Figure 2-50.
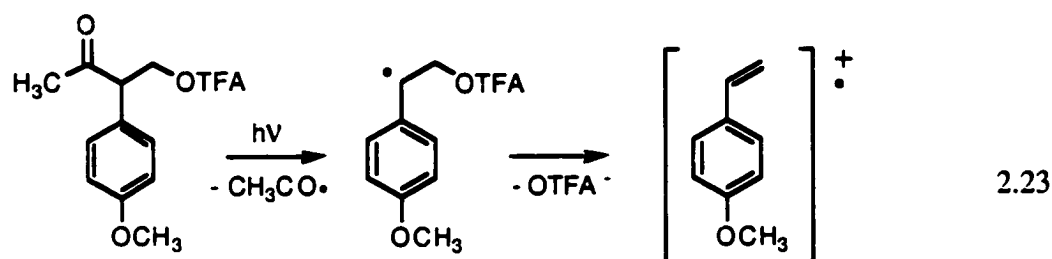
In addition to radical cation absorption bands, a band centred around 400 nm is also present in the spectrum, Figure 2-49. This band is tentatively assigned to the triplet excited state of the 4-methoxyphenyl chromophore for three reasons. First, the 400 nm is completely quenched by oxygen as expected for a triplet state. In addition, triplet states of methoxybenzenes are known to have absorption maxima near 400 nm in solution. Finally, the intensity of the 400-nm band increases considerably upon going from LiY to CsY, Figure 2-51. Such behaviour is consistent with a heavy atom effect whereby large

atoms like Cs enhance intersystem crossing from the singlet excited state to the triplet excited state. The heavy atom effect in zeolites has been observed previously.[125,232]

The diffuse reflectance spectra obtained upon 266 nm laser irradiation of AcOTFAVA within MY zeolite shown in Figure 2-51 illustrate that the 4-methoxystyrene radical cation at 360 and 600 nm is generated in LiY, NaY and KY, eq. 2.24.

2.24
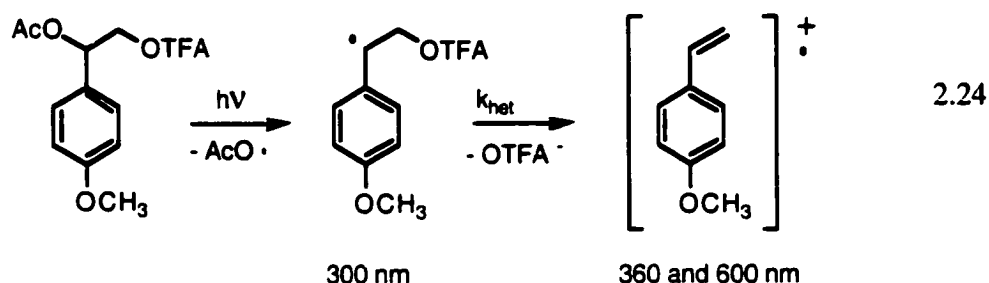
In these three zeolites, the growth of radical cation was sufficiently slow to be resolved and for rate constants for β-heterolysis to be determined. These rate constants are summarized in Table 2-13. As expected, the rate constant for β-heterolysis of the trifluoroacetoxy group from 2-trifluroacetoxy-1-(4-methoxyphenyl)ethyl radical is sensitive to the nature of the counterbalancing zeolite cation. The fastest rate constant of 6.3×10^5 s^{-1} is found in NaY. The rate constant is reduced to 2.1×10^5 s^{-1} when the counterion is changed to KY. Surprisingly, heterolysis is slower in LiY than in NaY. This is likely due to the difficulties associated with removing water from LiY. As was previously discussed, hydration of the zeolite results in the probe molecule experiencing a less ionizing environment and thus lowers the rate constant for β-heterolysis.

The radical cation is not observed in RbY and CsY, indicating that no heterolysis takes place and that these zeolites are not sufficiently ionizing to promote the heterolysis reaction when the leaving group is a trifluoracetate group. The relatively strong absorption at 300 nm assigned to the radical is consistent with a heterolysis reaction that is too slow to significantly deplete the radicals formed upon laser irradiation.

Table 2-13. Rate constants for the heterolysis of chloride from the 2-trifluroacetoxy-1-(4-methoxyphenyl)ethyl radical (22 ± 1°C) in dry alkali-metal-cation-exchanged Y zeolites.

Counterion	k_{growth} / s^{-1}
Li$^+$	$(3.8 \pm 0.1) \times 10^5$
Na$^+$	$(6.3 \pm 0.7) \times 10^5$
K$^+$	$(2.1 \pm 0.4) \times 10^5$
Rb$^+$	not observed
Cs$^+$	not observed

As the reactivity of the 2-trifluoroacetoxy-1-(4-methoxyphenyl)ethyl radical had not been previously studied in solution, photolysis of AcOTFAVA in various solvents was undertaken. The slow rate constant for the heterolysis of this compound was evident in that only HFIP was sufficiently ionizing to generate the radical cation by β-heterolysis in solution, Figures 2-52 and 2-53. Kinetic analysis of the trace monitored at 600 nm revealed the 4-methoxystyrene radical cation was formed with a rate constant of $(3.1 \pm 0.1) \times 10^5$ s^{-1} in HFIP. In other solvents like 2,2,2-trifluoroethanol or 50% aqueous acetonitrile that are less ionizing then HFIP, only the radical and the unidentified 400 nm transient were observed, with no corresponding β-heterolysis.
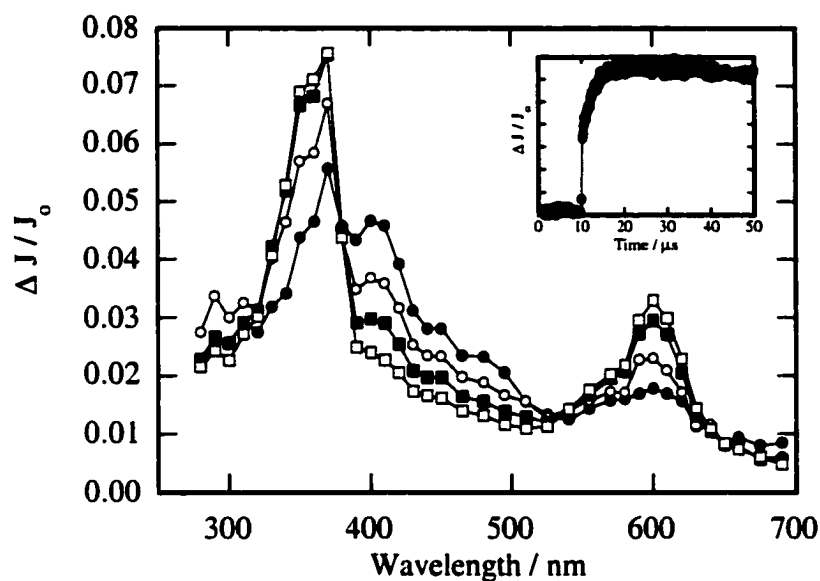
Figure 2-48. Transient diffuse reflectance spectrum of 2-trifluoroacetoxy-1-(4-methoxyphenyl)ethyl acetate in LiY under dry-nitrogen conditions (10^{-4} torr) after 266 nm excitation. Spectra were recorded (●) 0.32 μs, (○) 1.60 μs, (■) 4.80 μs and (□) 12.8 μs after the laser pulse at 22 ± 1 °C. The inset shows the time-resolved trace at 600 nm over 40 μs.
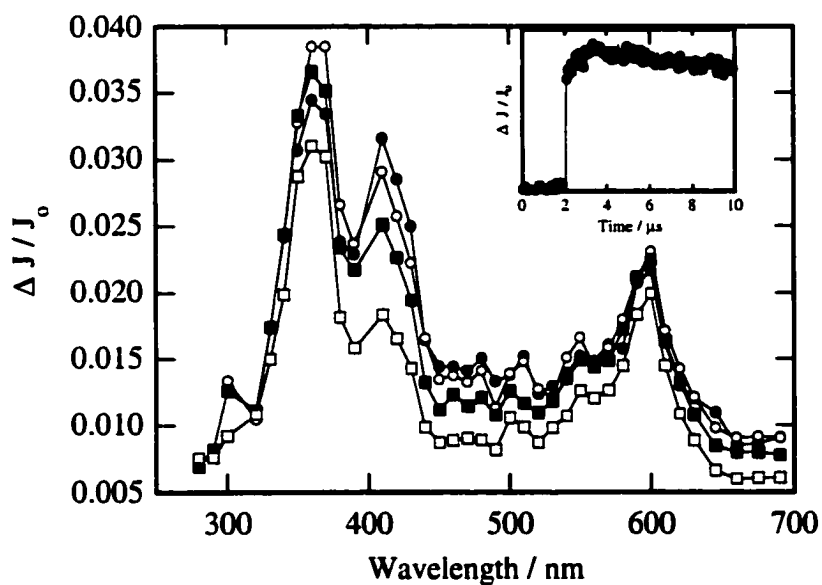
Figure 2-49. Transient diffuse reflectance spectrum of 3-oxo-2-(4-methoxyphenyl)-1-butyl trifluoroacetate in LiY under dry-nitrogen conditions (10^{-4} torr) after 266 nm excitation. Spectra were recorded (●) 0.40 μs, (○) 1.12 μs, (■) 3.36 μs and (□) 12.8 μs after the laser pulse at 22 ± 1 °C. The inset shows the time-resolved trace at 600 nm.
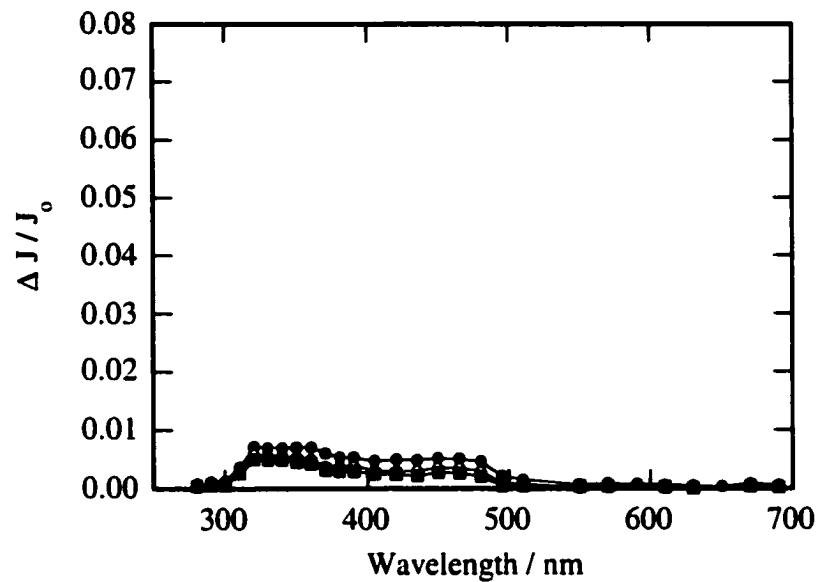
Figure 2-50. Transient diffuse reflectance spectrum of 2-trifluoroacetoxy-1-(4-methoxy-phenyl)ethyl acetate in LiY under oxygenated conditions after 266 nm excitation. Spectra were recorded (●) 0.48 μs, (○) 1.76 μs, (■) 4.72μs after the laser pulse at 22 ± 1 °C.
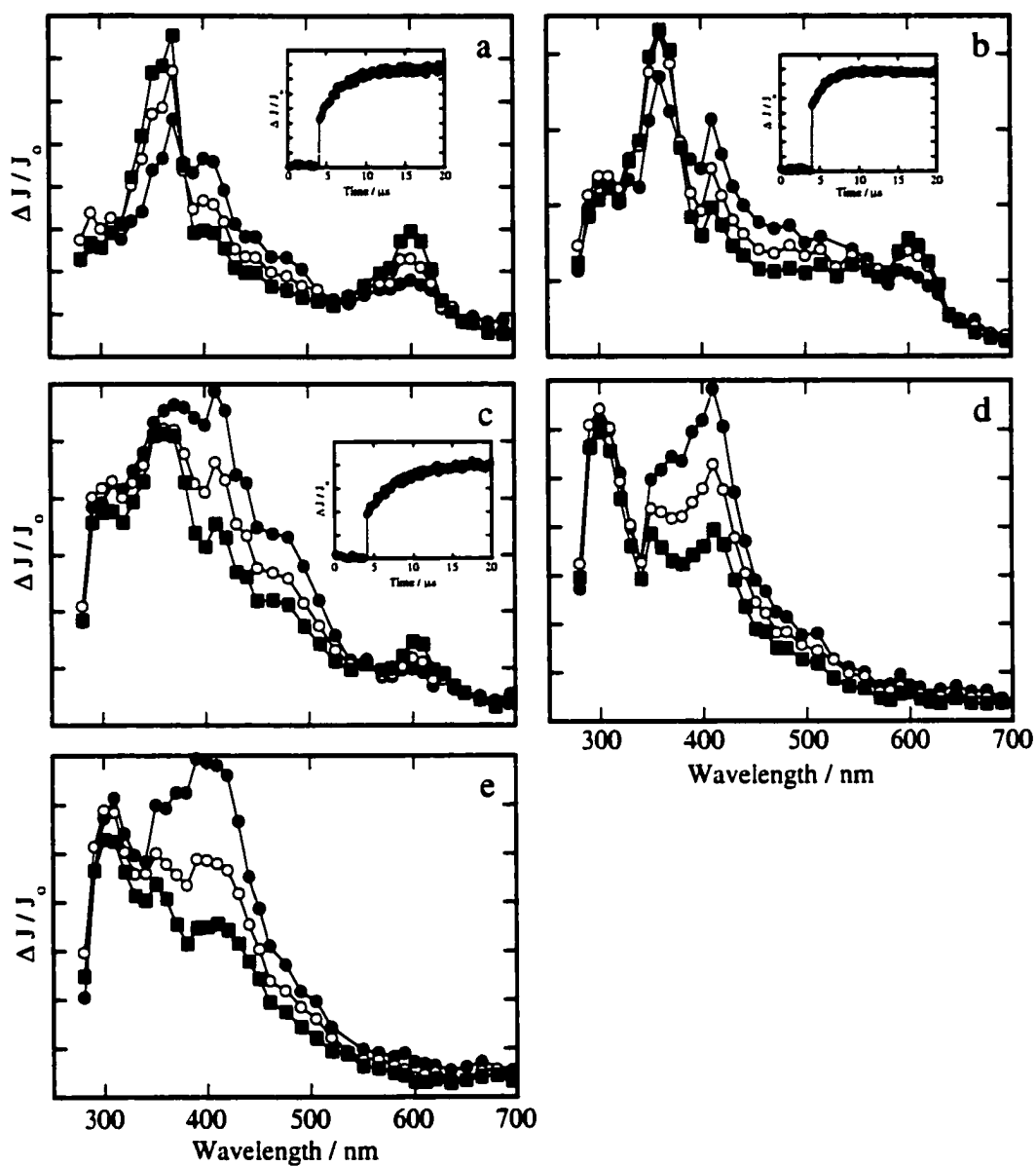
Figure 2.51. Transient diffuse reflectance spectrum of 2-trifluoroacetoxy-1-(4-methoxyphenyl)ethyl acetate in (a) LiY, (b) NaY, (c) KY, (d) RbY and (e) CsY under dry-nitrogen conditions after 266 nm excitation. Spectra were recorded ($\bullet$) 0.32 μs, (O) 1.60 μs, ($\blacksquare$) 4.80 μs after the laser pulse at 22 ± 1 °C. The inset shows the time-resolved trace at 600 nm over 16 μs.
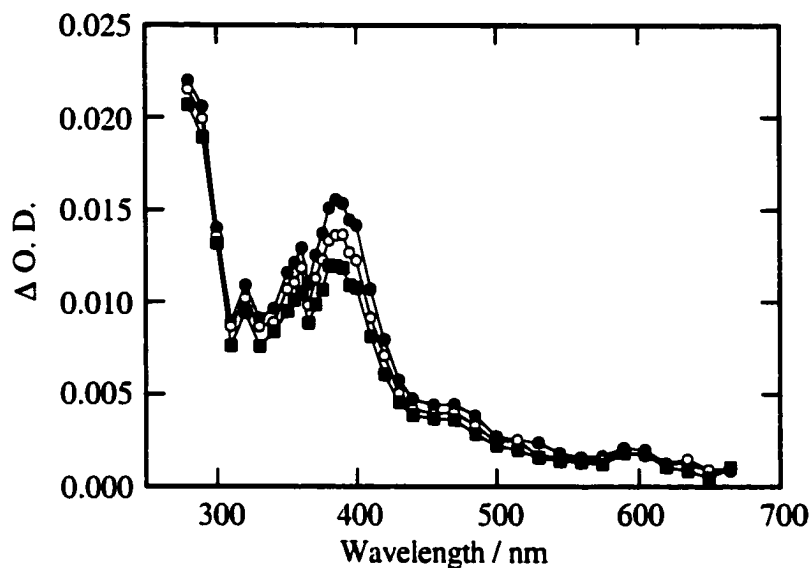
Figure 2-52. Transient absorption spectrum generated (●) 424 ns, (○) 876 ns and (■) 1.44 μs after 266 nm laser photolysis of 2-trifluoroacetoxy-1-(4-methoxyphenyl)ethyl acetate in nitrogen-saturated TFE.
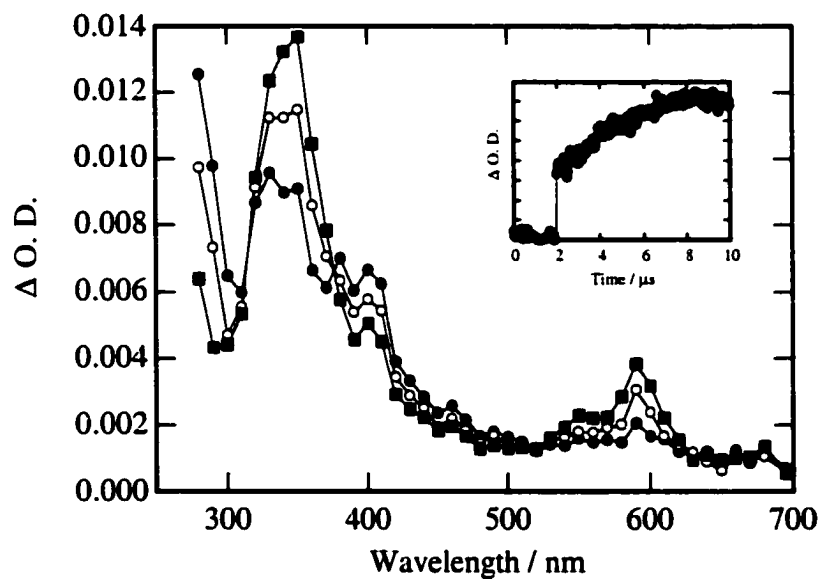
Figure 2-53. Transient absorption spectrum generated (●) 560 ns, (○) 2.2 μs and (■) 3.04 μs after 266 nm laser photolysis of 2-trifluoroacetoxy-1-(4-methoxyphenyl)ethyl acetate in nitrogen-saturated HFIP.

2.2.6.3. *2-Trifluoroacetoxy-1-(4-methoxyphenyl)propyl acetate*

The effect of an β-methyl group at the carbon containing the radical for the β-trifluoroacetoxy substrate was examined by the study of 2-trifluoroacetoxy-1-(4-methoxyphenyl)propyl acetate (AcOTFAAn) inside the cavities of zeolites and in solution. Laser flash photolysis of AcOTFAAn in nitrogen-purged MY zeolites led to the transient spectra shown in Figure 2-54. Each spectrum, except that taken in NaY, show the characteristic bands at 385 and 610 nm corresponding to the anethole radical cation generated *via* heterolysis from the β-chloro-1-(4-methoxyphenyl)ethyl radical, eq. 2.25.

$$
\begin{array}{ccc}
\underset{\underset{OCH_3}{|}}{\underset{|}{AcO}}\text{—CH(CH}_3\text{)—OTFA} & \xrightarrow[-\,AcO\bullet]{h\nu} & \bullet\text{CH(CH}_3\text{)—OTFA}\\
\text{300 nm} & \xrightarrow[-\,OTFA^-]{k_{het}} & \text{385 and 610 nm}
\end{array}
\qquad 2.25
$$
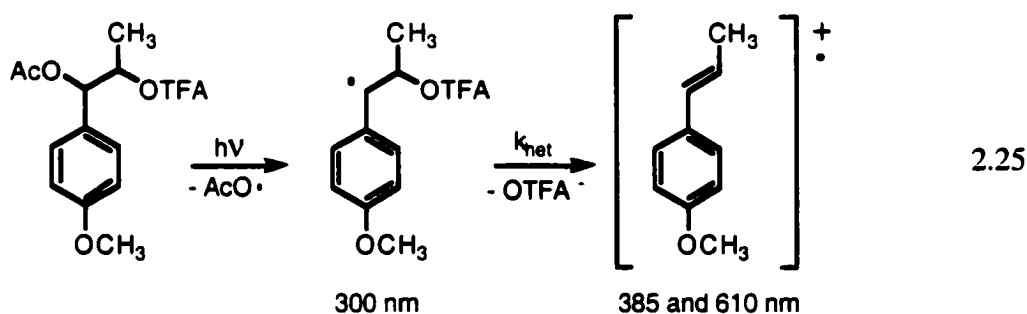
These spectra are however not very clean, with significant contamination originating from cation trapped electrons. This contamination was particularly acute with the NaY sample in which the 395 nm band from the radical cation was observed, but the 610 nm band was completely hidden.

The growth of the radical cation was also not clean. In LiY and NaY, the radical cation appeared to form promptly within the laser pulse with a rate constant > 5 x 10^7 s^{-1}. In KY, RbY and CsY a fast and slow component were observed. The fast components, which made up the greatest fraction of the growth, was barely resolved, and corresponded to a rate constant in each of these zeolites of 2 x 10^7 s^{-1}. However, such fast rate constants under conditions were the spectra are contaminated with trapped electrons are not likely to be very reliable. Rate constants associated with the slow component are listed in Table 2-14. However, these values are also likely to be unreliable due to the small contribution of the slow component to the overall increase in absorption of the radical cation.

While good kinetic data could not be obtained with this substrate, the results do suggest that ionization of the trifluoroacetate group from the radical is faster than ionization for the substrate lacking the methyl group at the β-position. This is similar to the results obtained with the β-chloro substituted systems described above.

Table 2-14. Rate constants for the heterolysis of chloride from the 2-trifluroacetoxy-1-(4-methoxyphenyl)propyl radical (22± 1°C) in dry alkali-metal-cation-exchanged Y zeolites.

Counterion	k_{growth} / s^{-1} fast component	k_{growth} / s^{-1} slow component
Li$^+$	not resolved	not resolved
Na$^+$	not resolved	not resolved
K$^+$	$(26.9 \pm 1.0) \times 10^6$	$(4.3 \pm 2.5) \times 10^5$
Rb$^+$	$(20.6 \pm 5.9) \times 10^6$	$(1.1 \pm 0.1) \times 10^6$
Cs$^+$	$(17.4 \pm 2.2) \times 10^6$	$(1.8 \pm 0.3) \times 10^6$

To ensure that the β-hetereolysis of trifluoroacetate in solution followed expected trends, the photolysis of AcOTFAVA in solution was also examined. In AcN, one predominant band at 295 nm assigned to the 2-trifluoroacetoxy-1-(4-methoxy-phenyl)propyl radical was observed, but no radical cation absorption was present, Figure 2-55. Similar results were observed in methanol. Thus, in these solvents of low ionizing ability, no ionization of trifluoroacetate takes place.

Transient spectra and kinetics obtained under nitrogen-saturated samples of AcOTFAAn in neat TFE, neat HFIP, TFE/AcN and HFIP/AcN mixtures, indicate the formation of the anethole radical cation from the β-trifluoroacetoxy radical, Figure 2-56. Concomitant to the growth of the radical cation at 385 and 610 nm is the decay of the 300 nm corresponding to the 2-trifluoroacetoxy-1-(4-methoxyphenyl)propyl radical. The β-heterolysis rate constants obtained for various solvent mixtures are listed in Table 2-15.

Table 2-15. Rate constants for the heterolysis of chloride from the 2-trifluroacetoxy-1-(4-methoxyphenyl)propyl radical (22± 1°C) in TFE/AcN and HFIP/AcN solvent mixtures.

Solvent Mixture	k_{growth} / 10^6 s^{-1}	Solvent Mixture	k_{growth} / 10^6 s^{-1}
100% TFE	1.1 ± 0.1	100% HFIP	7.4 ± 0.2
90% TFE in AcN	0.61 ± 0.01	90% HFIP in AcN	5.3 ± 0.3
80% TFE in AcN	0.57 ± 0.01	80% HFIP in AcN	2.0 ± 0.2
70% TFE in AcN	0.49 ± 0.01	70% HFIP in AcN	1.3 ± 0.2
60% TFE in AcN	0.37 ± 0.02	60% HFIP in AcN	0.50 ± 0.02
50% TFE in AcN	0.22 ± 0.01	50% HFIP in AcN	0.25 ± 0.02
40% TFE in AcN	0.19 ± 0.03	40% HFIP in AcN	0.17 ± 0.02
		30% HFIP in AcN	0.16 ± 0.02

The effect of solvent on the rate constant for the heterolytic cleavage of the carbon-trifluoroacetate bond is clearly illustrated in the Table above. As the proportion of fluorinated solvent increases the ionizing ability of the solvent also increases thus contributing to the increase of the β-heterolysis rate constant. Comparison of the rate constants obtained for the trifluoroacetoxy substituted radical with the chloro substituted radical, again demonstrates the lower propensity for the fluorinated leaving group to cleave.
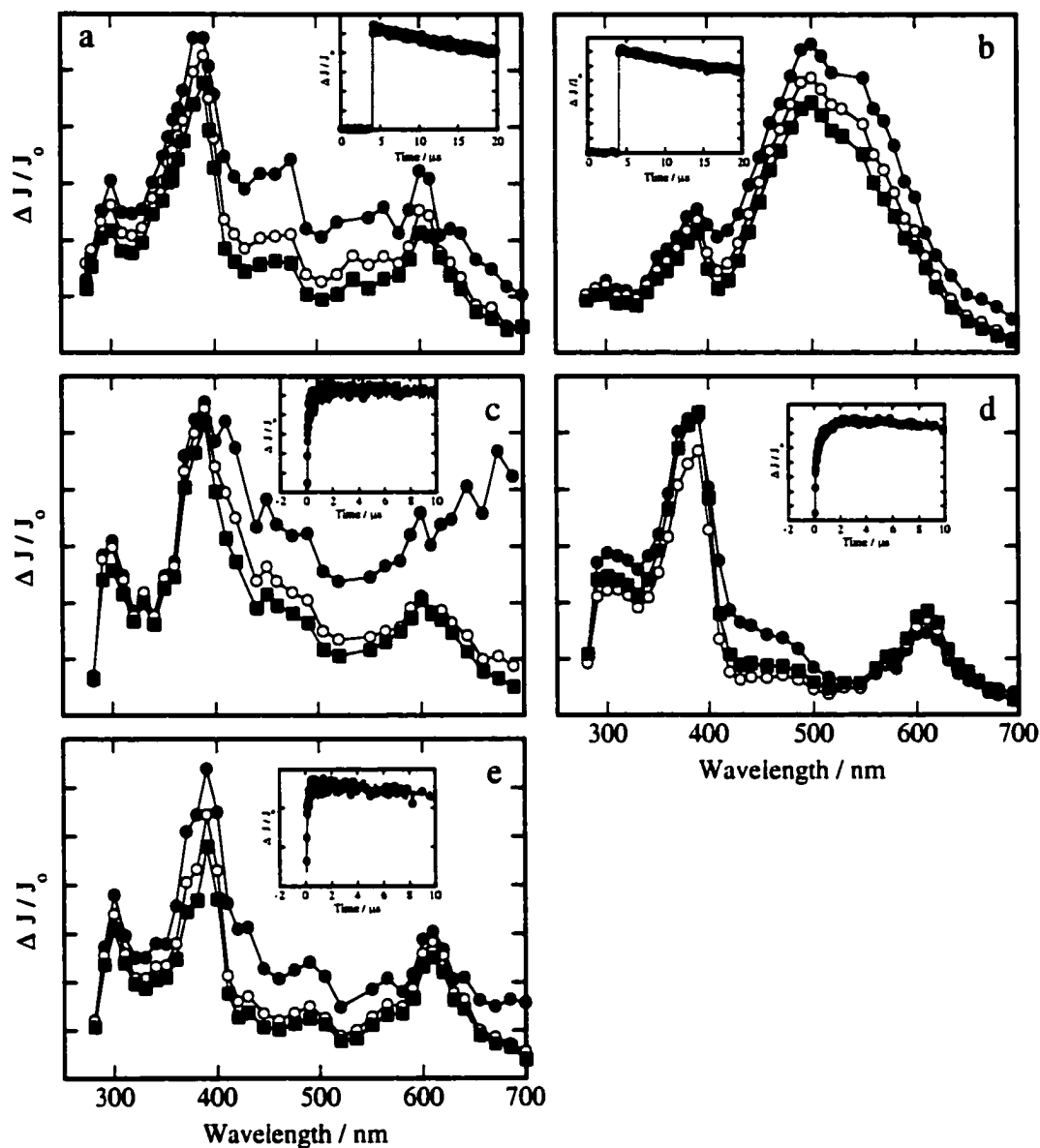
Figure 2-54. Transient diffuse reflectance spectrum of 2-trifluoroacetoxy-1-(4-methoxyphenyl)propyl acetate in (a) LiY, (b) NaY, (c) KY, (d) RbY and (e) CsY under dry-nitrogen conditions after 266 nm excitation. Spectra were recorded (●) 0.44 μs, (O) 4.88 μs, (■) 12.80 μs after the laser pulse at 22 ± 1 °C. The inset shows the time-resolved trace at 600 nm.
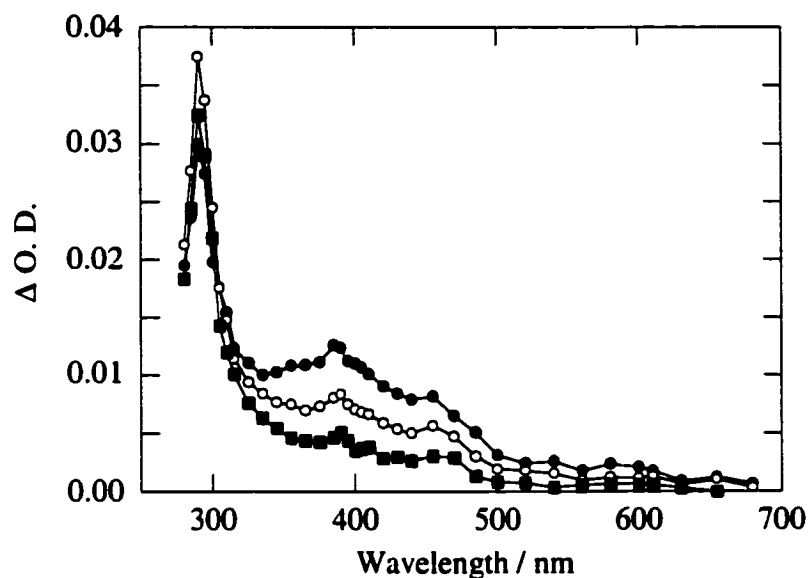
Figure 2-55. Transient absorption spectrum generated (●) 0.48 μs, (○) 1.50 μs, and (■) 4.50 μs after 266 nm laser photolysis of 2-trifluoroacetoxy-1-(4-methoxyphenyl)propyl acetate in nitrogen-saturated AcN.
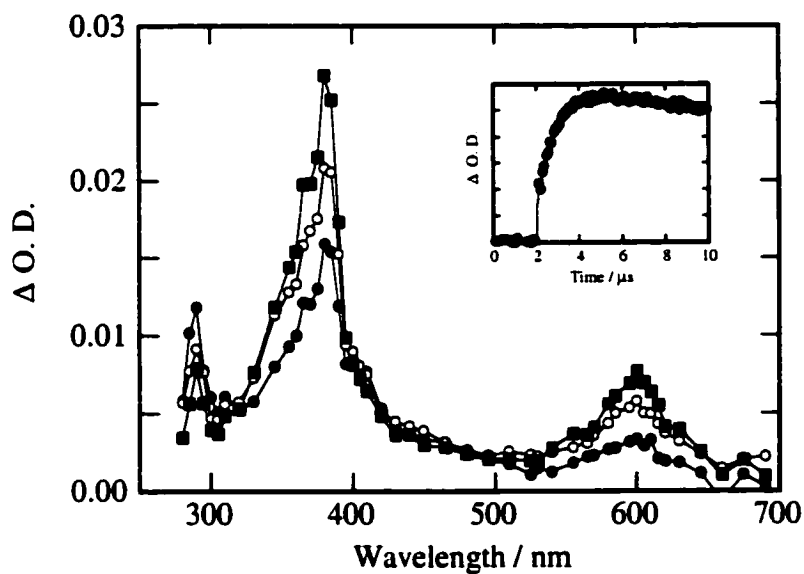
Figure 2-56. Transient absorption spectrum generated (●) 0.48 μs, (○) 0.88 μs, and (■) 1.88 μs after 266 nm laser photolysis of 2-trifluoroacetoxy-1-(4-methoxyphenyl)propyl acetate in nitrogen-saturated 100% TFE. The inset shows the time-resolved trace at 385 nm.

2.2.6.4. 2-Chloro-1-(2,4-dimethylphenyl)ethyl acetate

The 2,4-dimethylstyrene radical cation was anticipated to be a highly reactive species in solution and within MY zeolites. The radical cation was therefore generated by photoionization of 2,4-dimethylstyrene in TFE and in NaY in order to determine its reactivity. The diffuse reflectance spectra obtained upon 266 nm excitation of 2,4-dimethylstyrene in TFE and incorporated within NaY are shown in Figures 2-57 and 2-58, respectively. Both spectra are characterised by strong absorption bands centered at 350 and 590 nm corresponding to the 2,4-dimethylstyrene radical cation. The spectra also clearly indicate that the 2,4-dimethylstyrene radical cation is quite reactive and decays within 10 µs after the laser pulse in both TFE and in NaY.

The diffuse reflectance spectra obtained upon 266 nm laser irradiation of 2-chloro-1-(2,4-dimethylphenyl)ethyl acetate in alkali-metal exchanged Y zeolites are shown in Figure 2-59. With this substrate, the 2,4-dimethylstyrene radical cation with absorption maxima at 350 and 590 nm could only be observed in LiY and NaY. In KY, RbY and CsY, no radical cation absorption was detected. A strong absorption band at 330 nm is observed in each the spectra in the Y zeolites. This band is in the region expected for the 2-chloro-1-(2,4-dimethylphenyl)ethyl radical.

Contrary to the results obtained upon laser irradiation of 2-chloro-1-(4-methoxyphenyl)ethyl acetate where the radical produced by photohomolysis was barely detectable in NaY, the intensity of the 330 nm band due to 2-chloro-1-(2,4-dimethyl-phenyl)ethyl radical absorption is considerably larger relative to the intensity of the absorption of the radical cation bands.

2.26

330 nm   350 and 590 nm
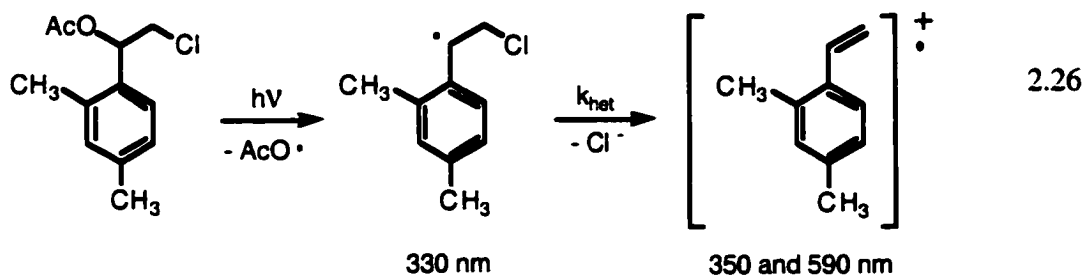
The spectra in LiY and NaY, Figure 2-59, also show a fast decaying transient in the 500-700 nm region. The species responsible for this band was completely quenched by electron scavengers such as oxygen and nitrous oxide. These characteristics are typical of a trapped electron within zeolites. Hence, the broad absorption band ca. 550 nm is assigned to one of the sodium complexes; most likely Na_4^{3+}.

Since the 2,4-dimethylstyrene radical cation is much less stable than the 4-methoxystyrene radical cation and the anethole radical cation, it was thought that formation of the 2,4-dimethylstyrene radical cation by heterolysis of chloride from 2-chloro-1-(2,4-dimethylphenyl)ethyl radical would be significantly slower than the same reaction of the 4-methoxy substituted radicals. The fact that no heterolysis takes place at all in solution, even in highly ionizing solvents like HFIP, is consistent with this expectation. However, when attempts were made to measure the dynamics of the formation of the 2,4-dimethylstyrene radical cation in LiY and NaY, radical cation formation was complete within the laser pulse with a rate constant $> 5 \times 10^7$ s^{-1}. Thus, it is likely that another process other than β-heterolysis is responsible for the rapid formation of the radical cation. The process responsible for 2,4-dimethylstyrene radical cation formation upon photolysis of 2-chloro-1-(2,4-dimethylphenyl)ethyl acetate was not studied in further detail.

2.2.6.5. 2-Chloro-1-(4-methylphenyl)ethyl acetate

Just as with the 2,4-dimethyl derivative, the heterolysis of the carbon-chlorine bond of the generated 2-chloro-1-(4-methylphenyl)ethyl radical is too slow to be observed in zeolites. The transient diffuse reflectance spectra of 2-chloro-1-(4-methylphenyl)ethyl acetate after 266 nm laser irradiation under vacuum (10^{-4} torr) conditions in the five alkali-exchanged Y zeolites are given in Figure 2-60. From the spectra shown in this Figure, it appears that the radical cation is generated in LiY and NaY, but there are other species present in the spectra that hinder the assignment of the 350 nm and 590 nm, typical of the 4-methylstyrene radical cation. There is a strong absorbing species in the 500-700 nm region which is assigned to complexed electron

species.[233] Common in all the spectra is the 320 nm band which is thought to correspond to the β-chloro radical generated upon photolysis. Assignment was confirmed by the quenching of the 320 nm band in the presence of oxygen and the comparison of the 320 nm absorption band to the known absorption spectra for similar radical species in zeolites.
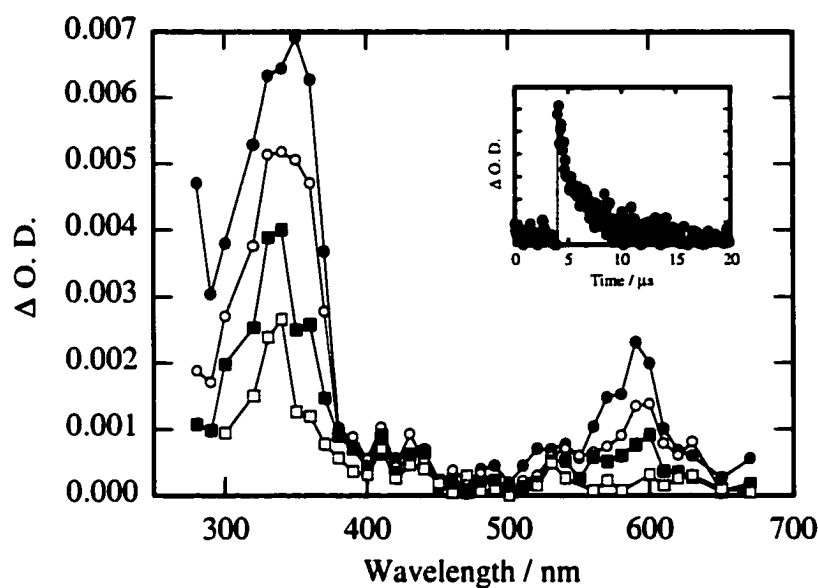
Figure 2-57. Transient absorption spectrum generated (●) 0.36 μs, (○) 1.04 μs, (■) 3.32 μs and (□) 12.7 μs after 266 nm laser irradiation of 2,4-dimethylstyrene in nitrogen-saturated TFE. Inset shows decay trace at 590 nm for the 2,4-dimethylstyrene radical cation.
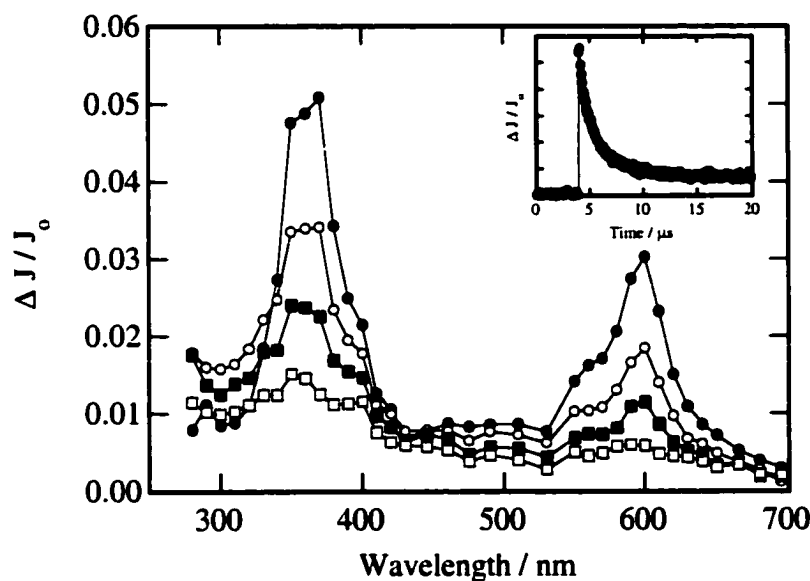
Figure 2-58. Transient diffuse reflectance spectrum generated upon 266 nm laser photolysis of 2,4-dimethylstyrene under vacuum (10^{-4} torr) in NaY using DCM as incorporating solvent. Spectra were recorded (●) 0.64 μs, (○) 1.76 μs, (■) 3.64 μs and (□) 12.8 μs after the laser pulse. Inset shows the decay trace at 590 nm for the 2,4-dimethylstyrene radical cation.
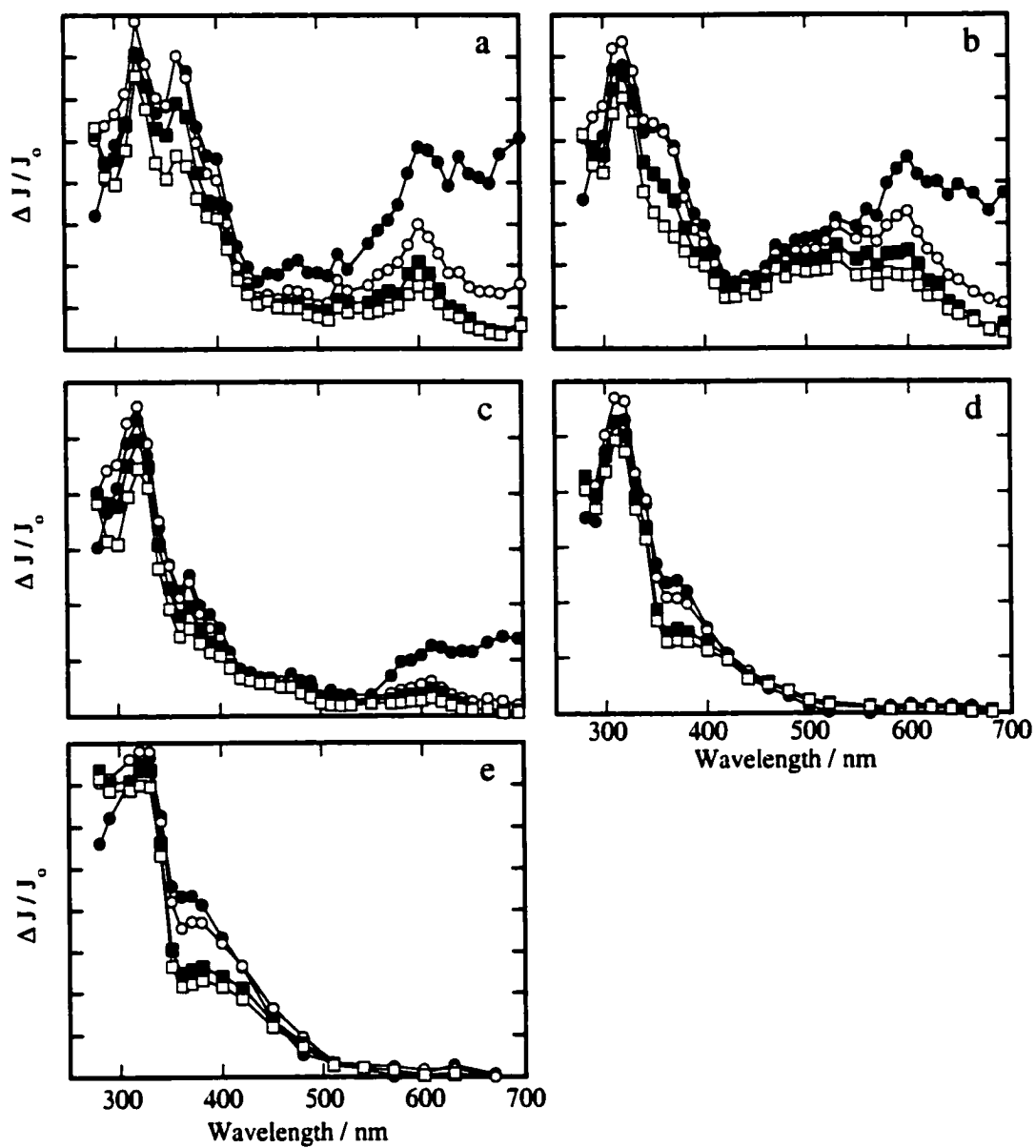
Figure 2-59. Transient diffuse reflectance spectrum of 2-chloro-1-(2,4-dimethylphenyl) ethyl acetate in (a) LiY, (b) NaY, (c) KY, (d) RbY and (e) CsY under vacuum conditions after 266 nm excitation. Spectra were recorded (●) 0.24 μs, (O) 0.80 μs, (■) 2.86 μs, and (□) 6.28 μs after the laser pulse at 22 ± 1 °C.
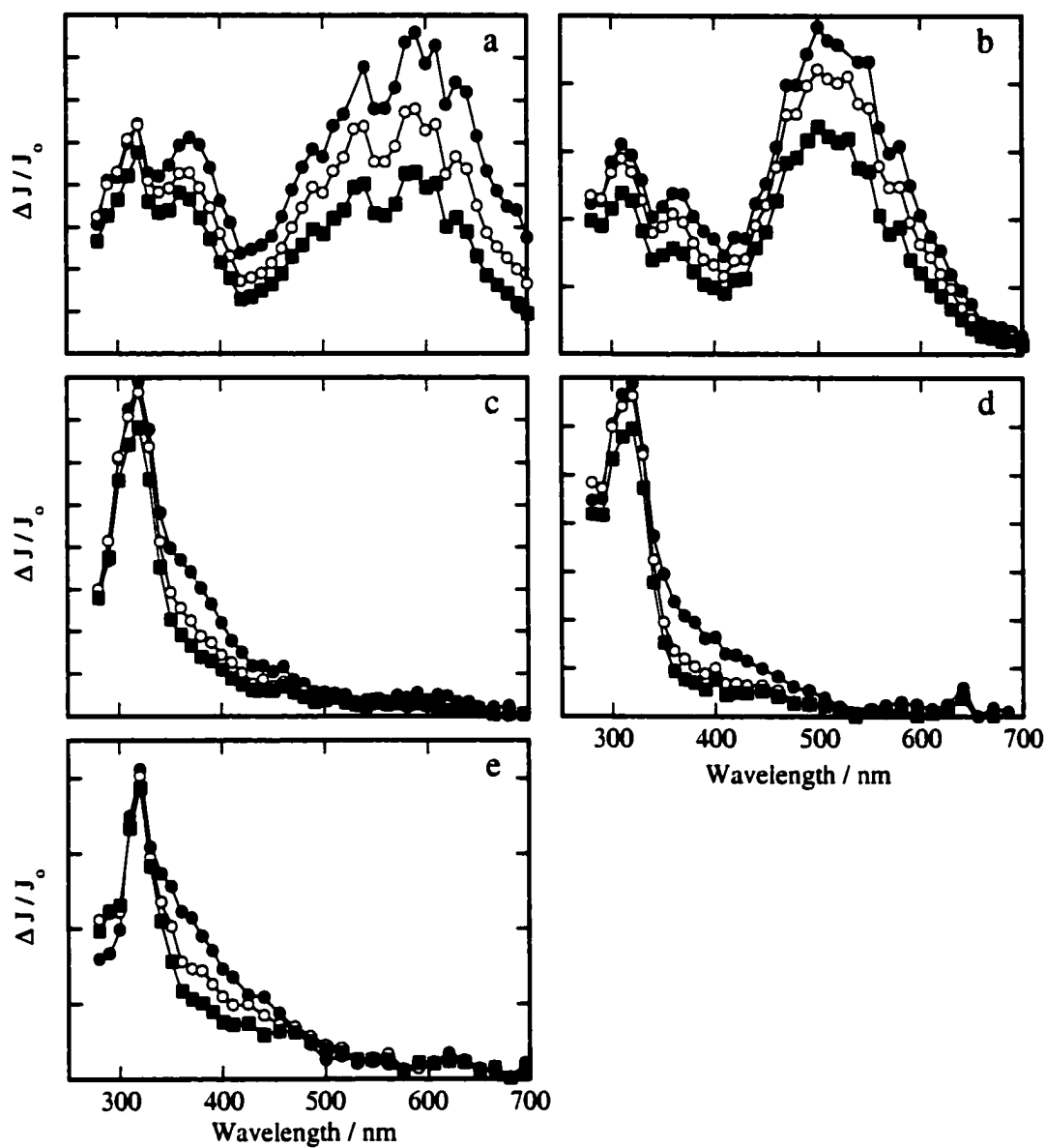
Figure 2-60. Transient diffuse reflectance spectrum of 2-chloro-1-(4-methylphenyl)ethyl acetate in (a) LiY, (b) NaY, (c) KY, (d) RbY and (e) CsY under dry-vacuum conditions after 266 nm excitation. Spectra were recorded (●) 0.60 μs, (○) 3.04 μs, (■) 12.80 μs after the laser pulse at 22 ± 1 °C.

2.2.6.6. 2-Bromo-1-(4-methoxyphenyl)ethyl acetate and 2-bromo-1-(4-methoxyphenyl)propyl acetate

The transient diffuse reflectance spectra for the 266 nm photolysis of 2-bromo-1-(4-methoxyphenyl)ethyl acetate (AcOBrVA) in alkali-metal exchanged Y zeolites are given in Figure 2-61. In all five cases, prompt formation of the characteristic bands for the 4-methoxystyrene radical cation are visible at 365 and 600 nm. However, the yield of radical cation formation was low in all cases and other unidentified bands are observed in the spectra. In the case of the CsY sample, there is a weaker band around 300 nm, which may be due to the β-bromo substituted radical.

In solution, the rate constants for heterolysis of bromide from the β-bromo-1-(4-methoxyphenyl)ethyl radical are on average about 3-6 times faster than the ionization of β-chloro-1-(4-methoxyphenyl)ethyl radical under the same conditions. As the reactivity of the β-bromo derivative is known to be only slightly higher than the β-chloro derivative, the β-heterolysis of bromide was anticipated to be observed within the series of MY zeolites, with a time resolved growth being detected in RbY and CsY. However, the time-resolved formation of the 4-methoxystyrene radical cation was not observed under any conditions within MY zeolites. Even in CsY where the rate constant for the reaction should be within the time resolution of the laser system no heterolysis was detected. This either indicates that in all cases the reactions are very fast or that the 2-bromo-1-(4-methoxyphenyl)ethyl radical does not undergo rapid heterolysis in MY zeolites and that the radical cations observed in the spectra are generated by another chemical route.

Photolysis of 2-bromo-1-(4-methoxyphenyl)propyl acetate AcOBrAn incorporated within NaY gave a spectrum with absorption bands that could not be identified. Analysis of the extracted material from zeolite samples containing AcOBrAn showed some indication of decomposition, evidenced by additional peaks other than neat compound in the gas chromatogram. Neither β-bromo compound was investigated in further detail.
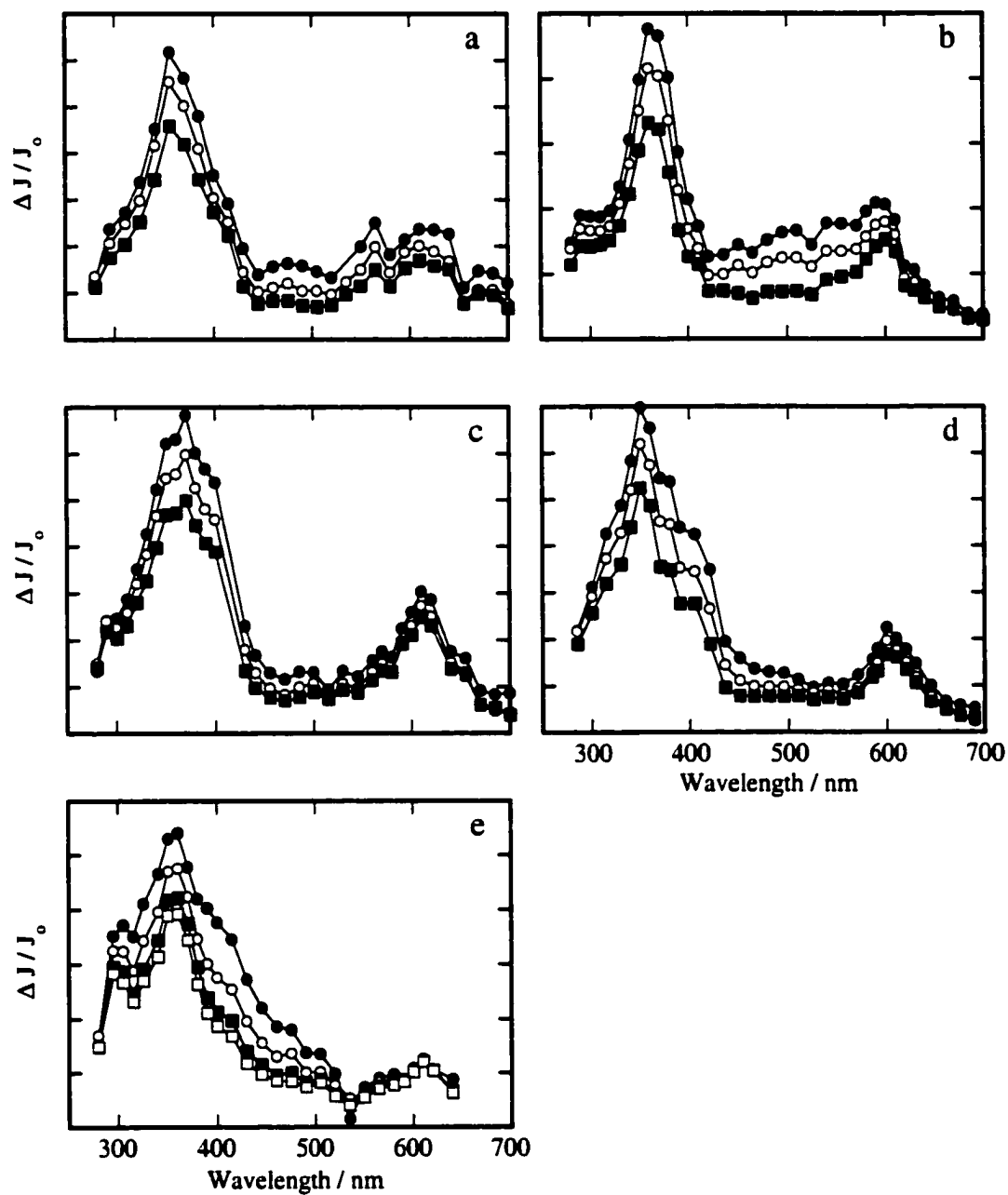
Figure 2-61. Transient diffuse reflectance spectrum of 2-bromo-1-(4-methoxy-phenyl)ethyl acetate in (a) LiY, (b) NaY, (c) KY, (d) RbY and (e) CsY under dry-vacuum conditions after 266 nm excitation. Spectra were recorded (●) 0.60 μs, (O) 2.80 μs, (■) 12.80 μs after the laser pulse at 22 ± 1 °C.

2.2.7. Reactivity of substituted styrene radical cations within faujasite Y zeolites

Results obtained from the reactivity of styrene radical cations generated in solution from neutral styrenes by photoionization or photoinduced electron transfer have shown that the main reaction of the radical cations is addition to the neutral styrenes.[185,186] As a result, the decay kinetics for the radical cation generated using these methods is typically strongly dependent on the concentration of the precursor. Similarly, all previous studies concerning the absolute reactivity of substituted styrene radical cations in zeolites also involved using photoionization or photoinduced electron transfer to generate the radical cations, and the decays of the radical cations were also likely to be influenced by addition to the neutral styrene precursor. As a result, the decays of the radical cations in previously published work were probably not so much determined by the nature of the zeolite environment, but instead were also influenced by the amount of precursor incorporated into the zeolite.

The formation of the styrene radical cations by β-heterolysis in the present study within various cation exchanged zeolites provided the opportunity to examine the decay of the radical cation in the absence of the corresponding styrene. In this way, a more detailed examination of the effect of zeolite composition of the inherent decay of the radical cation could be obtained. Results from these studies are summarized below. For the sake of comparison, the kinetics for the decay of the same radical cations generated by photoionization are also included.

2.2.7.1. Reactivity of Radical Cations Generated by β-Heterolysis

4-Methoxystyrene Radical Cation

The time-resolved traces shown in Figure 2-62 correspond to the decay of the 4-methoxystyrene radical cation generated from β-heterolysis of 2-chloro-1-(4-methoxy-phenyl)ethyl radical in the five alkali-exchanged Y zeolites under nitrous oxide. Nitrous oxide conditions were chosen in order to remove any complications due to the presence of complexed electrons. Qualitatively, these plots clearly show that the decay of the 4-

methoxystyrene radical cation is affected strongly by the nature of the charge balancing cation of the zeolite. Specifically, the rate of decay increases as the size of the alkali-metal cation increases in size from Li^+ to Cs^+.

A more quantitative analysis of the decay traces would be useful to compare the actual reactivity of the radical cation in each of the zeolites. However, the time-resolved data did not fit well to a simple single first-order rate expression. Such complex kinetic behaviour is not uncommon for reactions in zeolites due to the heterogeneous nature of the intrazeolite environment which can lead to a distribution of decay rate constants, or the possibility of more than one distinct reaction pathway for the intermediate. In addition, the radical cation decay could only be followed for up to 800 μs after laser pulse. This maximum time was not long enough for the radical cation to completely decay. The decay traces were therefore analyzed either using a two-component equation, eq. 2.27 or a three component equation, eq. 2.28, where k_i represents a first-order decay rate constant and $(\Delta J/J_o)_i$ is the total change in diffuse reflectance associated with k_i. The term corresponding to end absorption was omitted from these equations. Thus, equations 2.27 and 2.28 were used on the basis of the assumption that the radical cation decayed to the baseline. As a result of this assumption, the values associated with the slowest rate constant extracted from the two- or the three-component fits can only be considered to be estimates.

$$\left(\frac{\Delta J}{J_o}\right)_t = \left(\frac{\Delta J}{J_o}\right)_1 \exp(-k_1 t) + \left(\frac{\Delta J}{J_o}\right)_2 \exp(-k_2 t) \qquad 2.27$$

$$\left(\frac{\Delta J}{J_o}\right)_t = \left(\frac{\Delta J}{J_o}\right)_1 \exp(-k_1 t) + \left(\frac{\Delta J}{J_o}\right)_2 \exp(-k_2 t) + \left(\frac{\Delta J}{J_o}\right)_3 \exp(-k_3 t) \qquad 2.28$$

The decays in LiY, NaY, and KY were analyzed by using the three component equation, while the decay in RbY and CsY fit well to the two component form. The results of the analysis of the decay traces are presented in Table 2-16. Support for the use of complex rate expression as a suitable method for analyzing the decay traces was

obtained by further analysis using the Exponential Series Method (ESM). This is a technique commonly used to account for possible distribution of lifetimes of reactive intermediates in heterogeneous media.[42,234,235] The results from the ESM are shown in Figure 2-63. As can be observed, three distinct maxima corresponding to three dominant lifetimes were calculated for the decay of the radical cation in LiY, NaY and KY, and strongly indicates that the use of a three component rate expression to analyze the decay traces is justified. The ESM results for the decay traces observed in RbY and CsY show two sharp maxima. In CsY and RbY, the two dominant lifetimes identified by ESM correspond to the good fit of the decay trace to a two component expression. A third long-lived component was observed in the ESM for RbY. However, since the decay fit well to a double exponential equation and the third component in the ESM was very weak, only two rate constants are considered to be important in RbY.

The rate constants obtained from the reciprocal of the dominant lifetimes obtained in each of the zeolites by ESM analysis correspond nicely to those measured by the more standard method. These similarities provide even more evidence that the method of analysis is justified.

The results from the calculations using the decay in LiY, NaY and RbY all show the presence of a fast component, $k_{fast} = 2.3 \times 10^5$ s^{-1} to 4.3×10^5 s^{-1}, that is not observed in RbY and CsY. This may suggest that a fast decay mechanism for the radical cation exists in the zeolites with the small metal cation, but is absent in RbY and CsY. However, the growth of the radical cation by β-heterolysis in RbY and CsY takes place with a rate constant that is similar to or smaller than the rate constant for the fast component in the other zeolites. Thus, a fast component that may be present in RbY and CsY is obscured by the slower growth of the radical cation.

The absolute value of the rate constant for the second component associated with the decay of the 4-methoxystyrene radical cation did not vary substantially in the different zeolites, as presented in Table 2-16. However, the contribution of this component to the overall decay of the radical cation increased substantially upon going from LiY to CsY. Thus, the second component in LiY accounted for 20% of the overall

decay of the radical cation (26% if the fast decay component is neglected), while in CsY the decay rate constant of similar magnitude accounted for 63% of the decay of the radical cation.

The absolute values for the slowest component of the decay profile of the 4-methoxystyrene radical cation did change as a function of zeolite, and increased over 10-fold upon going from LiY to CsY. However, the contribution of this slow decay decreased in the same direction, accounting for 62% of the overall decay in LiY and only 37% in CsY.

Table 2-16. Rate constants for the decay of the 4-methoxystyrene radical cation generated from β-heterolysis of 2-chloro-1-(4-methoxyphenyl)ethyl radical under a nitrous oxide environment.

Zeolite	k_{decay} / s^{-1}		
	first component (% contribution)	second component (% contribution)	third component (% contribution)
LiY	$(4.4 \pm 0.5) \times 10^5$ (18%)	$(3.1 \pm 0.2) \times 10^4$ (20%)	$8.1 \pm 0.1) \times 10^2$ (62%)
NaY	$(2.3 \pm 0.2) \times 10^5$ (19%)	$(1.5 \pm 0.1) \times 10^4$ (26%)	$(1.3 \pm 0.1) \times 10^3$ (55%)
KY	$(4.2 \pm 1.0) \times 10^5$ (9%)	$(5.2 \pm 0.6) \times 10^4$ (32%)	$(7.1 \pm 0.7) \times 10^3$ (59%)
RbY	not detected	$(4.6 \pm 0.1) \times 10^4$ (49%)	$(7.5 \pm 1.3) \times 10^3$ (51%)
CsY	not detected	$(4.2 \pm 0.1) \times 10^4$ (63%)	$(1.4 \pm 0.1) \times 10^4$ (37%)

Anethole radical cation

The decay traces shown in Figure 2-64 are due to the decay of the anethole radical cation generated from β-heterolysis of the 2-chloro-1-(4-methoxyphenyl)propyl radical in the five alkali-exchanged Y zeolites under nitrous oxide. The rate constants for the decay of the anethole radical cation in the alkali-exchanged Y zeolites was obtained by the two component exponential equation, eq. 2.27, using the assumption that the radical cations decayed completely. The decay rate constants and their relative contribution to the total

decay as determined by fitting the data to this equation are presented in Table 2-17. The lifetime of the anethole radical cation obtained using the ESM analysis support these values, and the plots for the lifetime distribution in the five MY zeolites are shown in Figure 2-65.

As the data show, the magnitude of the rate constant for the fast component decreases slightly upon going from LiY to CsY, while the rate constant for the slow component increases. At the same time, the fast component becomes increasingly important going from LiY to CsY, while the slow component is less significant. Overall, these rate constants are all smaller than those determined for the 4-methoxstyrene radical cation discussed earlier. In addition, the main component to the total decay profile of the anethole radical cation is in all cases the slower decay rate constant, while the fast component tends to be more significant for the 4-methoxystyrene radical cation. The data therefore is consistent with previous results in solution showing that the anethole radical cation is less reactive than the 4-methoxystyrene radical cation.[185]

Table 2-17. Rate constants for the decay of the *trans*-anethole radical cation generated from β-heterolysis of 2-chloro-1-(4-methoxyphenyl)propyl radical under dry vacuum (10⁻⁴ torr) conditions.

Zeolite	k_{decay} / s^{-1}	
	first component (% contribution)	second component (% contribution)
LiY	$(2.3 \pm 0.1) \times 10^4$ (17%)	$(7.9 \pm 0.1) \times 10^2$ (83%)
NaY	$(3.1 \pm 0.1) \times 10^4$ (24%)	$(1.1 \pm 0.2) \times 10^3$ (76%)
KY	$(8.6 \pm 0.7) \times 10^3$ (20%)	$(1.6 \pm 0.1) \times 10^3$ (80%)
RbY	$(1.8 \pm 0.1) \times 10^4$ (26%)	$(1.8 \pm 0.1) \times 10^3$ (74%)
CsY	$(9.9 \pm 0.3) \times 10^3$ (47%)	$(2.3 \pm 0.1) \times 10^3$ (53%)
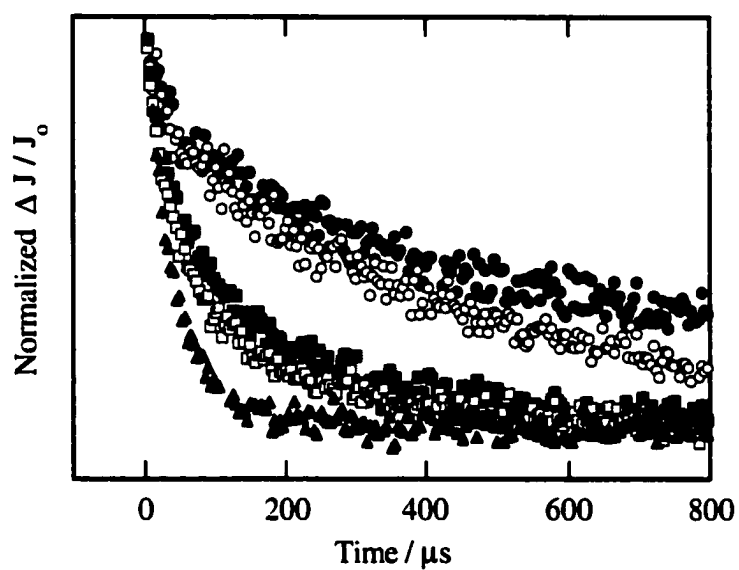
Figure 2-62. Normalized transient decay kinetics generated upon 266 nm excitation of 2-chloro-1-(4-methoxyphenyl)ethyl acetate in (●) LiY, (○) NaY, (■) KY, (□) RbY and (▲) CsY. The normalized traces were monitored at 600 nm under vacuum (10^{-4} torr) conditions over 800 μs.
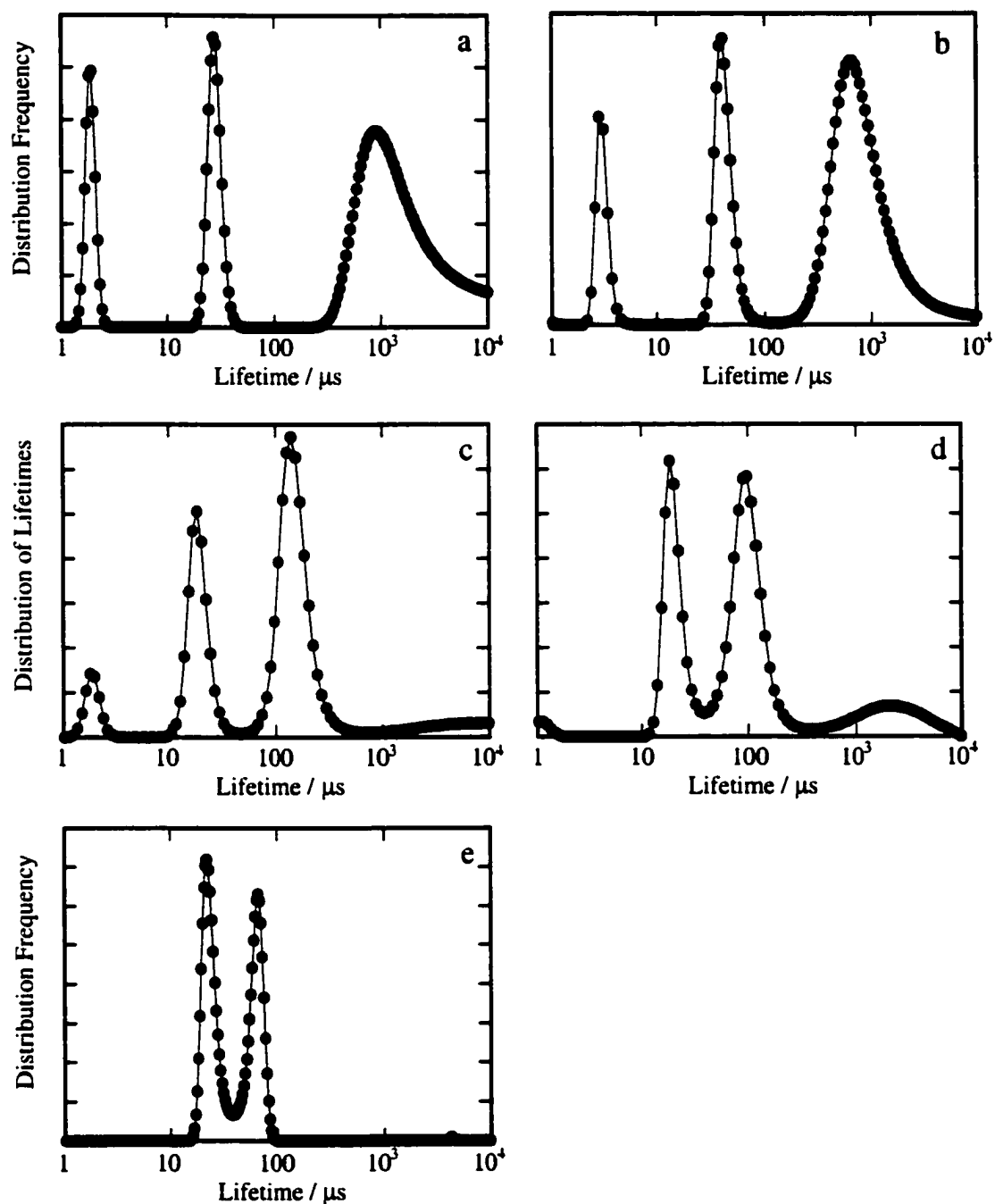
Figure 2-63. Distribution of lifetimes for the decay of the 4-methoxystyrene radical cation generated upon 266 nm excitation of 2-chloro-1-(4-methoxyphenyl)ethyl acetate in (a) LiY, (b) NaY, (c) KY, (d) RbY and (e) CsY.
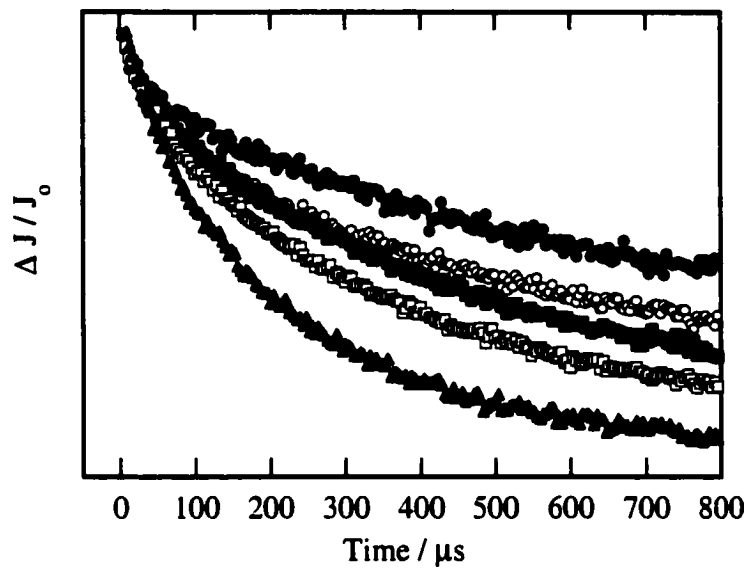
Figure 2-64. Normalized transient decay kinetics generated upon 266 nm excitation of 2-chloro-1-(4-methoxyphenyl)propyl acetate in (●) LiY, (○) NaY, (■) KY, (□) RbY and (▲) CsY. The normalized traces were monitored for the 385 nm band under vacuum (10^{-4} torr) conditions over 800 μs.
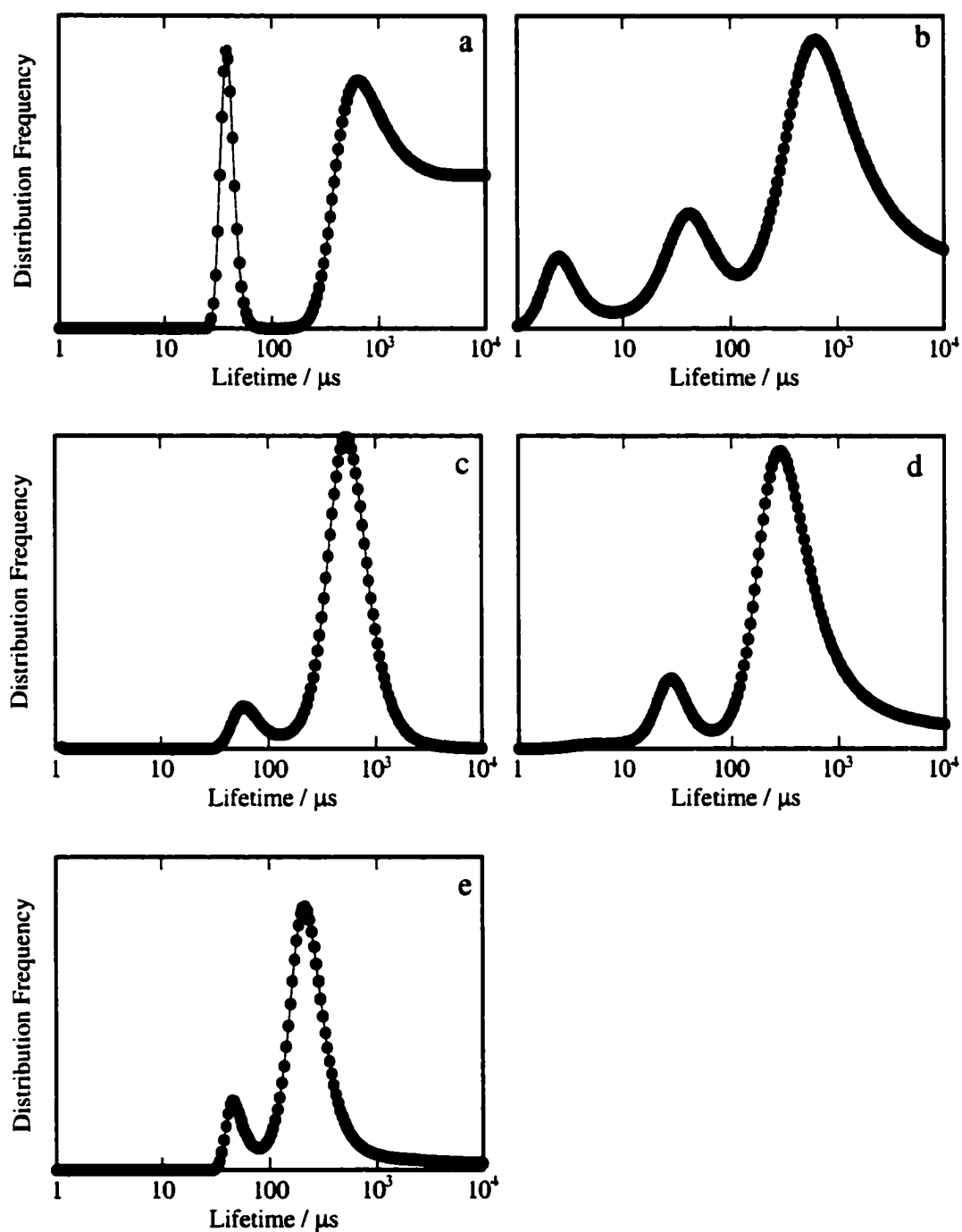
Figure 2-65. Distribution of lifetimes for the decay of the anethole radical cation generated upon 266 nm excitation of 2-chloro-1-(4-methoxyphenyl)propyl acetate in (a) LiY, (b) NaY, (c) KY, (d) RbY and (e) CsY.

4-Methoxystyrene and anethole radical cations generated by β-heterolysis of trifluoroacetate

As described earlier, irradiation of 2-trifluoroacetoxy-1-(4-methoxyphenyl)ethyl acetate (AcOTFAVA) and 2-trifluoroacetoxy-1-(4-methoxyphenyl)propyl acetate (AcOTFAAn) also lead to the formation of the 4-methoxystyrene and anethole radical cations, respectively. In these cases, the leaving group is a non-nucleophilic trifluoroacetate group, while the much more nucleophilic chloride ion is the leaving group in the reactions described above. To determine if the nature of the leaving group has an effect on the subsequent decay of the radical cation, we analyzed the decay kinetics for the radical cations generated using the trifluoroacetoxy derivatives.

The kinetics traces for the decay of the 4-methoxystyrene and anethole generated upon ionization of trifluoroacetoxy substituted precursor in the alkali metal exchanged zeolites were analyzed using a double exponential rate expression. The results of such analyses are summarized in Tables 2-18 and 2-19. Results for the 4-methoxystyrene radical cation are only available for the reaction in LiY and NaY since trifluoroacetoxy is not sufficiently good leaving group in the other zeolites for the radical cation to be formed.

In both cases, the decay of the 4-methoxystyrene and the anethole radical cations, did not seem to be affected significantly when the precursor was the 2-trifluoroacetoxy-1-(4-methoxyphenyl)alkyl radical or the chloro substituted compound. The similarity between the decays can be readily observed upon comparing the kinetic traces shown in Figures 2-66 and 2-67. This suggests that the nature of the leaving group does not affect the reactivity of the radical cation generated.

Table 2-18. Rate constants for the decay of the 4-methoxystyrene radical cation generated from β-heterolysis of 2-trifluoroacetoxy-1-(4-methoxyphenyl)ethyl radical under nitrous oxide conditions.

Zeolite	k_{decay} / s^{-1}	
	first component (% contribution)	second component (% contribution)
LiY	$(1.7 \pm 0.3) \times 10^4$ (27%)	$(1.1 \pm 0.3) \times 10^3$ (73%)
NaY	$(2.1 \pm 0.3) \times 10^4$ (30%)	$(1.7 \pm 0.3) \times 10^3$ (70%)
KY^a	not observed	not observed
RbY	not observed	not observed
CsY	not observed	not observed

^{a}The signal for the decay of the 600 nm band was too noisy for reliable analysis.

Table 2-19. Rate constants for the decay of the anethole radical cation generated from β-heterolysis of 2-trifluoroacetoxy-1-(4-methoxyphenyl)propyl radical under nitrous oxide conditions.

Zeolite	k_{decay} / s^{-1}	
	first component (% contribution)	second component (% contribution)
LiY	$(2.0 \pm 0.4) \times 10^5$ (19%)	$(9.2 \pm 0.5) \times 10^3$ (81%)
NaY	$(3.1 \pm 0.7) \times 10^4$ (22%)	$(3.5 \pm 0.5) \times 10^3$ (78%)
KY^a	$(1.1 \pm 0.3) \times 10^4$	
RbY	$(1.8 \pm 0.2) \times 10^4$ (45%)	$(3.8 \pm 0.6) \times 10^3$ (55%)
CsY	$(6.2 \pm 1.0) \times 10^4$ (27%)	$(1.1 \pm 0.1) \times 10^4$ (73%)

^{a}The signal for the decay of the 600 nm band was very weak and only one decay rate constant could be resolved.
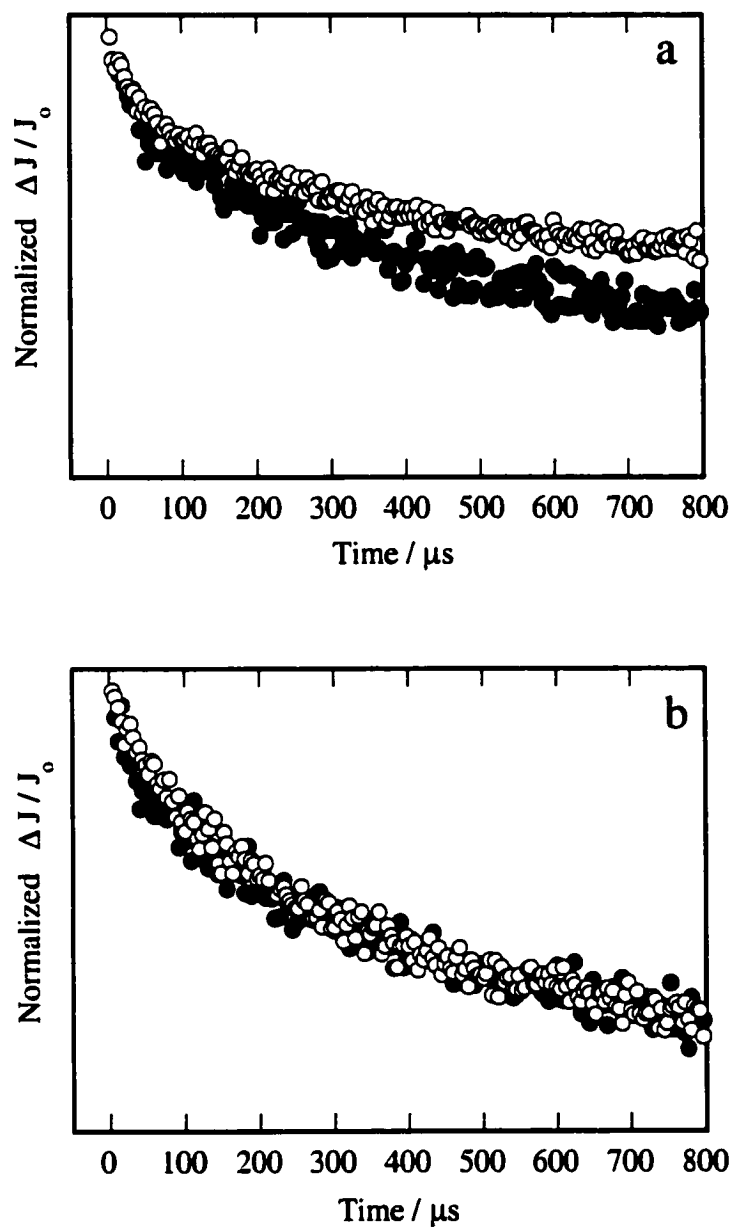
Figure 2-66. Normalized transient decay kinetics generated upon 266 nm excitation of (●) 2-chloro-1-(4-methoxyphenyl)ethyl acetate (AcOClVA) and (O) 2-trifluoroacetoxy-1-(4-methoxyphenyl)ethyl acetate (AcOTFAVA) in (a) LiY and (b) NaY. The normalized traces for the olefin radical cations were obtained at 600 nm under nitrous oxide conditions over 800 μs.
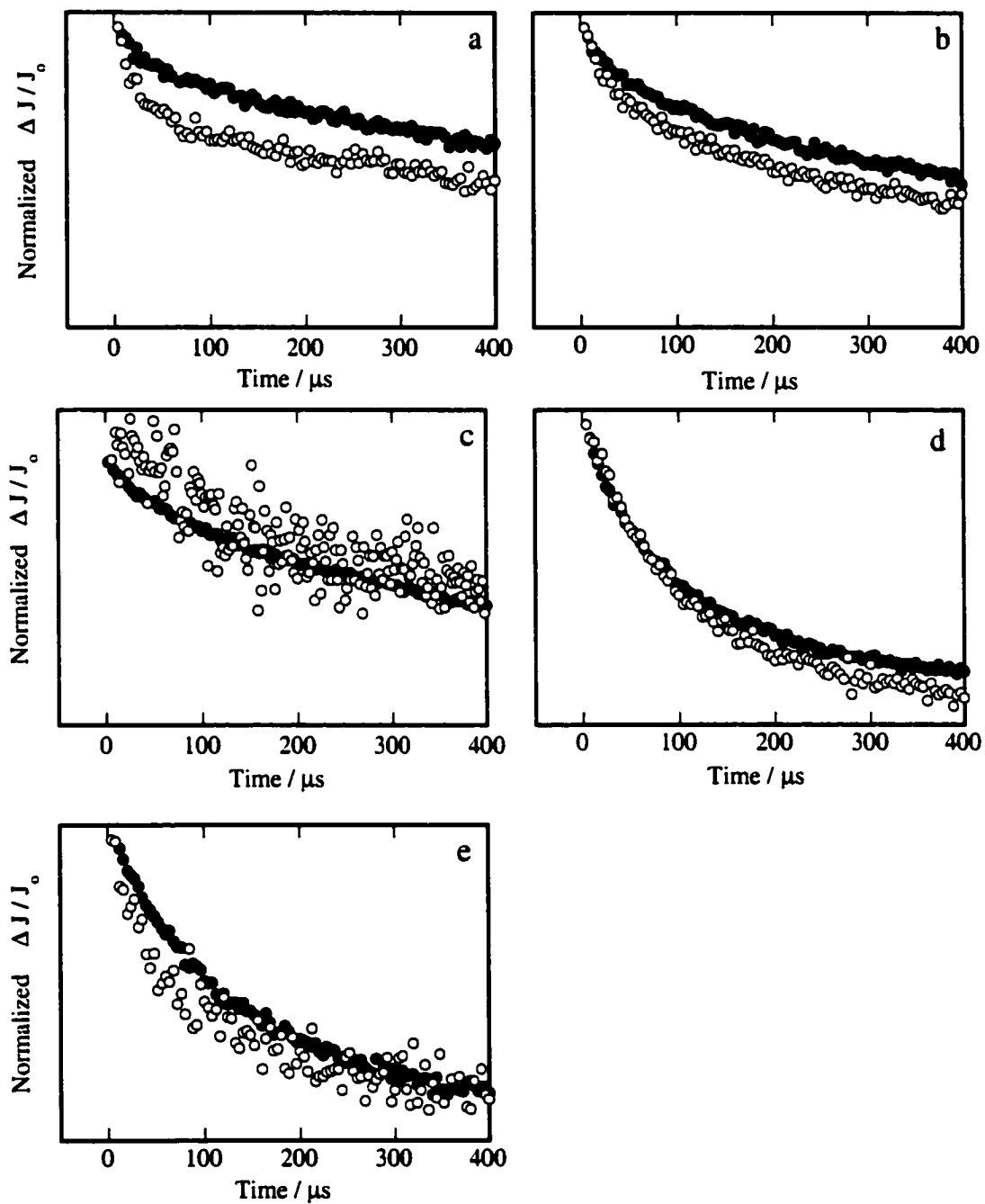
Figure 2-67. Normalized transient decay kinetics generated upon 266 nm excitation of (●) 2-chloro-1-(4-methoxyphenyl)propyl acetate (AcOClAn) and (○) 2-trifluoroacetoxy-1-(4-methoxyphenyl)propyl acetate (AcOTFAAn) in (a) LiY, (b) NaY, (c) KY, (d) RbY and (e) CsY. The normalized traces for the olefin radical cation were obtained at 385 or 600 nm over 400 μs.

2.2.7.2. Reactivity of radical cations generated by photoionization

4-Methoxystyrene radical cation

As described in previous work, photoionization of 4-methoxystyrene in NaY leads to the formation of the 4-methoxystyrene radical cation, eq. 2.29.[92,183]
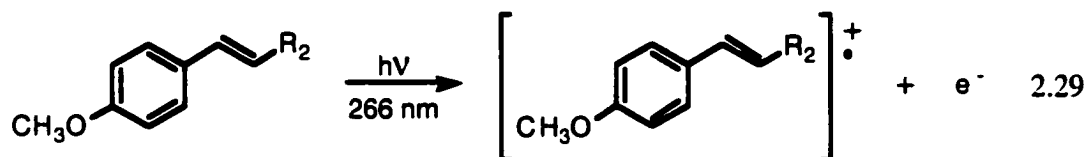
The same method is efficient in generating the same radical cation in all of the alkali-metal exchanged Y zeolites as shown in Figure 2-68, except LiY where the 4-methoxystyrene thermally decomposed. The presence of the 4-methoxystyrene radical cation is clearly shown in these spectra by the presence of the characteristic bands at 365 and 600 nm.[92,181,183,185,186]

The spectra shown in Figure 2-68 were all obtained under oxygen conditions. In the absence of oxygen, a broad and structureless band was observed in the 400-700 nm region, as shown for the spectrum obtained using NaY, Figure 2-69. The broad absorption at high wavelengths is assigned to a mixture of metal cation-electron complexes. In addition to the spectral characteristics, this assignment was supported by the quenching of this band by oxygen, and nitrous oxide as well. The presence of the trapped electrons generated upon 266 nm excitation of 4-methoxystyrene in zeolites is also consistent with photoionization of the molecule.

Introduction of oxygen or nitrous oxide into the sample had the effect of improving the characteristic absorption bands of the 4-methoxystyrene radical cation due to quenching of other transients. Therefore, kinetic traces obtained under an O_2 or N_2O atmosphere were no longer contaminated by the overlapping decay of the metal cation-electron complexes. As shown in Figure 2-70, the time-resolved decay traces for the disappearance of the 4-methoxystyrene radical cation were not affected by oxygen or

nitrous oxide, thus, all of the decay traces for quantitative kinetic analysis were obtained under these conditions.

Figure 2-71 shows the decay profiles for the 4-methoxystyrene radical cation in the four alkali-metal exchanged zeolites (<S> = 1/10). The kinetics traces fit well to a two-component exponential equation giving the rate constants summarized in Table 2-20. These rate constants are considerably different from those obtained for the same radical cation generated by β-heterolysis of 2-chloro-1-(4-methoxyphenyl)ethyl radical (*vide supra*) in two ways. First, the rate constants determined using the radical cation generated by photoionization are considerably larger than those determined from the decay of the radical cation generated by β-heterolysis. Second, the nature of the counterbalancing cation within zeolites does not affect the decay of the 4-methoxystyrene radical cation.

Table 2-20. First order rate constants for the decay in N_2O-saturated MY zeolites for the 4-methoxystyrene radical cation generated via photoionization (<S> = 1/10).

Zeolite Cation	k_{decay}[a] / 10^6 s^{-1}	
	fast component	slow component
Na$^+$	1.1 ± 0.2 (74 %)	0.20 ± 0.05 (23 %)
K$^+$	1.1 ± 0.2 (58 %)	0.22 ± 0.05 (43 %)
Rb$^+$	1.0 ± 0.2 (65 %)	0.16 ± 0.05 (35 %)
Cs$^+$	1.6 ± 0.2 (67 %)	0.23 ± 0.01 (33 %)

[a] The rate constants were obtained by averaging the values for both the 365 and 600 nm band for various experiments.

While addition of nucleophiles,[185] electron transfer,[60,165] carbon-carbon bond cleavage,[236,237] dimerization,[182,186] and deprotonation[169] are all possible reactions that lead to increased decays of radical cations, the only reaction available to the 4-methoxystyrene generated from photoionization that is not available to the same radical cation from β-heterolysis is dimerization. To test for the importance of this reaction,

laser experiments with different loading levels of 4-methoxystyrene radical cation encapsulated within NaY zeolites were carried out. The decay kinetics for the disappearance of the 4-methoxystyrene radical cation monitored at 365 nm under an O_2 atmosphere at different loading levels within the cavities of NaY are shown in Figure 2-72. Simple inspection of the traces shows that the decay of the 4-methoxystyrene radical cation increases with increasing amount of precursor molecule present within the cavities of the zeolite. Furthermore, the initial intensity of the radical cation immediately after the laser pulse is considerably smaller at the higher loading of <VA> = 1/5.

The rate constants calculated by fitting the decay traces to a biexponential equation are given in Table 2-21. The rate constant for the decay of the 4-methoxystyrene radical cation clearly increases with increasing amount of the precursor substrate incorporated within zeolites. This supports the notion that dimerization of the 4-methoxystyrene radical cation with the precursor 4-methoxystyrene is a major reaction for the disappearance of the 4-methoxystyrene radical cation.

Table 2-21. First order decay rate constants for the 4-methoxystyrene radical cation (VA) monitored at 600 nm in N_2O-purged NaY.

Loading level	k_{decay} / 10^6 s^{-1}	
<VA>	fast component	slow component
1/20	1.2 ± 0.1 (39 %)	0.14 ± 0.01 (61 %)
1/10	1.4 ± 0.1 (59 %)	0.23 ± 0.01 (41 %)
1/5	3.6 ± 0.6 (46 %)	0.62 ± 0.04 (54 %)

The decrease in the amount of 4-methoxystyrene detected after the laser pulse at the highest loading level of <VA> = 1/5 supports the presence of a dimerization reaction for this system. In particular, it suggests that at higher loadings two molecules may be present within the same cavity such that prompt reaction between a radical cation and a neutral 4-methoxystyrene molecule takes place.

The concentration dependence of the decay kinetics for the disappearance of the 4-methoxystyrene and anethole radical cations generated *via* β-heterolysis was also examined, Figure 2-73. As the concentration of the molecule encapsulated within the cavities of NaY increases the intensity of the signal attributed to the aryl alkene radical cation increases. However, Figure 2-74 showing the decay kinetics for the disappearance of the 4-methoxystyrene radical cation, and Figure 2-75 for the anethole radical cation demonstrate that the decay of these transients is not dependent on the loading level of the substrate. These results suggest that unreacted precursor when the radical cation is generated by β-heterolysis does not participate in the decay mechanisms.
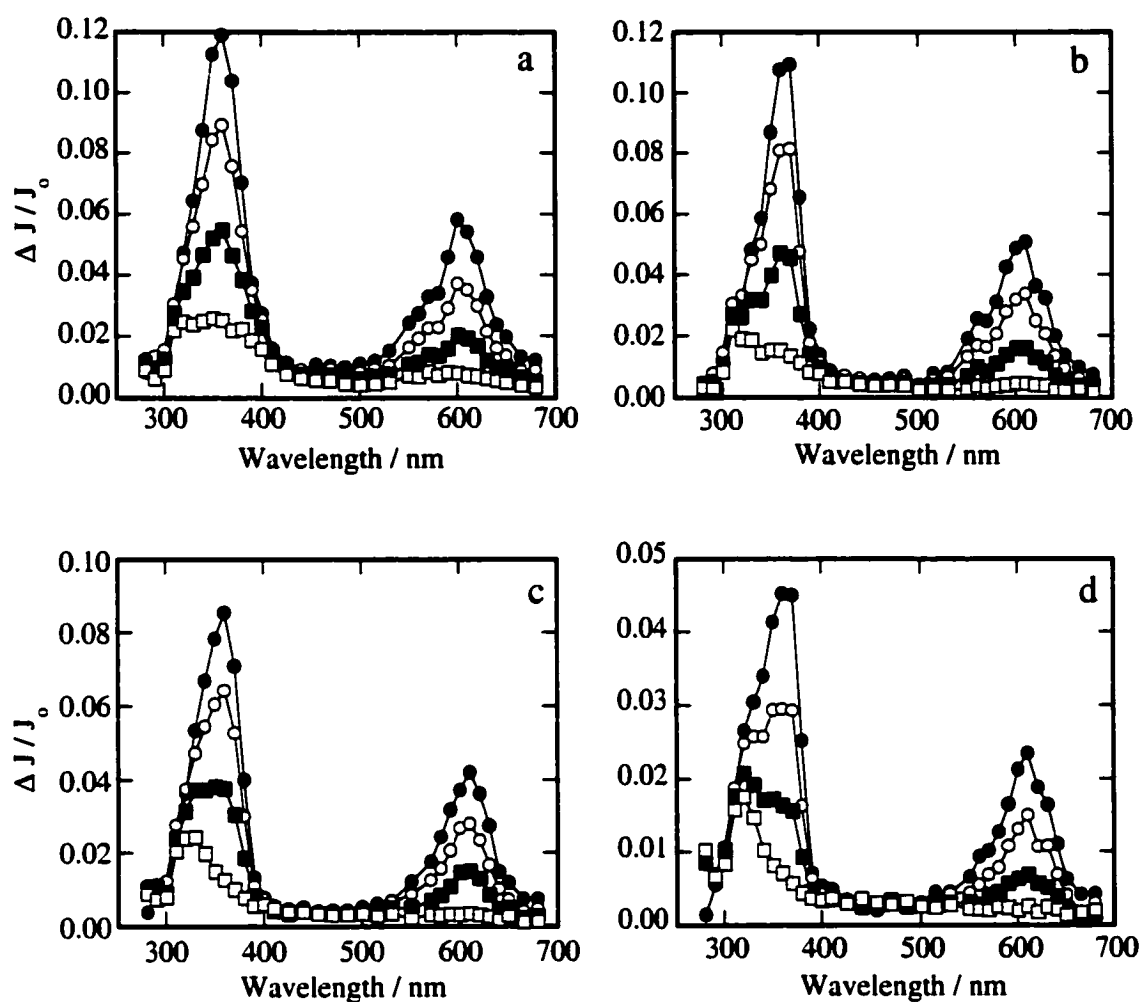
Figure 2-68. Transient diffuse reflectance spectra generated upon 266 nm laser photolysis 4-methoxystyrene (<VA> = 1/10) under oxygen conditions in (a) NaY, (b) KY, (c) RbY, and (d) CsY. Spectra were recorded (●) 0.32 μs, (○) 0.84 μs, (■) 2.24 μs and (□) 12.7 μs after the laser pulse.
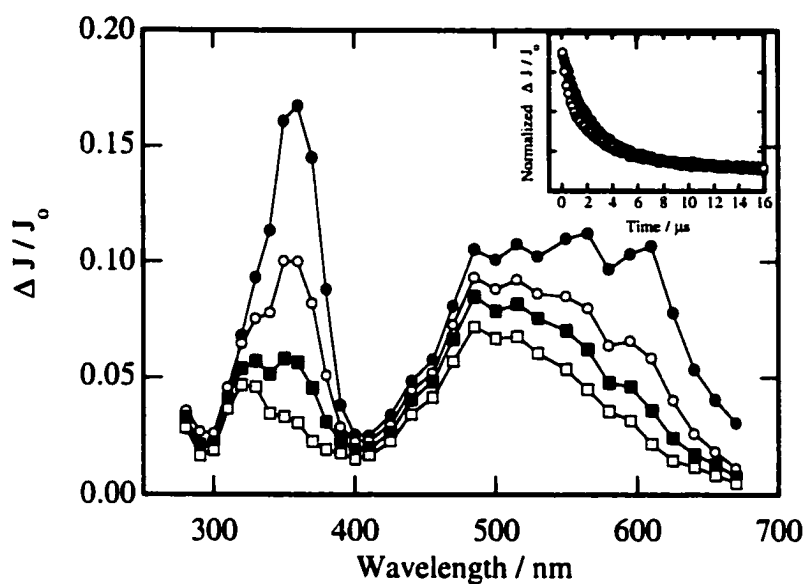
Figure 2-69. Transient diffuse reflectance spectrum generated upon 266 nm laser photolysis of 4-methoxystyrene (<VA> = 1/10) under dry vacuum (10^{-4} torr) conditions in NaY. Spectra were recorded (●) 0.28 μs, (O) 1.80 μs, (■), 4.52 μs and (□) 12.8 μs after the laser pulse. Inset: transient decay kinetics at (●) 365 nm and (O) 600 nm over 16 μs.
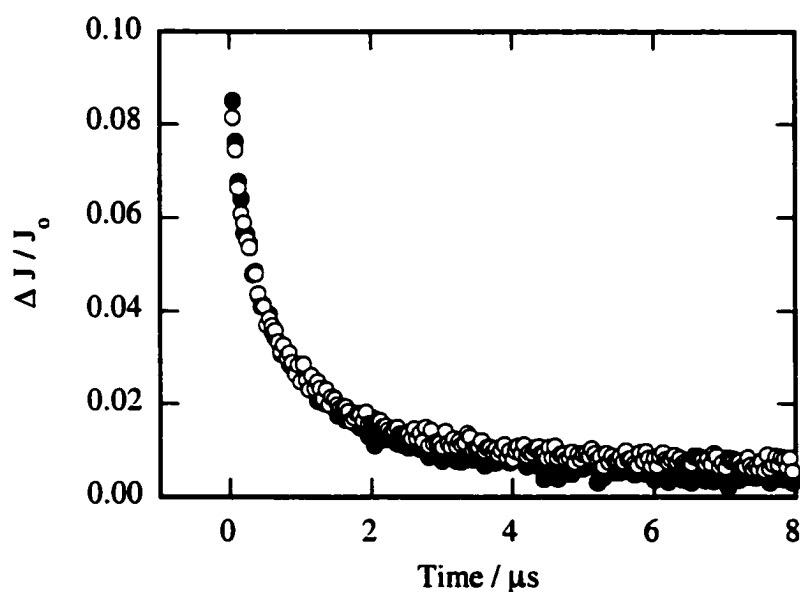
Figure 2-70. Transient decay kinetics generated upon 266 nm excitation of 4-methoxystyrene (<VA> = 1/10) in NaY under (●) N_2O and (O) O_2. Traces were monitored at 600 nm over 8 μs.
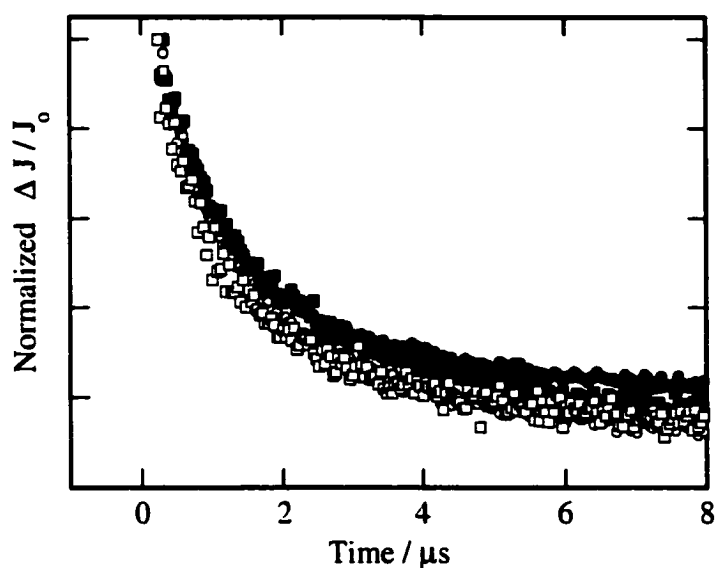
Figure 2-71. Transient decay kinetics generated upon 266 nm excitation of 4-methoxystyrene (<VA> = 1/10) in (●) NaY, (O) KY, (■) RbY, and (□) CsY under oxygen conditions. The normalized traces were monitored for the 600 nm band under vacuum (10^{-4} torr) conditions over 8 μs.
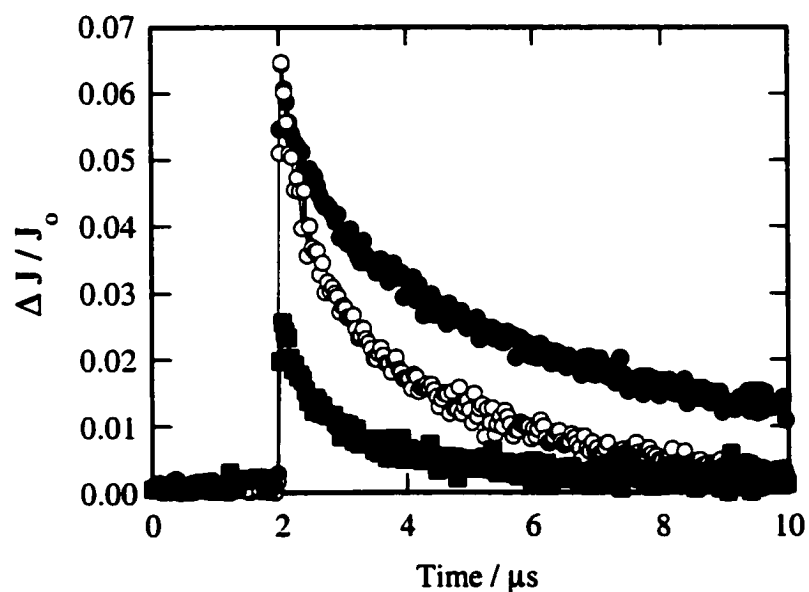
Figure 2-72. Decay traces monitored at 600 nm following 266 nm excitation of oxygen-saturated NaY containing various concentrations of 4-methoxystyrene (<VA>): (●) 1/20, (O) 1/10, and (■) 1/5.
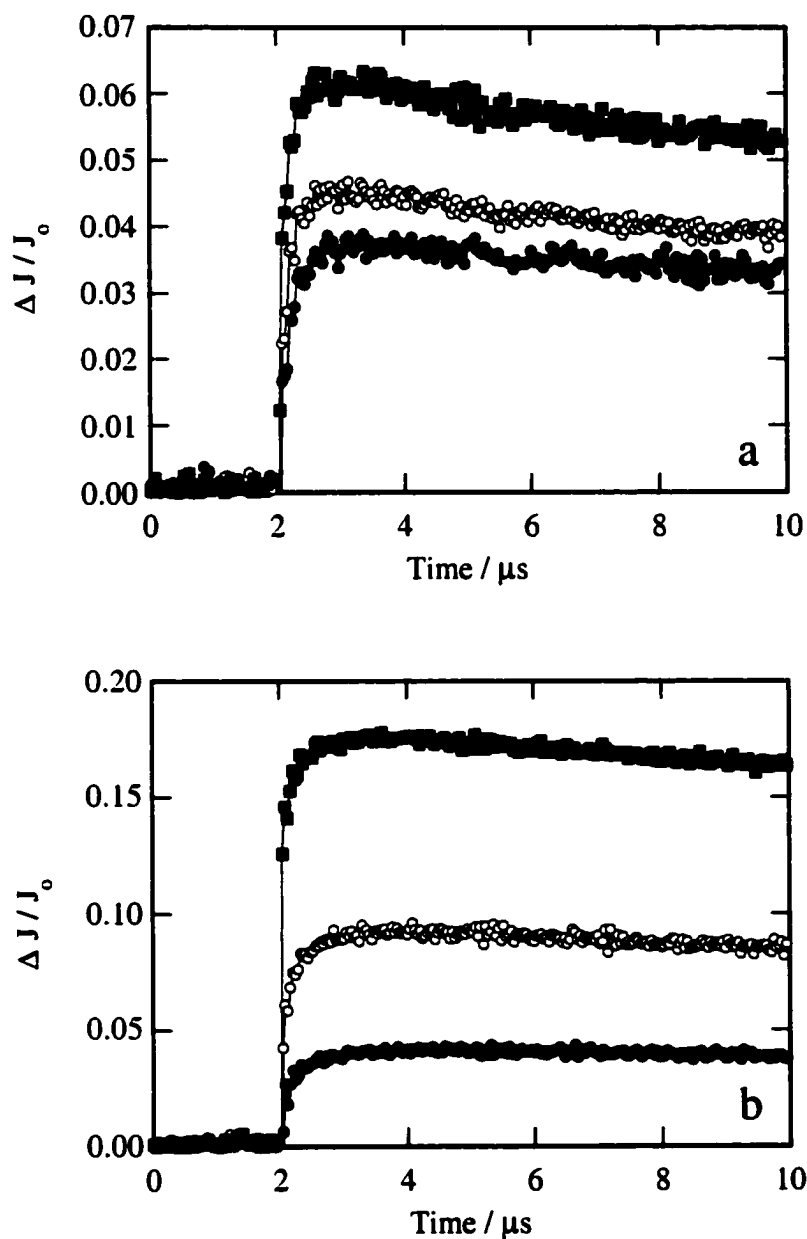
Figure 2-73. (a) Transient decay traces obtained at 365 nm after photolysis of AcOClVA in dry NaY under nitrous oxide conditions at loading levels of (●) <S> = 1/20, (O) <S> = 1/10, and (■) <S> = 1/5. (b) Transient decay traces obtained at 385 nm after photolysis of AcOClAn in dry NaY under nitrous oxide conditions at loading levels of (●) <S> = 1/50, (O) <S> = 1/10, and (■) <S> = 1/2.
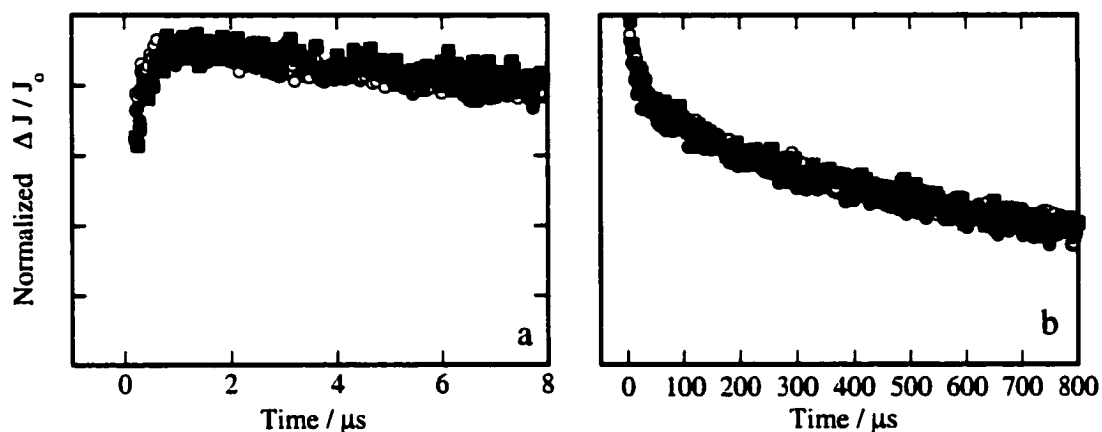
Figure 2-74. Normalized kinetic traces observed at 365 nm following 266 nm laser irradiation of AcOClVA in dry NaY at a loading level of (●) <S> = 1/20, (O) <S> = 1/10, and (■) <S> = 1/5 over (a) 8 μs and (b) 800 μs.
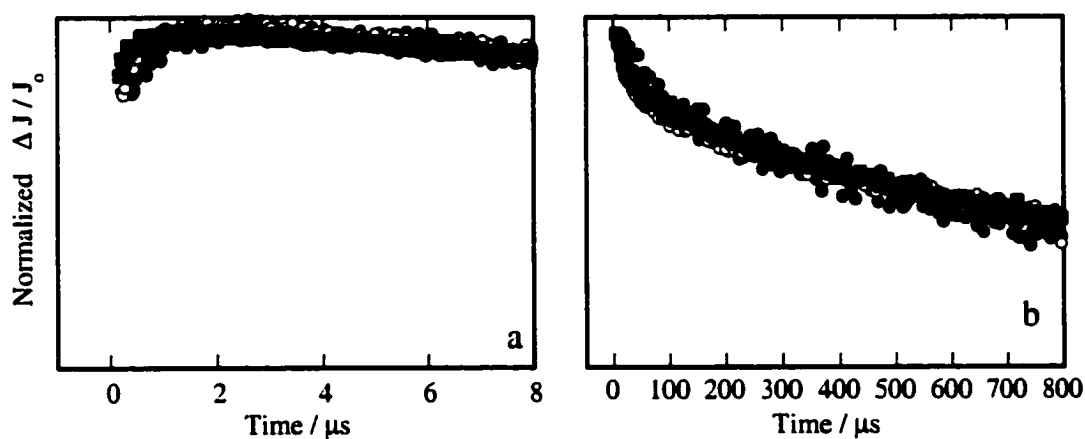
Figure 2-75. Normalized kinetic traces observed at 365 nm following 266 nm laser irradiation of AcOClAn in dry NaY at a loading level of (●) <S> = 1/50, (O) <S> = 1/10, and (■) <S> = 1/2 over (a) 8 μs and (b) 800 μs.

Anethole radical cation

Figure 2-76 shows the transient diffuse reflectance spectra obtained upon 266 nm laser excitation of anethole in oxygen-purged alkali-metal exchanged Y zeolites. In each case, the characteristic absorptions of the anethole radical cation (365 and 615 nm) are readily observable. Oxygen-purged conditions were used to remove complications caused by metal cation-electron complexes in the same manner as described above for the experiments with 4-methoxystyrene. For example, in the absence of oxygen (or nitrous oxide) the sodium-electron complexes are clearly evident upon photoionization of anethole in NaY as a broad absorption stretching from 400 to 700 nm, Figure 2-77. The presence of an electron quencher also simplified analysis of the decay traces by removing time-resolved changes caused by the decay of the complex. As for the 4-methoxystyrene radical cation generated by photoionization, the decay of the anethole radical cation was unaffected by the presence of oxygen.

Kinetic traces for the decay of the anethole radical cation are shown in Figure 2-78. The analysis of the decay traces required the use of a three component equation. Rate constants associated with each component are listed in Table 2-22. The data clearly illustrate that the anethole radical cation generated by photoionization decays much more slowly than the 4-methoxystyrene radical cation generated in the same way. In addition, distinct differences in the decay of the anethole radical cation in the various alkali-metal Y zeolites are immediately obvious, Figure 2-78. For example, the radical cation decays slowest in NaY and fastest in CsY. The decay traces for KY and RbY are very similar and their decays lie in between the slower NaY and faster CsY decay profiles.

The decay traces obtained for anethole incorporated in NaY with increasing loading amounts is shown in Figure 2-79. Just as with the 4-methoxystyrene radical cation system, the rate constant for each component increases with increasing amount of anethole present inside the cavities, Table 2-23. In addition, the contribution of the faster decay rate constant for each sample increases in the same order. For example, the faster decay rate constant for <An> = 1/50 is 3.9×10^5 s^{-1} with a contribution of only 12%. This contribution increases when the loading level for anethole is 1/20 to 18%, and continues

to increase up to a contribution of 40% when there is one anethole molecule per two zeolite cavities. The reactivity of the anethole radical cation in the <An> = 1/5 and 1/2 samples appear to decay with the same rate constants. This suggests that a maximum speed for the decay of the anethole radical cation may exist under these conditions.

In addition to the increase in the rate of decay for the anethole radical cation with concentration increase, there is also a concentration dependence of the initial diffuse reflectance intensity for the anethole radical cation, Figure 2-80. The relative yield of radical cation generated upon photolysis of anethole gradually increases from an anethole concentration of <An> = 1/50 to a maximum value at a loading of one anethole molecule per ten zeolite cavities (<An> = 1/10). The yield of radical cation detected immediately after photolysis then decreases with increasing concentration, Figure 2-81. These results demonstrate that the concentration of the anethole radical cation not only affects the rate of the reaction but also the amount of radical cation generated or detected.

Table 2-22. First order decay rate constants for the anethole radical cation in O_2-purged alkali-exchanged Y zeolites.[a]

Zeolite <An> = 1/10	first component k_{decay} / 10^5 s^{-1}	second component k_{decay} / 10^4 s^{-1}	third component k_{decay} / 10^3 s^{-1}
NaY	4.6 ± 0.5 (26 %)	3.6 ± 0.2 (40 %)	5.0 ± 0.1 (34 %)
KY	7.6 ± 0.3 (26 %)	6.0 ± 0.1 (44 %)	11.5 ± 0.1 (28 %)
RbY	7.8 ± 0.1 (30 %)	7.4 ± 0.3 (35 %)	9.8 ± 0.5 (35 %)
CsY	7.1 ± 0.2 (43 %)	6.8 ± 0.2 (42 %)	9.8 ± 0.3 (15 %)

[a]Values were obtained by averaging rate constants at 385 and 610 nm.

Table 2-23. First order decay rate constants for the anethole radical cation in O_2-purged NaY as a function of precursor concentration.[a]

Loading Level <An>	first component k_{decay} / 10^5 s^{-1}	second component k_{decay} / 10^4 s^{-1}	third component k_{decay} / 10^3 s^{-1}
1/50	3.9 ± 0.2 (12 %)	1.5 ± 0.2 (41 %)	2.0 ± 0.2 (47 %)
1/20	3.3 ± 0.2 (18 %)	3.8 ± 0.2 (35 %)	4.4 ± 0.1 (47 %)
1/10	3.5 ± 0.3 (26 %)	4.1 ± 0.5 (36 %)	4.7 ± 0.5 (38 %)
1/5	5.3 ± 0.3 (37 %)	6.1 ± 0.3 (35 %)	7.0 ± 0.5 (29 %)
1/2	5.6 ± 0.2 (40 %)	6.0 ± 0.2 (37 %)	6.4 ± 0.2 (24 %)

[a]Values were obtained by averaging constants at 385 and 610 nm.
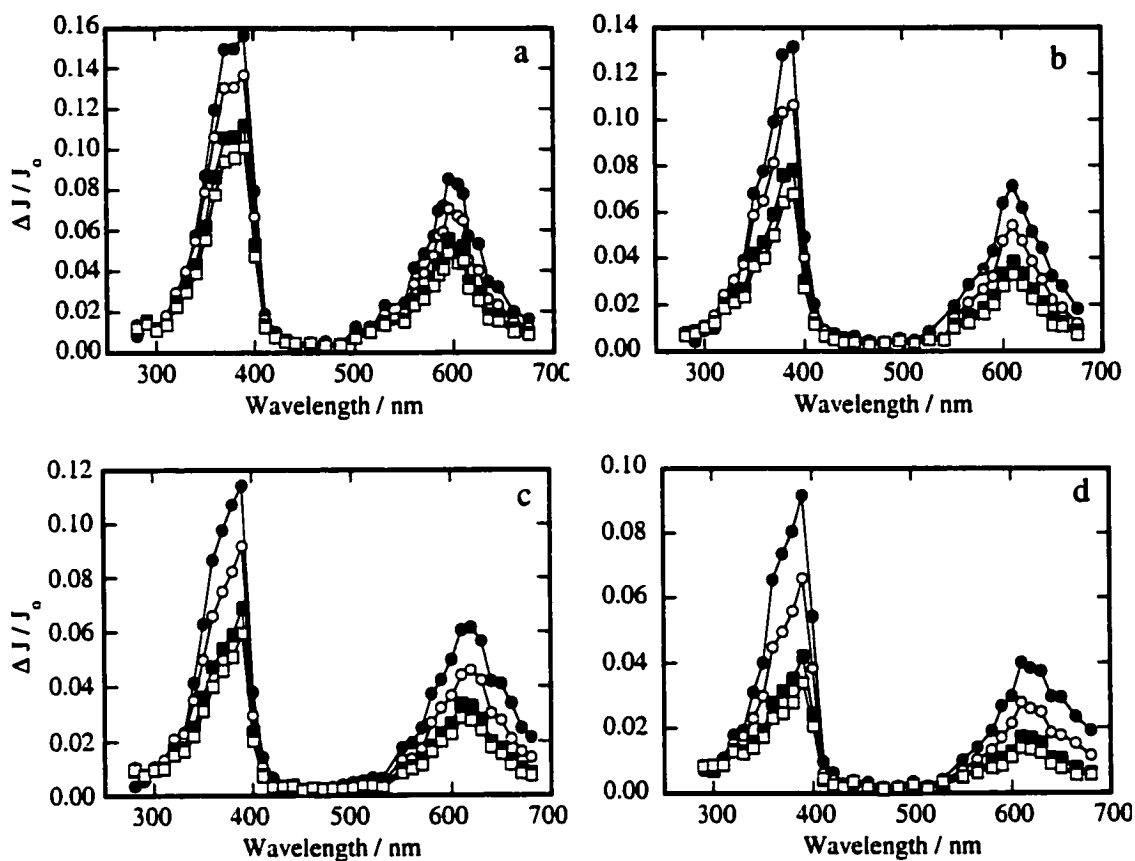
Figure 2-76. Transient diffuse reflectance spectrum generated upon 266 nm laser photolysis of anethole (<An> = 1/10) under dry oxygen conditions in (a) NaY, (b) KY, (c) RbY, and (d) CsY. Spectra were recorded (●) 0.36 μs, (○) 1.88 μs, (■) 7.68 μs and (□) 12.9 μs after the laser pulse.
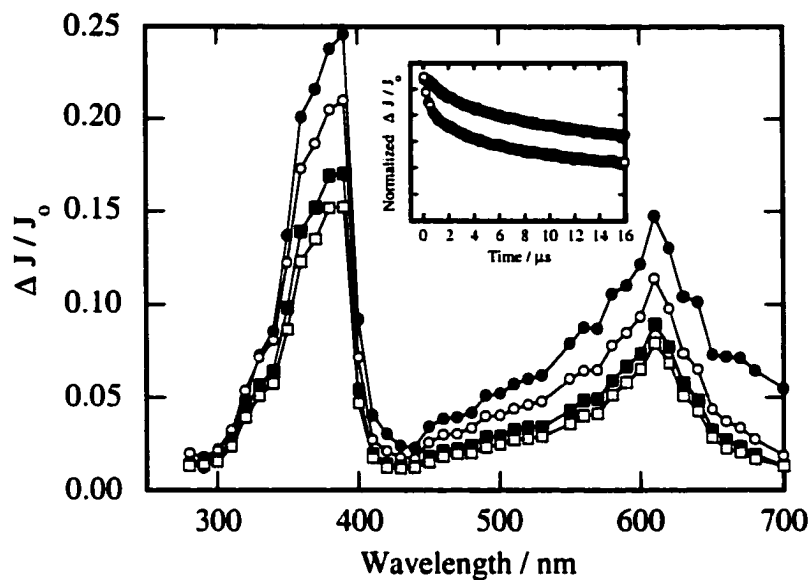
Figure 2-77. Transient diffuse reflectance spectrum generated upon 266 nm laser photolysis of anethole (<An> = 1/10) under dry vacuum (10^{-4} torr) conditions. Spectra were recorded (●) 0.44 µs, (○) 2.28 µs, (■), 7.60 µs and (□) 12.8 µs after the laser pulse. Inset: transient decay kinetics at (●) 365 nm and (○) 600 nm over 16 µs.
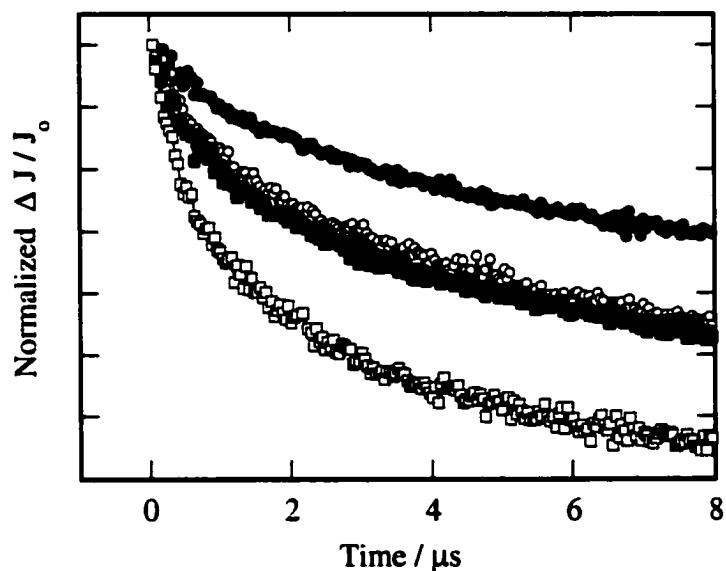
Figure 2-78. Transient decay kinetics generated upon 266 nm excitation of anethole (<An> = 1/10) in (●) NaY, (○) KY, (■) RbY and (□) CsY. The normalized traces were monitored at 365 nm under oxygen conditions.
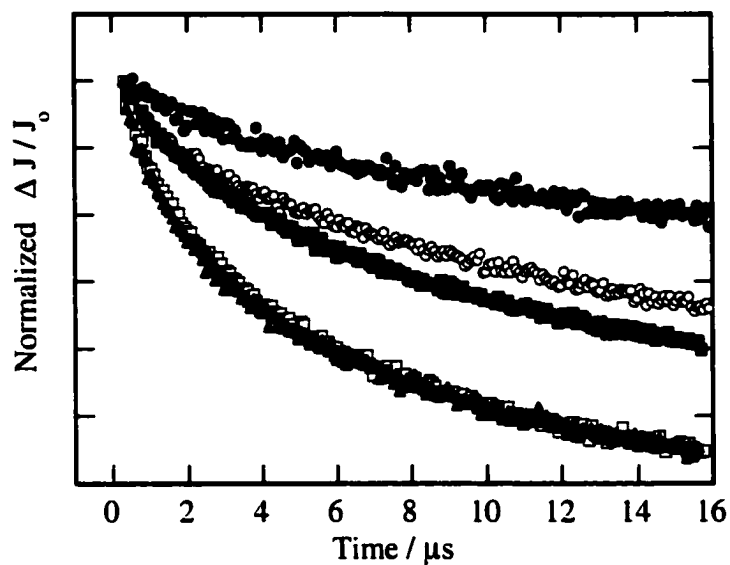
Figure 2-79. Normalized decay traces monitored at 600 nm following 266 nm excitation of oxygen-saturated NaY containing various concentrations of anethole (<An>): (●) 1/50, (○) 1/20, (■) 1/10, (□) 1/5, (▲)1/2.
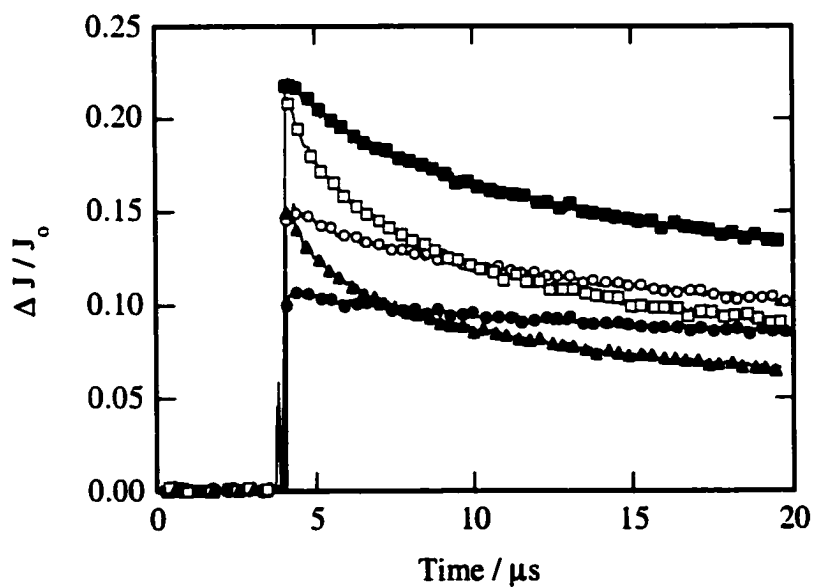
Figure 2-80. Decay traces monitored at 600 nm following 266 nm excitation of oxygen-saturated NaY containing various concentrations of anethole (<An>): (●) 1/50, (○) 1/20, (■) 1/10, (□) 1/5, (▲) 1/2.
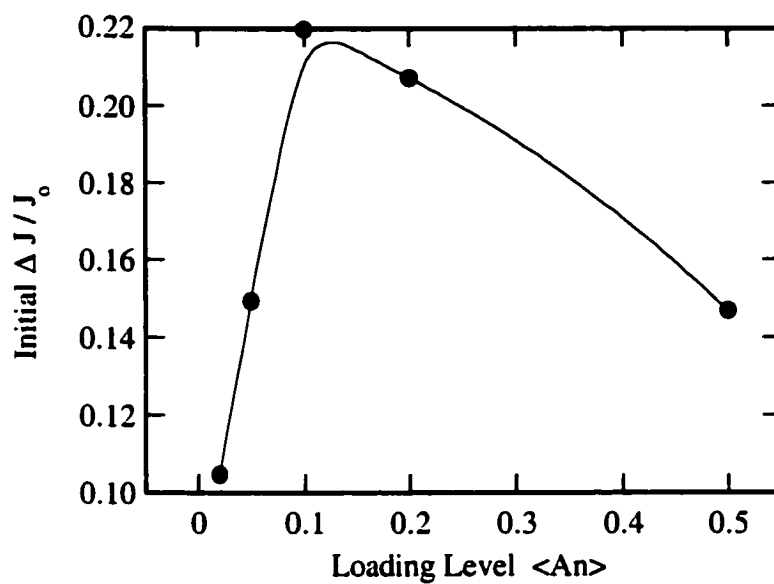
Figure 2-81. Initial change in diffuse reflectance intensity observed upon 266 nm laser photolysis of anethole in oxygen-saturated NaY as a function of anethole molecules per cavity (<An>).

2.3. Discussion

2.3.1. Generation of aryl alkene radical cations in zeolites via β-heterolysis

Laser irradiation of β-substituted 4-methoxyphenethyl acetates has previously been shown to give β-substituted radicals that, depending on the leaving group ability of the β-substituent, rapidly undergo ionization to give 4-methoxystyrene radical cations.[200] Direct observation of the time-resolved growth of 4-methoxystyrene radical cations upon laser irradiation of the same substrates in zeolites provides unambiguous evidence that the β-substituted radicals also undergo heterolytic cleavage of the carbon-leaving group bond in this media, eq. 2.30. In agreement with the proposed mechanism for formation of the radical cation is the observation that the decay of the β-substituted radical takes place with concomitant growth of the radical cation. In addition, since olefin radical cations are not expected to react with oxygen, the observed quenching of the radical cation upon trapping of the β-substituted radical with oxygen further supports this mechanism.

2.30
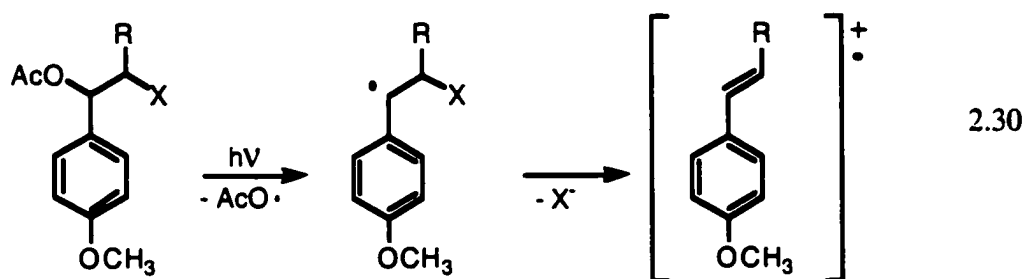
On the other hand, in the MY zeolites where the 2,4-dimethylstyrene and 4-methylstyrene radical cations are detected in this work, these radical cations do not appear to be generated via thermal β-heterolysis of the corresponding 2-chloro-1-(arylalkyl)ethyl radicals. In particular, no time-resolved growth associated with the formation of the 2,4-dimethylstyrene radical cation or the 4-methylstyrene radical cation was observed. Instead, in both cases, the weak absorption of the radical cation occurred promptly during the laser pulse. Furthermore, the rapid β-heterolysis reaction that is

implied by the prompt growth is contrary to expectation based on the relative stability of the methyl substituted styrene radical cations compared to the methoxy substituted radical cations, and to previous results showing that β-heterolysis of a good leaving group, bromide, from 2-bromo-1-(4-methylphenyl)ethyl radical is too slow to observe in solution even in highly ionizing solvents such as water/acetonitrile, TFE and HFIP solvents.[200] In addition, the 2-chloro-1-arylethyl radicals are the main species clearly present in the spectra but their decay is not associated with the growth of the corresponding radical cation. The large radical signals in addition to the weak prompt radical cation signals lead to the suggestion that methyl-substituted styrene radical cations are generated upon irradiation of the precursors AcOCldMeSty and AcOClMeSty by a different pathway. One possible pathway involves a two-photon process, eq. 2-31. According to this equation, the β-chloro radical absorbs a photon during the initial laser pulse to generate an excited state of the radical. Cleavage of the carbon-chlorine bond from the excited state then occurs rapidly to generate the radical cation. Such two photon processes have been observed previously upon laser irradiation of 2-chloro-1-(4-methoxyphenyl)ethyl acetate in non-ionizing solvents like acetonitrile.[238] As the extinction coefficients of the styrene type radical cations are significantly larger than that of the benzylic radicals the overall efficiency of radical cation formation is very low with these methyl-substituted substrates.

R = 4-CH$_3$ or 2,4-diCH$_3$
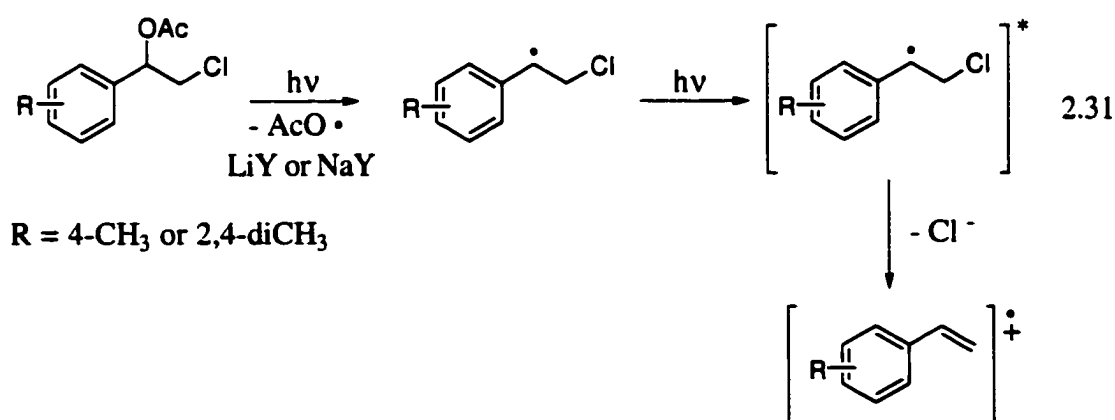
Given the possibility of a different pathway for the generation of arylalkene radical cations from the methyl-substituted substrates, one must ask if the second pathway is also present for the methoxy-substituted compounds. However, this possibility can be discounted as a major pathway on the basis of the observation that the absorption due to the presence of the 4-methoxystyrene radical cations grows in over a time period much longer than that defined by the laser pulse. Furthermore, for the zeolite systems where β-heterolysis is directly monitored, Figure 2-9, formation of 4-methoxystyrene radical cations occurs from the baseline. Thus, it is clear that prompt radical cation formation is not a primary pathway for the methoxy-substituted substrates.

2.3.2. Determination of Ionizing Ability of Zeolites

An important result obtained in this work is that the rate constant for ionization of chloride from the 2-chloro-1-(4-methoxyphenyl)ethyl radical is strongly influenced by the identity of the counterion and increases monotonically upon going from LiY to CsY. Since it has previously been demonstrated that the rate constant for the same ionization reaction in solution is determined largely by the ionizing ability of the medium, the observed counterion effect leads to the suggestion that the ionizing ability of the zeolite changes as a function of the alkali-metal cation. In particular, the conclusion can be made that LiY has the highest ionizing ability and CsY has the lowest.

One parameter that plays an important role in defining the ionizing ability of zeolites is the electrostatic field within supercages. In fact, a good correlation is observed between the rate constants for the heterolysis and the strength of the electrostatic field for the different alkali-metal exchanged zeolites, Figure 2-82. The electrostatic field can influence the reaction by participating in the polarization of guest reactant molecules.[77] As such, the zeolite supercage polarizes the included guest molecule distorting the electron density of the molecule, thereby promoting the ionization reaction.

The time-resolution of our laser system prevented the measurement of the heterolysis rate constant in LiY. The good correlation between the rate constants for heterolysis and the electrostatic field within the zeolites also allows for this rate constant

to be estimated. Thus, based on electrostatic field strength in LiY, the rate constant for heterolysis in dry LiY is estimated to be ~ 1 x 10^9 s^{-1}.
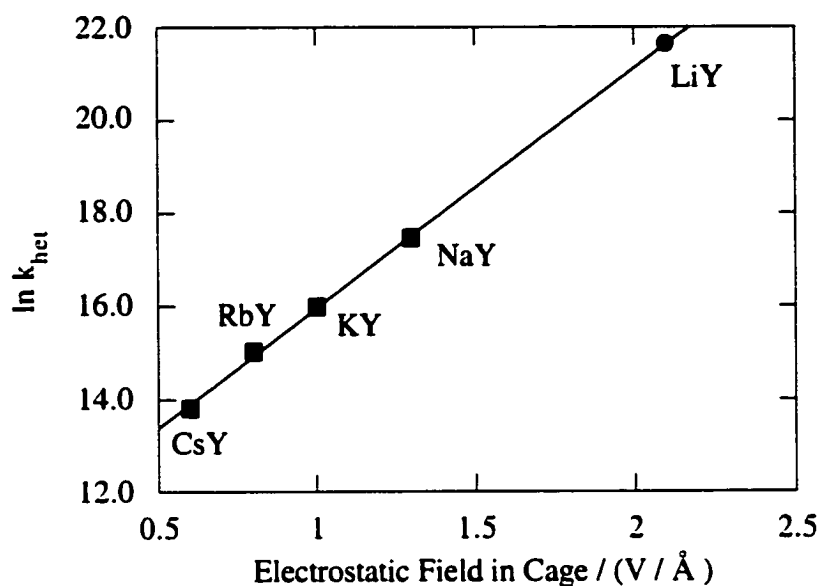
Figure 2-82. Rate constants for the ionization for the β-chloro arylethyl radicals in Y zeolites as a function of the electrostatic field experienced in the cage due to the included alkali cation.

The use of the 2-chloro-1-(4-methoxyphenyl)ethyl radical to probe the internal environment of zeolites allows us to make estimates of the ionizing ability of zeolites by comparison to the rate constants for the same heterolysis reaction measured previously in solution, Table 2-1. For example, the rate constants for heterolysis obtained in dry zeolites ranged from 1.0 x 10^6 s^{-1} to 3.9 x 10^7 s^{-1}. These values are smaller than the rate constants of > 1 x 10^8 s^{-1} for the same reaction in highly ionizing solvents such as water and HFIP. Thus, the conclusion can be made that the ionizing ability of the alkali-metal cation exchanged Y zeolites is significantly lower than that for HFIP. On the other hand, no β-heterolysis of chloride from 2-chloro-1-(4-methoxyphenyl)ethyl radical is observed in methanol. Thus, the ionizing ability of the Y zeolites must be greater than of methanol.

The comparison made above allowed for the ionizing ability of the zeolites to be placed somewhere between the ionizing abilities of HFIP (or water) and methanol. A more precise placement of the zeolite ionizing power can be made by comparisons with mixed solvent systems. The results show that the ability of Y zeolites to support heterolytic reactions is more comparable to methanol-water (aq. MeOH), acetonitrile-water (aq. AcN), TFE/AcN and HFIP/AcN solvent mixtures. For example, the rate constant for ionization of chloride in CsY, $k_{het} = 1 \times 10^6$ s^{-1}, is similar to the rate constants observed for the same reaction in mixed solvent systems such as 35%TFE:65%AcN, 25%H$_2$O: 75%MeOH, and 10%H$_2$O: 90%AcN. The rate constant for ionization in NaY, $k_{het} = 3.9 \times 10^7$ s^{-1}, is similar to the rate constant in 80%H$_2$O:20%MeOH and 90% H$_2$O: 10% AcN mixtures.

Figure 2-83 contains a summary of general comparisons that can be made between the rate constants measured in the Y zeolites and those made in solution. The Figure illustrates that the ionizing power of NaY is stronger than neat TFE, weaker than neat HFIP, but very similar to 80% water: 20 % methanol mixture. The ionizing abilities of KY, RbY and CsY are all stronger than neat methanol and all weaker than TFE. These zeolites having ionizing abilities similar to ca. 55%, 40% and 25% aqueous methanol, respectively.
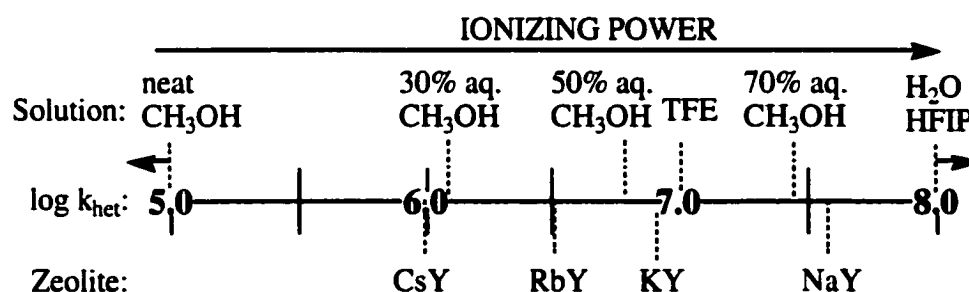
Figure 2-83. Schematic representation of the ionizing power of dry alkali-metal cation exchanged Y zeolites relative to the ionizing power of common solvents.

The solvent ionizing scale, or Y-scale, was developed to represent the extent to which any substrate will undergo heterolytic bond cleavage without direct solvent

nucleophilic assistance.[218] Y-scales reflecting the ability of various solvents to support the ionization reactions of different substrates are widely available, but Y-values for zeolites have never before been determined. Such a Y-scale for the alkali-metal cation exchanged zeolites can be estimated from a correlation plot of the β-heterolysis rate constants for 2-chloro-1-(4-methoxyphenyl)ethyl radical obtained in water-methanol solvent mixtures as a function of the Y_{AdCl} values for the solvent mixtures, Figure 2-84. Thus, the rate constants measured in the zeolites can be entered into the equation-of-the-line determined from the correlation plot to calculate Y_{AdCl} for the zeolites. In this manner, the Y_{AdCl} values listed in Table 2-24 were determined. As can be seen, the values range from 1.4 for CsY to 4.1 for NaY under dry conditions. A Y-value estimate of 6.6 is predicted for LiY based on the extrapolated k_{het} rate constant of 1×10^9 s^{-1} obtained from Figure 2-82.

Table 2-24. Y_{AdCl} values estimated for dry and hydrated Y zeolites based on k_{het} of 2-chloro-1-(4-methoxyphenyl)ethyl radical.

Zeolite	Y_{AdCl} (dry)	Y_{AdCl} (hydrated)
LiY	> 4.7 (6.6)^a	1.7
NaY	4.1	1.3
KY	3.0	1.2
RbY	2.3	0.1
CsY	1.4	0.1

^{a}The Y_{AdCl} of 6.6 for dry LiY is estimated using the extrapolated value of $k_{het} = 1 \times 10^9$ s^{-1}.

Several 1- and 2- substituted adamantanes, in addition to other substrates such as t-butyl chloride, have been used as reference standards for establishing individual Y_x scale. Such an extended list of parameters is required since ionizing abilities of solvents are not absolute and depend on a variety of factors, including the nature of the leaving group and the substrate itself. Similarly, the ionizing ability of zeolites measured in the present work may not universally apply to all substrates included within zeolites. As mentioned in the introduction, the electrostatic fields present within the cavities are

direction and distance dependent from the alkali-metal cations.[100] As a result, the location of the probe molecule with respect to the field generators will have a direct effect on the ionizing environment experienced by a particular molecule.

The possibility that the absolute ionizing ability of zeolites is substrate dependent is in fact exhibited in the results obtained upon ionization of the 2-trifluoroacetoxy-1-(4-methoxyphenyl)ethyl radical. In LiY and NaY, the reaction occurred with rate constants of 3.8×10^5 and 6.3×10^5 s^{-1} that were faster than the rate constant of 3.1×10^5 s^{-1} for the same reaction in neat HFIP. Thus, for this probe molecule, the ionizing environment experienced due to zeolites is slightly greater than that experienced in HFIP, whereas the opposite was observed for the 2-chloro-1-(4-methoxyphenyl)ethyl system. Similarly, the ionizing power of KY, RbY and CsY is estimated to be greater than 70%HFIP:30%AcN based on heterolysis rate constants of 2-trifluoroacetoxy-1-(4-methoxyphenyl)propyl radical, whereas the same zeolites have a ionizing power considerably less than 70%HFIP:30% AcN with regard to the ionization of chloride.
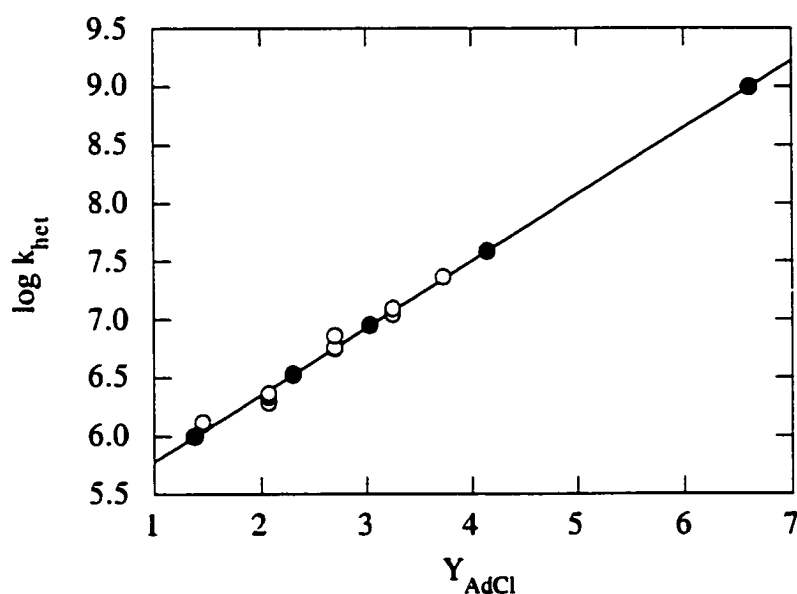
Figure 2-84. Relationship between the observed rate constants for the formation of p-methoxystyrene radical cation at 600 nm upon 266 nm irradiation of 2-chloro-1-(4-methoxyphenyl)ethyl acetate and solvent ionizing ability (Y$_{AdCl}$ values) of methanol/water mixtures (O) and zeolite values (●). LiY value is extrapolated.

Regardless of which substrate was examined, the zeolites consistently exhibited properties that are similar to those found in strongly ionizing and highly polar solvents. Thus, the results clearly indicate that the internal cavities of zeolites possess an ionizing power that is analogous to polar, hydroxylic solvents such as aqueous methanol and TFE. In addition, while some variability from substrate to substrate is expected, the results obtained using the 2-chloro-1-(4-methoxyphenyl)ethyl acetate probe system provide a general template upon which to determine ionizing abilities of zeolites.

A reduction in the rate constants for heterolysis of 2-chloro-1-(4-methoxy-phenyl)ethyl radical was observed in zeolites with co-incorporated water. Thus, water has the effect of reducing the absolute ionizing ability experienced by the probe molecule when encapsulated in the supercages of Y zeolites. Y-values were calculated for hydrated MY zeolites in the same manner as those calculated in the dry zeolites, and these values are given in Table 2-24. The data clearly show that Y-values for the hydrated zeolites are considerably smaller than those for the dry sample. In fact, the Y-values indicate that the ionizing abilities of the hydrated zeolites are weaker than that for 30% aq. methanol solvent mixtures, while the ionizing abilities of the dry zeolites are all greater than that for 30% aqueous methanol. Furthermore, the spread in the Y values for the hydrated zeolites ($\Delta Y=1.6$) is smaller than those in dry zeolites ($\Delta Y=5.2$). These observations indicate that the effect of the counterbalancing cation is not as effective in the presence of water compared to the dry zeolite and provide support for the notion that these cations are crucial to the polarity present within the cavities. Presumably, the water molecules coordinate to the alkali-metal cations and effectively shield the probe from the electrostatic field effects, thereby reducing the ionizing ability of the zeolite.

2.3.3. Mechanism of ionization

Ionization within zeolites is thought to occur due to the electrostatic fields sensed in the dry zeolite originating from unshielded "naked" cations. These fields facilitate the generation of the 4-methoxystyrene radical cation by providing a suitable polar environment capable of stabilizing this type of charged organic compounds. The present

results indicate that the polarity is higher in zeolites with a smaller size charge-compensating cation because of their larger charge density which gives rise to the stronger electrostatic field within the cages; thus, fast rate constants for heterolysis are obtained.

In addition to the internal ionizing environment, direct participation of the alkali-metal cation may also play a role by acting as an electrophilic catalyst, Scheme 2-5. In this scenario, the smaller and more electropositive lithium cation could strongly interact with the chloride and thus accelerate the heterolytic cleavage of the carbon-chlorine bond. In contrast, the large and more charge diffuse cesium cation would be less able to assist the ionization reaction due to the weaker interactions between the chloride and the cation.

Scheme 2-5.
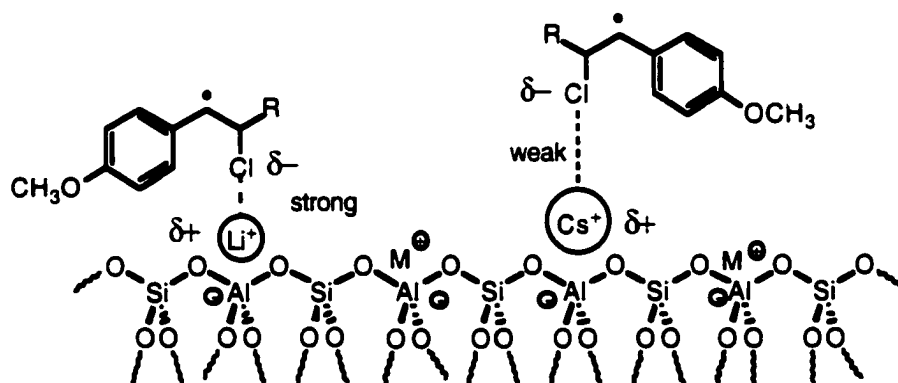
Some support for such an interaction between the leaving group and the balancing cation was evident in the heterolysis experiments in the presence of small amounts of oxygen. Under 10% oxygen conditions (90% nitrogen), heterolytic cleavage of the carbon-chlorine bond was still observed to take place in the alkali-metal Y zeolites but the rate of decay of the product, 4-methoxystyrene radical cation, was considerably faster than in the absence of oxygen. Moreover, the effect of oxygen on the decay of the 4-methoxystyrene radical cation increased as the cation was varied from LiY to CsY. Since

the 4-methoxystyrene radical cation is typically unreactive toward oxygen, one explanation for the observed oxygen effect is the presence of a dynamic equilibrium between the 2-chloro-1-(4-methoxyphenyl)ethyl radical and the 4-methoxystyrene radical cation, eq. 2.32. Thus, in the presence of oxygen, the radical cation decay can appear to increase due to trapping of the radical by oxygen. The observation that the oxygen effect changes as a function of counterion can be understood by considering the position of the equilibrium between these two species in each of the zeolites. In LiY where the Li^+ interacts strongly with the chloride ion, the equilibrium lies far to the side of the radical cation. In this situation, the presence of oxygen inside the zeolite has little effect as there is little or no radical to quench. In contrast, in CsY where the Cs^+ interaction with Cl⁻ is weak, the radical component of the equilibrium is sufficiently high for a larger oxygen effect to be observed.

$$\qquad\qquad\qquad 2.32$$
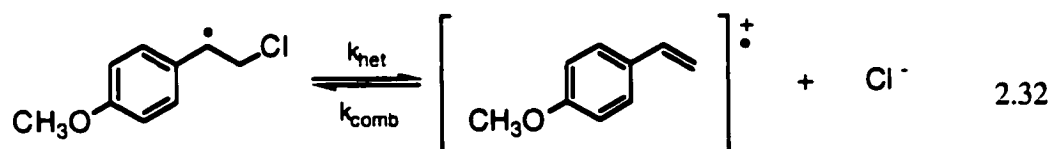
While the reversibility of the β-heterolysis reaction of the 2-chloro-1-(4-methoxyphenyl)ethyl radical in zeolites is best explained through alkali metal cation-chloride anion interactions, volume restrictions within the suprastructure may also play a minor role. In LiY, the larger supercage volume can potentially allow the free movement and escape of the chloride ion from the supercage thus removing the chloride ion from having easy access to the 4-methoxystyrene radical cation. On the other hand, CsY has a smaller cavity volume which reduces the probability that the chloride ion can escape to a neighboring cavity, thus enhancing the reversibility of the heterolysis reaction. The effect in the variation in free volume among the various cation-exchanged zeolites is schematically represented in Figure 2-85.

CH3O · · Li+   CH3O · · K+   CH3O · · Cs+
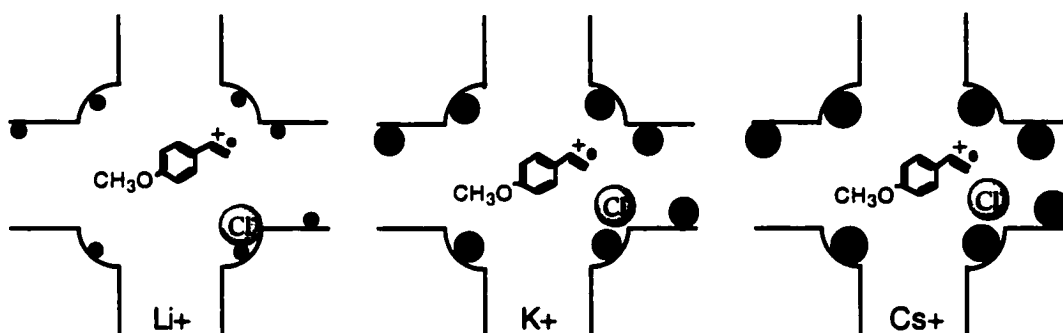
Figure 2-85. Schematic representation of the reduced free movement of the species within the supercages as the size of the countercation increases (not drawn to scale).

The results also showed that the rate constants are highly sensitive toward the hydration state of the zeolite. In particular, the ionization reaction in the slightly hydrated zeolites was consistently slower than in the corresponding dry zeolites. This is consistent with the notion that the counterbalancing cations are the source of the electrostatic fields. In the absence of water, the probe molecule is able to interact and experience the full electrostatic field created by these cations. On the other hand, since water molecules have a high affinity for the cationic sites and the framework oxygen, they tend to line the inner surface of the zeolites and weaken the direct interaction of the aromatic guest molecule with the cationic sites. In other words, the association of the water molecules with the cations attenuate the zeolite electrostatic fields, thereby reducing the ionizing power and causing a decrease in the heterolysis rate constants. Similar water effects have been observed by other researchers, whereby the polarity of a supercage depends on the presence of water and other organic solvents present.[67,107,114,239]

2.3.4. Activation parameters

Several trends were observed in the activation parameters determined for the ionization 2-chloro-1-(4-methoxyphenyl)ethyl radical to the 4-methoxystyrene radical cation and chloride anion methanol/water, TFE/AcN and HFIP/AcN mixtures. In methanol/water mixtures, the enthalpy of activation became more positive as the water

content decreased, while the entropy of activation first became less negative upon going from 70% water to 50% water, but then became more negative upon going to 30% water. Thus, in mixtures containing mostly water, the decrease in rate constant observed as the water content decreased from 70% to 50% is mostly due to an increase in the enthalpy of activation. In mixtures containing mostly methanol, both the enthalpy and entropy of activation contribute to the slower rate constant observed as the water content decreased. In the TFE/AcN and HFIP/AcN mixtures, the enthalpy of activation decreased as the content of TFE or HFIP decreased, while the entropy of activation became more negative. Thus, the slower rate constants for heterolysis measured in these mixtures as the alcohol component decreased is due to increasingly unfavorable entropy effects.

Some similarities can also be observed in activation parameters for the ionization reaction in the different media. In particular, all of the entropies of activation are negative, while the enthalpies of activation all lie in a relatively narrow range of 18 to 28 kJ/mol.

The observation of negative entropies for the ionization of chloride from the 2-chloro-1-(4-methoxyphenyl)ethyl radical is typically observed for conventional S_N1 ionization reactions in solution. In such reactions where the products are two separated ions, partial ionization must be present in the activated complex requiring more solvation of the transition state than of the reactants. That is, solvent molecules must organize themselves around the transition state to a greater degree than the solvation shell present in the reactant molecules to prepare for the solvation of the free ions. This leads to a decrease in entropy and the negative $\Delta S^{\ddagger}$. Consider a picture whereby the activated complex resembles the ion pair, Figure 2-86. Each end of the polarized transition state would contain a layer of solvent molecules. This solvation shell around the polar complex is necessary in order for the process of ion separation to continue to stabilize the charged species. As the separation occurs, the solvent shell becomes more ordered so that a further decrease in entropy occurs in going from the transition-state to the products.

A comparison of the activation parameters obtained for the ionization of chloride from 2-chloro-1-(4-mthoxyphenyl)ethyl radical in zeolites with activation parameters

measured in selected solvent mixtures is given in Table 2-25. Each solvent mixture was chosen so that the free energy of activation is similar to the free energy of activation for the zeolite in the same row in Table 2-25.

Table 2-25. Enthalpies, entropies and free energies (25 °C) of activation for the β-heterolysis of 2-chloro-1-(4-methoxyphenyl)ethyl radical in dry alkali-exchanged Y zeolites.

Zeolite	$\Delta H^{\ddagger}$ (kJ/mol)	$\Delta S^{\ddagger}$ (J/mol·K)	$\Delta G^{\ddagger}$ (kJ/mol)	Solvent	$\Delta H^{\ddagger}$ (kJ/mol)	$\Delta S^{\ddagger}$ (J/mol·K)	$\Delta G^{\ddagger}$ (kJ/mol)
NaY	39	22	32	70% H₂O in MeOH	18	-45	31
KY	42	23	35	70% HFIP in AcN	21	-46	34
RbY	41	14	36	40% H₂O in MeOH	27	-29	35
CsY	52	40	40	60% TFE in AcN	19	-69	39

The comparison indicates that significant differences are present in the enthalpy of activation and the entropy of activation for the reactions in the two types of media, even when the overall free energy of activation is fairly similar. One significant difference is that the enthalpy of activation for the ionization of chloride from 2-chloro-1-(4-methoxyphenyl)ethyl radical in zeolites are in most cases at least twice as large as those obtained in solution. Thus, the energy required for heterolysis to occur in the zeolites is considerably greater than that required in solution. On the other hand, the entropy of activation is positive in all the alkali-exchanged Y zeolites, while the entropy of activation in all solutions is negative. Thus, while in solution, entropy changes upon going from the initial state to the transition state cause an increase in the activation free energy, the opposite situation exists in the zeolite. Indeed, for the specific comparisons given in Table 2-25, the positive entropies of activation are sufficient to balance the

larger activation enthalpies such that the rate constants for heterolysis at 25 °C are similar in zeolites and in solution.
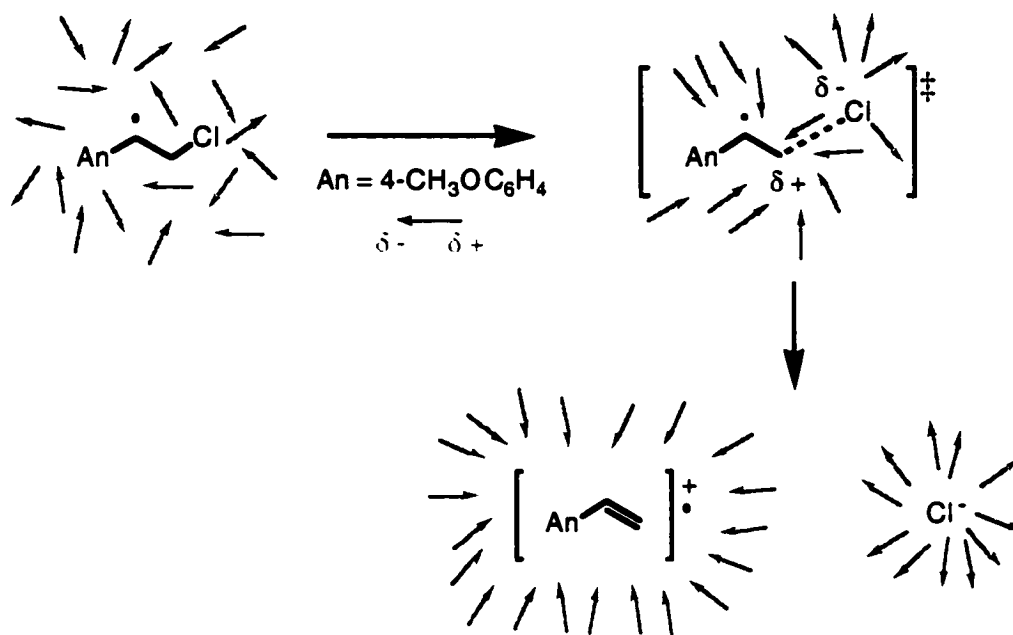
Figure 2-86. Schematic representation for the behaviour of the solvent molecules immediately surrounding the solute as the reaction proceeds through the transition state in the ionization reaction of 2-chloro-1-(4-methoxyphenyl)ethyl radical in solution. The arrows represent polar or polarized solvent molecules where the head of the arrow represents the electronegative end.

These fundamental differences in the activation parameters thus indicate that factors which contribute to the rapid heterolysis reaction in zeolites are considerably different from those in solution. In particular, as the reaction progresses from the initial state to the transition state in solution, the energy required to break the strong C-LG bond is partially compensated for by the formation of a fairly strong solvation shell around the incipient ions. Since the solvation shell presumably involves the formation of electrostatic interactions that are greater than the solvent-solvent interactions present in the initial state, the activation enthalpy is overall attenuated. In zeolites, the energy required for heterolysis is also compensated for by ion-pairing with the alkali-metal cation, but the formation of this interaction presumably requires the removal of a strong

alkali-metal cation-framework interaction. Thus, the extent to which the activation enthalpy is attenuated in the zeolite is less than that observed in solution.
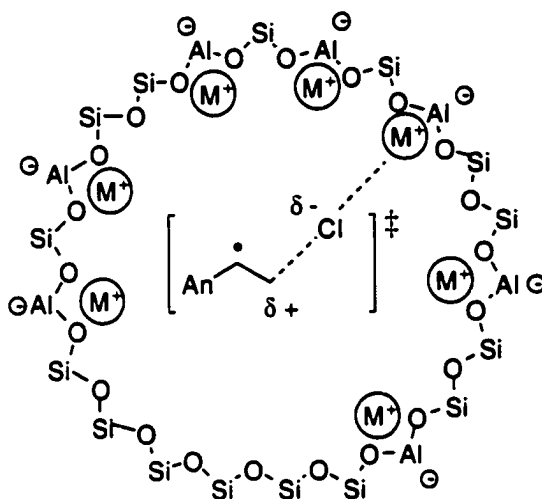
Figure 2-87. Schematic representation of the transition state for the β-heterolysis reaction of 2-chloro-1-(4-methoxyphenyl)ethyl radical in alkali-metal exchanged Y zeolites.

On the other hand, since the zeolite is not likely capable of changing its structure to accommodate the formation of the partially charged transition state, the changes in entropy upon going from the initial state to the transition state will be dominated by an increase in degrees of freedom due to the formation of two "separate" entities. Figure 2-87 schematically represents the transition state of the heterolysis of 2-chloro-1-(4-methoxypheny)ethyl radical within a zeolite supercage. This Figure illustrates the interaction between the charge-balancing cation and the leaving group thereby aiding the heterolytic cleavage of the carbon-chlorine bond. However, Figure 2-87 also shows that the *many* other counterbalancing cations significantly contribute to the overall electrostatic fields felt by the probe molecule depicting the importance of these forces as the driving force for the reaction.

As shown in Table 2-25, the enthalpy of activation increases upon going from NaY, KY, RbY and CsY. This increase is consistent with the observed decrease in the magnitude of the rate constant observed upon going from NaY to CsY. Presumably, the

strength of the coordination between the smaller cations and the negatively charged component of the transition state is greater than that involving the large cations. In addition, the stronger electrostatic field in NaY may have a greater ability to increase the polarization of the C-Cl bond prior to heterolysis. Such an increased polarization in the bond would be exhibited in a decrease in enthalpy of activation.

Conversely, the increase in the entropy of activation upon going from NaY to CsY represents a negative contribution to the overall free energy of activation, and works to increase the rate constant of heterolysis. Since the rate constants in fact change in the opposite direction, the increased entropy must be overwhelmed by the increase in enthalpy. The greater disorder in the transition state upon going from NaY to CsY is probably a reflection of the weaker interaction between the large Cs^+ cation and the newly formed partial negative charge.

The changes in enthalpy and entropy upon going from NaY to CsY may represent another manifestation of the entropy-enthalpy compensation principle which states that any increase in a reaction enthalpy is compensated by a parallel increase in the reaction entropy, and vice versa. Entropy-enthalpy compensation is a widely observed phenomenon in chemistry and biochemistry. For example, they are commonly observed in studies of thermodynamics of molecular recognition and guest-host complexation of cyclodextrins and other supramolecular systems.[240-243] In particular, binding and association equilibrium constants for many supramolecular systems have been found to follow such behaviour. Despite the fact that the entropy-enthalpy compensation principle was developed for equilibrium systems, Figure 2-88 clearly shows the trend predicted by the entropy-enthalpy compensation principle. Thus, as the activation enthalpy increases, a corresponding increase in the entropy of activation is observed.
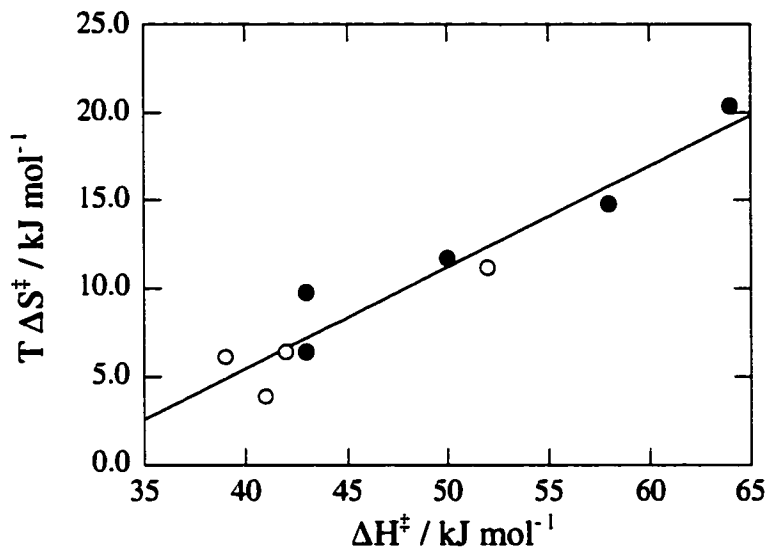
Figure 2-88. Enthalpy-entropy compensation plot for ionization of 2-chloro-1-(4-methoxyphenyl)ethyl radical in (●) dry and (○) partially hydrated MY zeolites under vacuum (10^{-4} torr) at 25 °C.

The co-incorporation of water into the MY zeolites resulted in activation parameters for the β-heterolysis reaction of 2-chloro-1-(4-methoxyphenyl)ethyl radical that exhibited similar trends as with the dry zeolite samples, Table 2-26. However, the overall changes in $\Delta H^{\ddagger}$ for the hydrated samples were now more pronounced. For example, the difference between the absolute values in activation enthalpy $\Delta(\Delta H^{\ddagger}_{CsY}-\Delta H^{\ddagger}_{LiY})$ from CsY to LiY were 13 kJ/mol and 21 kJ/mol for dry and hydrated zeolites, respectively. It is reasonable that a lower ionizing environment due to hydration leads to higher activation barriers and correspondingly slower β-heterolysis rate constants.

The initial motivation for measuring the activation entropies in the hydrated zeolites was to see if the values were negative as observed in aqueous solution. Clearly, however, the activation entropies in the hydrated zeolites are all positive, and in fact are

more positive than those determined in the dry zeolites. Presumably, water molecules within the zeolites cavities are tightly bound to the zeolite framework, particularly the alkali-metal cations, and interact only weakly with the β-chloro radical. However, solvation of the transition state requires an electrostatic interaction with water molecules and/or the framework. This disrupts the structure of the highly organized water-framework complex, and creates a less structured solvated transition state, causing an increase in the entropy of the system, Figure 2-89.

Table 2-26. Enthalpies, entropies and free energies (at 25 °C) of activation for β-heterolysis reaction of 2-chloro-1-(4-methoxyphenyl)ethyl radical in hydrated alkali-exchanged Y zeolites.

Dry Zeolites				Hydrated Zeolites			
Zeolite	$\Delta H^{\ddagger}$ (kJ/mole)	$\Delta S^{\ddagger}$ (J/mol·K)	$\Delta G^{\ddagger}$ (kJ/mol)	Zeolite	$\Delta H^{\ddagger}$ (kJ/mole)	$\Delta S^{\ddagger}$ (J/mol·K)	$\Delta G^{\ddagger}$ (kJ/mol)
				LiY	43	23	36
NaY	39	22	32	NaY	43	35	33
KY	42	23	35	KY	50	42	37
RbY	41	14	36	RbY	58	53	42
CsY	52	40	40	CsY	64	73	42

These results further support the importance of the interaction between the probe molecule and the zeolite counterions. That is, if the solvent molecule (water) can provide a better coordination with the cations than that of the probe molecule, the latter will be pushed away from the cations. As a result, the probe molecule will experience a smaller electrostatic field and a less ionizing environment.
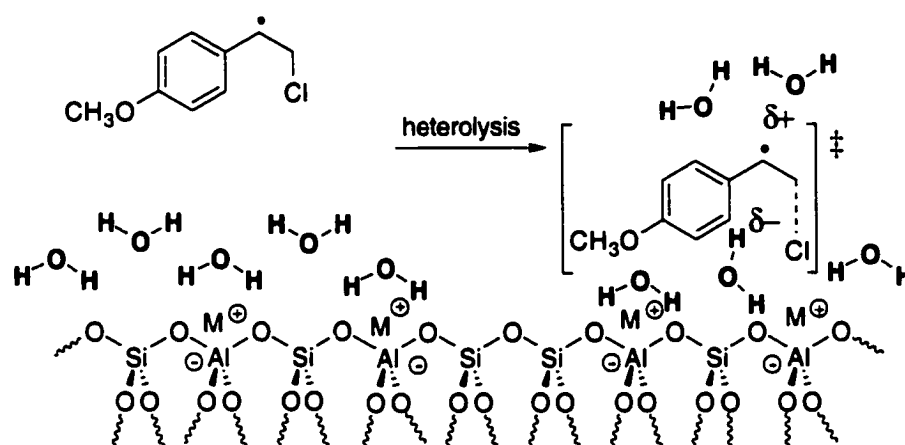
Figure 2-89. Schematic representation of the increase in entropy observed in the formation of the transition-state.

2.3.5. Substituent effects on the β-heterolysis reaction in alkali-metal zeolites

While several different arylalkyl acetates were examined in this thesis, only those with 4-methoxy substituents were found to be suitable probe substrates for the exploration of ionization reactions in zeolites. Despite this limitation, some general conclusions can be made about the influence of substrate structure on β-substituted carbon-centered radical reactivity.

Effect of structure

Both the 2-chloro-1-(4-methoxyphenyl)ethyl radical and its β-methyl substituted derivative, the 2-chloro-1-(4-methoxyphenyl)propyl radical showed clear evidence for ionization of the chloride leaving group to give, respectively, the 4-methoxystyrene radical cation and the anethole radical cation. However, the reactivity of the substituted propyl radical was considerably greater than that of the substituted ethyl radical. This is consistent with the well-known ability of electron-donating methyl groups attached directly to the carbon undergoing ionizing to enhance the overall reaction rate constant.

Whereas the formation of the 4-methoxystyrene radical cation via β-heterolysis was observed to occur with a single first-order rate constant, the formation of the anethole radical cation consisted of two distinct parameters. There was a fast heterolysis rate constant greater than 5×10^7 s^{-1} and a significantly slower heterolysis rate constant that varied with the zeolite counterion. Such a phenomenon highlights the heterogeneous nature of the zeolite where two distinct kinds of environments are observed for the β-chloro radical with a β-methyl moiety. The fast, prompt formation of the radical cation most likely corresponds to heterolysis taking place at sites in which the radical can adopt the proper orientation for efficient heterolysis. In the case of the slower reaction, the β-methyl group may force the radical into a conformation where overlap between the singly occupied p-orbital and the orbitals in the C-LG bond is diminished. This situation would result in a reduced rate constant because the fast β-heterolysis rate constants require assistance from the singly-occupied orbital of the radical center. Presumably, these steric impediments would not be present in the 2-chloro-1-(4-methoxyphenyl)ethyl radical system which does not carry the β-methyl group.

Alternatively, if the 2-chloro-1-(4-methoxyphenyl)propyl radical has a sufficiently strong interaction with, for example, an alkali metal cation attached to the internal wall of a cavity within the zeolite, the radical might exist in two reactive conformations. One of these conformations would lead directly the *trans*-anethole radical cation upon ionization, while the other would give the spectroscopically indistinguishable *cis*-anethole radical cation. Due to the unfavourable steric interactions that exist between the methyl and anisyl group of the *cis* isomer of the anethole radical cation, its formation by heterolysis might be slower than the formation of the radical cation of *trans* isomer. Thus, the fast component would correspond to ionization of chloride from those radicals that give the trans isomer, while the slow component is due to radicals giving the *cis*-isomer.

Effect of leaving group

In addition to chloride as a leaving group, some results were obtained using trifluoroacetoxy as the leaving group. In solution, these two groups have similar leaving group abilities with respect to solvolysis of 1-adamantyl chloride and 1-adamantyl trifluoacetate.[214,223] For example, the solvolysis rate constant for 1-adamantyl chloride in 80% aq. ethanol, k_{-Cl-} = 2.6 x 10^{-7} s^{-1} (50 °C), is identical to the rate constant for solvolysis of 1-adamantyl trifluoroacetate, k_{TFA} = 2.6 x 10^{-7} s^{-1} (50 °C). However, the nature of the solvent can modify the observed relative leaving group abilities. In 40% aq. methanol, the rate constant for the solvolysis of the chloride is 2.7 times faster than the trifluoroacetate group. Similarly, the solvolysis rate constant for the chloride is 1.7 times faster than the trifloroacetate in 96% TFE (4% H_2O). The subtle superiority of the chloride ion as a leaving group is rationalized as a higher sensitivity to electrophilic solvent assistance.

Significantly greater differences between the leaving group ability of chloride ion and the trifluoroacetoxy group were observed for the β-heterolysis reaction of β-substituted radicals in solution and in zeolites, Table 2-27. The rate constant for the formation of the 4-methoxystyrene radical cation from the 2-chloro-1-(4-methoxyphenyl)ethyl radical is at least 300 times faster than the heterolysis of the 2-trifluoroacetoxy substituted radical in HFIP. Similarly, the rate constants for the ionization of the chloride ion was on average 15-30 times faster than the trifluoroacetoxy substrate for the formation of anethole radical cation from the 2-chloro-1-(4-methoxyphenyl)propyl radical in a variety of solvents. These results clearly illustrate the significant reduction in the heterolysis rate constant for β-trifluoroacetoxy substrates.

Similar results were also obtained in zeolites for the formation of 4-methoxystyrene via β-heterolysis. The heterolysis rate constants for 2-chloro-1-(4-methoxyphenyl)ethyl radical are 62 and 42 times faster than the heterolysis rate constants for 2-trifluoroacetoxy-1-(4-methoxyphenyl)ethyl radical in NaY and KY, respectively. Due to the prompt formation of the anethole radical cation from the 2-substituted arylpropyl radicals comparison of the leaving group ability of chloride and

trifluoroacetate via β-heterolysis is not possible. However, the slow component observed for the formation of the anethole radical cation for the chloride and the trifluoroacetate moiety show similar heterolysis rate constants.

The results described above illustrate the interesting reactivity of β-substituted radicals due to the radical moiety. Whereas in closed-shell systems the leaving group ability of chloride and trifluoroacetate are comparable, the trifluoroacetate group in the open-shell β-substituted radicals has consistently much smaller ionization rate constants in solution and in zeolites. The radical moiety is therefore interacting with the leaving group thereby enhancing the stability of the β-substituted radical, Scheme 2-6. Formation of the cyclic radical is analogous to the mechanism of the β-(acyloxy)alkyl radical rearrangement.

Table 2-27. Rate constants for β-heterolysis of 2-chloro and 2-trifluoroacetoxy-1-(4-methoxyphenyl)alkyl radicals in selected media.

Solvent	Rate constants for β-heterolysis k_{het} / 10^6 s^{-1}			
	AcOClVA	AcOTFAVA	AcOClAn	AcOTFAAn
97% HFIP	> 100	0.31		
50% HFIP in AcN			6.6	0.25
70% HFIP in AcN			16.5	1.3
50% TFE in AcN			6.4	0.22
70% TFE in AcN			10.6	0.36
Zeolite	AcOClVA	AcOTFAVA	AcOClAn[a]	AcOTFAAn[a]
LiY				
NaY	39	0.63		
KY	8.9	0.21	1.5	0.43
RbY			1.2	1.1
CsY			0.3	1.8

[a]The fast β-heterolysis rate constants for the 2-substituted-1-(4-methoxyphenyl)propyl radical were too fast, so the slow component of the growth of the anethole radical cation

are listed for comparison; keep in mind that this slow component is not the main component to the growth.

Interestingly, the differences in rate constants between the two leaving groups is significantly less pronounced in zeolites than in solution, particularly for the 4-methoxystyrene system. One possible explanation for the smaller difference in zeolites is that the restricted space within the cavity inhibits formation of the stabilized, cyclic radical.

Scheme 2-6
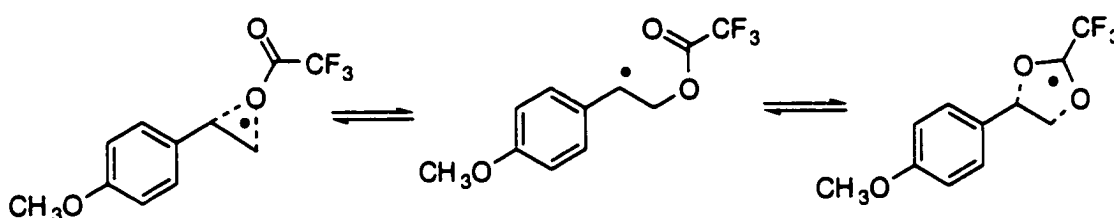
2.3.6. Decay of the styrenes radical cation in zeolites

Figure 2-90 summarizes the information obtained for the decay of the styrene-type radical cations generated via β-heterolysis of the corresponding β-chloro radicals. The decay profiles obtained for the photogenerated 4-methylstyrene, 4-methoxystyrene and anethole radical cations follow typical reactivity where the least stable radical cation is more reactive and the most stable radical cation is the least reactive.

The mechanism of the styrene-type radical cation decay was not investigated in the present thesis. However, the trend observed whereby the decay of the radical is slowest in LiY and fastest in CsY is the same as the trend established previously from a detailed examination of the effect of zeolite structure on the decay of the 4-methoxycumyl cation.[244] From that work, the conclusion was made that the 4-methoxycumyl cation decayed primarily via nucleophilic addition of a framework oxygen located in a Si-O-Al bridge. Thus, the intrazeolite decay of the present styrene radical cations may also proceed via nucleophilic addition of the zeolite framework.
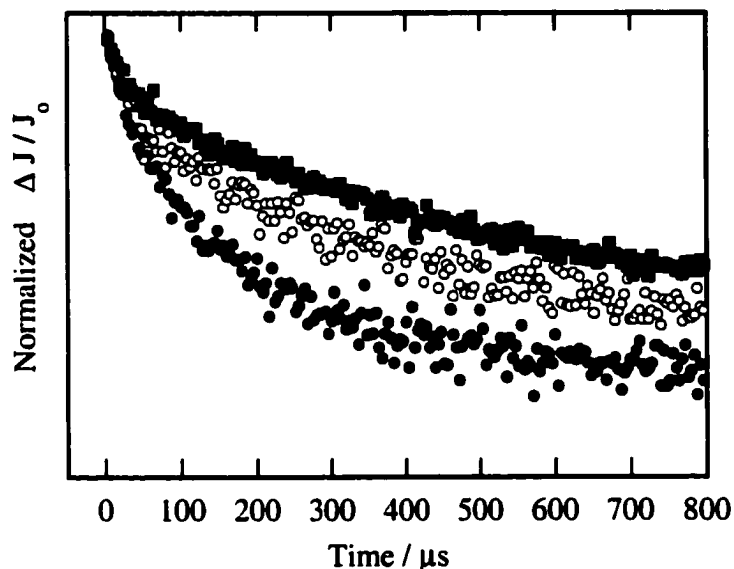
Figure 2-90. Transient decay kinetics generated upon 266 nm excitation of (●) 2-chloro-1-(4-methylphenyl)ethyl acetate (AcOClMeSty), (O) 2-chloro-1-(4-methoxyphenyl)ethyl acetate (AcOClVA), and (■) 2-chloro-1-(4-methoxyphenyl)propyl acetate (AcOClAn) in LiY. The normalized traces for the olefin radical cation were obtained at 360-385 nm under vacuum conditions (10^{-4} torr) over 800 μs.

The nucleophilicity or electron-donor ability of the zeolite associated with the Si-O-Al active sites within the framework are affected by the zeolite counterion. The strong interaction between the Li^+ cation and the electron-rich framework oxygen renders these sites considerably less nucleophilic than sites where the counterion is larger and the charge more diffuse, e.g. Cs^+. Thus, the observed effect can be understood by a gradual decrease in the interaction efficiency between the nucleophilic oxygen sites and the zeolite counterion as the alkali-metal increases in size and decreases in electronegativity.

The styrene-type radical cations generated through photoionization were much shorter lived than the same radical cation generated via β-heterolysis from the β-substituted arylethyl radicals, Figure 2-91. This trend was observed in all the alkali-exchanged Y zeolites. The increased reactivity of the radical cations generated via photoionization is attributed to the well-known dimerization reaction taking place between the radical cation and a neutral styrene molecule.[186] This method of decay is not available to the radical cations formed through β-heterolysis as there are no already-

existing neutral styrene molecules in the system. Consistent with the above mechanism, loading level experiments showed an increase in the reactivity of the radical cation with higher loading levels of precursor styrene. In addition, these experiments suggested that at very high loading levels fast dimerization between the radical cation and the neutral styrene molecule within a zeolite cavity occurred resulting in overall smaller yields of styrene radical cation.
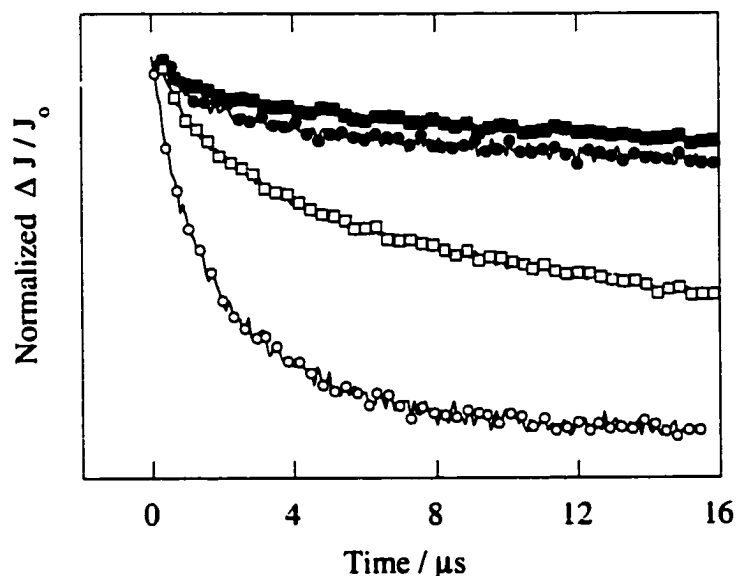
Figure 2-91. Normalized decay traces monitored at ca. 600 nm after 266-nm irradiation of (●) 2-chloro-1-(4-methoxyphenyl)ethyl acetate, (O) 2-chloro-1-(4-methoxyphenyl)-propyl acetate, (■) 4-methoxystyrene and (□) anethole in NaY.

2.3.7. Conclusions

The results presented in this thesis established that β-heterolysis was a good kinetic probe reaction to investigate the absolute ionizing power of cation-exchanged Y zeolites. The ability of zeolites to support the generation of reactive species and stabilize carbocation intermediates is well documented and the present investigation has provided further understanding for efficient carbocation formation via bond heterolysis of leaving groups as observed in S_N1 reactions.

Dry alkali cation exchanged Y zeolites consist of highly ionizing environments, and the extent of their polarity is dependent on the balancing cation charge density. Comparison of the ionization reaction of the probe molecule in zeolites with the results obtained in solution allowed for a direct comparison between these two media and to generate Y-values for zeolites. The Y values obtained for alkali-metal zeolites are comparable to solvents like TFE and methanol/water mixtures with a range between 1.4 and 6.6. Some evidence for the effect of substrate structure on the ionizing environment experienced by the guest molecule was observed, but further work to find suitable probe structures that exhibit detectable ionization reactions in these zeolites is necessary.

When water is co-incorporated into the zeolite (slight hydration), the contribution of the electrostatic fields from the cations toward the polarity of a zeolite is reduced due to buffering of the intrazeolite electrostatic fields.

The active role of zeolites in the ionization reaction of β-substituted radicals was evident in the results. The temperature studies of the reaction in zeolites in contrast to solution studies provided information about the interactions between the substrate and the zeolite framework as the reaction proceeds, verifying that zeolites are not only inert polar vessels which provide stabilization to intermediates but that actively participate in the observed reactivity.

Chapter 3. Generation and reactivity of simple aryl radicals in non-acidic zeolites

3.1. Introduction

Organic free radicals are among the best known and most important intermediates in organic chemistry. They are neutral molecules that possess an unpaired electron typically either centered on a carbon atom or on an oxygen atom to make a carbon centered or phenoxyl radical species, respectively. Due to the odd number of electrons, free radicals are usually highly reactive species. These reactive species may undergo various reactions. For example, they may combine with one another or with single atoms that also possess free electrons to form neutral stable molecules (radical-radical coupling), eq. 3.1. Radicals may also react with non-radical species by abstracting a hydrogen atom, thereby generating a different free radical, eq. 3.2. Other types of radical-related reactions include addition, rearrangement, elimination, or fragmentation.

$$-\overset{|}{\underset{|}{C}}\bullet \quad \bullet A \quad \longrightarrow \quad -\overset{|}{\underset{|}{C}}-A \tag{3.1}$$

$$-\overset{|}{\underset{|}{C}}\bullet \quad H-\overset{|}{\underset{|}{C}}-R \quad \longrightarrow \quad -\overset{|}{\underset{|}{C}}-H \quad \bullet\overset{|}{\underset{|}{C}}-R \tag{3.2}$$
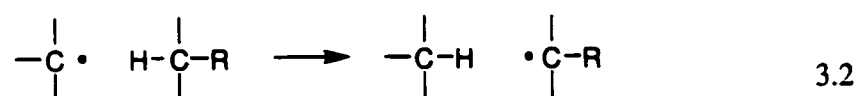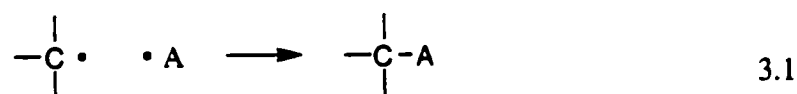
In an inert, de-oxygenated solvent, the lifetime of a carbon-centered radical is determined primarily by the rate of radical-radical combination and/or disproportionation. These reactions are often diffusion-controlled bimolecular reactions susceptible to intramolecular steric factors that can slow the radical-radical reactions. However, since the concentration of radicals is typically low, the diffusion-controlled coupling process can readily be diverted by reaction of the radical with a radical quencher. Common quenchers of carbon-centered radicals include the oxygen molecule, which typically adds to the radical center to generate a peroxyl radical.

A wide variety of techniques have been employed to examine the reactivity of radicals, especially electron spin resonance spectroscopy (ESR) and laser flash photolysis.[245-248] The latter technique is particularly well suited for examining arylmethyl radicals which are easily generated photochemically and have characteristic UV-Vis absorption bands. A comprehensive summary of the reactivity of arylmethyl radicals in solution is beyond the scope of this chapter. However, the vast amount of information obtained using laser flash photolysis regarding the properties of arylmethyl radicals in solution makes these radicals an ideal choice for examining the effect of zeolite structure and composition on radical reactivity.

3.1.1. Radical reactivity in zeolites

In contrast to the β-heterolysis reaction of β-substituted radicals discussed in the previous chapter, the non-polar nature of benzyl radicals suggests that benzyl radical reactivity is not likely to be highly sensitive to environmental factors such as the strength of the electrostatic field or the polarity within the zeolite cavities. One decay pathway that would be sensitive to such environmental factors is oxidation to a benzyl cation; however, given the relatively high oxidation potential of most simple benzyl radicals, thermal oxidation of the carbon-centered radical to generate a carbocation is not likely.[249,250] In addition, the strong Si-O-Si and Si-O-Al bonds that make up the zeolite framework are not likely to be susceptible to direct attack by the radical. As a result, the internal zeolite environment is expected to behave almost exclusively as a 'passive' host that exerts its effect on the reactivity of the included radical through the size and shape restrictions of the zeolite framework. Thus, examining the reactions and reactivity of radicals within zeolites provides an ideal opportunity to focus on how purely passive effects can influence chemical reactions.

The research groups of Turro and Ramamurthy have extensively studied the application of supramolecular concepts, such as size and shape of the void spaces of zeolites, to control the selectivity of reactions of radicals produced by photochemical excitation of organic molecules adsorbed on zeolites.[15,251-255] The photochemical

precursors for the generation of arylmethyl radicals within zeolites have been dibenzyl ketones which, upon photolysis, produce two primary geminate radicals by a Norrish type I reaction followed by rapid decarbonylation of the acyl radical to produce two benzyl radicals,[256-259] eq. 3.3. Hence, mainly radical-radical combinations of the benzyl radicals are observed in the products formed.[260,261] These investigations have shown that the reactivity of these types of radicals is controlled by the *supramolecular features* of the host-guest system. The exceptional control of zeolites is demonstrated in the chemistry of radicals in that the products of radical-radical reactions, which are non-selective in solution, can be made selective and can be controlled by supramolecular effects.[15,262,263]

3.3
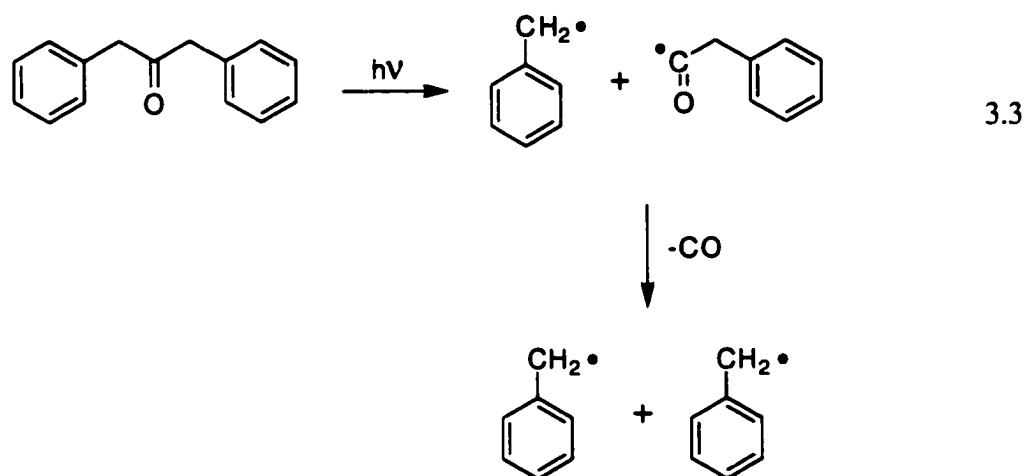
The majority of these studies have been based on the ratio of products formed upon steady-state photolysis of dibenzyl ketone and its methylated derivatives. Thus, both the reactivity and mobility of the monoaryl radicals within the zeolite framework have been inferred from the yield and distribution of the product mixtures. Any unsymmetrically substituted dibenzyl ketone is an A-B type molecule that upon photolysis yields products A-A, B-B, or A-B according to the cage effect of the system. The cage effect (CE) represents the product ratios observed in the photolysis and will depend on the diffusion restriction of the system, as given in equation 3.4.

$$\text{Cage Effect (CE)} = \frac{[AB] - [AA + BB]}{AA + AB + BB}$$

3.4

The basic concept behind this probe molecule is that photolysis of the A-B system gives two fragments, A and B, whose radical-radical coupling reactions reflect the chemical nature of the container environment where the radicals are initially generated, Scheme 3-1. Thus, if the environment containing the radicals allows the two fragments to separate and become completely independent free radicals, the product radio will be 1 A-A: 2 A-B: 1 B-B and the cage effect will be zero, CE = 0. Alternatively, if the two fragments remain as a close-contact radical pair, the only product will be A-B and CE = +100%. Finally, if the environment induces selective coupling such that only A-A and B-B products are formed, CE = -100%. Thus, the extent of the cage effect will be reflected in the relative yield of the products A-B, A-A, and B-B. For example, in non-viscous solutions such as benzene or 2-propanol, photolysis of diaryl ketones gives cage effects close to zero because the two fragments are able to separate from each other and then randomly couple.

Strong cage effects have been observed in the product distribution for the reaction in zeolites where both positive and negative cage effects are obtained. For example, the photolysis of o-methylbenzylbenzyl ketone in the zeolite ZSM-5 (6 Å channel diameter; approximate diameter of unsubstituted benzene ring) yielded only symmetrical dibenzyls (AA, BB type; negative cage effect), while the p-methylbenzylbenzyl ketone yielded unsymmetrical dibenzyl (AB type; positive cage effect).[15,251,264] The o-substituted benzyl radical is thought to be too sterically bulky to be accommodated by the zeolite channel and thus diffuses into the zeolite-solvent slurry. Thus, the zeolite acts as a 'sieving' host that separates the two radical segments and the o-methylbenzyl radical dimerizes only in solution. The unsubstituted and p-methylbenzyl radicals, on the other hand, are able to dimerize in the interior of the zeolite. The cage effects were observed to be concentration dependent. At low loading, all the molecules were embedded in the zeolite framework yielding positive and negative cage effects. The cage effect gravitated toward zero as the loading was increased due to an increasing number of free, unbound molecules.

Scheme 3-1[15]

$$A \overset{O}{\underset{B}{\bigwedge}} \quad \xrightarrow[\text{- CO}]{hv} \quad A^{\bullet} \; + \; B^{\bullet}$$

$$\xrightarrow{CE = 100\%} \quad A\!-\!B \quad \begin{array}{l}\text{Spatially Restricted}\\ \text{Diffusion}\\ \textit{Geminate combination}\end{array}$$

$$\xrightarrow{CE = 0\%} \quad \begin{array}{l}A\!-\!A\\ 2\; A\!-\!B\\ B\!-\!B\end{array} \quad \begin{array}{l}\text{Spatially Unrestricted}\\ \text{Diffusion}\\ \textit{Random combination}\end{array}$$

$$\xrightarrow{CE = -100\%} \quad \begin{array}{l}A\!-\!A\\ B\!-\!B\end{array} \quad \begin{array}{l}\text{Spatially Selective Diffusion}\\ \textit{Combination after sieving}\end{array}$$
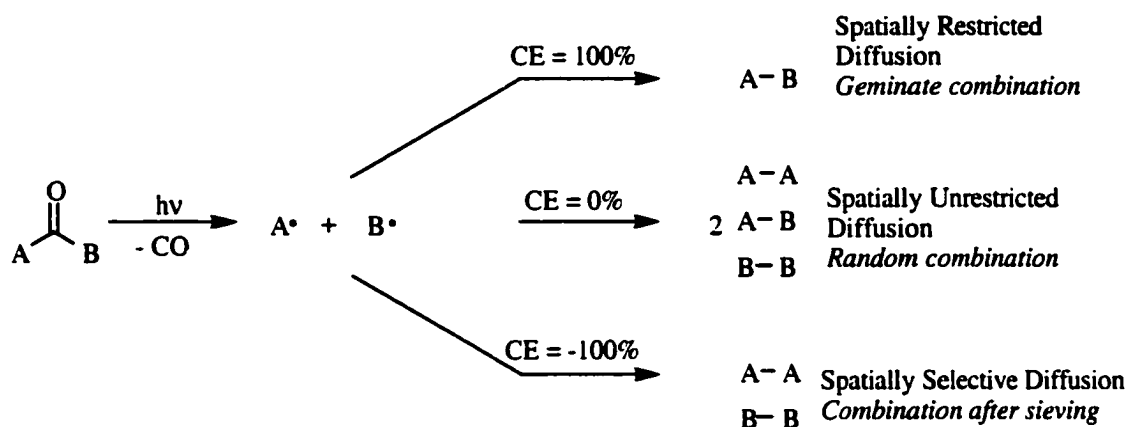
Subsequent studies have unmistakably established that the radical derived coupling products vary dramatically as a function of the internal structure of the zeolite as well as the framework composition and nature of the zeolite charge-balancing cation.[262,265] Therefore, the bimolecular coupling reaction, as it depends on the distribution and transport of the reactant within the various sites of the zeolite environment, can be influenced by experimental manipulations such as ion exchange and the use of small amounts of unreactive additives. Similarly, the escape and recombination probabilities in the zeolite are also determined by the occupancy of the neighboring sites due to the existence of local and global space effects.[252,253] In all cases, product formation and the cage effect reveal the steric constraints experienced by the radical pairs in a supercage thereby providing information about the rotational and diffusional motions of radical pairs produced in zeolite supercages. Thus, the chemistry of incorporated radicals and product distribution can be controlled through the choice of zeolite, substrate concentration and magnetic effects.

Although no direct information about the benzyl radical diffusion was obtained using dibenzylketone, based on the assumption that the rate of intracrystalline diffusion for the radical was that of benzene $(D = 10^{-10} \text{ m}^2\text{s}^{-1})$ and using the random-walk model it was estimated that a benzyl radical is able to explore as many as 25 supercages before decarbonylation occurs (ca. 100 ns). As a result, at low loadings the primary radical pair

(PhCH$_2$CO· and PhCH$_2$·) is able to escape and diphenylethane makes up the major product. On the other hand, high yields of rearranged products due to coupling of the primary radical pair are observed at high occupancy values.

Turro's research group has also used a "supramolecular approach" to the formation of persistent carbon centered radicals. The basis for this approach is the use of steric or dynamic supramolecular effects to lengthen the lifetime of the intermediate in zeolites. The steric effect results from the limited space available for a radical to move in the vicinity of cavities and channels and a dynamic mechanism is explained as a diffusional maze effect. For example, when the molecular traffic patterns of the radicals lead to infrequent encounters between two radicals the lifetime of the transient is prolonged. For the phenethyl radical generated photochemically from an alkyl substituted dibenzyl ketone precursor in ZSM-5, this steric approach allowed the radical to become persistent for hours at room temperature.[266] More recently, they have been able to make the diphenylmethyl radical 'supramolecularly persistent' in LZ-105 zeolite (similar to ZSM-5) where a half-life of weeks has been reported.[168,249,267] Furthermore, the steric inhibition of radical-radical reactions responsible for the long endurance allow the reversibility of the oxygenation of the diphenylmethyl radical to be detected using EPR spectroscopy.[15,254,255] The diphenylmethyl radical was first observed to decay over a wide range of lifetimes from several microseconds to minutes depending on conditions in faujasite zeolites in the early 90's.[268,269] This early result suggested a wide range of possible environments for the decay of the radicals reflecting the distribution of the radicals with respect to each other and the starting ketone, results that were supported by local and global environments described by Turro.

The photolysis of benzyl phenylacetate adsorbed on pentasil and faujasite zeolites leads to the formation of the benzyl radical and these results have also been shown to differ greatly from results obtained in solution.[270,271] Similar to the results obtained for the dibenzyl ketones, the research by Tung et al. has been explained in terms of the size and shape sorption selectivity of the zeolite, restriction of diffusional and rotational mobility of the radical pair imposed by the zeolite surface.

The direct observation of a small transient radical, the acetyl radical, in NaY zeolite was recently achieved by the use of step-scan FT-infrared spectroscopy.[272] The radical was observed to have a lifetime of 71 μs when the photochemical precursor was 1-naphthyl acetate and 315 μs when the precursor was pinacolone. The kinetic results were interpreted in terms of complete separation of the photogenerated pairs from the parent supercage, followed by random walks in subspaces of the zeolite lattice imposed by the much less mobile precursor molecules. In this manner, the molecular restrictions forced the geminate radicals to react and thereby contribute to the high selectivity of these photoreactions in zeolites.

3.2. Generation of benzyl radicals in zeolites

The direct monitoring of transient species in zeolites and other microporous solids by time-resolved spectroscopy has given essential mechanistic understanding of the chemical transformations in these host materials. Aside from structural information on short-lived intermediates in these environments, elucidation of the kinetic behaviour reveals direct insight into the factors that determine product selectivities and yields. However, despite the vast amount of benzyl radical research in zeolites, no time-resolved studies of the benzyl radical produced upon photolysis of dibenzyl ketone within the cavities of zeolites have been reported. The main reason is that laser excitation of dibenzyl ketone yields an ill-defined absorption band around 330-350 nm, Figure 3-1, that is not due to the presence of the benzyl radical which has a sharp absorption band at 318 nm in solution.[273-277] Presumably, rapid in-cage coupling of the geminate radical pair when the radicals are generated in the same zeolite cavity, is most likely responsible for the elusive detection of the benzyl radical in zeolites.

Therefore, in order to directly observe the benzyl radical within zeolites using nanosecond diffuse reflectance spectroscopy, it is necessary to attain a source of carbon-centered radicals where a lone free benzyl radical is generated within a single zeolite cavity. Our approach was to utilize the precursor, phenylacetic acid, that upon 266 nm

laser photolysis would generate only one benzyl radical species within a given zeolite cavity.

There are numerous photocleavage steps available to a carboxylic acid derivative. Flash photolysis, CIDNP, kinetic measurements, and product studies have been used as tools to probe this reaction.[278-282] These studies have shown that mechanistically the photodecarboxylation of carboxylic acids is quite complex. The mechanism in which carbon dioxide is eliminated from photoexcited carboxylic acids has been classified into several types with the simple heterolytic and homolytic mechanisms being the most readily observed. These studies have led to the conclusion that a variety of mechanisms are operable, depending on the substrate and conditions employed. For example, the photolysis of phenylacetic acid in hexane produces toluene and 1,2-diphenylethane from an intermediate benzyl radical, eq. 3.4, whereas the photolysis of sodium phenylacetate in methanol produces toluene through the intermediacy of the benzyl anion, eq. 3.5.
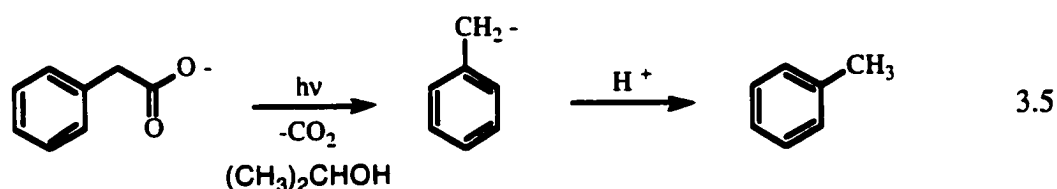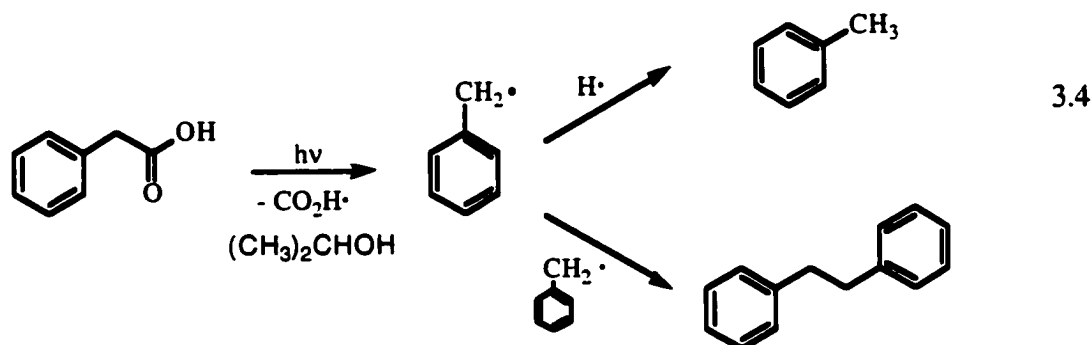
The Kolbe reaction is another well-known reaction that has been used for the production of carbon-centered radicals, eq. 3.6. This reaction refers to the anodic oxidation of salts of carboxylic acids to acyloxyl radicals that yield carbon centered radicals via decarboxylation.[283] Photoinduced electron transfer (PET) reactions of

carboxylate ions also give carbon centered radicals via a similar mechanism. In this case, the carboxyl radicals are typically produced by electron-transfer from the carboxylate ion to a photoexcited electron-acceptor.[284,285]

$$\text{(Ph-CH}_2\text{-CO-O}^-) \xrightarrow{-e^-} \text{(Ph-CH}_2\text{-CO-O}^\bullet) \xrightarrow{-CO_2} \text{(Ph-CH}_2^\bullet) \qquad 3.6$$
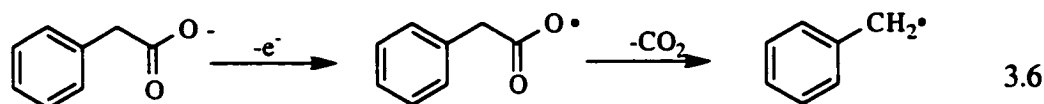
The use of salts of carboxylic acids to generate radicals within zeolites has recently been demonstrated, where investigations in our laboratory have shown that the xanthyl radical is produced by photo-oxidative decarboxylation of xanthene carboxylic acids within MY zeolites, eq. 3.7.[285]

$$\text{(xanthene-CO-O}^-) \xrightarrow[\text{MY}]{h\nu} \text{(xanthene-CO}^\bullet) \xrightarrow{-CO_2} \text{(xanthyl radical)} \qquad 3.7$$
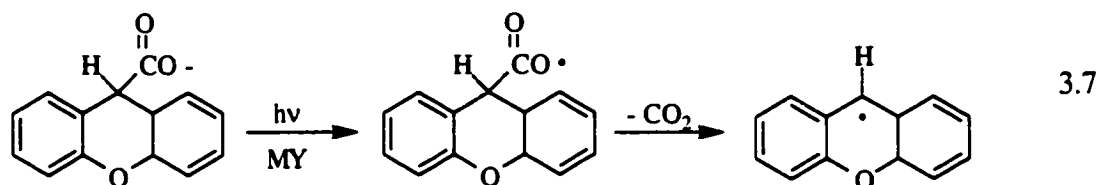
3.3. Results

The following sections report the observation of photogenerated benzyl radicals within cation-exchanged Y faujasites using nanosecond diffuse reflectance spectroscopy.[167] Evidence is also presented for the simultaneous detection of the benzyl anion. In each case, the radicals have been generated photochemically from the appropriate phenylacetic acids.

3.3.1. Generation of the benzyl radical in alkali-metal cation zeolites

Phenylacetic acid was readily incorporated into NaY with a loading level of <S> = 1/2 (and also into the other MY zeolites) using hexane as the carrier solvent. In most cases, UV-Vis analysis of the decanted hexane solutions supported 100% incorporation

of phenylacetic acid. No colour formation was observed upon incorporation of the molecule into the zeolite, and only phenylacetic acid was recovered from NaY upon continuous solid-liquid extraction, indicating that phenylacetic acid is thermally stable within the zeolites for the duration of the experiment.

Previous work with the xanthene carboxylic acid suggested that carboxylic acids exist within the zeolites in the carboxylate ion form.[285] As a result, IR spectra of the phenylacetic acid-NaY composite were obtained to determine if the phenylacetic acid also existed to a significant extent as the carboxylate ion. The spectra obtained in NaY and also CsY showed a strong carbonyl band centered at 1620 cm^{-1} and no signal above 1700 cm^{-1}, which is consistent with the carboxylate ion being the predominate species within the zeolite environment, eq. 3-8.

$$\underset{\text{minor species in MY}}{\text{C}_6\text{H}_5\text{CH}_2\text{COOH}} \quad \underset{\longrightarrow}{\overset{-H^+}{\rightleftharpoons}} \quad \underset{\text{major species in MY}}{\text{C}_6\text{H}_5\text{CH}_2\text{COO}^-} \qquad 3.8$$
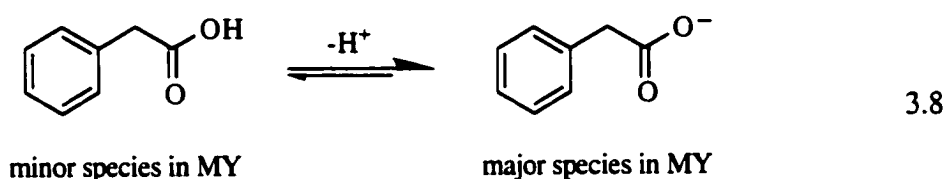
Figure 3-2 shows the transient diffuse reflectance spectrum generated upon 266 nm laser excitation of phenylacetic acid (<S> = 1/2) in dry NaY under reduced pressure (10^{-4} torr). The spectrum shows a strong absorption band centered at 315 nm and a shoulder at 305 nm that coincide nicely with the known absorption spectrum for the benzyl radical in solution.[275-277] The transient species at 315 nm is completely quenched by the addition of oxygen to the sample, which is characteristic of a radical species,[268,286] Figure 3-3. On the basis of the close similarity between the spectrum generated within the zeolite and the known spectrum of the benzyl radical, together with the observed oxygen quenching, the transient species at 315 nm is identified as the benzyl radical. The radical is generated by photoionization of the phenylacetate anion to generate the acyloxy radical that then rapidly loses CO_2[287-289] to yield the benzyl radical, eq. 3.9. Consistent with the formation of the benzyl radical is that one of the major products upon steady-

state photolysis in NaY in the absence of oxygen is 1,2-diphenylethane, the product from radical-radical coupling (*vide infra*).

3.9
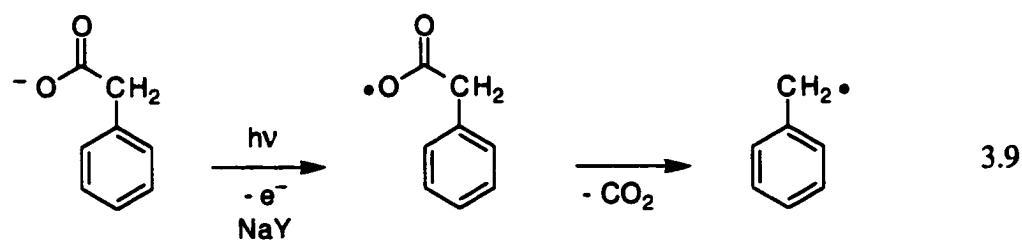
Rate constants for decarboxylation of acyloxy radicals typically are in 10^9 s^{-1} range. In particular, the rate constant for decarboxylation for the benzyl acyloxy radical has been estimated to be 5.0 x 10^9 s^{-1}.[287] Hence, it is unlikely that the acyloxy radical would be sufficiently long-lived to be detected with a nanosecond laser flash photolysis system. Furthermore, the absorption maximum of this radical is expected to be at wavelengths shorter than 300 nm.[280]

Further evidence that the benzyl radical is generated from decarboxylation of the acyloxy radical is provided *via* protoinduced electron-transfer conditions.[285,288,289] Electron transfer between co-incorporated methyl viologen (MV^{2+}) and phenylacetate anion produces the methyl viologen radical cation ($MV^{+•}$) and the acyloxy radical that then goes on to form the benzyl radical, eq. 3.10.

3.10
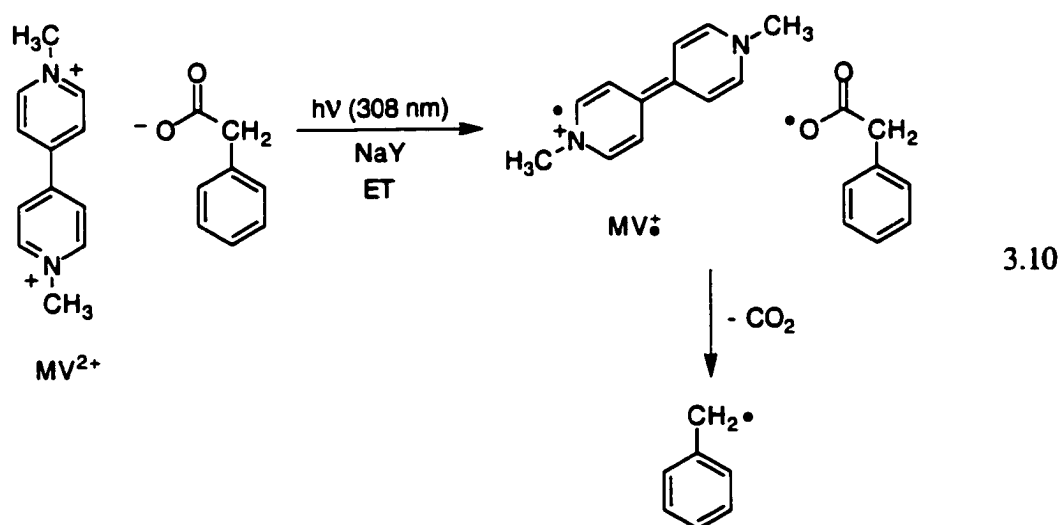
Selective 308 nm irradiation of MV^{2+} in NaY with co-incorporated phenylacetic acid under vacuum conditions (10^{-4} torr) resulted in the transient diffuse reflectance spectrum shown in Figure 3-4. The methyl viologen radical cation ($MV^{+}\bullet$) has characteristic absorption bands at 400 and 600 nm which are clearly present in the spectrum.[285,288,289] In addition, a much weaker absorption band around 315 nm corresponding to the benzyl radical is clearly detected. The detection of both these transients supports the conclusion that the benzyl radical is derived by rapid decarboxylation of the phenylacyloxy radical formed by electron transfer between the phenylacetate anion and photoexcited MV^{2+}, as shown in equation 3.10.

A second route for the generation of the benzyl radical is the direct irradiation of phenylacetate anion incorporated within the zeolite, eq. 3.11. Due to the highly hygroscopic nature of the zeolite it is unwise to use water to incorporate a salt into the framework. Thus, tetrabutylammonium phenylacetate was prepared so that hexanes could be used as the carrier solvent. Photolysis of tetrabutylammonium phenylacetate in evacuated-NaY with 266 nm laser light generated the spectrum shown in Figure 3-5. The spectrum is dominated by a single strong band at 315 nm, which corresponds nicely to that of the benzyl radical. The generation of the benzyl radical under these conditions provides further evidence for the mechanism of photochemical formation of the benzyl radical, eq. 3.9.

3.11
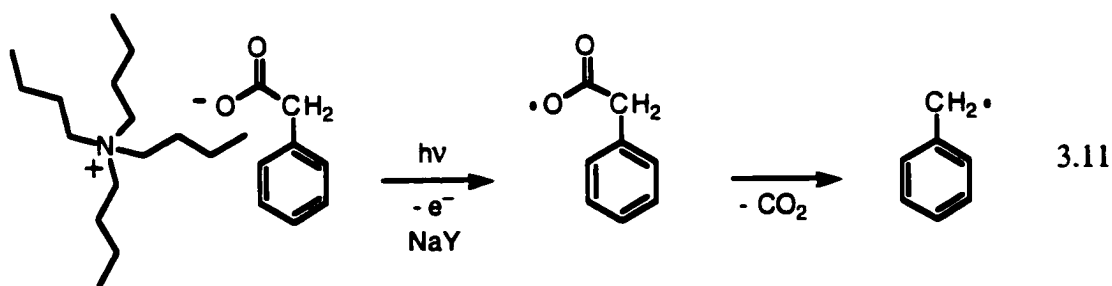
3.3.2. Decay kinetics for the benzyl radical in MY zeolites

A transient decay profile obtained by combining individual decay profiles for the decay of the benzyl radical at 315 nm band in NaY over several different time-scales ranging from 2 μs to 400 μs is shown in Figure 3-6. One obvious feature from this stretched decay trace is that the benzyl radical decays with at least two distinctly different decay components. A fast component is clearly present which is responsible for the decay of approximately 60% of the initially generated radicals. The remaining 40% of the radicals decay much more slowly and represent the second, slower component.

The multicomponent nature of the decay of the benzyl radical presumably arises from the heterogeneous nature of the intrazeolite environment and highlights the difficulties associated with analysis of the decay traces to determine quantitative rate constants. Decay kinetics consisting of a distribution of rate constants over several orders of magnitude are common for radical decay in heterogeneous media.[268] Although a uniform distribution of the substrate is assumed to exist for small molecules in alkali-metal zeolites, one can envisage scenarios where there exists various distribution of sites within the zeolite. For example, the situation may arise where two phenylacetic acid molecules are present within a cavity. In this case, the two benzyl radicals generated upon 266 nm photolysis would rapidly couple to generate 1,2-diphenylethane in a first order fashion. On the other hand, benzyl radicals generated in different cavities would have to travel through one or more cavities to find a reacting partner; thus, second-order rate constants would be obtained. In addition, the local position of the radicals within the cavities would also have an effect on the observed kinetics; that is, are the radicals facing each other for the reaction to take place or are they tail to head? This means that one must consider first- and second-order kinetic analysis to adequately describe the kinetic traces for the disappearance of the radical.

The most likely scenario that would lead to a significant first-order component is one in which two benzyl radicals created in the same cavity couple to give 1,2-diphenylethane. This requires two phenylacetate ions to occupy the same cavity and for

both precursors to undergo photochemical conversion to the benzyl radical pair. Since photoionization is likely to be quite inefficient, the probability that two phenylacetate anions in the same cavity will undergo photoionization seems remote. In addition, under circumstances where geminate benzyl radicals are produced upon photolysis of dibenzyl ketone, geminate benzyl radical coupling is so rapid that no benzyl radicals are observed. In fact, results from studies in other heterogeneous media like micellar solutions indicate that geminate benzyl radical coupling takes place quite quickly with rate constants on the order of $\sim 1.2 \times 10^7$ s^{-1}.[290] Analysis of the fast component for the decay of the benzyl radical in NaY using a first-order expression leads to a first-order rate constant of approximately 3×10^5 s^{-1} that seems far too small to correspond to a geminate radical coupling process. In addition, the first-order expression does not fit the data well, as shown by the residual plot included in Figure 3-7a.

On the basis of the arguments outlined above, it is reasonable to assume that the decay of the benzyl radicals is better represented as a second-order radical-radical coupling process involving migration of a benzyl radical generated in one cavity to another benzyl radical generated in another cavity. In fact, the fast component which decays over 15 μs after the laser pulse fits better to a second-order rate expression as illustrated in the residual plot in Figure 3-7b. In this expression, C_o represents the absorption remaining due to the presence of the slow decaying radicals and C_1 represents the change in absorption due to the fast decay, eq. 3.12. The parameter k_1 represents the second-order rate constant for the fast component, while ε is the extinction coefficient for the benzyl radical and S is a term for the scattering coefficient of the zeolite.

$$\left(\frac{\Delta J}{J_o}\right)_t = C_o + \frac{1}{\left(C_1 + \frac{S}{2\varepsilon}k_1 t\right)}$$

3.12

Analysis of the decay trace in Figure 3-7b leads to a value of $k_1 S/2\varepsilon = 1 \times 10^7$ s^{-1}. To obtain k_1, a second-order rate constant in NaY, requires values for ε and S. The extinction coefficient of the benzyl radical has been a source of debate for several

years.[291] Values ranging from 1100 cm^{-1} M^{-1} to 12000 cm^{-1} M^{-1} have been reported.[258,275,281,291,292] As an estimate of the extinction coefficient of the benzyl radical in zeolites, the value of 8800 cm^{-1} M^{-1} measured in cyclohexane was chosen. The scattering coefficient for silica gel ($S = 64$ cm^{-1}) was used as an estimate for the S value of zeolites.[293] Using these values, the rate constant k_1 can be calculated to be 2.7 x 10^9 M^{-1} s^{-1}.

Finding a suitable rate expression to fit the slow component of the decay profile in Figure 3-6 is even more problematic. In particular, the radicals do not completely decay to the baseline and insufficient information is available with respect to the slow decay for any reliable quantitative information to be obtained. The approach taken to estimate the kinetic data is based on the assumptions that the slow decay consists of two components, with the faster of these two components being due to a second-order reaction. The second component remains indeterminate and is represented by a residual absorption due to radicals that do not decay at all over the longest available time-scale of 800 μs. Overall, the rate expression used to fit kinetic data obtained over 800 μs is a double second-order rate expression that will give rate constants for the fast (k_1) and slow (k_2) components, as well as a residual term, C_0, that accounts for the radicals that do not decay at all over the time-scale of the experiment, eq. 3.13. For the decay of the benzyl radical in NaY, the rate expression leads to values of $k_1 = 3.6$ x 10^9 M^{-1} s^{-1} for the fast component, $k_2 = 1.9$ x 10^8 M^{-1} s^{-1} for the slow component, and a residual absorption of 0.018 due to long-lived radicals.

$$\left(\frac{\Delta J}{J_o}\right)_t = C_o + \frac{1}{\left(C_1 + \frac{S}{2\varepsilon}k_1 t\right)} + \frac{1}{\left(C_2 + \frac{S}{2\varepsilon}k_2 t\right)} \qquad 3.13$$

In solution, the main decay pathway for the benzyl radical has been shown to be dimerization to generate 1,2-diphenylethane. Therefore, one would expect the rate of decay of the benzyl radical to be dependent on the concentration of benzyl radicals. Indeed, this is observed to be the case for the irradiation of phenylacetic acid incorporated into NaY at various loading levels. The decay traces at 315 nm upon laser

photolysis of phenylacetate ion within NaY as a function of loading level are shown in Figure 3-8. In addition to an increase in the signal due to an increase in the number of benzyl radicals generated, the fraction of radicals that decay rapidly over the first 16 µs also increases significantly, Figures 3-8 and 3-9. Thus, as more radicals are produced, the probability of finding a neighbouring cavity containing another benzyl radical is higher than that at low loading levels.

The decay of the benzyl radical over the first 16 µs after the laser pulse at each of the loading levels was examined quantitatively using the simple second-order rate expression described above, eq. 3.12. Fitting the decay trace to this expression gives the apparent rate constants, k_{app} = $k_1 S/2\varepsilon$, summarized in Table 3-1. These values were converted to second-order rate constants, k_1, using ε = 8800 cm^{-1}M^{-1} and S = 64 cm^{-1}. The similarity of the values in Table 3-1 clearly shows that the dynamics for the decay of the benzyl radical remains essentially constant as a function of loading level.

Table 3-1. Second-order rate constants for the fast decay of the benzyl radical in NaY as a function of substrate concentration obtained over 16 µs.

Loading $<S>$	k_{app} / 10^6 s^{-1}	k_1 / 10^9 M^{-1}s^{-1}
1/100	too weak	too weak
1/10	8.4 ± 0.4	2.3
1/5	6.4 ± 0.2	1.8
1/2	6.3 ± 0.1	1.7
1/1	6.2 ± 0.1	1.7
2/1	6.7 ± 0.1	1.8

The diffuse reflectance spectra generated upon 266 nm laser irradiation of phenylacetic acid ($<S>$ = 1/2) included in the five alkali-metal cation zeolites under vacuum (10^{-4} torr) conditions are shown in Figure 3-10. In each case, the transient spectrum immediately after the laser pulse is dominated by an intense absorption at 315

nm. Inclusion of oxygen into the zeolite samples quenched the 315 nm band. Thus, for the same reasons as outlined above, the transient species responsible for the 315 nm absorption band can be identified as the benzyl radical. The insets in Figure 3-10 also show that the benzyl radical (315 nm band) is quite long-lived in these zeolites. For example, at least 30% of the original radical signal remains as residual absorption at long time scales.

The decay kinetics at 315 nm for the benzyl radical in NaY and CsY over a time period of 16 μs after the laser pulse are shown in Figure 3-11. Qualitatively, the plot obtained at the faster time scale demonstrates that the decay of the benzyl radical is distinctly faster in NaY than in CsY. This suggests that the benzyl radical decays in a fast manner by a coupling reaction with a second benzyl radical and that the mobility decreases slightly as the size of the counterion increases. In addition, as shown in Figure 3-12, which displays the decay of the benzyl radical over a longer time-period of 400 μs, the end absorption which indicates the number of radicals remaining after the fast decay, is significantly greater in CsY than in NaY. Thus, there seems to be two major types of reactive radicals in alkali-metal exchanged Y zeolites: slow-decaying radicals generated within local domains where diffusion is restricted and inefficient, and fast-decaying radicals generated in open void spaces that are sufficiently mobile to cavity-jump into neighboring cavities.

The transient decay kinetics obtained by combining several different time-scales ranging from 2 μs to 800 μs are shown in Figure 3-13. Examination of the kinetic traces in this Figure reveals that the decay-profile in all the zeolites follows very similar behaviour. The decay rate constants for the reactivity of the benzyl radical were analyzed by using the double second-order expression described above, eq 3.13, with the endpoint calculated from the fit. The results from these calculations are summarized in Table 3-2. The data reveal no distinct trend regarding the effect of zeolite composition on the coupling of the benzyl radical. In fact, the results suggest that the benzyl radical decays in a second-order manner with an apparent rate constant for the fast compound of around $3 \times 10^9 \ M^{-1} \ s^{-1}$ in all of the zeolites. For the slow component, the apparent rate constant

appears to decrease slightly upon going from NaY to RbY, but the rate constants are all similar at around 1×10^8 M^{-1} s^{-1}. In CsY, the slow apparent rate constant was considerably smaller at 0.12×10^8 M^{-1} s^{-1}. However, this latter result is misleading as the fitting program calculated the end Δ J/J_0 to be close to zero which significantly decreases the calculated rate constant of the second component.

Table 3-2. Second-order rate constants for the decay of the benzyl radical in MY as a function of zeolite counterion.

Zeolite	k_1 / 10^9 M^{-1} s^{-1}	k_2 / 10^8 M^{-1} s^{-1}	end Δ J / J_0
LiY	1.8 ± 0.1	1.4 ± 0.1	0.016
NaY	4.5 ± 0.5	2.5 ± 0.2	0.010
KY	5.8 ± 0.9	3.0 ± 0.2	0.007
RbY	3.2 ± 0.2	1.2 ± 0.1	0.007
CsY	2.1 ± 0.1	0.12 ± 0.07	0.002

On the other hand, significant differences are observed with respect to the relative contribution of the fast component and the slow component and the end absorption in the different zeolites. As shown in Table 3.3, the contribution of the fast component to the overall decay of the benzyl radical is highest when the counterion is Li^+ and smallest when the counterion is Cs^+. At the same time, the contribution due to the slow component increases considerably upon going from Li^+ to Cs^+ exchanged Y zeolites. Such a change in relative contribution clearly indicates that the counterion has an effect on the combined lifetime of the benzyl radical such that the lifetime increases as the size of the counterion increases.

Table 3-3. Contributions of the second-order and non-decaying components for the decay of the benzyl radical in MY as a function of zeolite counterion.

Zeolite	% contribution of fast component	% contribution of slow component	% contribution of end $\Delta J / J_o$
LiY	61	20	19
NaY	46	31	23
KY	43	40	17
RbY	50	35	15
CsY	44	53	3

Incorporation of oxygen into MY zeolites containing less than one molecule of phenylacetic acid in every two cavities ($<S> \leq 1/2$) led to complete quenching of the benzyl radical. On the other hand, the amount of quenching by oxygen of the 315 nm band in a highly concentrated ($<S> = 3/2$) zeolite sample is not complete as illustrated in Figure 3-14. Of particular interest is the fact that the inability of oxygen to quench the radical is highly dependent on the nature of the alkali metal cation. For example, the maximum intensity of the benzyl radical in LiY under vacuum conditions is 2 times greater than the maximum intensity in the same zeolite under oxygen conditions, whereas intensities of the benzyl radical in CsY under both vacuum and oxygen conditions are essentially identical. These results clearly show that the mobility of oxygen within the zeolite framework is strongly dependent on the free void space associated with the zeolite.

3.3.3. Benzyl anion

All of the results described so far refer to the dominant 315 nm band observed upon laser irradiation of phenylacetic acid in the MY zeolites. However, a second weaker absorption band at 350 nm is clearly observed in the transient spectrum upon 266 nm photolysis of phenylacetic acid in NaY, Figure 3-2. The decay rate constant for this 350 nm band, 5×10^5 s^{-1}, is significantly faster than the decay of the radical at 315 nm,

indicating that the species responsible for this absorption is not the benzyl radical. The 350 nm band is completely quenched by oxygen, indicating that the transient is not due to a carbocation or radical cation intermediate.

The transient responsible for the absorption at 350 nm is assigned to the benzyl anion generated upon laser photolysis of phenylacetate on the basis of the following information, eq. 3.14. The benzyl anion is known to be a photoproduct upon photolysis of phenylacetate in polar environments.[278-281] The benzyl anion is also known to have a strong absorption in the 350 nm region and to be rapidly quenched by oxygen.[294-296] In addition, the second major product generated upon steady-state photolysis of phenylacetic acid within NaY in the absence of oxygen is toluene, which is the product expected from the benzyl anion (*vide infra*).

$$3.14$$
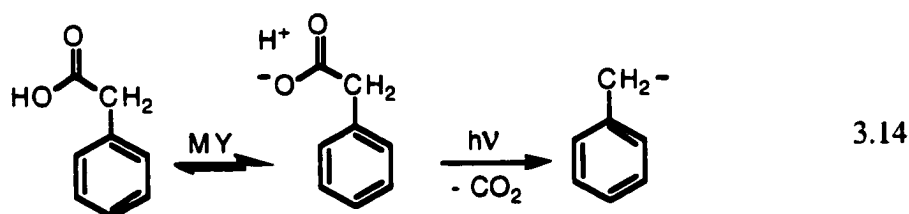
Our initial interest in the 350 nm band originated from observations that the 350 nm band seemed to increase in intensity under conditions where the zeolite samples were not flame-sealed, but instead were sealed by a stopcock assembly, Figure 3-15. These types of seals are not sufficiently tight and allow water from the atmosphere to be incorporated into the sample, thus changing the conditions within the zeolite cavities. The effect of water was even more dramatic when a zeolite sample was purposely hydrated by exposure to the atmosphere for 10 seconds, and then evacuated under reduced pressure to remove oxygen, Figure 3-16. Under these conditions, the intensity of the 350 nm band increased to the point where it almost matched the intensity of the benzyl radical signal at 315 nm.

Representative spectra obtained after laser irradiation of phenylacetic acid included in all of the alkali-metal cation zeolites under evacuated, hydrated conditions are shown in Figure 3-17. The spectra obtained in LiY, NaY and KY clearly show the

presence of the absorption band at 350 nm due to the benzyl anion, in addition to the 315 nm band of the benzyl radical. In contrast to the spectra obtained under dry conditions, Figure 3-10, the benzyl radical is no longer the dominant absorption band in these zeolites. Although the intensity at 350 nm in the spectra obtained in RbY and CsY is not as intense as the radical band, the transient is more intense than was observed under dry conditions. These results suggest that the ability of the zeolite to generate the benzyl anion from photolysis of phenylacetic acid decreases in the order of LiY to CsY.

While the presence of water clearly has a dramatic effect on the yield of the benzyl anion, the decay at 350 nm was largely unaffected. Thus, the kinetic decay traces shown in "dry" NaY sample, Figure 3-15, and the hydrated NaY, Figure 3-16, are virtually identical. In addition, the decay of the anion was found not to be dependent on the zeolite counterion, Figure 3-18. In each case, the benzyl anion decayed with closely similar kinetics, $k \sim 5 \times 10^5$ s^{-1} in a first-order fashion.

3.3.4. Product studies of steady-state irradiations of phenylacetic acid in NaY

The samples were prepared as outlined in the experimental section using ~ 2 grams of zeolite and appropriate amounts of phenylacetic acid to achieve a loading level of $<S> = 0.3$ to 2 to give a range of loading levels. The zeolite-substrate composite was kept either under vacuum or a nitrogen atmosphere at all times to minimize exposure to the oxygen and water in the atmosphere. The sample was irradiated in a cylindrical pyrex vessel fitted with an apical quartz window. Irradiation was performed using a medium-pressure 450 W mercury lamp passed through a quartz filter. Although the sample was constantly magnetically stirred, clumping was observed to occur; however, occasional manual shaking broke apart the clusters. On average, the photolysis lasted for 10-15 hours. After irradiation each sample was extracted using a continuous-extraction apparatus using dichloromethane for 24-48 hours. Overall, the mass balance recovery ranged between 16-60% depending on experimental conditions and irradiation time. The low yield of recovery is attributed to the strong interaction between the phenylacetate anion and the alkali-metal cations within the zeolite framework thus reducing the amount

of phenylacetic acid recovered. The photochemical conversion was calculated to be 50% of starting materials based on amount of material recovered from the zeolite.

The main products obtained from the steady-state photolysis of phenylacetic acid in nitrogen-purged NaY are 1,2-diphenylethane, benzaldehyde, toluene and 1,2-diphenylethanol, Table 3-4, eq. 3.15.

$$3.15$$

Table 3-4. Relative product yields obtained from steady-state irradiation of phenylacetic acid ($<S> = 1/2$) in nitrogen-saturated NaY.

Product	Rel. % Yield
Toluene	60
Benzaldehyde	10
1,2-Diphenylethane	20
1,2-Diphenylethanol	10

1,2-Diphenylethane (bibenzyl) is the expected coupling-product for the reaction between two benzyl radical species. 1,2-Diphenylethane formation as one of the major isolated products provides good evidence to support the conclusion based on the results from the diffuse reflectance laser experiments that irradiation of phenylacetic acid in the zeolites leads to benzyl radical formation. In addition, close examination of the GC/FID and GC/MS chromatograms obtained upon photolysis of phenylacetic acid in NaY revealed very small GC peaks (<1%) in the vicinity of the 1,2-diphenylethane signal. These peaks had a molecular ion of 182 mass units identical to that of 1,2-diphenylethane suggesting that the GC signals were due to structural isomers of 1,2-diphenylethane.

These compounds made up less than 1 % of the photoproducts and as a result could not be characterized by NMR spectroscopy. Methyl substituted diphenylmethanes, which are structural isomers of 1,2-diphenylethane, have been observed previously upon photolysis of dibenzyl ketone on silica gel and zeolites.[254,270,297] These materials are also derived upon the coupling of two benzyl radicals, but in this case a head-to-tail coupling occurs to give a semibenzene (ortho or para) which then undergoes aromatization to form the more stable 4-methylphenylphenylmethane, or 2-methylphenylphenylmethane, eq. 3.16.

$$3.16$$
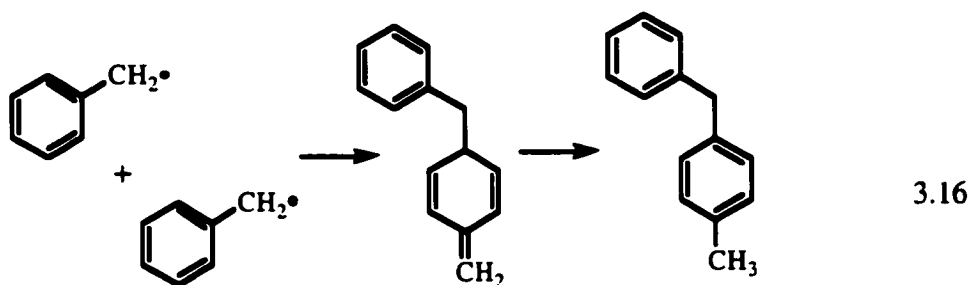
The major monomeric product of photodecarboxylation of phenylacetic acid within zeolites is toluene. This product can potentially arise from either of the two major transients observed in the transient diffuse reflectance studies, the benzyl radical or benzyl anion, Scheme 3-2. The benzyl anion would generate toluene by protonation with the proton either originating from phenylacetic acid or from water that may be present in trace amounts within the zeolite. Alternatively, generating toluene from the benzyl radical requires a suitable hydrogen donor.

Scheme 3-2
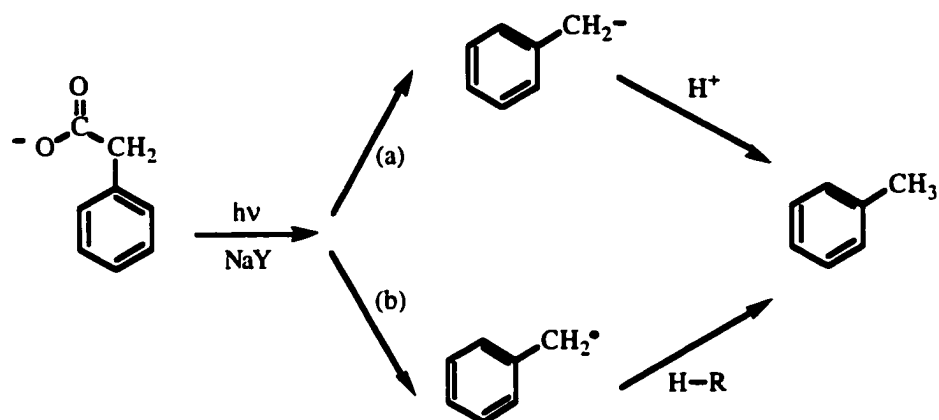
Given the high concentration of phenylacetic acid present within the cavities of the zeolites examined in this work, the most likely source of hydrogen atoms if toluene was being made by hydrogen abstraction would be the benzylic hydrogens of phenylacetic acid. Thus, phenylacetic-α,α-d_2 acid was used to discriminate between the benzyl anion and benzyl radical mechanisms. With this substrate, toluene-α,α,α-d_3 would be the expected product if the radical mechanism is the dominant pathway, while toluene-α,α-d_2 would be generated if the benzyl anion mechanism is being followed. The results upon irradiation of phenylacetic-α,α-d_2 acid in NaY in the absence of oxygen showed that toluene-α-α-d_2 produced by protonation of the benzyl-α,α-d_2 anion was obtained as the major product along with 1,2-diphenylethane-$\alpha,\alpha,\alpha,\alpha$-$d_4$, eq. 3.17. No toluene-$\alpha,\alpha,\alpha$-$d_3$ was observed, indicating that toluene is not generated by reaction of the benzyl radical with the precursor. "Spectator" hydrocarbon molecules have been shown not to participate to a great extent in hydrogen-abstraction reactions with the benzyl radical in zeolites.[298] However, some of the toluene may arise from hydrogen abstraction of the benzyl radical and residual hexane.
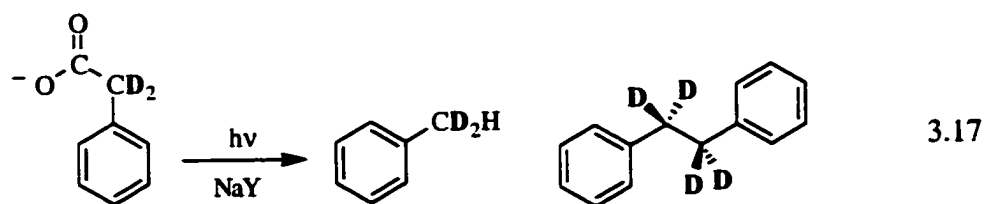
3.17

In addition, when unlabeled phenylacetic acid was photolyzed within nitrogen-saturated NaY in the presence of methanol-d (CH_3OD), the major products obtained were toluene, toluene-α-d, and 1,2-diphenylethane, eq. 3.18. Since the benzyl radical would preferentially abstract a methyl hydrogen rather than the hydroxyl deuterium, the formation of the toluene-α-d provides further evidence for the presence of the benzyl anion.

3.18
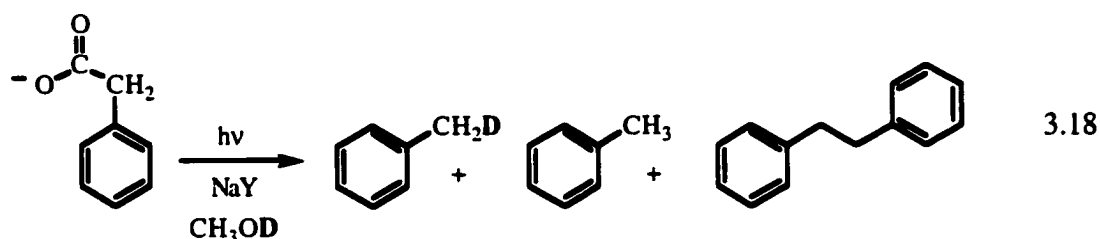
Benzaldehyde is also a significant photoproduct observed upon irradiation of phenylacetic acid in NaY. This product can arise by reaction of both the benzyl radical and the benzyl anion with oxygen, eq. 3.19.

3.19
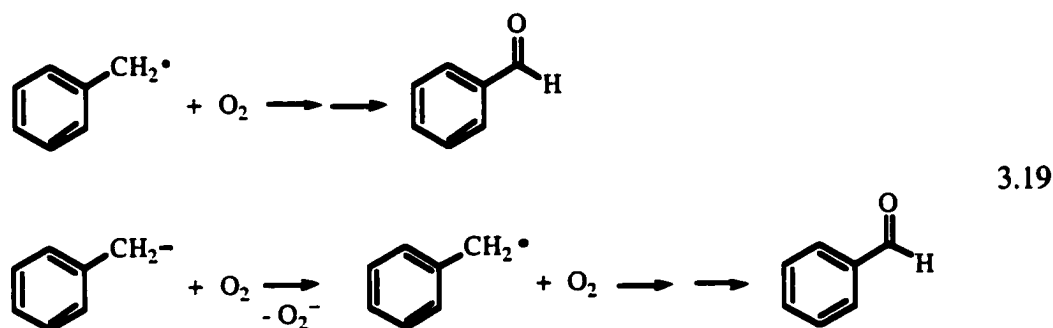
Steady-state irradiation of phenylacetic acid in oxygen-saturated NaY led exclusively to the formation of benzaldehyde thus supporting this conclusion. Most likely a continuous nitrogen flow throughout the photolysis is unable to exclude all oxygen from the internal cavities of the zeolite. The occurrence of tightly framework-bound oxygen in zeolites has been reported previously,[177,252,298] thus the formation of benzaldehyde in the photolysis products is not completely unknown.[165] However, it is also possible that a portion of the benzaldehyde generated may arise from persistent

benzyl radicals which are inaccessible to react with other large molecules during the photolysis but readily react with the smaller oxygen molecule after exposure to the atmosphere.

1,2-diphenylethanol is likely a secondary photolysis product that arises from the reaction of benzaldehyde and toluene,[298,299] eq. 3.20. This reaction is known to take place in zeolites by hydrogen abstraction of the excited carbonyl group and toluene. In addition, at high loading levels the amount of 1,2-diphenylethanol obtained increased significantly to ~ 70% of the total products. An increase in concentration of starting material leads to the formation of greater amounts of primary photolysis products. As a result, there is a greater chance of two of these species further reacting upon secondary photolysis thus increasing the amount of 1,2-diphenylethanol generated.
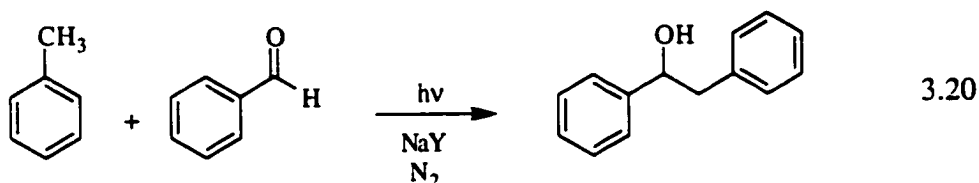
Irradiation of phenylacetic acid in NaY with co-incorporated CH_3OD under conditions where 1,2-diphenylethanol is a dominant product (long irradiation times or high loadings), showed the presence of deuteration in the mass spectrum for this compound. Such a result supports the formation of toluene from a benzyl anion intermediate. The secondary reaction between toluene-α-d and benzaldehyde yields deuterated 1,2-diphenylethanol, whereas a radical pathway would yield only undeuterated 1,2-diphenylethanol.

3.3.5. Cumyl radical in Y zeolites

The examination of the chemistry of the benzyl radical within the Y zeolites has focused on the decay of the radical, especially with respect to the coupling of two benzyl radicals to give 1,2-diphenylethane. This reaction should be sensitive to bulkier groups like methyl groups at the α-position, which would be expected to slow the coupling

process and increase the lifetimes of the radicals. To examine this possibility, the cumyl radical was generated by photolysis of 2-methyl-2-phenylpropanoic acid (cumyl-carboxylic acid) in the alkali-metal cation exchanged Y zeolites.

The transient diffuse reflectance spectra generated upon 266 nm laser irradiation of cumylcarboxylic in all of the alkali-metal cation exchanged zeolites are shown in Figure 3-19. The spectra are dominated by a sharp absorption band at 320 nm that matches nicely with the known absorption maximum of the cumyl radical generated previously in solution. The 320 nm band is also quenched by oxygen in each of the zeolites (insets). These observations identify the 320 nm band generated by irradiation of cumylcarboxylic acid as the cumyl radical.

Figure 3-20 shows the decay of the cumyl radical in all of the zeolites, and clearly indicates that the radical barely decays over the first 16 μs after the laser pulse. This is in sharp contrast to the benzyl radical, which decays noticeably over the same time scale. As observed in the stretched decay traces, obtained by combining several decay traces over 2 μs to 800 μs, some decay of the cumyl radical is observed over longer time scales, Figure 3-21. Analysis of these decays using eq. 3.13 double second-order fit leads to the rate constants listed in Table 3-5. These data show that the decay of the cumyl radical is fastest in LiY and NaY and slowest for KY, RbY and CsY. Although the rate constants in the latter zeolites are very similar in value, KY has a lower residual absorbance than the RbY and CsY which indicates that a greater portion of generated cumyl radicals are able to decay by fast processes, Table 3-6.

Table 3-5   Second-order rate constants for the decay of the cumyl radical in MY as a function of zeolite counterion.

Zeolite	$k_1 / 10^9 \, M^{-1} \, s^{-1}$	$k_2 / 10^7 \, M^{-1} \, s^{-1}$	end $\Delta \, J/J_0$
LiY	7.4	7.4	.014
NaY	4.6	2.2	0.009
KY	0.74	0.7	0.00
RbY	0.55	1.2	0.02
CsY	1.0	0.50	0.00

Table 3-6.   Contributions of the second-order rate constants and non-decaying component for the decay of the cumyl radical in MY as a function of zeolite counterion.

Zeolite	% contribution of fast component	% contribution of slow component	% contribution of end $\Delta \, J/J_0$.
LiY	24.7	40	35.3
NaY	31.7	50.2	18.1
KY	38.3	61.7	0
RbY	22.9	27.1	50.0
CsY	34.6	65.4	0

Product studies for the photolysis of cumylcarboxylic acid in NaY were also performed. The preparation procedure for the steady-state irradiation was as described in the experimental section. Mass balance recovery was ~ 58% and the photochemical conversion after 5 hrs of irradiation was ~ 37 % based on compounds recovered.

The products generated upon irradiation of cumylcarboxylic acid incorporated in NaY under a continuous nitrogen-flow were acetophenone, cumene and 2,3-diphenyl-3-methyl-2-butanol, eq. 3.21, Table 3-7.

3.21
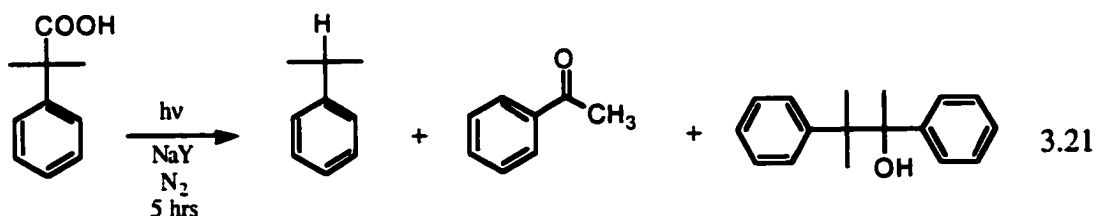
Noticeably absent was any evidence for the formation of 2,3-dimethyl-2,3-diphenylbutane, or bicumene, which is the product that would have been observed upon coupling of two cumyl radicals. The absence of bicumene suggests that the main decay pathway followed by the cumyl radical is not radical-radical coupling.

Acetophenone, the major product representing about 60% of the total product mixture, presumably arises from reaction of the cumyl radical with oxygen that remained in the zeolite after evacuation, or that was introduced after exposure of the zeolite to atmosphere after photolysis. Cumene is also present in the product mixture in a 30% yield. The amount of cumene and acetophenone decreases slightly with increasing loading level of precursor cumylcarboxylic acid with a joint increase of the 2,3-diphenyl-3-methyl-2-butanol. As before, the 2,3-diphenyl-3-methyl-2-butanol is presumed to be formed by secondary photolysis of acetophenone in the presence of cumene.
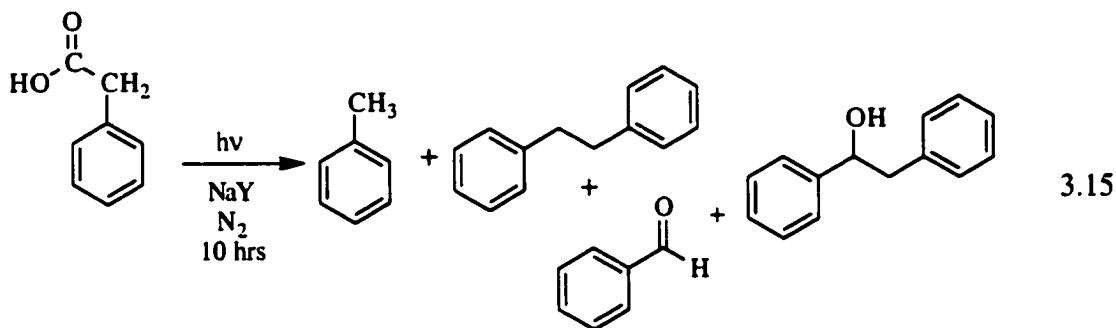
Table 3-7. Relative product yields obtained from steady-state irradiation of cumylcarboxylic acid ($<S> = 1/2$) in nitrogen-saturated NaY.

Product	Rel. % Yield
Cumene	30
Acetophenone	61
2,3-diphenyl-3-methyl-2-butanol	9

Clearly, the steady-state photolysis results indicate that although the cumyl radical is generated, increased steric factors introduced by the methyl groups at the carbon-radical center prevent radical-radical coupling of two cumyl radicals within the confined space of zeolites. Similar steric effects have been observed with 2,4-diphenylpentan-3-one in ZSM-5, which generates the phenylethyl radical.[266] In this system, olefin formation is observed to be an alternate radical reaction pathway. A total of five steady-state photolysis of cumylcarboxylic acid in NaY zeolites under high and low occupancy levels were performed. In only one of the GC and GC/MS of the extracted solutions did

a peak corresponding to the α-methylstyrene, generated by H-abstraction reaction between two cumyl radicals, was detected. However, during the 24-48 hr continuous-extraction procedure, some solvent evaporation often occurred so evaporation of the volatile α-methylstyrene is plausible. Alternatively, oxidation of α-methylstyrene may be the source of the acetophenone product. Further experiments on this system were not performed.
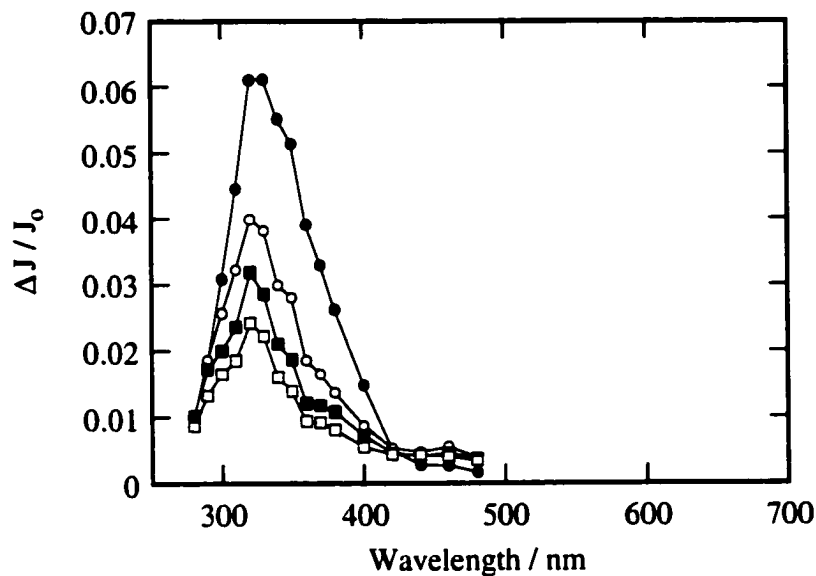
Figure 3-1. Transient diffuse reflectance spectrum obtained upon 266 nm photolysis of dibenzyl ketone in NaY under dry vacuum (10^{-4} torr) conditions. Spectra were recorded (●) 0.24 µs, (O) 0.78 µs, (■), 1.80 µs, and (□) 6.40 µs after the laser pulse.
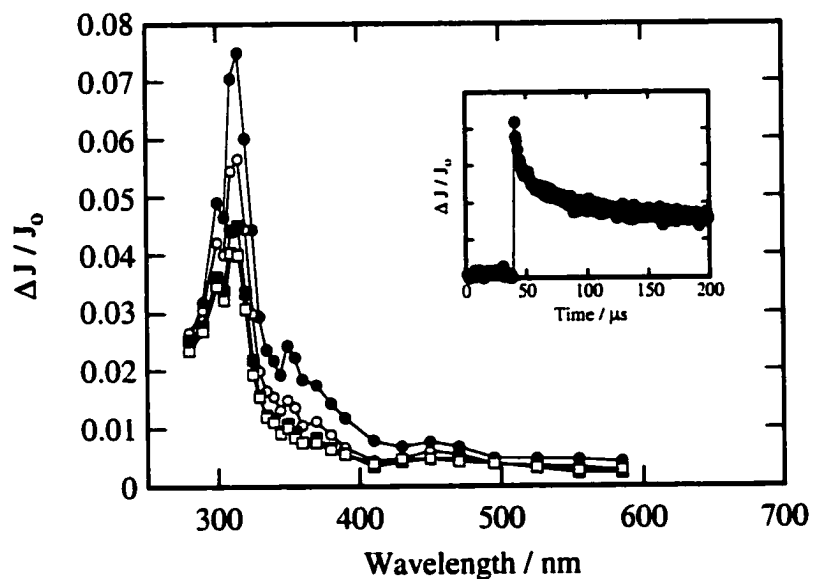
Figure 3-2. Transient diffuse reflectance spectrum generated upon 266 nm laser photolysis of phenylacetic acid, <S> = 1/2, in evacuated (sealed cell; 10^{-4} torr) NaY under dry conditions. Spectra were recorded (●) 0.68 µs, (O) 2.96 µs, (■), 7.60 µs, and (□) 12.80 µs after the laser pulse. The inset shows the decay trace at 315 nm for the benzyl radical.
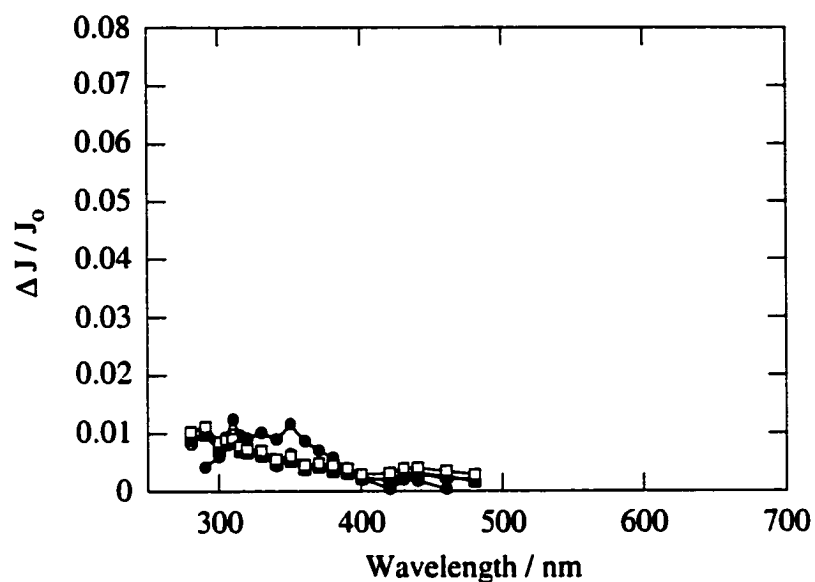
Figure 3-3. Transient diffuse reflectance spectrum generated upon 266 nm laser photolysis of phenylacetic acid, <S> = 1/2, in oxygen-saturated NaY under dry conditions. Spectra were recorded (●) 0.24 µs, (O) 0.80 µs, (■) 3.80 µs, and (□) 12.80 µs after the laser pulse.
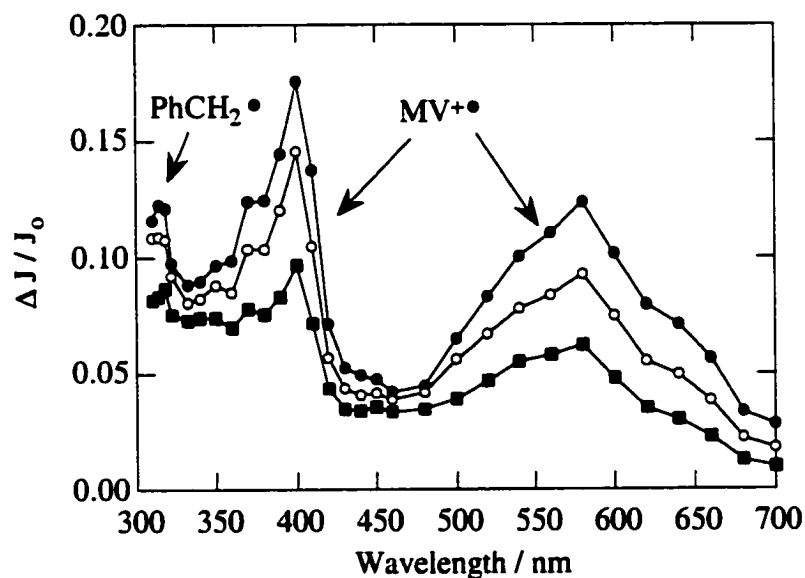
Figure 3-4. Diffuse reflectance spectrum obtained upon 308 nm laser irradiation of methyl viologen (MV^{2+}) and phenylacetic acid incorporated into NaY under vacuum (10^{-4} torr) conditions. Spectra were recorded (●) 0.44 µs, (O) 1.16 µs, (■) 3.12 µs after the laser pulse.
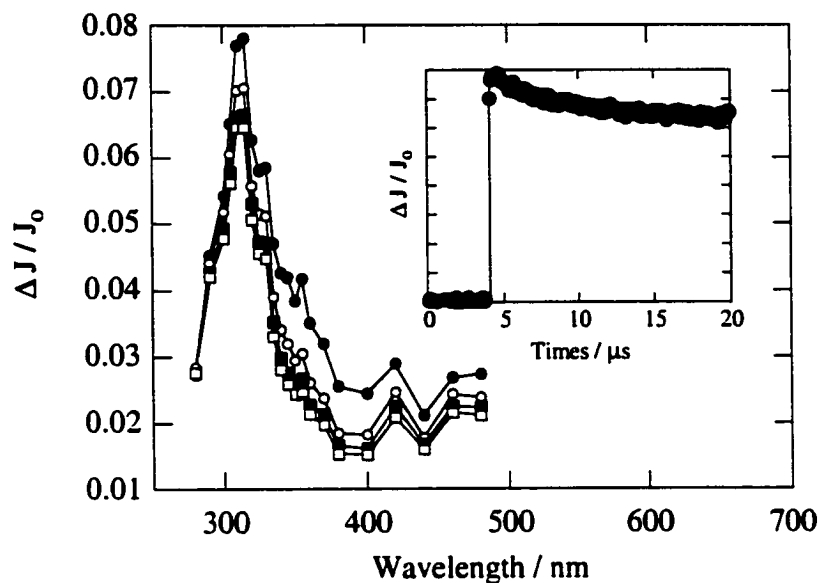
Figure 3-5. Transient diffuse reflectance spectrum generated upon 266 nm laser photolysis of tetrabutylammonium phenylacetate, <S> = 1/2, in evacuated (sealed cell; 10^{-4} torr) NaY under dry conditions. Spectra were recorded (●) 0.68 μs, (○) 3.48 μs, (■), 7.68 μs, and (□) 12.9 μs after the laser pulse. The inset shows the decay trace at 315 nm for the benzyl radical.
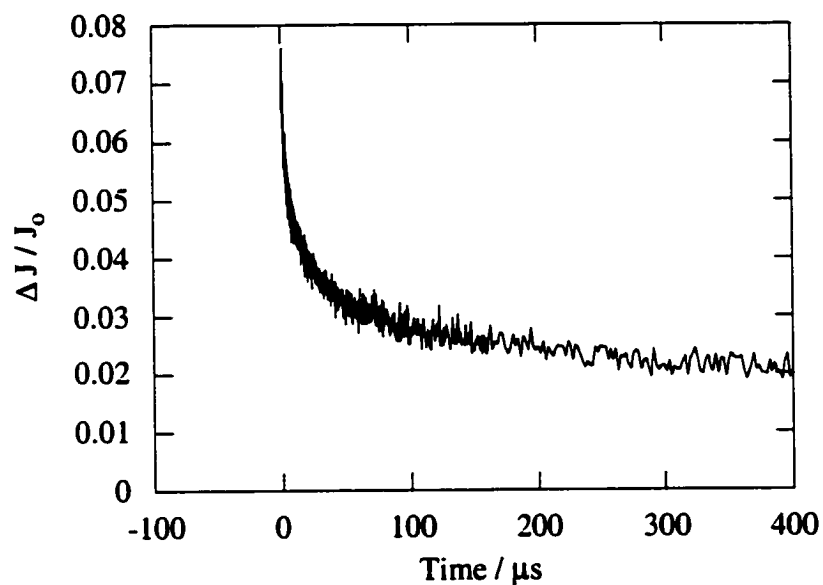
Figure 3-6. Time resolved changes, $\Delta J/J_o$, at 315 nm obtained upon 266 nm laser irradiation of phenylacetic acid incorporated into NaY under vacuum (10^{-4} torr).
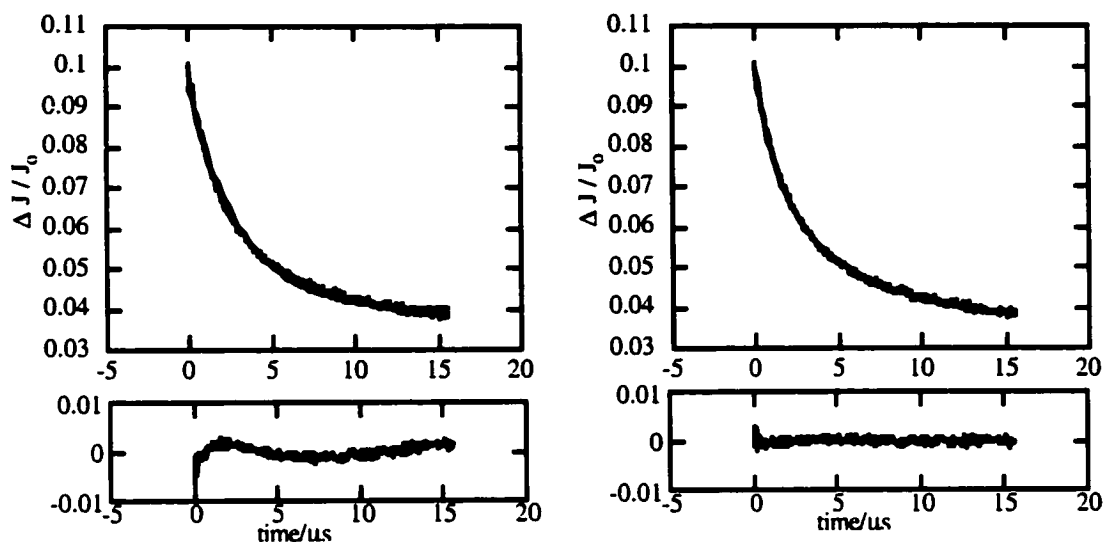
Figure 3-7. Time resolved changes, $\Delta J/J_o$, at 315 nm obtained over 15 μs after 266 nm laser irradiation of phenylacetic acid incorporated into NaY under vacuum. The line-of-best-fit in (a) was obtained using a first-order expression. The line-of-best-fit in (b) was obtained using a second-order expression. The residual plots represent the difference between calculated data using the line-of-best-fit and the experimental data.
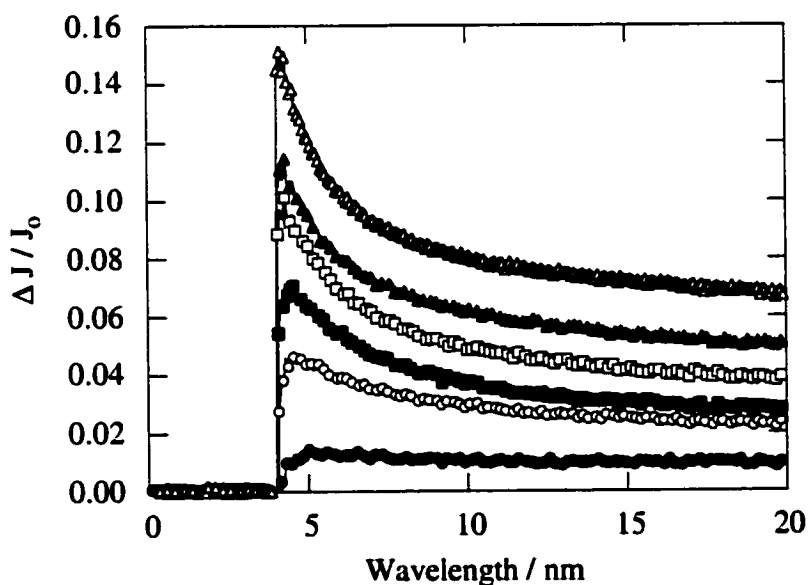
Figure 3-8. Transient decay traces at 315 nm for the benzyl radical generated upon 266 nm laser excitation of phenylacetic acid in dry evacuated (sealed cells; 10^{-4} torr) NaY with loading levels (<S>) of (●) 1/100, (O) 1/10, (■), 1/5, (□) 1/2, (▲) 1/1 and (△) 2/1.
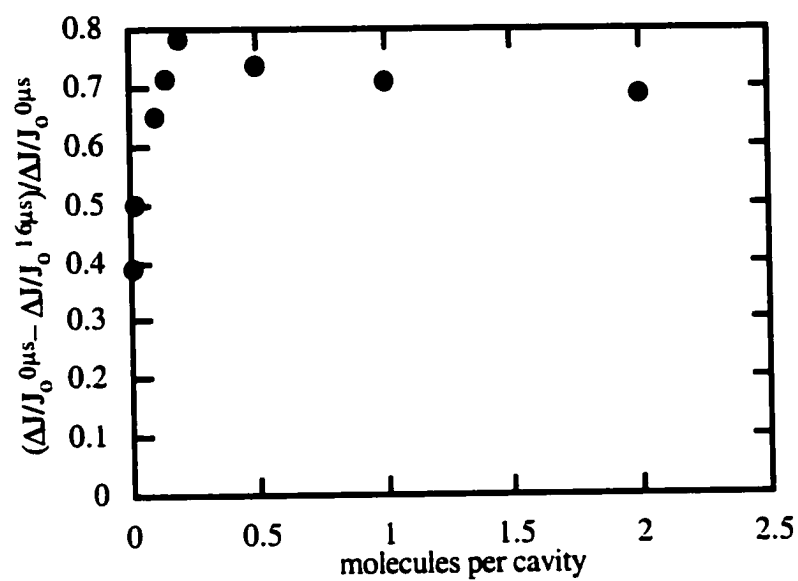
Figure 3-9. Relative amount of fast-decaying benzyl radicals generated in NaY upon 266 nm photolysis of phenylacetic acid as a function of phenylacetic acid loading level.
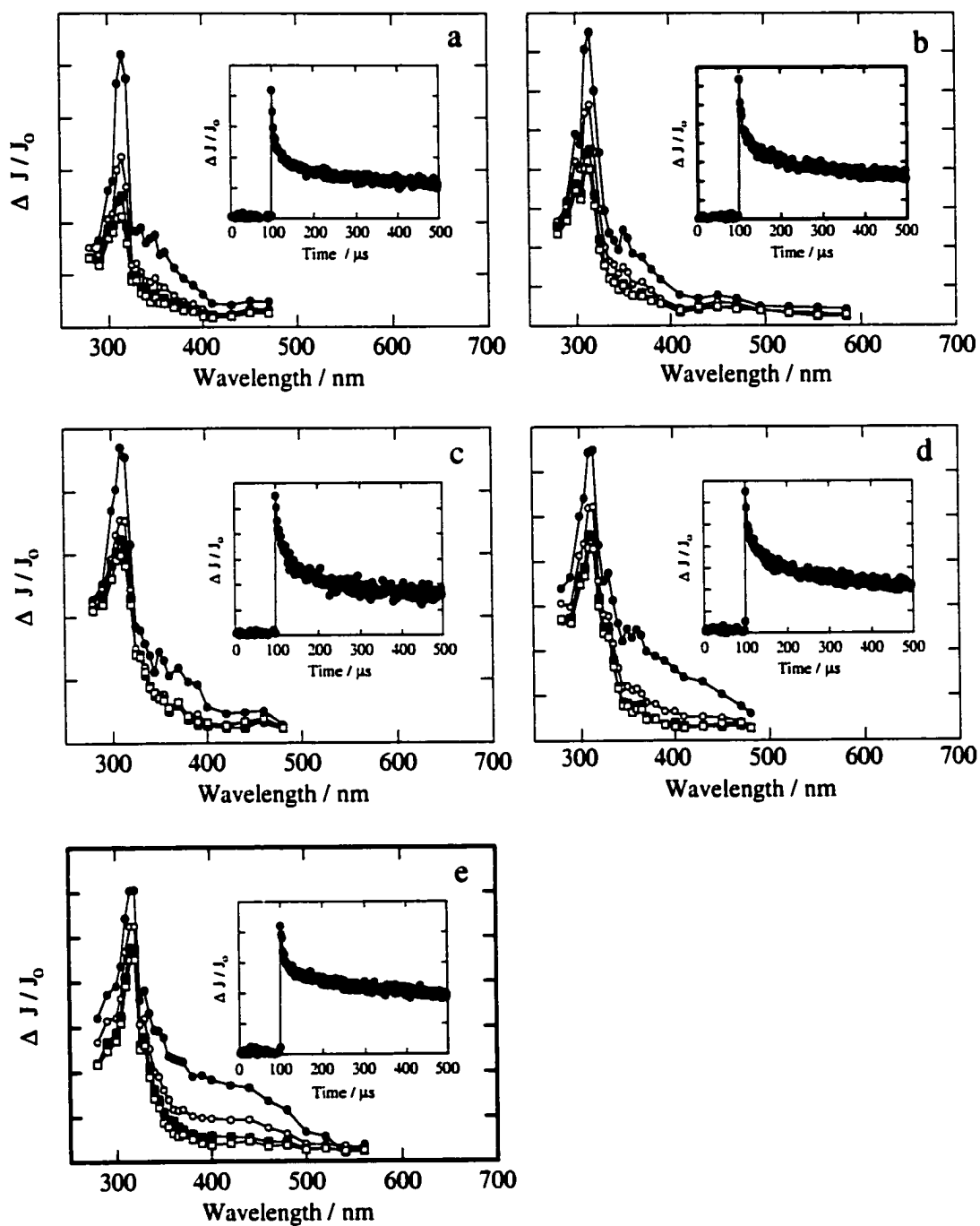
Figure 3-10. Transient diffuse reflectance spectrum generated (●) 0.56 μs, (○) 3.76 μs, (■) 7.52 μs and (□) 12.7 μs after 266 nm photolysis of phenylacetic acid under vacuum (sealed cell; 10^{-4} torr) in (a) LiY, (b) NaY, (c) KY, (d) RbY and (e) CsY. Inset shows decay trace monitored at 315 nm.
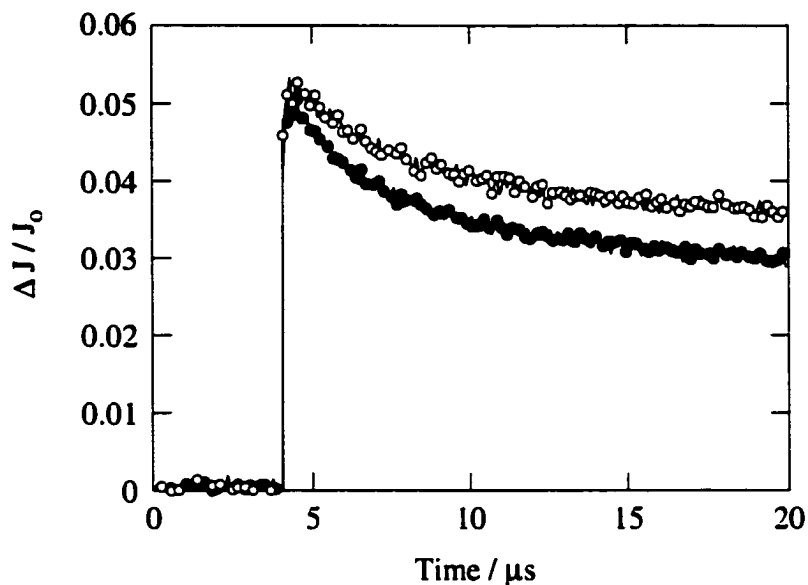
Figure 3-11. Transient decay traces at 315 nm for the benzyl radical generated upon 266 nm laser excitation of phenylacetic acid in dry evacuated (sealed cells; 10^{-4} torr) (●) NaY and (O) CsY over 16 μs.
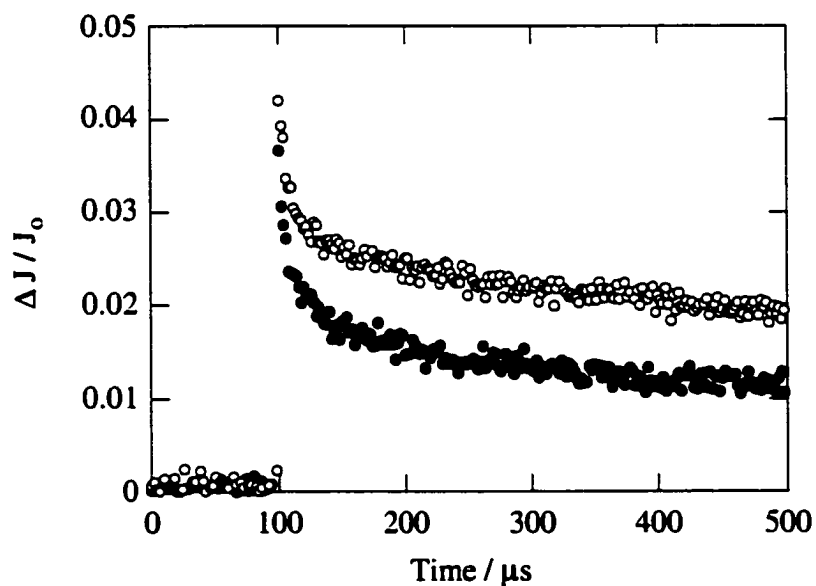
Figure 3-12. Transient decay traces at 315 nm for the benzyl radical generated upon 266 nm laser excitation of phenylacetic acid in dry evacuated (sealed cells; 10^{-4} torr) (●) NaY and (O) CsY over 400 μs.
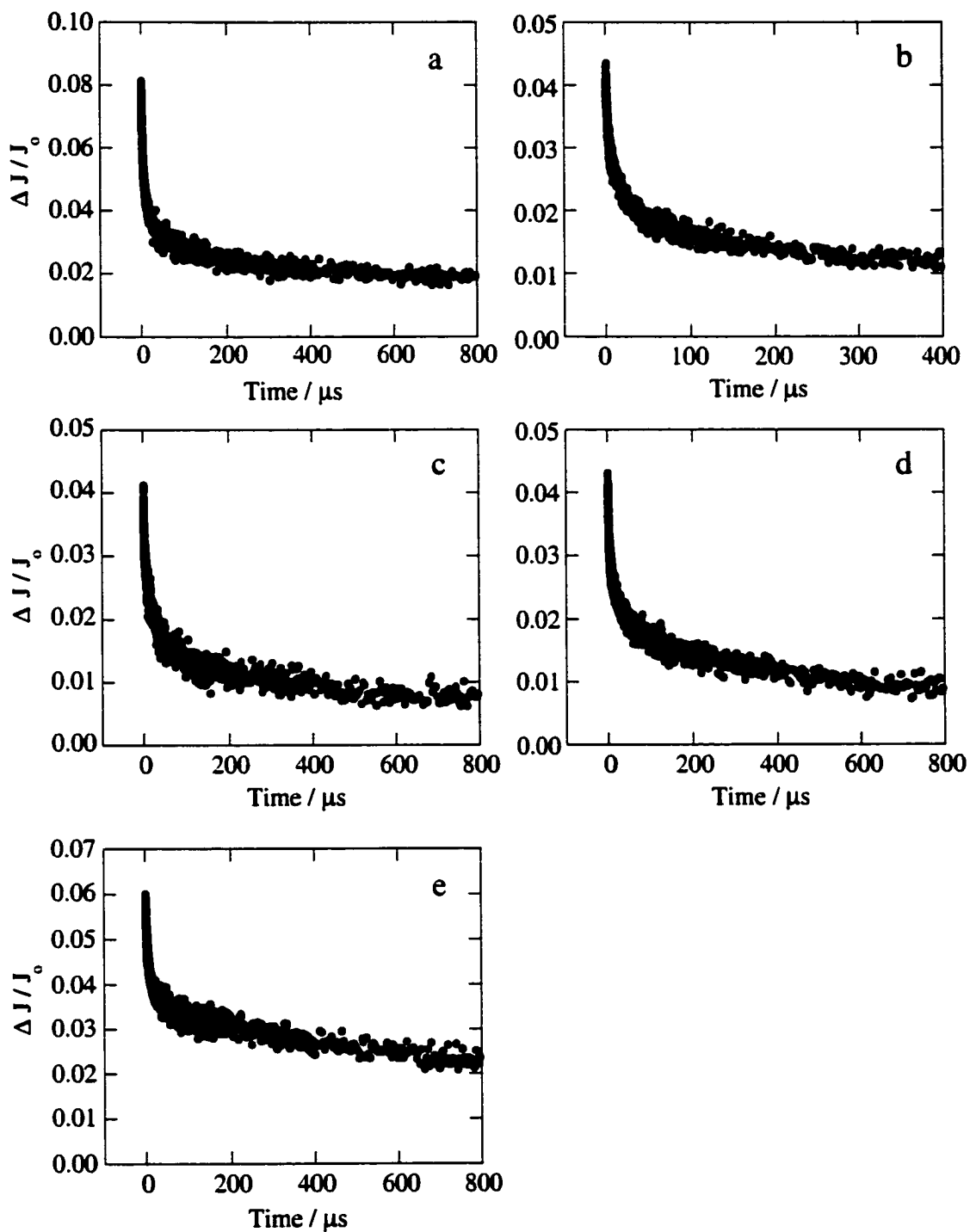
Figure 3-13. Time resolved changes in $\Delta J/J_0$ at 315 nm obtained upon 266 nm laser irradiation of phenylacetic acid incorporated in (a) LiY, (b) NaY, (c) KY, (d) RbY and (e) CsY.
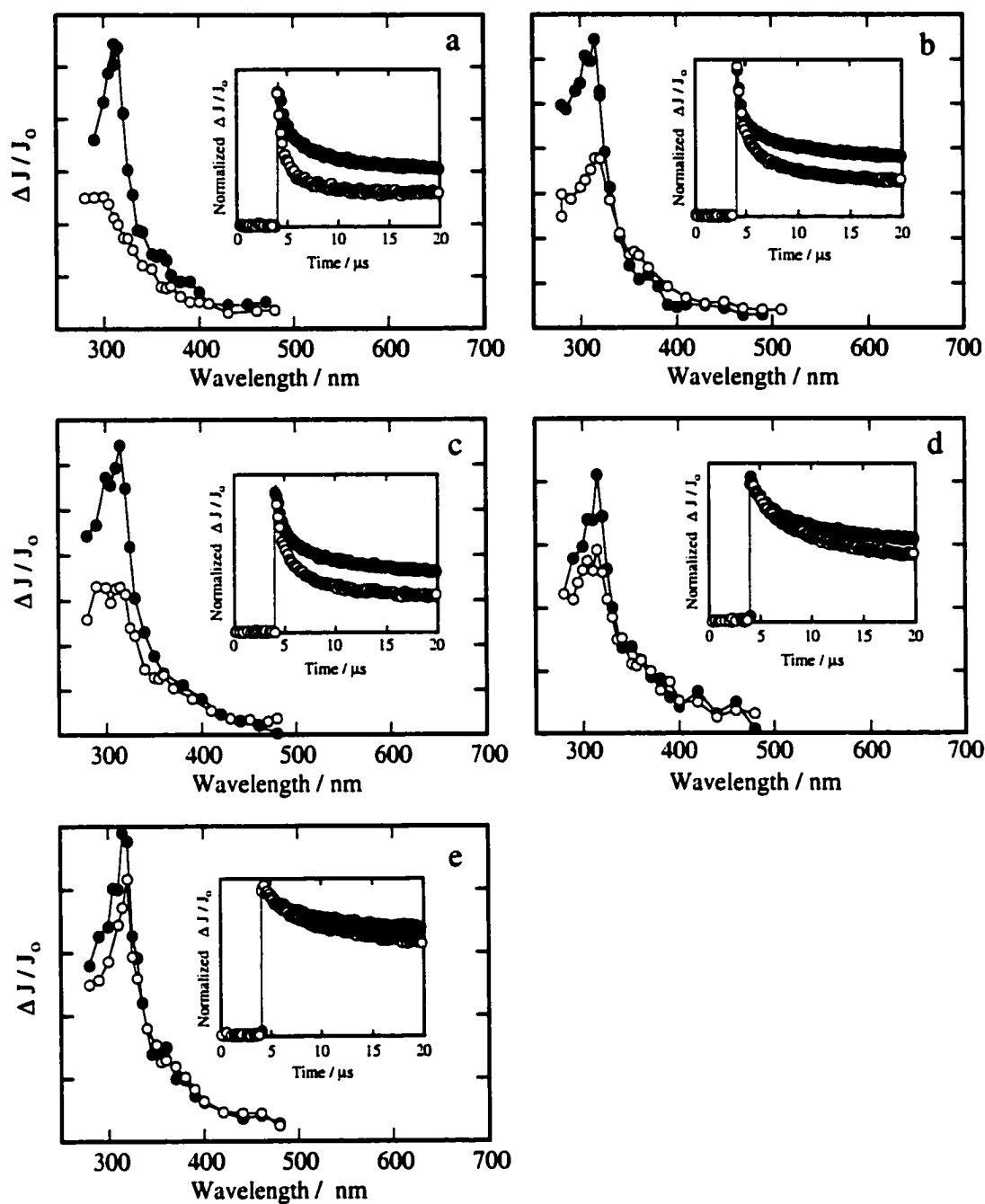
Figure 3-14. Transient diffuse reflectance spectra upon 266 nm excitation of phenylacetic acid (<S> = 3/2) in (a) LiY, (b), NaY, (c) KY, (d) RbY, and (e) CsY under (●) vacuum and (O) oxygen conditions. Spectra were recorded 6.40 µs after the laser pulse. Inset shows the decay kinetics for the 315 nm band over 16 µs under (●) vacuum and (O) oxygen conditions.
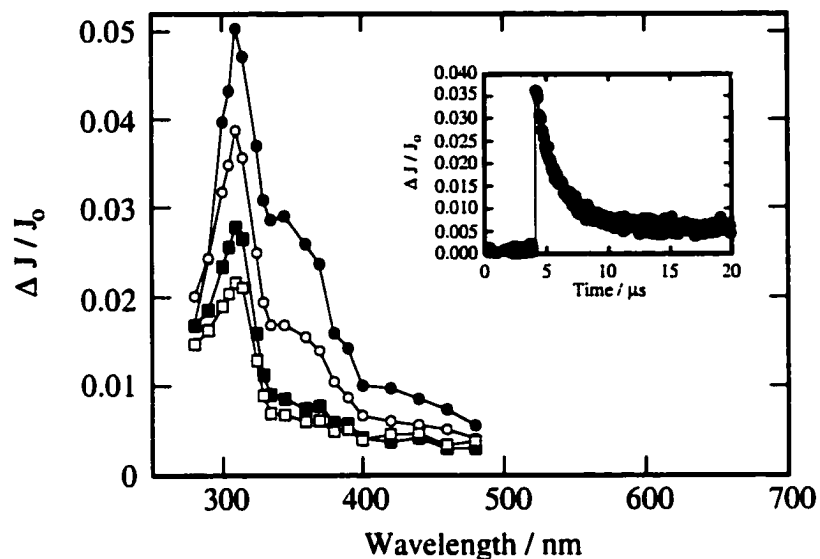
Figure 3-15. Transient diffuse reflectance spectrum generated upon 266 nm laser photolysis of phenylacetic acid, <S> = 1/2, in evacuated (not sealed cell; 10^{-4} torr) NaY. The inset shows the decay trace at 350 nm.
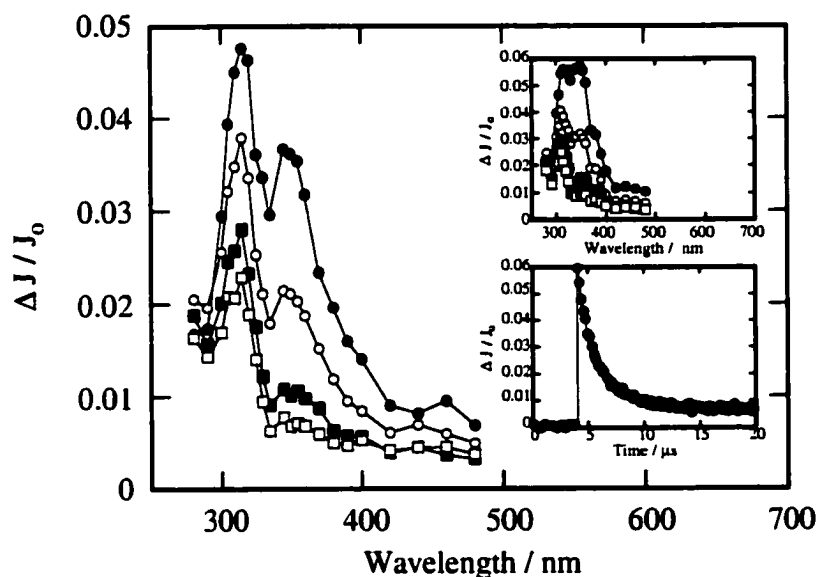
Figure 3-16. Transient diffuse reflectance spectrum generated upon 266 nm laser photolysis of phenylacetic acid, <S> = 1/2, in evacuated (not sealed cell; 10^{-4} torr) NaY after the sample was exposed to the atmosphere for a period of 10 seconds and then re-evacuated. Inset shows the transient spectrum after further atmospheric exposure and re-evacuation and the corresponding decay trace at 350 nm.
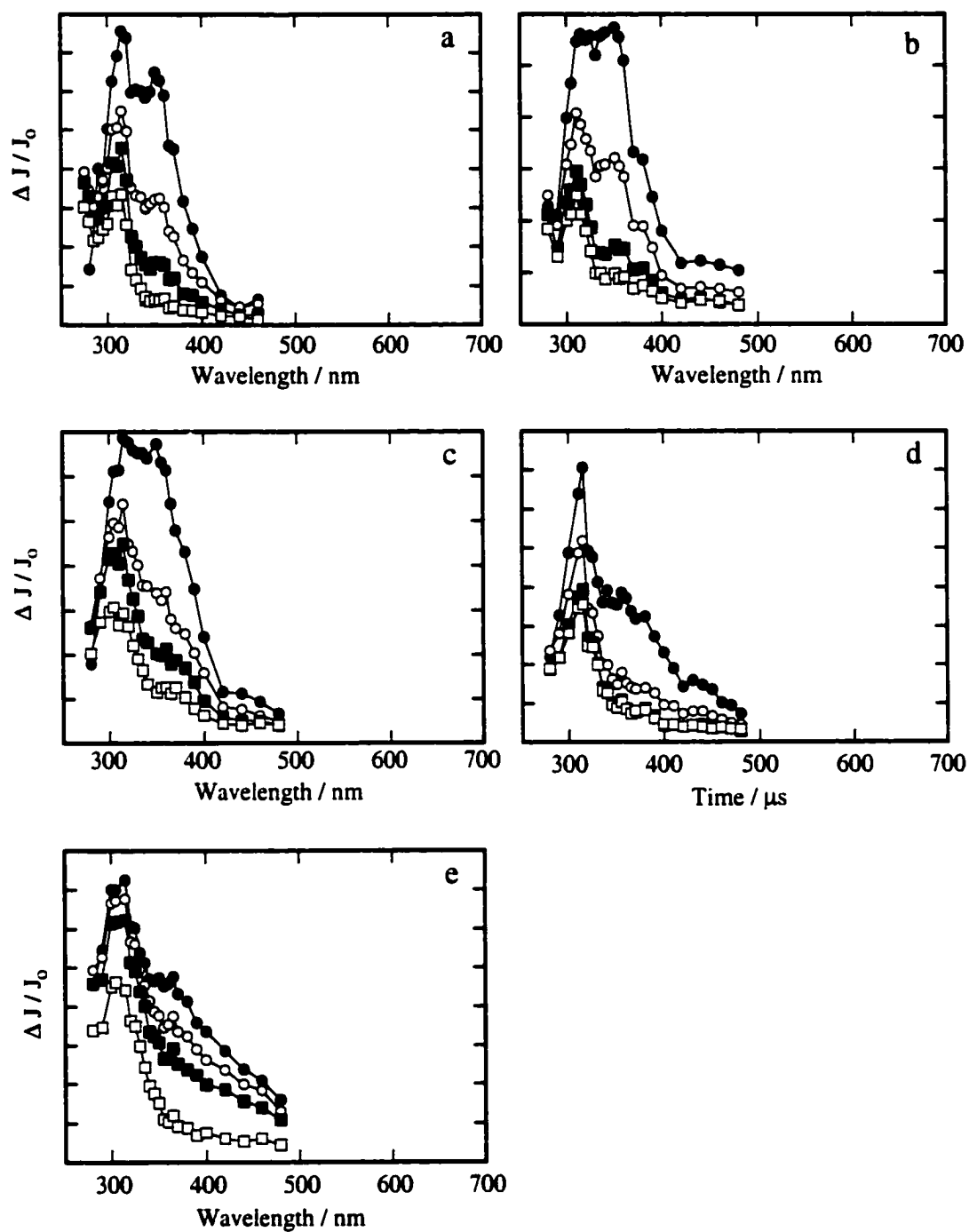
Figure 3-17. Transient diffuse reflectance spectrum generated (●) 0.36 μs, (○) 0.92 μs, (■) 1.72 μs and (□) 12.9 μs after 266 nm photolysis of phenylacetic acid under vacuum $(10^{-4}$ torr) in partially hydrated (a) LiY, (b) NaY, (c) KY, (d) RbY and (e) CsY.
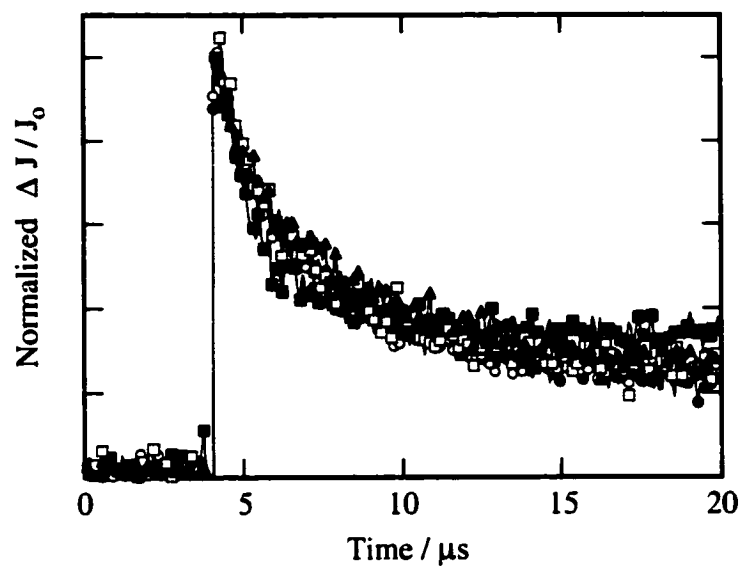
Figure 3-18. Transient decay traces at 350 nm for the benzyl anion generated upon 266 nm laser excitation of phenylacetic acid in partially hydrated and evacuated (sealed cells; 10^{-4} torr) (●) LiY, (O) NaY, (■) KY, (□) RbY and (▲) CsY over 16 μs.

Figure 3-19. Transient diffuse reflectance spectrum generated (●) 2.00 μs, (○) 6.56 μs, and (■) 12.8 μs after 266 nm photolysis of cumylcarboxylic acid under vacuum (10^{-4} torr) in (a) LiY, (b) NaY, (c) KY, (d) RbY and (e) CsY. Insets show the spectra under oxygen conditions.
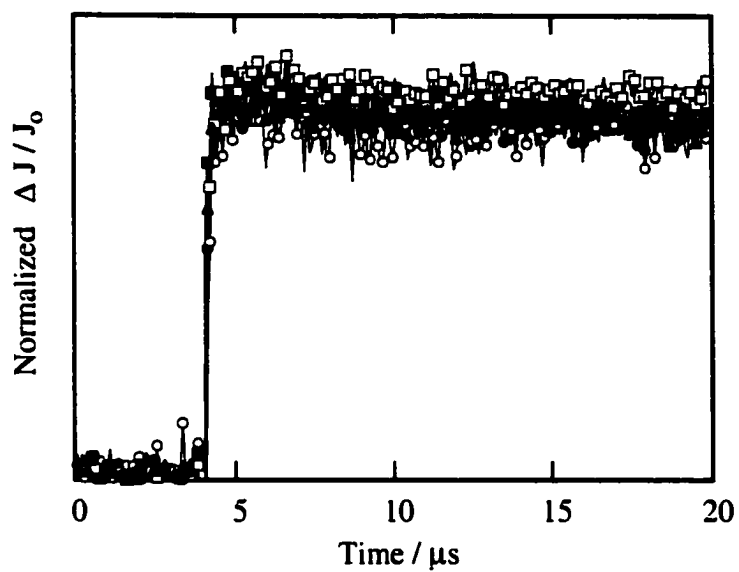
Figure 3-20. Transient decay traces at 320 nm for the cumyl radical generated upon 266 nm laser excitation of cumylcarboxylic acid in dry evacuated (10^{-4} torr) (●) LiY, (○) NaY, (■) KY, (□) RbY and (▲) CsY over 16 μs.
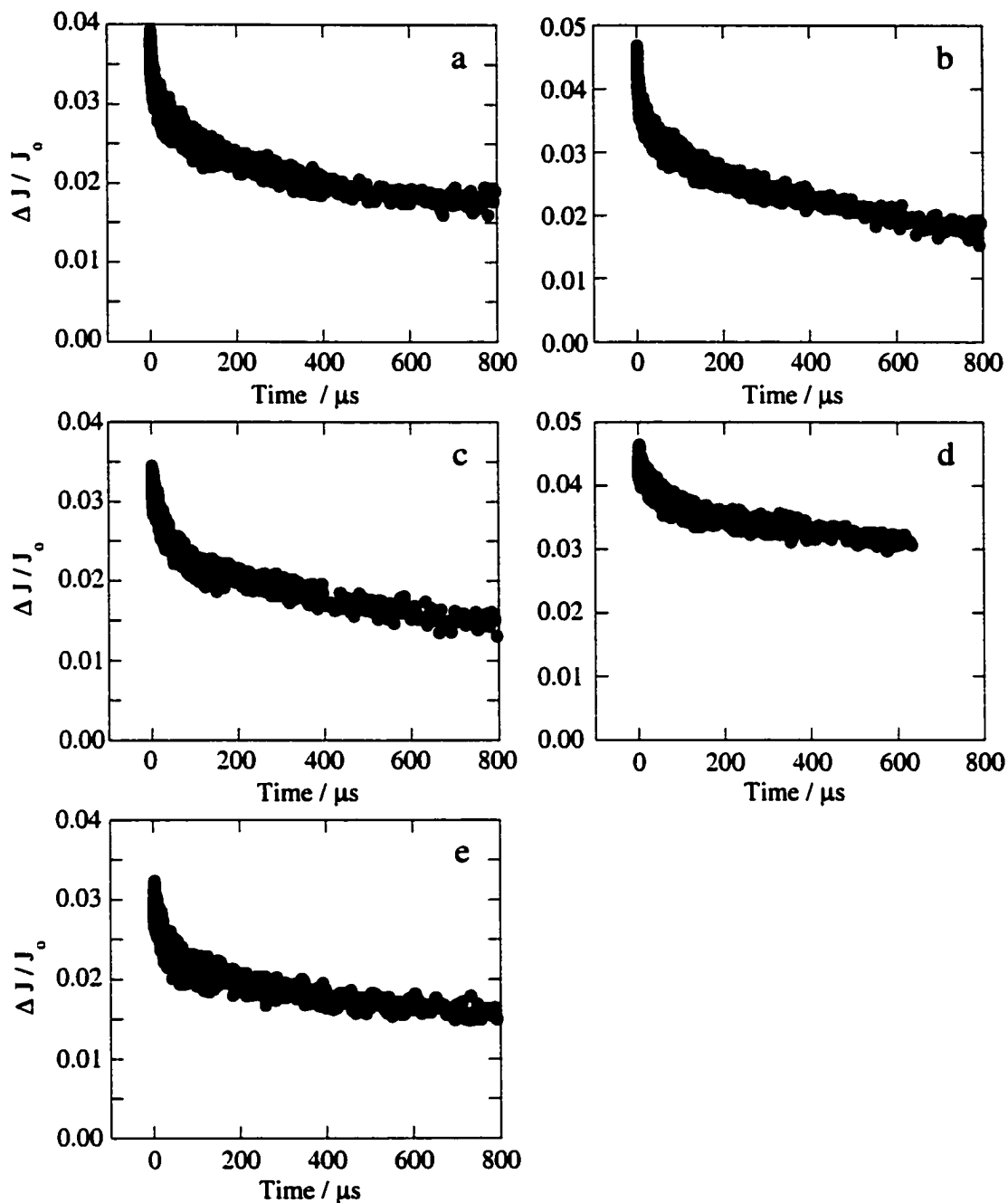
Figure 3-21. Time resolved changes in $\Delta J/J_0$ at 320 nm obtained upon 266 nm laser irradiation of cumylcarboxylic acid incorporated in (a) LiY, (b) NaY, (c) KY, (d) RbY and (e) CsY. All traces were monitored at 320 nm.

3.4. Discussion

3.4.1. Mechanism of radical formation

The proposed mechanism for the formation of the benzyl radical is photoionization of the phenylacetate anion to give the acyloxy radical, which then rapidly loses carbon dioxide to yield the benzyl radical, eq. 3-9. This mechanism is in agreement with the photochemical behaviour of phenylacetate in solution.[279-281] Further support for the proposed mechanism was the direct detection of the benzyl radical following direct excitation of incorporated phenylacetate anion and upon electron transfer from phenylacetate to photoexcited MV^{2+} within the cation-exchanged zeolites. Evidence for the phenylacetate anion being the major species found within the zeolites and therefore the precursor to the photogenerated benzyl radical is provided by the IR spectra obtained upon incorporation of phenylacetic acid within MY zeolites. The IR spectra indicate that the dominant form of the carboxylic acid is the conjugate base, phenylacetate.

The carboxylate ion is presumably generated via a mechanism such as that shown in Scheme 3-3. Upon incorporation of phenylacetic acid into the zeolite the carboxylic acid group faces the zeolite wall.[300] An interaction can exist between the carbonyl group and the alkali metal cation, as well as a hydrogen-bonding interaction between the carboxylic acid proton and the bridging oxygen of a Si-O-Al site. The metal cation interaction may increase the acidity of the carboxylic acid by stabilizing the incipient negative charge of the carboxylate anion and the bridging oxygen is also ideally set-up to act as a Brønsted base to accept the proton.

Scheme 3-3.
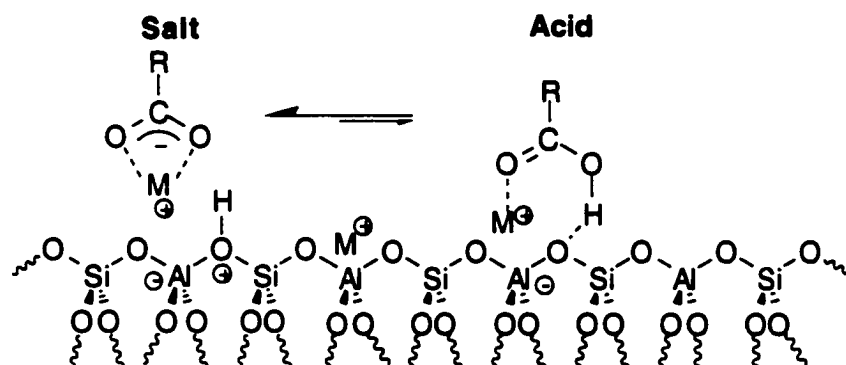
Evidence for the acyloxy radical in the mechanism for radical generation was obtained from the electron-transfer reaction between zeolite-incorporated phenylacetic acid and the methyl viologen dication (MV^{2+}). The observation of both the $MV^{+\bullet}$ and the benzyl radical with selective excitation of the MV^{2+} cation indicates that radical formation involves an electron transfer step. That is, electron transfer from the carboxylate ion to excited methyl viologen generates the aryl acyloxy radical, which then rapidly decarboxylates to give the benzyl radical. The rapid decarboxylation is consistent with fast decarboxylation rates measured for the same benzyl acyloxy radical and other similar acyloxy radicals in solution.[287-289]

3.4.2. Radical decay mechanism

All of the available evidence presented in this work suggests that the main pathway for benzyl radical decay is dimerization to generate 1,2-diphenylethane. In particular, product studies demonstrated that dimerization was the main decay pathway for the benzyl radical in the absence of quenchers. In addition, results from kinetic experiments in which the radical decay was examined as a function of loading level, and hence as a function of initial radical concentration, displayed classic second-order behaviour expected for the coupling of two radicals. As illustrated in Figure 3-22, the higher number of radicals formed at the higher loading levels increases the probability

that a radical generated in a specific cavity will find another radical in a nearby cavity. The time needed for these two closely situated radicals to find each other will be reduced, and the rate of decay of the radicals will appear to increase. On the other hand, when fewer radicals are generated at low loading levels, the probability that radicals will be generated in closely spaced cavities decreases and the overall rate of decay of the radicals after the laser pulse also decreases.

The importance of radical mobility to the decay of the benzyl radical was evident in the decay profile of this radical generated photochemically from *n*-tetrabutylammonium phenylacetate. Interestingly, the benzyl radical generated *via* this path is significantly longer lived than the same radical generated from phenylacetic acid. Supramolecular steric factors play a dominant role in the reactivity of this transient. The presence of the large and bulky tetrabutylammonium ion significantly reduces the mobility of the benzyl radical. As a result, less decrease in the signal at 315 nm due to fast reacting radicals is observed indicating that these radicals are unable to escape to neighboring cavities to react with fellow benzyl radicals.

Two slow components were observed for the decay of the benzyl radical in MY zeolites. One of these slow components is represented by the second, slower second-order rate constant calculated for each of the zeolites, and the other slow component originates from radicals that do not react at all over the longest, 800 μs, time-scale available to our laser system. The mechanism by which these radicals decay is more difficult to determine. Some of these slow radicals presumably are generated in sites that reduce the ability of the radical to cavity jump in order to find possible partners for reaction.

low loading   high loading
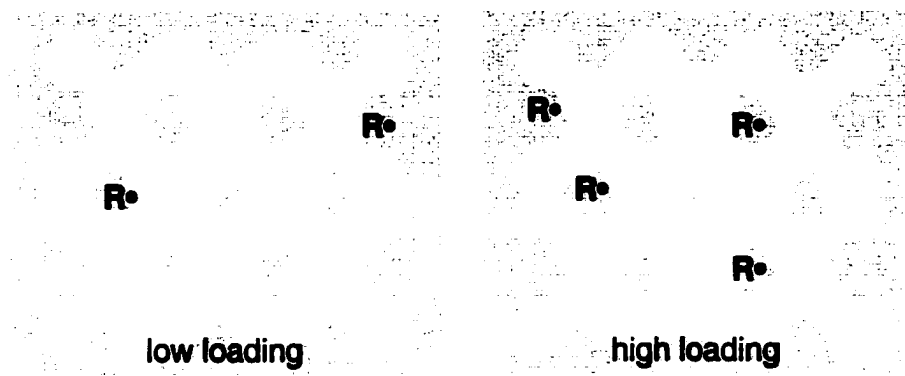
Figure 3-22. Schematic representation for the distribution of benzyl radicals (R•) generated in a low loading and high loading phenylacetic acid-NaY sample.
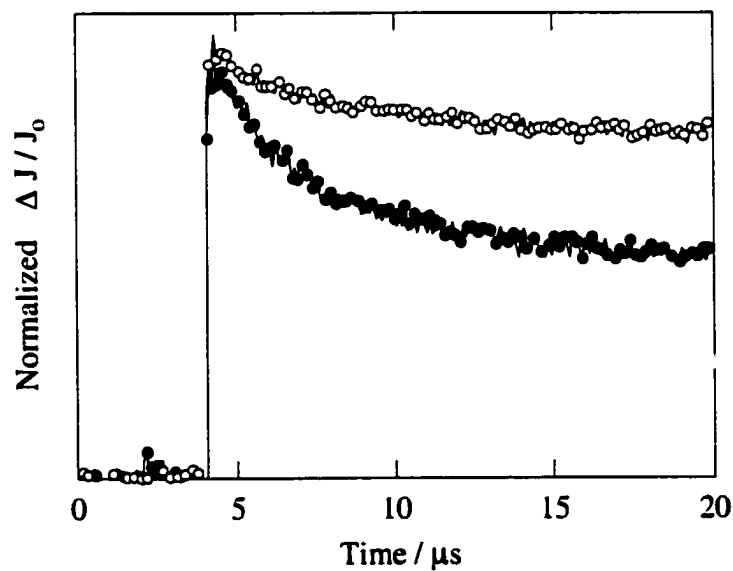
Figure 3-23. Transient decay traces at 315 nm for the benzyl radical generated upon 266 nm laser excitation of (●) phenylacetic acid and (O) n-tetrabutylammonium phenylacetate in evacuated (10^{-4} torr) NaY at a loading of <S> = 1/2.

3.4.3. Effect of counterion on the decay of the benzyl radical

In the present study, there was no evidence for the direct interaction between the benzyl radical and the zeolite suprastructure, either with the balancing cations or with the aluminosilicate framework. The results obtained for the decay of the arylmethyl radicals as a function of zeolite counterion can be easily understood by means of diffusion and steric factors. The increasing amount of radicals undergoing the fast process as a function of free-available space further supports that the benzyl radical decays in a fast manner by a coupling reaction with a second benzyl radical and that the radical mobility decreases slightly along the series from LiY to CsY. This sterically-controlled radical behaviour is schematically represented in Figure 3-24. In this scenario, the larger cation, Cs$^+$, hinders the diffusion of a greater number of benzyl radicals through the zeolite framework so that the amount of radicals undergoing fast coupling is reduced.
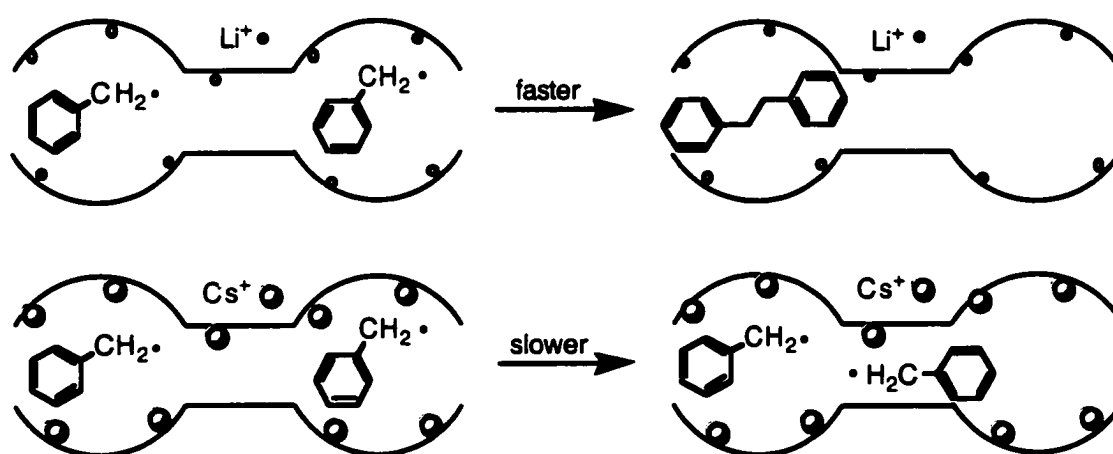
Figure 3-24. Schematic representation of the steric restrictions for diffusion and rotational movement encountered by a benzyl radical in LiY versus CsY zeolites.

These steric interactions in the alkali-metal zeolites become more significant when the substrate loading level is increased in the presence of a radical quencher. Oxygen is known to react rapidly with carbon-centered radicals in solution and in zeolites

with rate constants in the order of 10^8-10^9 s^{-1}.[261] Thus, the fact that inefficient quenching of the benzyl radical takes place in a highly concentrated sample of phenylacetic acid suggests that there are many sites that oxygen has no access due to steric restrictions. The efficiency of oxygen quenching was observed to be dependent on the loading level of the compound, consistent with the accessibility of oxygen to the benzyl radical. Furthermore, in the larger cation zeolites such as RbY and CsY, this accessibility was very limited such that very little differences between the reactivity in the absence and the presence of oxygen was observed for the measured decay of the radical over 16 µs. This was further demonstrated by the amount of radical quenched immediately after the laser pulse. In the smaller cation zeolites, a significant reduction of the radical signal was observed whereas a very small reduction was obtained in CsY. This indicates that only oxygen molecules that were present within the radical enclosing-cage are able to react with the benzyl radical, however, diffusion of oxygen molecules into the 'cage' is restricted by steric factors. That is, despite the fact that some of the radicals react reasonably efficiently with oxygen, the residual absorption indicates that there are others which are very well protected from the small quencher molecules.

3.4.4. Reactivity of benzyl radical vs cumyl radical

Figure 3-25 shows a comparison between the decay of the benzyl radical and the cumyl radical over short-time periods in each of the MY zeolites. Inspection of these plots shows that the benzyl radical is clearly more reactive than the cumyl radical under these conditions. The difference in reactivity becomes less clear when examining the fast component of the actual second-order rate constants, Tables 3-2 and 3-5. The rate constants in these tables suggest that the fast decay of the cumyl radical in LiY and NaY is more rapid than the fast decay of the benzyl radical in the same zeolites. While in the presence of the large cations, K$^+$, Rb$^+$, and Cs$^+$, coupling of benzyl radicals becomes more

rapid than the cumyl decay. However, the data also show that the contribution of the fast decay of the cumyl radical to its overall decay is considerably smaller than that observed for the benzyl radical. In addition, the second, slower component for the decay of the cumyl radical is always smaller than that for the benzyl radical. Thus, on the basis of the decay traces which clearly show that the benzyl radical decays more quickly, and the relative contributions of the fast and slow components, the data suggests that, overall, the cumyl radical is considerably less reactive than the benzyl radical in the MY zeolites. The differences in the decay second-order rate constants observed among these radicals can be rationalized in terms of steric hindrance to rotational motion of the molecule and to restrictions to its diffusion throughout the zeolite lattice.

In addition, product studies demonstrated that the mobility of the benzyl radical decreases considerably upon addition of two methyl groups at the radical center. No bicumene ($PhC(CH_3)_2C(CH_3)_2Ph$) was detected in the photolysis product mixture of cumylcarboxylic acid, whereas, bibenzyl ($PhCH_2CH_2Ph$) was the main radical coupling product observed upon photolysis of phenylacetic acid in MY zeolites in the absence of radical quenchers. Turro and co-workers have reported 99% formation of the secondary radical-coupling product (bicumene) upon photolysis of 1,1,3,3-tetramethyl-1,3-diphenyl acetone (tetramethyldibenzyl ketone) in MY zeolites.[254] In our studies, the mass balance recovery of ~ 50% for most irradiations in zeolites may be attributed to the absence of bicumene in the extracted product mixture from the photolysis of cumylcarboxylic acid in NaY. However, the similar sized bicumene alcohol ($PhC(CH_3)_2C(CH_3)(OH)Ph$) was extracted in reasonable yields. Furthermore, this latter product would be expected to interact more strongly with the zeolite framework than the bicumene due to the hydroxy moiety. Therefore, trapped-bicumene within the zeolite cavities is not likely the explanation for its absence in the extracted product mixture. The various time-resolved studies of arylmethyl radicals suggest that bicumene does not efficiently form in NaY due

to steric restrictions for the approach of the two cumyl radicals centers within the confined spaces of zeolites. The photolysis experiments performed by Turro and Ramamurthy's research groups are normally performed in hexane-zeolite slurry solutions.[254] Thus, the distinct experimental conditions may explain the differences observed in the formation of bicumene from the cumyl radical in Turro's work and its absence in our study. In a slurry solution, diffusion of the adsorbed molecules is facilitated such that coupling of the two radicals at the external surface of the zeolite framework can occur, thereby generating the bicumene product, which is known to readily form in solution.

A better understanding of the decay pathways and mobility of the zeolite is necessary to create a model for the radical behaviour within the suprastructure of zeolites. For example, the main decay pathway for these radicals should be dimerization. However, in the case of the cumyl radical, no coupling products are observed in the steady-state photolysis products. The major photolysis product, acetophenone, was attributed to reaction between the cumyl radical and oxygen. The oxygen concentration under vacuum conditions in the laser experiments cannot account for the observed partial decay of the cumyl radical over 800 μs. Therefore, other quenching processes for the cumyl radical must exist within MY zeolites. Equation 3.22 describes the most likely reaction pathway for the cumyl radicals trapped within the cavities of zeolites. Due to the steric hindrance introduced by the methyl groups at the carbon radical center, the hydrogen transfer reaction between two cumyl radicals becomes the preferred decay pathway. As the mobility and diffusion of the cumyl radical is still the determining factor for the reaction to take place, the observed reactivity is consistent with the behaviour of the benzyl radicals studied and explains the time-resolved decay profile observed. Further experiments are necessary to verify the proposed mechanism. Specifically, the

deuterium labeled precursor of cumylcarboxylic acid would be useful to validate the H-abstraction step in the intrazeolite reaction.
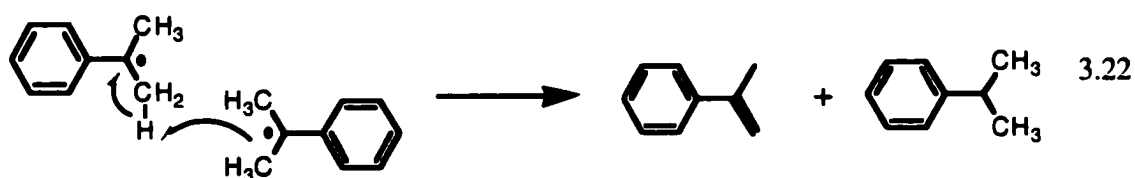
In addition, further studies are necessary to establish the proportion of cumene formed from the cumyl radical and anion source. As previously discussed, the α-methylstyrene was not detected in the steady-state photolysis of cumylcarboxylic acid. The styrene molecule may oxidize to generate acetophenone or further react with other cumyl radicals forming a polymeric material which is not extracted from the zeolite under the conditions of the photolysis reactions.
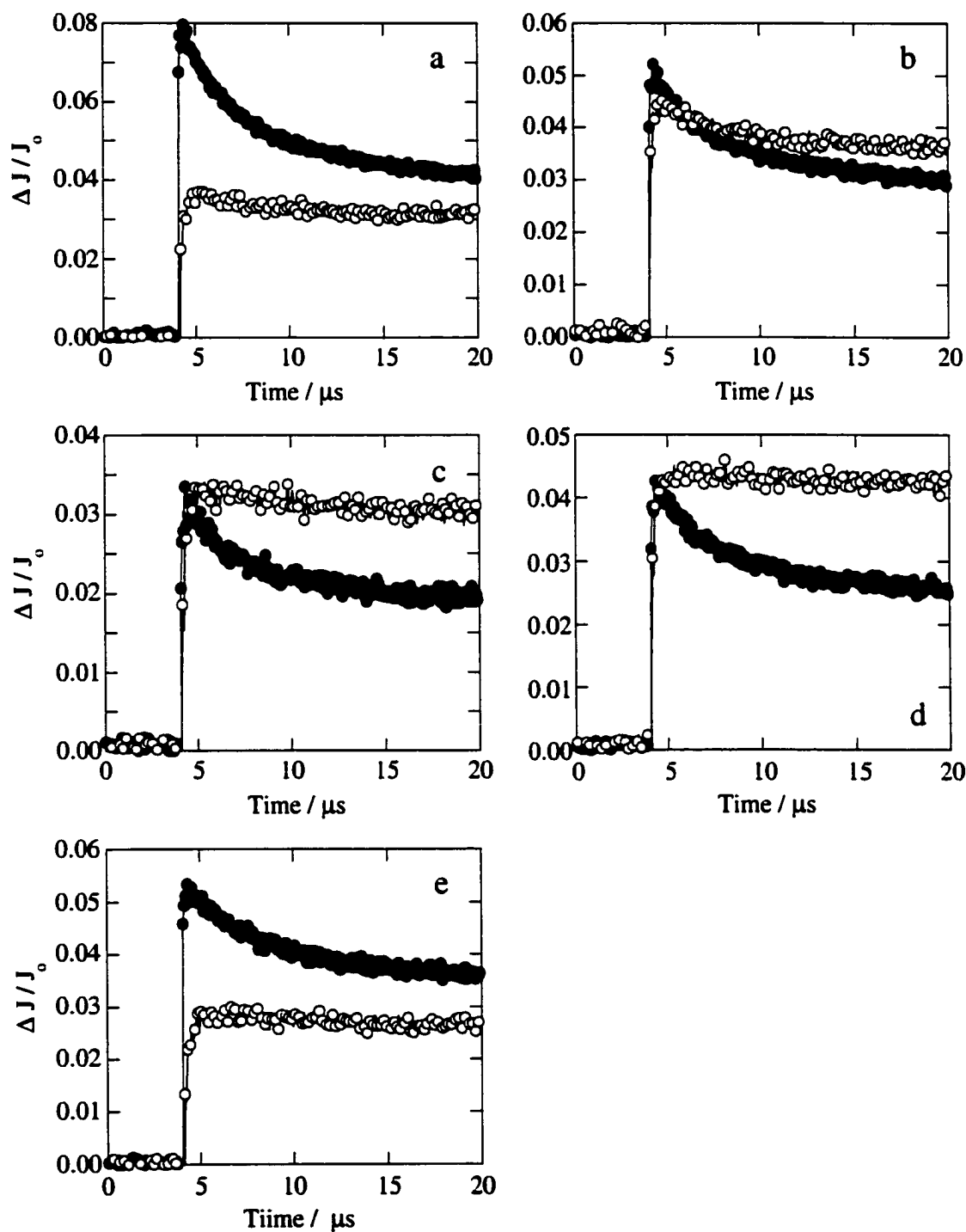
Figure 3-25. Transient diffuse kinetics for the decay of the (●) benzyl radical and the (○) cumyl radical in (a) LiY, (b) NaY, (c) KY, (d) RbY and (c) CsY under vacuum (10^{-4} torr) over 16 μs.

3.4.5. Diffusion of arylmethyl radicals in zeolites

Rates of diffusion-controlled reactions in homogeneous solutions can be calculated from the Smuluchowski equation. A modified version of this equation has been used to study bimolecular reactions in zeolites to obtain the diffusion coefficient of the reacting species, eq. 3.23.[301]

$$D_q = \frac{1000 k_q R_q}{p \pi R_c^2 N_{avg}}$$
<div align="right">3.23</div>

where D_q is the diffusion coefficient of the reactive species, k_q is the bimolecular rate constant, R_q is the radius of the molecule ($R_q = 3 \times 10^{-8}$ cm for benzyl radical), p is the probability that the encounter between reactants will result in a successful reaction ($p = 1$), R_c represents an average radius of zeolite channel ($R_c = 3.7 \times 10^{-8}$ cm), and N_{avg} is Avogadro's number. The rate of intracrystalline diffusion of the benzyl radical (D) can then be approximated by using eq. 3.23. The calculated diffusion coefficients for the benzyl and cumyl radicals studied are given in Table 3-8.

The diffusion coefficient of the arylmethyl radicals presented are comparable to the diffusion of toluene within zeolites[253] ($\sim 10^{-10}$ m^2 s^{-1}) and the diffusion for the benzyl radical in solution[291] ($\sim 1 \times 10^{-9}$ m^2 s^{-1}). These results also support the notion that the mobility of the cumyl radical is more hindered than diffusion of the benzyl radical.

Table 3-8. Diffusion coefficients of arylmethyl radicals in NaY derived from second-order rate constants for the disappearance of the radical.

Radical	$D_q / 10^{-9}$ m^2 s^{-1} (fast component)	$D_q / 10^{-10}$ m^2 s^{-1} (slow component)
benzyl radical	4.3	2.3
cumyl radical	2.3	0.32

3.4.6. Other arylmethyl transients

Photolysis of phenylacetic acid also resulted in the formation of the benzyl anion. The lifetime ($\tau = 1/k_{decay} \sim 2$ μs) of the benzyl anion within the MY zeolites did not vary significantly with changes in the counterbalancing cation. This high reactivity indicates that the decay pathway available to the benzyl anion is a fast reaction where electrostatic forces do not play a crucial role. Product studies demonstrated that toluene was formed mainly by the reaction of the benzyl anion with a protic source. One must consider that the carbanion most likely is generated in a cavity containing a silanol group formed by the interaction of the starting phenylacetic acid with the zeolite framework, Scheme 3-3. As a result, at the time of photolysis, the benzyl anion is formed in the vicinity of this protic silanol site, Scheme 3-4, and rapid reaction between the two is observed. This conclusion is supported by the fact that even though co-incorporated water and methanol increase the amount of benzyl carbanion generated, these species had little influence on the observed decay kinetics.

Scheme 3-4.
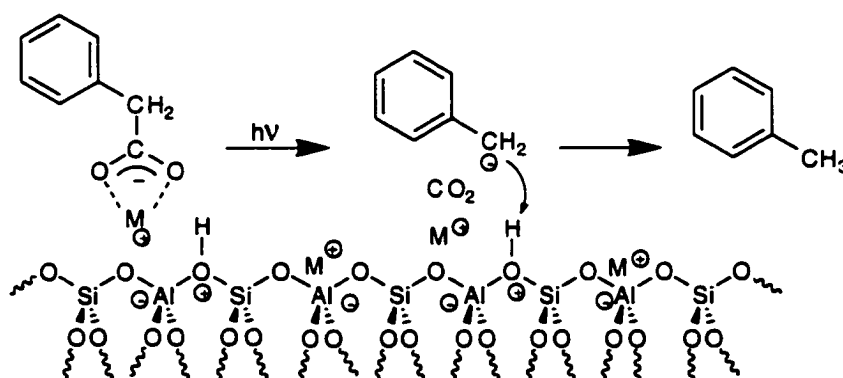
Although the reactivity of the benzyl anion did not vary among the faujasite Y zeolites, the amount of transient detected was sensitive to the nature of the counterbalancing cation. For example, more benzyl anion was obtained in LiY and NaY, whereas significantly less carbanion was obtained in RbY and CsY. These results, and

the identical kinetics for the decay of the transient in the various zeolites indicates that the formation of the benzyl anion becomes less efficient as the zeolite framework becomes less ionizing. This is consistent with the results obtained in the previous chapter which demonstrated that the ionizing ability of the zeolite decreased in the order of LiY to CsY.

3.5. Conclusions

The main goal of this research was to detect the benzyl radical as *a reactive intermediate* within the cavities of faujasite zeolites. The generation of carbon-centered radicals from carboxylate ions can be achieved through the photolysis of aryl acetic acids. Intrazeolite motion of benzyl radicals adsorbed on zeolites has been demonstrated to take place and evidence for restrictions to radical movement have been noted. Both zeolite counterion and the substrate structure have been shown to significantly affect the reactivity of simple arylmethyl radicals within zeolites.

Future work

The work presented in this chapter were preliminary studies on the reactivity of simple arylmethyl radicals within the suprastructure of zeolites. Extensive work regarding the type of motions and distribution of these molecules is still necessary. Some insights into the location and motion of this transient could be extracted from the sort of experiments discussed below. The main question that is still not answered is how far away from their original location the benzyl radicals are able to travel. Although the benzyl radical has been shown to be mobile within the intrazeolite framework, the type of motions that are responsible for their decay kinetics are not fully understood. Is there a rotational component to the decay and does this affect the possibility of two species reacting together? How strong are the π-cation electrostatic interactions between the benzyl radical and the counterbalancing cation affecting the mobility of the radical?

Studies of oxygen concentration on the radical decay kinetics and as a function of loading level should be very interesting. This type of investigation would provide information regarding the availability of the radical center to oxygen when precursor molecules are abundant in their local environment. In addition, bimolecular rate constants for the oxygenation reaction of the benzyl radical in zeolites would be provided.

Product studies examining the reactivity of radicals using a mixture of precursors would be useful in identifying the distribution and mobility of the various radicals within zeolites. By using a mixture of two different arylmethyl radicals a pseudo A-B system can be used to examine the mobility of the radicals; for example, the most mobile benzyl radical paired up with the cumyl radical or the bulkier diphenylmethyl radical. The various product distributions would indicate whether there is a random distribution of molecules within the internal zeolite framework or clusters of molecules are present. This experimental approach would have to examine various preparation conditions: a) zeolite with "random" distribution of radicals by simultaneously adding a mixture of arylacetic acids to the zeolite slurry during preparation, b) non-random distribution of radicals by mixing separate batches of arylacetic acid-zeolite composite, and c) pseudo-random distribution of radicals by adding each arylacetic acid at different times during the preparation so that non-random incorporation is permitted. The possibility exists that the more mobile benzyl radicals would be better able to reach the deeper cavities than the cumylcarboxylic acid, as a result, a non-random distribution of products would be expected.

Transient spectroscopy could be used to directly monitor the reactivity of each arylmethyl radical as a function of a second radical if the two transients have different absorption characteristics. For example, the benzyl radical (λ_{max} = 310 nm) or the 4-methoxybenzyl radical (λ_{max} = 290 nm) and the diphenylmethyl radical (λ_{max} = 330 nm). By directly observing the two different reacting species the bimolecular rate constants for their coupling reactions would be better understood.

Temperature studies for the reactivity of the arylmethyl radical in zeolites should give information about the energetics necessary for intrazeolite transit within the cavities of faujasite zeolites. The effect of substrate structure, loading level, and zeolite counterion would be assessed to quantify their contribution to the radical reactivity and to provide a better model (equation) that fully explains the decay behaviour of these radicals.

A more extensive study of the benzyl anion is clearly necessary. The decay of this transient in zeolites has been observed to be very fast, thus optimization of its formation and lengthening of the lifetime in this environment would be an important aspect of the investigation. The generation of other carbanions should also be examined. The generation of the benzyl anion is thought to be photochemical, but reduction of the benzyl radical by the zeolite framework to form the benzyl anion has not been excluded.

Chapter 4. Experimental

4.1. General techniques

Proton (^{1}H) and carbon (^{13}C) nuclear magnetic resonance (NMR) spectra were obtained using a Bruker AC-250 NMR spectrometer in automation mode in CDCl$_3$. Chemical shifts are reported in parts per million (δ) relative to tetramethylsilane (0.00) as an internal standard. Multiplicities are abbreviated as follows: s = singlet, d = doublet, t = triplet, q = quartet, m = multiplet.

Infrared spectra of guest-zeolite complex were obtained on a Nicolet 205 FTIR spectrometer and the frequencies are reported in wavenumbers (cm^{-1}). UV-vis absorption spectra were obtained in hexane solution in a 1 cm quartz cuvette on a Varian Cary UV-vis spectrometer. Gas chromatography (GC) analyses were performed using a Perkin Elmer Autosystem Gas Chromatograph with a DB5 15 meter column. GC/MS analyses were done on a Perkin Elmer Autosystem XL GC coupled with TurboMass Spectrometer.

4.2. Materials

The compounds used in this study are summarized in Scheme 4-1. 4-Methoxy-styrene, *trans*-anethole, 2,3-dimethoxystyrene, 2,4-dimethylstyrene, 4-methylstyrene, phenylacetic acid, and starting materials for synthesis procedures were commercially available from Aldrich and used as received. Other compounds discussed in the thesis have been previously reported and the procedures for their preparation are described below. The 2-bromo-1-(4-methoxyphenyl)ethyl acetate (AcOBrVA) and 2-bromo-1-(4-methoxyphenyl)propyl acetate (AcOBrAn) were prepared by Roumiana Stefanova using a similar synthetic procedure.

Solvents used in the preparation of zeolite and solution samples for low-intensity photolysis and laser flash photolysis experiments were of spectroscopic grade (Omnisolv, BDH, and Aldrich) and used without further purification.

231

Scheme 4-1

R_1 = H, R_2 = CH$_3$O, R_3 = H, LG = Cl R_1 = H, R_2 = H

R_1 = CH$_3$, R_2 = CH$_3$O, R_3 = H, LG = Cl R_1 = H, R_2 = CH$_3$

R_1 = H, R_2 = CH$_3$O, R_3 = H, LG = Br

R_1 = CH$_3$, R_2 = CH$_3$O, R_3 = H, LG = Br

R_1 = H, R_2 = CH$_3$, R_3 = CH$_3$, LG = Cl

R_1 = H, R_2 = CH$_3$, R_3 = CH$_3$, LG = Cl

R_1 = H, R_2 = CH$_3$O, R_3 = H, LG = OC(O)CF$_3$

R_1 = CH$_3$, R_2 = CH$_3$O, R_3 = H, LG = OC(O)CF$_3$
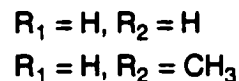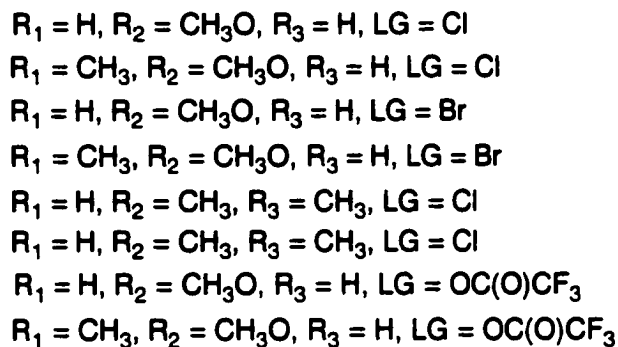
4.2.1. Synthetic procedures

4.2.1.1. Synthesis of 2-halogen-1-arylalkyl acetate compounds

The 2-halogen-1-arylalkyl acetate compounds used in this study were prepared according to procedures previously reported in the literature.[200] A general synthetic scheme for the preparation of these compounds is given in eq. 4.1. The reaction involves bromination or chlorination of the appropriate styrene followed by a substitution in glacial acetic acid.

$$\text{4.1}$$
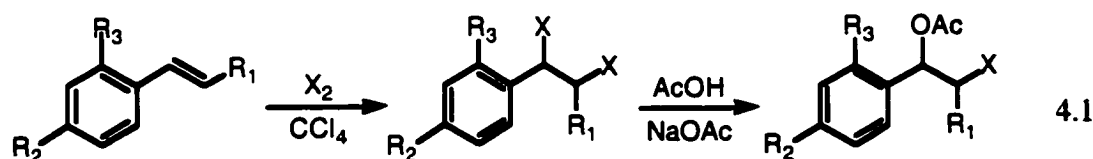
To a stirred solution of the aromatic olefin (~ 0.015 mole) in 50 mL of carbon tetrachloride, a solution of Cl$_2$ or Br$_2$ in CCl$_4$ was added dropwise until a faint yellow colour persisted in the reaction flask.[302] The reaction mixture was then allowed to stir for three hours and excess chlorine or bromine was removed by suction. The crude reaction

mixture was washed twice with cold H_2O and dried over $MgSO_4$. After filtration and solvent evaporation under reduced pressure, the crude liquid (80-95% yield) was reacted with 0.5 g of sodium acetate in 70 mL of glacial acetic acid. This mixture was allowed to react with constant heating and stirring for about six hours. Cloudiness of the solution was evidence that the expected reaction was taking place. The final reaction mixture was washed twice with dichloromethane. The organic portions were combined and washed as follows: H_2O (2x), aq. 10% $NaHCO_3$ (2x), and H_2O (1x). Finally, the organic solution was dried over $MgSO_4$. After filtration the solvent was removed by rotary-evaporation. The required compounds were purified by flash-column chromatography using 5-30% ethyl acetate in hexane as eluent and characterized using ^1H, ^{13}C NMR and GC/MS. Typical yields of purified 2-halogen-1-arylalkyl acetate compounds varied from 10-40% depending on the substituent, quantity of styrene precursor used and reaction times. Purities greater than 95% were determined by GC and NMR.

2-Chloro-1-(4-methoxyphenyl)ethyl acetate (AcOClVA): transparent liquid; ^1H NMR 7.1 (dd, 4H), 5.9 (dd, 1H), 3.8 (s, 3H), 3.7 (m, 2H), 2.1 (s, 3H); ^{13}C NMR δ 169.9, 159.9, 129.3, 128.1, 114.1, 74.8, 55.3, 46.4, 21.0.

2-Chloro-1-(4-methoxyphenyl)propyl acetate (AcOClAn): transparent liquid; diastereomers; ^1H NMR 7.1 (dd, 4H), 5.8 (dd, 1H), 4.3 (m, 1H), 3.8 (s, 3H), 2.1 (d, 3H), 1.4 (m, 3H); ^{13}C NMR δ 170.9, 169.8, 159.9, 159.7, 129.1, 128.8, 128.6, 127.7, 114.0, 113.7, 78.9, 77.9, 75.0, 69.3, 59.0, 58.7, 55.3, 53.5, 21.3, 21.0.

2-Chloro-1-(2,4-dimethylphenyl)ethyl acetate (AcOCldiMeSty): transparent liquid; ^1H NMR 7.2 (m, 3H), 6.1 (dd, 1H), 3.7 (m, 2H), 2.4 (s, 3H), 2.3 (s, 3H), 2.1 (s, 3H); ^{13}C NMR δ 169.9, 138.5, 135.5, 132.8, 131.5, 127.1, 126.0, 72.1, 45.9, 21.1, 21.0, 19.2.

2-Chloro-1-(4-methylphenyl)ethyl acetate (AcOClMeSty): transparent liquid; ^{1}H NMR 7.2 (dd, 4H), 5.9 (dd, 1H), 3.7 (m, 2H), 2.3 (s, 3H), 2.1 (s, 3H); ^{13}C NMR 169.9, 138.8, 134.3, 129.4, 126.7, 75.1, 46.5, 21.2, 21.0.

4.2.1.2. Synthesis of 2-trifluoroacetoxy-1-arylalkyl acetate compounds

The general procedure for the synthesis of the β-trifluoroacetoxy compounds involved a three-step synthesis and is summarized in Scheme 4-2. Several literature procedures were attempted in the synthesis of the diols,[303-310] but the procedure described by Akashi et al.[311] allowed the oxidation control of the olefin to produce adequate yields of the diol to proceed to the next synthetic step. The conversion of the diol to the ditrifluoroacetoxy compound was achieved by the organic synthetic procedure described in Vogel's Textbook of Practical Organic Chemistry followed by a variation of the acetate substitution reaction described above for the 2-halogen-1-arylalkyl acetate synthesis.

Preparation of 1-(4-methoxyphenyl)-1,2-alkyldiols. A 0.05% solution of osmium tetraoxide solution was prepared by adding a 250 mg ampule of solid OsO_4 to 55 mL of anhydrous tert-butyl alcohol. The solution was kept in the freezer between uses.[310]

In a 1L flask, 4.60g (25 mmol) of tetraethylammonium chloride ($Et_4NCl\cdot H_2O$) and 6.80 g (50 mmol) of sodium acetate ($NaOAc\cdot 3H_2O$) were mixed in 200 mL of distilled acetone to generate the tetraethylammonium acetate salt (Et_4NOAc) "in situ". The styrene (0.05 mol) and 25 mL of tert-butyl hydroperoxide were added to this solution and allowed to stir for 10 minutes. The solution was cooled in an ice bath for 10 minutes and 5 mL of a 0.05% OsO_4 catalyst was added in one portion. After stirring for one hour the ice bath was removed, the flask was slightly stoppered and the contents left to stand at room temperature overnight. To the resulting golden solution 400 mL of ether were added and the mixture cooled by stirring in an ice bath. Subsequently, 50 mL of freshly prepared 10% $NaHSO_3$ was added to the solution and stirred for an additional hour. Sufficient sodium chloride salt was added to saturate the aqueous layer and the phases

were separated. The organic layer was washed with 50 mL of brine. The aqueous layers were extracted with two 100 mL portions of ether. The combined organic layers were dried (Na_2SO_4) and concentrated to yield a viscous oil. The 1,2-diol was purified by flash chromatography using first dichloromethane to encourage the impurities to exit the column. Subsequently, ether was used to force the 1,2-diol product to be released. Yields of pure solid diol ranged between 40-80%.

Scheme 4-2.
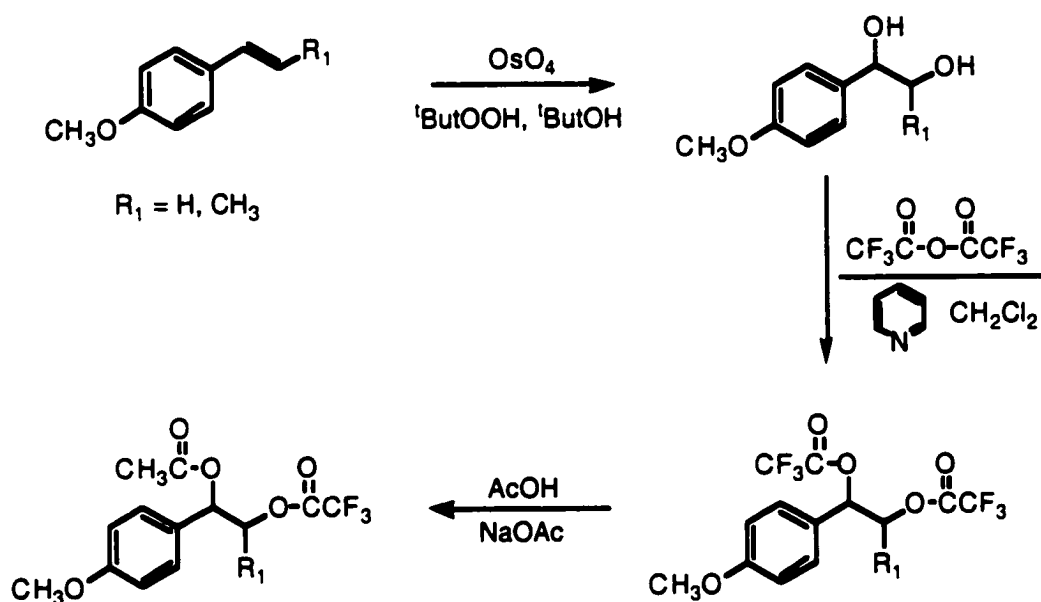
1-(4-methoxyphenyl)-1,2-ethanediol: white solid; ^1H NMR 7.0 (dd, 4H), 4.7 (m, 1H), 3.8 (s, 3H), 3.7 (m, 2H), 3.4 (s, 2H); ^{13}C NMR δ 159.2, 132.7, 127.4, 113.9, 74.3, 68.0, 55.2.

1-(4-methoxyphenyl)-1,2-propanediol: white solid; ^1H NMR 7.1 (dd, 4H), 4.3 (d, 1H), 3.8 (s, 3H), 3.8 (m, 1H), 3.0 (s, 2H), 1.0 (d, 3H); ^{13}C NMR δ 159.5, 133.2, 128.0, 113.9, 79.1, 72.3, 55.3, 18.7.

Preparation of 1-(4-methoxyphenyl)-1,2-ditrifluoroacetoxyalkanes. About 0.01 mol of the 1,2-diol was dissolved in 30 mL of dichloromethane. With stirring, two equivalents of pyridine were added followed by two equivalents of trifluoroacetic anhydride. The mixture was allowed to stir between 5-15 minutes. The reaction mixture was then washed as follows: 10 mL of H_2O, 5% HCl, 5% NaOH, 5% HCl, and finally H_2O. The dichloromethane layer was dried over magnesium sulphate and the solvent removed under reduced pressure. The yield for this synthetic step was greater than 95% with negligible impurities. The thermal instability of this compound prevented its storage for more than 24 hrs, even when kept in a dark freezer, thus the third step of the procedure in the synthesis of AcOTFAAn and AcOTFAVA was performed immediately after its isolation.

1-(4-methoxyphenyl)-1,2-ditrifluoroacetoxyethane: colourless liquid; ^1H NMR 7.2 (m, 4H), 6.2 (dd, 1H), 4.6 (dd, 2H); 3.8 (s, 3H).

1-(4-methoxyphenyl)-1,2-ditrifluoroacetoxypropane: colourless liquid; ^1H NMR 7.1 (dd, 4H), 5.8 (d, 1H), 5.5 (m, 1H), 3.8 (s, 3H), 1.2 (d, 3H).

Preparation of 2-trifluoroacetoxy-1-(4-methoxyphenyl)alkyl acetates. The ditrifluoroacetoxy substituted olefin and glacial acetic acid were heated using a warm water bath for *ca.* 3 hrs. The reaction was followed by GC to ensure that the reaction was stopped before a significant amount of the diacetate substitution compound was formed. The final product was isolated using flash-column chromatography using 5-30% ethyl acetate in hexane as eluant. Typical yields of 2-trifluoroacetoxy-1-(4-methoxyphenyl)alkyl acetate varied from 10 to 30%.

2-trifluoroacetoxy-1-(4-methoxyphenyl)ethyl acetate (AcOTFAVA): transparent liquid; ^1H NMR 7.0 (dd, 4H), 6.0 (dd, 1H), 4.6 (s, 2H), 3.8 (m, 3H), 2.1 (s, 3H); ^{13}C NMR δ 169.9, 160.2, 157.5, 128.2, 127.2, 116.7, 114.3, 112.2, 72.0, 68.7, 55.3, 20.9.

2-trifluoroacetoxy-1-(4-methoxyphenyl)propyl acetate (AcOTFAAn): transparent liquid; diastereomers; ^{1}H NMR 7.1 (dd, 4H), 5.9 (d, 1H), 5.4 (m, 1H), 3.8 (s, 3H), 2.0 (s, 3H), 1.2 (d, 3H);

4.2.1.3. Synthesis of cumyl carboxylic acid[312]

Cumyl carboxylic acid was prepared by hydrolysis of cumyl cyanide, eq. 4.2. This latter compound in turn was obtained by methylation of the commercially-available benzyl cyanide, eq. 4.3.
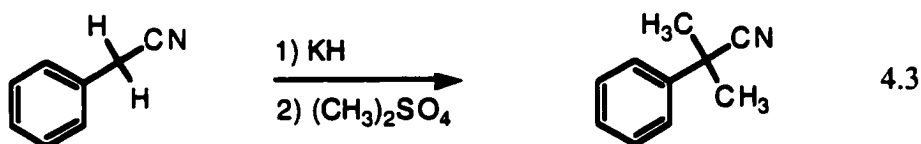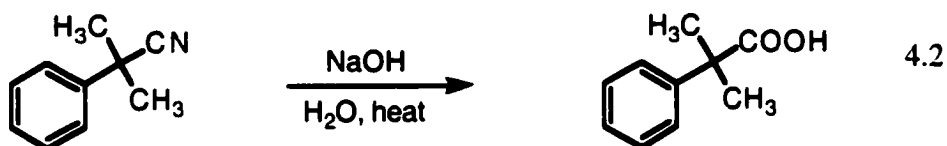
Preparation of cumyl cyanide. Using a refluxing set-up, the appropriate benzyl cyanide (0.05 mol) was diluted with dry benzene (25 mL) and added to a stirred mixture of potassium hydride (0.15 mol) and dry benzene (25 mL) under a flow of nitrogen. Evolution of hydrogen gas (H_2) was observed immediately and the reaction was encouraged by heating for 30 minutes on a warm water bath. An orange-yellowish sticky solid was formed. Through a dropping funnel, dimethylsulfate (0.15 mol) dissolved in 20 mL of dry benzene was added dropwise with continuous stirring so that the mixture refluxed gently. The reaction was refluxed until GC chromatograms showed the complete conversion to the cumyl cyanide.[313] The reaction mixture was then allowed to cool. The residual hydride was destroyed by the addition of 40 mL of 50% aq. ethanol. The aqueous layer was extracted with benzene, and the combined benzene solutions

thoroughly washed with water and then dried over magnesium sulfate. Most of the benzene was removed by distillation under atmospheric pressure. The remaining liquid was transferred to a smaller round-bottom flask. The resulting oil was distilled under reduced pressure to recover excess dimethylsulfate and pure cumylcyanide in 40-60% yield.

Cumylcyanide (CumCN): transparent liquid; b.p. 63-67 °C (10^{-3} torr); ^{1}H NMR 7.4 (m, 5H), 1.7 (s, 6H); ^{13}C NMR δ 141.5, 129.0, 127.8. 125.1, 124.6, 37.2, 29.2.

Preparation of cumylcarboxylic acid. The cumylcyanide and 10g of sodium hydroxide were dissolved in 35 mL of 70% aq. ethanol and refluxed for 48 hours. An additional 50 mL of water was added to the mixture and the solution was acidified with conc. HCl to precipitate the acid. The crystals were collected and dissolved in dichloromethane. To isolate the pure acid, the dichloromethane solution was extracted with 10% aq. NaOH. This water layer was acidified again, and the crystals recollected. The acid was recrystallized from water and dried under reduced pressure.

Cumylcarboxylic acid (CumCOOH): white needles; m.p. 76-77 °C; ^{1}H NMR 7.4 (m, 5H), 1.6 (s, 6H); ^{13}C NMR δ 181.8, 144.7, 128.5, 127.0, 125.8, 46.8, 26.3.

4.2.2. Zeolites

Zeolite NaY (Si/Al=2.6) used in this study were obtained from Aldrich. The Na$^+$ exchanged zeolites were used without additional purification. The exchanged zeolites (LiY, KY, RbY and CsY) were prepared by stirring ~ 5 g of commercially available NaY zeolite (Aldrich) with 100 mL of aqueous solutions of at least 3x excess concentration of the corresponding chloride (LiCl, KCl, RbCl, CsCl) at 80 °C for 2h. The zeolites were then washed with deionized water until no chloride ions appeared in the washing water (AgNO$_3$ test). This procedure was repeated three times and the zeolite was calcinated between each exchange. The typical percent exchange obtained using this procedure was

45% for LiY, 97% for KY, 44% for RbY and 57% for CsY. RbY and CsY have a low exchange value due to the size of the cations which are too big to fit in the silicalite cages (type I sites). LiY, due to its tight solvation sphere with water, also achieves low exchange with this particular procedure.

4.2.3. Sample preparation

4.2.3.1. *Preparation of solution samples*

Solutions of the required substrate were prepared by adding a small volume of stock solution (typically 2-20 μL) to 3 mL of the appropriate solvent (acetonitrile, hexane, water, dichloromethane, aq. methanol, etc). The substrate concentration was adjusted such that the absorbance of the solution at the laser wavelength (266 nm or 308 nm) was in the range of 0.4 – 0.6. Samples were contained in cells made of 7 x 7 mm^2 quartz tubing (static experiments) and capped with a rubber septum. Unless otherwise indicated, the samples were deaerated by bubbling a slow stream of UHP nitrogen for 20 mins prior to laser irradiation and were carried out at room temperature (22 $\pm$ 1 °C). Static samples were shaken after every two laser shots to minimize secondary photolysis. A typical experiment consisted of 2-4 replicate shots per measurement, and the average signal was processed by the computer.

For variable temperature experiments, 10-15 samples of the appropriate solvent composition were prepared simultaneously under identical conditions. The samples were stoppered and tightly covered with parafilm and bubbled with a slow-stream of nitrogen for exactly 20 mins at a flow rate of 5 mm/min. Each sample was allowed to temperature equilibrate for at least 30 minutes prior to being photolyzed. To ensure the viability of the compound under the various thermal conditions, the compound was injected immediately before the laser experiment was conducted. A different sample was used for each of the temperatures studied and the temperature reading of the sample was acquired immediately after the kinetic traces were obtained. The sample holder for the LFP

system was attached to a circulating bath with a temperature control. The experiments were performed in a temperature range of –20 to 40 °C.

4.2.3.2. Preparation of zeolite samples

In order to remove water, as well as n-hexane or dichloromethane, from the zeolite samples, evacuation for more than 12 h at less than 10^{-3} torr at an elevated temperature of ca. 100 °C has been recommended unless thermal decomposition or evaporation of the guest molecule is a problem. This treatment has been reported to give a water content of less than 0.4 wt % for NaY.[40] Literature reports also note that evacuation at room temperature even for a prolonged period is not completely effective for removing water and/or n-hexane from zeolites.[100] However, O'Neill, through detailed studies, has shown that our laboratory sample preparation methodology using a nitrogen-purged environment yields samples with less than 1% by weight water content and ca. 4-9% by weight hexane.[165] In addition, at atmospheric pressure, water adsorbed in MY zeolites can be completely removed only at 550, 370, 360, 220 and 210 °C, for LiY, NaY, KY, RbY and CsY, respectively.[72] However, the high temperature required for dehydration of LiY also leads to structural instability and Brønsted acid formation and lower temperatures are typically used for calcination purposes.

In view of these facts, a meticulous procedure for the preparation of zeolite samples was developed during the course of this thesis. Air exposure during sample preparation was kept to a minimum by carrying out the procedure under a nitrogen atmosphere through the use of a nitrogen-purged glove-bag or -box. In addition, after a minimum of 12-hr evacuation at 10^{-4} torr, the zeolite-containing quartz cell was permanently flame-sealed to avoid changes due to atmospheric conditions during the course of the experiments.

In all cases the zeolites were activated at 400 – 450 °C for at least 10 hrs before use to remove any absorbed water. The samples were prepared by stirring the dehydrated zeolite powder with dry n-hexane (< 0.02 % water) in a stoppered vial at room temperature. Typically 300-400 mg of zeolite was activated overnight and added directly

to the carrier solvent (20 mL of hexane). A known amount of substrate (pure compound or a concentrated stock solution) was added to the zeolite slurry. The sample was magnetically stirred for 45 minutes, then centrifuged and the solvent was decanted. Fresh solvent was then added in order to wash the zeolite surface. Fifteen minutes of additional stirring was applied, followed by centrifugation and solvent decantation. The organic-zeolite composite was immediately transferred to a vacuum-desiccator and evacuated (10^{-3} torr) for at least 5 hrs at room temperature to remove remaining solvent molecules. While under vacuum, the desiccator containing the zeolite sample was placed in a nitrogen-purged glove-bag or glove-box to avoid exposure of the anhydrous zeolite to moist atmospheric. The dried zeolite was transferred to 3 x 7 mm^2 quartz laser cell and evacuated under reduced pressure (10^{-4} torr) for at least 8 hrs (usually overnight) on a vacuum line equipped with a home-made oil diffusion pump which ensured good evacuation. Laser experiments were conducted immediately after sample preparation was complete unless otherwise stated. Samples prepared under vacuum conditions were permanently sealed under vacuum to prevent changes in the internal environment due to air exposure. For experiments performed in an oxygen, nitrous oxide, or nitrogen environment, the stoppered samples in quartz cells were purged with a stream of the UHP gas for at least 30 minutes prior to laser photolysis.

Analysis of the hexane-washing solutions with UV-visible spectroscopy was used to determine the amount of organic materials incorporated into the zeolite. This was calculated from the difference between the initial amount of compound and the amount recovered in the washing solutions. The use of hexane as the incorporating solvent typically yielded 100% incorporation, while only 10-50% was achieved using dichloromethane as the incorporating solvent. In addition, using dichloromethane as the carrier solvent sometimes resulted in the thermal decomposition of the zeolite-guest complex as evidenced by the colour change of the zeolite. Hence, hexane was the solvent chosen for the incorporation of all the compounds studied in this thesis.

The thermal stability of the precursor molecules was verified using GC and UV analysis of the decanted solutions and by removal of the compound from the zeolites

through exhaustive extraction using CH_2Cl_2. Unless otherwise stated, no evidence for thermal decomposition (within the time frame of the experiments) could be found for the compounds discussed in this report.

A typical laser experiment consisted of 3-20 replicate shots per measurement, and the average signal was processed by the computer. During the acquisition of transient spectra, the samples were shaken after 1-3 laser shots to ensure a fresh sample surface was irradiated. During the acquisition of kinetic traces, the zeolite quartz container was constantly moved in the holder so that the laser continually photolyzed a fresh surface of the sample. This precaution is necessary in order to avoid light induced degradation of the sample caused by repeated irradiation of laser light.

For variable temperature experiments, the vacuum-samples were allowed to temperature equilibrate for at least 30 minutes before being photolyzed at each temperature. A water bath versus zeolite temperature calibration was acquired on a NaY zeolite sample. The occasional shaking of the sample was also taken into account to ensure a more accurate temperature reading. The sample holder for the diffuse reflectance system was attached to a circulating bath with a temperature control. The experiments were performed in a temperature range of -20 to $40\,°C$.

Inclusion of water in the hydrated zeolites involved exposure of the hot calcinated zeolite to the ambient atmosphere for 1-2 minutes prior to sample preparation. The amount of water uptake was determined by placing typical amounts of hot zeolite in a crucible and measuring the increase in mass for the determined time-period using an analytical balance. Typical water uptake amounts varied from 2-4 wt % of water in the zeolite.

4.2.4. Determination of occupancy level

Occupancy level is defined as the average number of guest molecules per zeolite cavity, <S>:

$$\langle S \rangle = \frac{N_{cpd}}{N_{cavities}}$$

4.4

where N_{cpd} is the moles of compound incorporated into the zeolite and $N_{cavities}$ is the number of moles of zeolite cavities in the sample, eq. 4.4. The number of cavities is calculated using the general equation for faujasite zeolites, eq. 4.5 where each unit cell is known to contain eight zeolite cavities.[9]

$$N_{cavities} = \frac{mass_{zeolite}}{mass / mole_{unitcells}} x \ 8 \ cavities / unitcell$$

4.5

The molar masses of the alkali metal cation zeolites used for the investigations are given in the Table 4.1 below. As the zeolite was typically weighed while hydrated, the masses shown used the hydrated unit cell formulae given for faujasite zeolites:

Y type: $M_{56}(AlO_2)_{56}(SiO_2)_{136} \cdot 253H_2O$
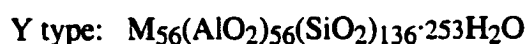
Table 4-1. Typical unit cell molar mass of alkali-metal cation faujasites.

Zeolite	Molar Mass (g/mole unit cell)
LiY	16421
NaY	17321
KY	18066
RbY	20819
CsY	23475

The loading level is often described and is the reciprocal of <S> or simply the number of cavities per molecule of compound incorporated. Typical loading levels used in this study were 1 molecule per 10 zeolite cavities.

4.2.5. Laser flash photolysis

4.2.5.1. *Transmission flash photolysis*

Laser flash photolysis (LFP) is a technique extensively used to generate, observe and study reactive species. The reactive species of interest is typically generated by a short intense pulse of laser light and then is detected by monitoring the change in absorption or reflectance of the sample as a function of time. There are three fundamental requirements for the successful use of laser flash photolysis for the study of reactive intermediates. The first is that the reactive intermediate must be generated by some photochemical reaction and that the precursor molecule is stable under the conditions that the photolysis is carried out. The second requirement is that the transients generated are observable using the detection system employed, typically UV-vis spectroscopy. Lastly, the transient must have a sufficient lifetime to be observed on the system employed, and that the light pulse used for transient generation must be shorter than the subsequent decay of the reactive intermediate to be studied. Essentially, the flash photolysis apparatus may be regarded as a time resolved absorption spectrophotometer.

The technique of flash photolysis was introduced by Norrish and Porter in the 1950s.[314,315] In these early works the sample was excited with light from a discharge lamp, and monitored either photographically over many wavelengths or photoelectrically at a single wavelength by a continuous lamp as a function of time. The relatively long duration of the exciting flash restricted the study of transient species to those with very long lifetimes; a requirement of the light source is that the pulse duration must be much shorter than any subsequent process monitored. This is called the 'blind time' of the system.

Today, laser flash photolysis provides an extremely powerful tool for the study of short-lived reactive species. The laser flash photolysis apparatus used for transmission experiments in this study is described schematically in Figure 4-1. The experiments were carried out using either the fourth harmonic of a Continuum Nd:YAG laser (266 nm, < 10 mJ/pulse, < 8 ns/pulse), or a Lambda-Physik excimer laser filled with Xe/HCl/He mixture (308 nm, < 100 mJ/pulse < 15 ns/pulse) as the excitation source. The time-resolved detection system consists of a pulsed 150 watt xenon-arc lamp, a monochromator to select the monitoring wavelength and a photomultiplier tube, which monitors changes in transmission as a function of time. Transient signals from the photomultiplier were captured with a Tektronix-620A digital oscilloscope, which was interfaced to a Macintosh PowerPC computer. The system was operated using a program written in LabVIEW® graphical programming language from National Instruments. This allowed the complete control over the experiment and over the acquisition of the data.

The set-up described above allowed for detailed kinetic and spectroscopic analysis of reactive intermediates in solution with lifetimes greater than 50 ns.
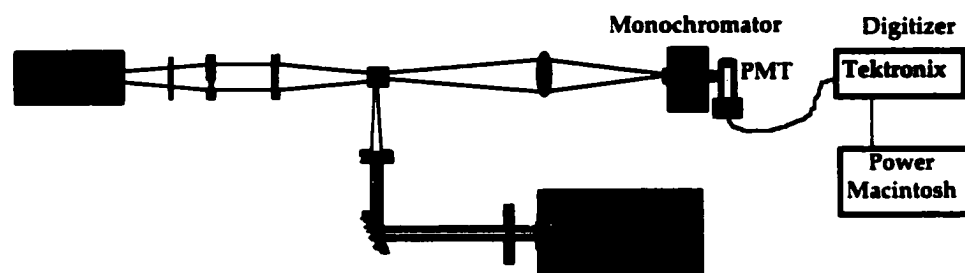
Figure 4-1. Schematic of laser flash photolysis apparatus.

The LFP system in transmission mode monitors the time-resolved change in light transmission through a sample as a function of time, generating a kinetic trace (growth or decay). A transient spectrum is then generated 'point-by-point' by obtaining absorbance values at a given point in time (time window) from traces at several different wavelengths selected with the monochromator.

The data received by the oscilloscope consists of the intensity of the monitoring beam (I_o) and an array of data points containing the photomultiplier signal voltage as a function of time, I_t. These data points are then transformed into changes in optical density (ΔO.D.) using equation 4.6.

$$\Delta A_t = A_{before} - A_{after} = \Delta O.D. = -\log\left(1 - \frac{signal}{I_o}\right) = -\log\left(\frac{I_t}{I_o}\right) \qquad 4.6$$

By the Beer-Lambert law we can assign an absorbance before (A_{before}) and after (A_{after}) excitation. The subtraction of these two values yields ΔO.D. and although we cannot obtain an absolute value for the absorbance of the transient, ΔO.D. is proportional to its concentration. Since I_o corresponds to the original intensity of the monitoring beam, it also represents the optical density of the starting material prior to flashing. As a result, a negative absorption in transient data represents a bleaching caused by higher absorption of the starting materials compared to products.

4.2.5.2. Diffuse reflectance flash photolysis

Diffuse reflectance laser photolysis is very popular for surveying transient species in various opaque solids such as organic microcrystals, powdered solid polymers, and inorganic semiconductor powders.[40,316] The technique has also been successfully applied to the photophysical and photochemical investigations of molecules adsorbed within solid supports including silica gel, alumina, and zeolites. The optical arrangement for experiments and the method of data analysis was established by Wilkinson's group in the late 1980s.[293,316,317] Time-resolved diffuse reflectance is very similar to that described above, except that the analysis of transmitted light is replaced by diffuse reflected light of a light-scattering sample.

The time-resolved diffuse reflectance experiments were carried out using a nanosecond laser system as described schematically in Figure 4-2. Typically, the excitation source was the fourth harmonic (266 nm, < 10 mJ/pulse, < 8 ns/pulse) from a Continuum Nd:YAG laser and a pulsed 75 Watt Xenon lamp was used for the monitoring

light. The powder sample was positioned at a 35-40° angle relative to both the excitation beam, and the monitoring beam (angles prevent collection of specular reflection). The diffuse reflected light from the surface of the sample cell was collected with a focusing lens and introduced into the monochromator.
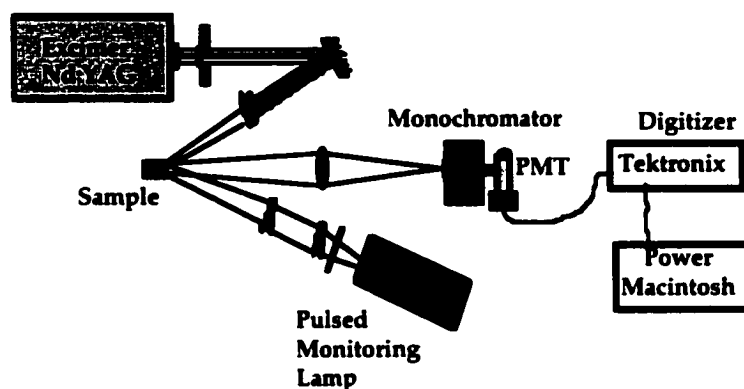
Figure 4-2. Schematic of time-resolved diffuse reflectance apparatus.

The choice of diffusely reflected light is its unpolarized and symmetrical distribution with respect to the surface normal that is irrespective of the angle of incidence or the state of polarization of the incident light. Light that has penetrated below the surface and into the interior of the zeolite particles and returns to the surface as a result of multiple scattering at individual particle surfaces is the diffuse reflected light collected and sent to the photomultiplier for data collection. Adsorbing species present within the sample after the laser pulse attenuate the reflected light from the sample and the disappearance of the absorbing species is then monitored as a function of time. In order to relate the diffuse reflected light collected from powder samples to transient concentration, it is necessary to use an analysis treatment different from that applied to solution samples. Since the diffuse reflected light from a sample consists of groups of photons with various optical pathlengths, the Beer-Lambert law cannot be directly applied to data obtained in diffuse reflection experiments. The Kubelka-Munk function has been applied for describing steady-state absorption within diffuse reflecting samples, eq. 4.7:[316]

$$F(R) = \frac{(1-R)^2}{2R} = \frac{k}{2S}$$

4.7

where $F(R)$ represents Kubelka-Munk remittance function; R the diffuse reflectance from a sample; k the absorption coefficient; and S the scattering coefficient. Thus plots of $F(R)$ versus wavelength represent absorption spectra if the scattering coefficient is wavelength-independent. The Kubelka-Munk function was extended to time-resolved spectroscopy and the transient absorption intensities were expressed by relative reflectance:

$$\text{Rel. Reflectance} = \left(1 - \frac{R}{R_o}\right) = \frac{\Delta J}{J_o} = \frac{(J_o - J_t)}{J_o}$$

4.8

in which R_o and R denote the intensity of diffusely reflected light of the probe pulse before excitation and after excitation, respectively, eq. 4.8. Reflectance data is thus given as a ratio of the reflectance of the sample (ΔJ) to the reflectance of the background (J_o) as a function of time. The value of relative reflectance is a linear function of the amount of transient present, when $\Delta J/J_o < 0.3$. This simplified kinetic analysis has been shown to be applicable to systems that have a concentration profile which decreases exponentially with penetration depth.[40,293]

4.2.5.3. Low-intensity photolysis (zeolite steady-state irradiation)

The steady-state photolysis of the aromatic carboxylic acids was carried out as follows: a large sample of dry zeolite (~2 g) containing the substrate was placed in a 400 cm^2 x 5 cm Pyrex cylinder with a quartz cover. The dry samples were magnetically stirred and purged for 30 mins before irradiation and then continuously with a slow stream of UHP-nitrogen or argon. The light source was a medium-pressure 450 W mercury lamp passed through a quartz or pyrex filter as required. The progress of the reaction could not be monitored as sampling of the zeolite and removal of the organic compound for analysis is not trivial. The duration of the photolysis usually ranged between 5-24 hrs. After photolysis, the organic components were either extracted from

the zeolite by continually washing the sample with fresh CH_2Cl_2 or by using a continuous solid-liquid extracting apparatus. Product distribution and the identity of the photoproducts were determined by GC and GC/MS in comparison to authentic compounds; the flame ionization detector was not calibrated for differences in detector response to the various products and starting materials. ^1H and ^{13}C NMR were performed on photolysis products when enough material was available. The photochemical conversions varied around 50% conversion, and the mass balance varied between 20-40% for the aromatic carboxylic acids. In all cases control experiments under dark conditions established that the products were thermally stable in the zeolite and to the extraction procedure.

4.2.6. Kinetic analysis in zeolites

In solution, the rapid diffusive movement of the solvent and solute molecules lends itself to simple averaged disruptions of solute environment and of kinetic events. As a result it is often possible to obtain simple rate constants to describe processes in fluid solution. In solid solutions, *i.e.* polymer films or solid surfaces, such simple considerations are not common. More complex situations arise such as a variety of adsorption sites for the solute which control the rates of reaction. Experiments have shown that the kinetic behavior of transients encapsulated within zeolites may be very different from simple first-order or second-order processes.[168,269] Non-exponential decay kinetics, extending over several orders of magnitude in time scale, are typically seen for solid systems. Qualitatively, these differences are well understood to have their origin in the space restriction and medium polarity of the zeolite due to its heterogeneous environment. For example, the channel and cavity structure of the zeolite may impose a considerable restriction on some types of molecular motion and these restrictions may differ depending on the location of the probe molecule within the solid support.

Decay or growth kinetic information for transient species were obtained by measuring decay traces on a number of different time scales (maximum of twelve) and then combining these into a single plot. It was sometimes necessary to normalize some

of the traces in the region where they overlapped in time; these corrections were relatively small (<5%) and arose due to variations in laser power. The data was acquired over a wide range of time scales varying from 2 μs to 1000 μs after the laser pulse. These time scales are limited by the laser system employed.

The observed non-exponential time dependence observed for a wide variety of processes within zeolites and other non-homogeneous media is often referred to as a "stretched" exponential decay. Many models have been proposed for these observations, the simplest of which leads to a distribution of first-order rate constants. Rate laws derived from reaction schemes consisting of any number and combination of consecutive and parallel first-order reaction steps can be integrated in closed form to give a sum of exponential terms:

$$A_{obs}(t) = A_o + A_1 exp(-k_1 t) + A_2 exp(-k_2 t) + \ldots \qquad 4.9$$

where each k_i value represents a rate constant for the reaction of the transient, eq. 4.9. Similarly, we can apply the above equation to diffuse reflectance changes with time. In this scenario, the processes can be described in terms of a distribution of first-order rate constants referring to a distribution of sites or reactions, eq. 4.10.

$$\left(\frac{\Delta J}{J_o}\right)_t = C_o + C_1 exp(-k_1 t) + C_2 exp(-k_2 t) + C_3 exp(-k_3 t) + \ldots \qquad 4.10$$

In the simplest case, transient decay or formation can be explained with a first-order or pseudo first-order kinetic equation, eq. 4.11. When using this method of a sum of exponentials, one must keep in mind that enough adjustable terms in the sum virtually assure a fit to the data, but the results may then have no physical significance.

$$\left(\frac{\Delta J}{J_o}\right)_t = C_1 exp(-k_1 t) \qquad 4.11$$

The program TimeMaster™ (version 1.2) by Photon Technology International uses the exponential series method[235] (ESM) to uncover the lifetime distribution (τ_i) from experimental decay data. This program uses a sum of exponentials with 10 to 200 terms of fixed lifetime values. The program chooses the best fit by varying the contribution of each lifetime (pre-exponential coefficient) to the total decay equation. This method allows the measurement of two or more vastly different lifetimes hidden within one set of data. In addition, the technique allows the study of transient kinetic behaviour within heterogeneous systems without prior assumption about the number of components present in the data.

Analysis of kinetic traces of zeolite systems using the ESM method often revealed that the traces are best described by two or three distinct lifetimes. Similar results were obtained for kinetic fits obtained assuming that two or three first-order exponential functions present in the system. As the time cost for the analysis using set exponential equations is much cheaper than the ESM analysis, rate constants given in this thesis were calculated using a multiple exponential fit, as appropriate.

In the case of bimolecular reactions, a simple approach as the one described above cannot be used since the combination process must be second order. However, the analysis method using a combination of second-order rate constants adequately reproduced the observed decay profile, equation 4.12 or 4.13. The decay was considered as a mixture of one or two second order process with a shift corresponding to non-decaying transients. This analysis method allowed to qualitatively describe the experimental results among the various radical systems.

$$\left(\frac{\Delta J}{J_o}\right)_t = C_o + \frac{1}{C_1 + \frac{S}{2\varepsilon}k_1 t} \qquad\qquad 4.12$$

$$\left(\frac{\Delta J}{J_o}\right)_t = C_o + \frac{1}{C_1 + \frac{S}{2\varepsilon}k_1 t} + \frac{1}{C_2 + \frac{S}{2\varepsilon}k_2 t} \qquad\qquad 4.13$$

References

1. Kleinman, M. H.; Bohne, C. In *Molecular and Supramolecular Photochemistry*; Marcel Dekker, Inc.: New York, 1997; Vol. 1.

2. Ramamurthy, V. In *Photochemistry in Organized and Constrained media*; VCH: New York, 1991, pp 429-493.

3. Ramamurthy, V.; Eaton, D. F. *Chem. Mater.* **1994**, *6*, 1128-1136.

4. Weiss, R. G.; Ramamurthy, V.; Hammond, G. S. *Acc. Chem. Res.* **1993**, *26*, 530-536.

5. Brotin, T.; Lesage, A.; Emsley, L.; Collet, A. *J. Am. Chem. Soc.* **2000**, *122*, 1171-1174.

6. Tao, W.; Barra, M. *J. Org. Chem.* **2001**, *66*, 2158-2160.

7. Ramamurthy, V.; Eaton, D. F.; Caspar, J. V. *Acc. Chem. Res.* **1992**, *25*, 299-307.

8. Breck, D. W. *J. Chem. Educ.* **1964**, *41*, 678-689.

9. Breck, D. W. *Zeolite Molecular Sieves: Structure, Chemistry and Use*; Robert E. Krieger Publishing Company: New York, 1974.

10. Dutta, P. K. *J. Incl. Phenom. Mol. Recog. Chem.* **1995**, *21*, 215-237.

11. Joy, A.; Scheffer, J. R.; Ramamurthy, V. *Org. Lett.* **2000**, *2*, 119-121.

12. Mumpton, F. A. *Proc. Natl. Acad. Sci. USA* **1999**, *96*, 3463-3470.

13. Sherman, J. D. *Proc. Natl. Acad. Sci. USA* **1999**, *96*, 3471-3478.

14. Thomas, J. M. *Sci. Am.* **1992**, 112-118.

15. Turro, N. J. *Acc. Chem. Res.* **2000**, *33*, 637-646.

16. Adam, W.; García, H.; Martí, V.; Moorthy, J. N.; Peters, K.; Peters, E. M. *J. Am. Chem. Soc.* **2000**, *122*, 3536-3537.

17. Weiqiang, G.; Warrier, M.; Ramamurthy, V.; Weiss, R. G. *J. Am. Chem. Soc.* **1999**, *121*, 9467-9468.

18. Scaiano, J. C.; García, S.; García, H. *Tetrahedron Lett.* **1997**, *38*, 5929-5932.

19. Park, Y. S.; Lee, K.; Lee, C.; Yoon, K. B. *Langmuir* **2000**, *16*, 4470-4477.

20. Heinemann, H. *Catal. Rev. Sci. Eng.* **1981**, *23*, 315-328.

21. Rabo, J. A.; Gajda, G. J. *Catal. Rev. Sci. Eng.* **1989-1990**, *31*, 385-430.

22. Clingenpeel, T. H.; Biaglow, A. I. *J. Am. Chem. Soc.* **1997**, *119*, 5077-5078.

23. Choudary, B. M.; Kantam, M. L.; Santhi, P. L. *Catal. Today* **2000**, *57*, 17-32.

24. Jayaraman, S.; Uppili, S.; Natarajan, A.; Joy, A.; Chong, K. C. W.; Netherton, M. R.; Zenova, A.; Scheffer, J. R.; Ramamurthy, V. *Tetrahedron Lett.* **2000**, *41*, 8231-8235.

25. Clennan, E. L.; P., S. J. *Tetrahedron* **2000**, *56*, 6945-6950.

26. Joy, A.; Uppili, S.; Netherton, M. R.; Scheffer, J. R.; Ramamurthy, V. *J. Am. Chem. Soc.* **2000**, *122*, 728-729.

27. Shailaja, J.; Ponchot, K. J.; Ramamurthy, V. *Org. Lett.* **2000**, *2*, 937-940.

28. Jones, C. W.; Tsapatsis, M.; Okubo, T.; Davis, M. E. *Microporous Mesoporous Mater.* **2001**, *42*, 21-35.

29. Scaiano, J. C.; García, H. *Acc. Chem. Res.* **1999**, *32*, 783-793.

30. Spackman, M. A.; Weber, H. P. *J. Phys. Chem.* **1988**, *92*, 794-796.

31. Li, W.; Lei, X.; Lem, G.; McDermott, A. E.; Turro, N. J. *Chem. Mater.* **2000**, *12*, 731-737.

32. Olson, D. H. *J. Phys. Chem.* **1970**, *74*, 2758-2764.

33. Hriljac, J. A.; Eddy, M. M.; Cheetham, A. K.; Donohue, J. A.; Ray, G. J. *J. Solid State Chem.* **1993**, *106*, 66-72.

34. Zhu, L.; Seff, K. *J. Phys. Chem. B* **2000**, *104*, 8946-8951.

35. Davidson, A. M.; Mellot, C. F.; Eckert, J.; Cheetham, A. K. *J. Phys. Chem. B.* **2000**, *104*, 432-438.

36. Lim, K. H.; Grey, C. P. *J. Am. Chem. Soc.* **2000**, *122*, 9768-9780.

37. Fyfe, C. A.; Bretherton, J. L.; Lam, L. Y. *Chem. Commun.* **2000**, 1575-1576.

38. Klinowski, J. *Chem. Rev.* **1991**, *91*, 1459.

39. Davis, M. E. *Acc. Chem. Res.* **1993**, *26*, 111-115.

40. Hashimoto, S. In *Solid State and Surface Photochemistry*; Marcel Dekker, Inc.: New York, 2000; Vol. 5, pp 253-294.

41. Loewenstein, W. *Am. Mineral* **1954**, *39*, 92-96.

42. Ramamurthy, V.; Sanderson, D. R.; Eaton, D. F. *J. Phys. Chem.* **1993**, *97*, 13380-13386.

43. Ramamurthy, V.; Sanderson, d. R.; Eaton, D. F. *Photochem. Photobiol.* **1992**, *56*, 297-303.

44. Ramamurthy, V.; Turro, N. J. *J. Inclus. Phenom. Mol. Recog. Chem.* **1995**, *21*, 239-282.

45. Liu, X.; Iu, K. K.; Thomas, J. K.; He, H.; Klinowski, J. *J. Am. Chem. Soc.* **1994**, *116*, 11811-11818.

46. Richardson, J. T. *J. Catal.* **1967**, *9*, 178-181.

47. Corma, A. *Chem. Rev.* **1995**, *95*, 559-614.

48. Kamble, V. S.; Gupta, N. M. *Phys. Chem. Chem. Phys.* **2000**, *2*, 2661-2665.

49. Kamble, V. S.; Gupta, N. M. *J. Phys. Chem. B* **2000**, *104*, 4588-4592.

50. Ramamurthy, V.; Corbin, D. R.; Johnston, L. J. *J. Am. Chem. Soc.* **1992**, *114*, 3870-3882.

51. Corma, A.; García, H.; Sastre, G.; Viruela, P. M. *J. Phys. Chem. B* **1997**, *101*, 4575-7582.

52. Huang, M.; Kaliaguine, S.; Auroux, A. *J. Phys. Chem.* **1995**, *99*, 9952-9959.

53. Norby, P.; Poshni, F. I.; Gualtieri, A. F.; Hanson, J. C.; Grey, C. P. *J. Phys. Chem. B* **1998**, *102*, 839-856.

54. Hunger, B.; Klepel, O.; Kirschhock, C.; Heuchel, M.; Toufar, H.; H., F. *Langmuir* **1999**, *15*, 5937-5941.

55. Kirschhock, C. E. A.; Hunger, B.; Marten, J.; Jacobs, P. A. *J. Phys. Chem. B* **2000**, *104*, 439-448.

56. Yoon, K. B. In *Solid State and Surface Photochemistry*; Marcel Dekker, Inc.: New York, 2000; Vol. 5, pp 143-251.

57. Yang, S.; Navrotosky, A. *Microporous Mesoporous Mater.* **2000**, *37*, 175-186.

58. Iu, K.; Liu, X.; Thomas, J. K. *J. Phys. Chem.* **1993**, *97*, 8165-8170.

59. Iu, K. K.; Liu, X. S.; Thomas, J. K. *J. Photochem. Photobiol. A: Chem.* **1994**, *79*, 103-107.

60. Gessner, F.; Scaiano, J. C. *J. Photochem. Photobiol. A: Chem.* **1992**, *67*, 91-100.

61. Hashimoto, S.; Mutoh, T.; Fukumura, H.; Masuhara, H. *J. Chem. Soc., Faraday Trans.* **1996**, *92*, 3653-3660.

62. Hashimoto, S.; fukazawa, N.; Fukumura, H.; Masuhara, H. *Chem. Phys. Lett.* **1994**, *219*, 445-451.

63. Zhang, Z.; Turro, N. J.; Johnston, L.; Ramamurthy, V. *Tetrahedron Lett.* **1996**, *37*, 4861-4864.

64. Ramamurthy, V.; Sanderson, D. R.; Eaton, D. F. *J. Am. Chem. Soc.* **1993**, *115*, 10438-10439.

65. Shailaja, J.; Sivaguru, J.; Robbins, R. J.; Ramamurthy, V.; Sunoj, R. B.; Chandrasekhar, J. *Tetrahedron* **2000**, *56*, 6927-6943.

66. Matsubara, C.; Kojima, M. *Tetrahedron Lett.* **1999**, *40*, 3439-3442.

67. Corma, A.; Esteve, P.; Martínez, A. *J. Catal.* **1996**, *161*, 11-19.

68. Kao, H. M.; Grey, C. P.; Pitchumani, K.; Lakshminarasimhan, P. H.; Ramamurthy, V. *J. Phys. Chem. A* **1998**, *102*, 5627-2638.

69. Thomas, K. J.; Ramamurthy, V. *Langmuir* **1998**, *14*, 6687-6692.

70. Lavalley, J. C.; Anquetil, R.; Czyzniewska, J.; Ziolek, M. *J. Chem. Soc., Faraday Trans.* **1996**, *92*, 1263-1266.

71. Sánchez Sanchez, M.; Blasco, T. *Chem. Commun.* **2000**, 491-492.

72. Ward, J. W. *J. Catal.* **1968**, *11*, 238-250.

73. Farneth, W. E.; Gorte, R. J. *Chem. Rev.* **1995**, *95*, 615-635.

74. Liu, X.; Iu, K.; Thomas, J. K. *J. Phys. Chem.* **1994**, *98*, 7877-7884.

75. Barthomeuf, D. In *Acidity and Basicity of Solids*; Fraissard, J., Petrakis, L., Eds.; Kluwer Academic Publishers: Netherlands, 1994, pp 181-197.

76. Huang, M.; Adnot, A.; Kaliaguine, S. *J. Catal.* **1992**, *137*, 322-332.

77. Ward, J. W. *J. Catal.* **1968**, *10*, 34-46.

78. Okamoto, Y.; Ogawa, M.; Maezawa, A.; Imanaka, T. *J. Catal.* **1988**, *112*, 427-436.

79. Liu, X.; Thomas, J. K. *Langmuir* **1993**, *9*, 727-732.

80. Cano, M. L.; Corma, A.; Fornes, V.; Garcia, H. *J. Phys. Chem.* **1995**, *99*, 4241-4246.

81. Gener, I.; Moisette, A.; Brémard, C. *Chem. Commun.* **2000**, *17*, 1563-1564.

82. Choi, S. Y.; Park, Y. S.; Hong, S. B.; Yoon, K. B. *J. Am. Chem. Soc.* **1996**, *118*, 9377-9386.

83. Uytterhoeven, L.; Dompas, D.; Mortier, W. J. *J. Chem. Soc., Faraday Trans.* **1992**, *88*, 2753.

84. Deka, R. C.; Roy, R. K.; Hirao, K. *Chem. Phys. Lett.* **2000**, *332*, 576-582.

85. Ramamurthy, V.; Lakshminarasimhan, P.; Grey, C. P.; Johnston, L. J. *Chem. Commun.* **1998**, 2411-2424.

86. Panov, A. G.; Larsen, R. G.; Totah, N. I.; Larsen, S. C.; Grassian, V. H. *J. Phys. Chem. B* **2000**, *104*, 5706-5714.

87. Rao, V. J.; Perlstein, D. L.; Robbins, R. J.; Lakshminarasimhan, P. H.; Kao, H.; Grey, C. P.; Ramamurthy, V. *Chem. Commun.* **1998**, 269-270.

88. Corrent, S.; Martínez, L. J.; Scaiano, J. C. *J. Phys. Chem. B* **1999**, *103*, 8097-8103.

89. Scaiano, J. C.; Kaila, M.; Corrent, S. *J. Phys. Chem. B* **1997**, *101*, 8564-8568.

90. Corrent, S.; Hahn, P.; Phlers, G.; Connolly, T.; Scaiano, J. C.; Fornés, V.; García, H. *J. Phys. Chem. B* **1998**, *102*, 5852-5858.

91. Li, X.; Ramamurthy, V. R. *Tetrahedron Lett.* **1996**, *37*, 5235-5238.

92. Cozens, F. L.; Bogdanova, R.; Regimbald, M.; Garcia, H.; Marti, V.; Scaiano, J. C. *J. Phys. Chem. B* **1997**, *101*, 6921-6829.

93. Zhou, W.; Clennan, E. L. *J. Am. Chem. Soc.* **1999**, *121*, 2915-2916.

94. Evans, D. F. *J. Chem. Soc.* **1953**, 345-347.

95. Rabo, J. A.; Angell, C. L.; Kasai, P. H.; Schomaker, V. *Discuss. Faraday Soc.* **1966**, *41*, 328-349.

96. Sastre, G.; Lewis, D. W.; Corma, A. *Phys. Chem. Chem. Phys.* **2000**, *2*, 177-185.

97. Preuss, E.; Linden, G.; Peuckert, M. *J. Phys. Chem.* **1985**, *89*, 2955-2961.

98. Stich, I.; Gale, J. D.; Terakura, K.; Payne, M. C. *J. Am. Chem. Soc.* **1999**, *121*, 3292.

99. Martínez Morales, E.; Zicovich-Wilson, C. M.; Sánchez Sánchez, J. E.; Alvarez, L. J. *Chem. Phys. Lett.* **2000**, *327*, 224-229.

100. Ramamurthy, V.; Robbins, R. J.; Thomas, K. J.; Lakshminarasimhan, P. H. In *Organised Molecular Assemblies in the Solid State*; Whitesell, J. K., Ed.; John Wiley & Sons Ltd.: New York, 1999; Vol. 2, p 63.

101. Baretz, B.; Turro, N. J. *J. Photochem.* **1984**, *24*, 201-205.

102. Yoon, K. B.; Kochi, J. K. *J. Am. Chem. Soc.* **1989**, *111*, 1128-1130.

103. Yoon, K. B.; Kochi, J. K. *J. Am. Chem. Soc.* **1988**, *110*, 6587-6588.

104. Liu, X.; Iu, K. K.; Thomas, J. K. *J. Phys. Chem.* **1989**, *93*, 4120-4128.

105. Iu, K. K.; Thomas, J. K. *Langmuir* **1990**, *6*, 471-478.

106. Sarkar, N.; Das, K.; Natha, D. N.; Bhattacharyya, K. *Langmuir* **1994**, *10*, 326-329.

107. Uppili, S.; Thomas, K. J.; Crompton, E. M.; Ramamurthy, V. *Langmuir* **2000**, *16*, 265-274.

108. Lindley, S. M.; Flowers, G. C.; Leffler, J. E. *J. Org. Chem.* **1985**, *50*, 607-610.

109. Turbeville, W.; Dutta, P. K. *J. Phys. Chem.* **1990**, *94*, 4060-4066.

110. Dutta, P. K.; Turbeville, W. *J. Phys. Chem.* **1991**, *95*, 4087-4092.

111. Handreck, G. P.; Smith, T. D. *J. Chem. Soc., Faraday Trans. 1* **1988**, *84*, 1847.

112. Frei, H.; Blatter, F.; Sun, H. *Chemtech.* **1996**, *26*, 24-30.

113. Yoon, K. B.; Hubig, S. M.; Kochi, J. K. *J. Phys. Chem.* **1994**, *98*, 3865-3871.

114. Hashimoto, S.; Hagiwara, N.; Asahi, T.; Masuhara, H. *Langmuir* **1999**, *15*, 3123-3133.

115. Blatter, F.; Sun, H.; Frei, H. *Catal. Lett.* **1995**, *35*, 1-12.

116. Blatter, F.; Frei, H. *J. Am. Chem. Soc.* **1993**, *115*, 7501-7502.

117. Blatter, F.; Frei, H. *J. Am. Chem. Soc.* **1994**, *116*, 1812-1820.

118. Ramamurthy, V. *J. Am. Chem. Soc.* **1994**, *116*, 1345-1351.

119. Klein, H.; Kirschhock, C.; Fuess, H. *J. Phys. Chem.* **1994**, *98*, 12345-12360.

258

120. Liu, S. B.; Ma, L. J.; Lin, M. W.; Wu, J. F.; Chen, T. L. *J. Phys. Chem.* **1992**, *96*, 8120-8125.

121. Pearson, J. G.; Chmelka, B. F.; Shykind, D. N.; Pines, A. *J. Phys. Chem.* **1992**, *96*, 8517-8522.

122. Hong, S. B.; Cho, H. M.; Davis, M. E. *J. Phys. Chem.* **1993**, *97*, 1622-1628.

123. Su, B. L.; Norberg, V. *Langmuir* **2000**, *16*, 6020-6028.

124. Parise, J. B. *J. Inclusion Phenom. Molec. Recog. Chem.* **1995**, *21*, 79-112.

125. Ramamurthy, V.; Caspar, J. V.; Corbin, D. R.; Eaton, D. F. *J. Photochem. Photobiol. A: Chem.* **1989**, *50*, 157-161.

126. Ramamurthy, V.; Caspar, J. V.; Corbin, D. R.; Eaton, D. F.; Kauffman, J. S.; Dybowski, C. *J. Photochem. Photobiol. A: Chem.* **1990**, *51*, 259-263.

127. Demontis, P.; Suffritti, G. B. *Chem. Rev.* **1997**, *97*, 2845-2878.

128. Auerback, S. M.; Metiu, H. I. *J. Chem. Phys.* **1996**, *105*, 3753-3760.

129. Thomas, K. J. *Langmuir* **2000**, *16*, 4912-4921.

130. Hunger, M.; Schenk, U.; Buchholz, A. *J. Phys. Chem. B* **2000**, *104*, 12230-12236.

131. Yeom, Y. H.; Kim, A. N.; Y., K.; Song, S. H.; Seff, K. *J. Phys. Chem. B* **1998**, *102*, 6071-6077.

132. Hashimoto, S.; Ikuta, S.; Asahi, T.; Masuhara, H. *Langmuir* **1998**, *14*, 4284-4291.

133. Hepp, M. A.; Ramamurthy, V.; Corbin, D. R.; Dybowski, C. *J. Phys. Chem.* **1992**, *96*, 2629-2632.

134. Auerbach, S. M.; Metiu, H. I. *J. Chem. Phys.* **1997**, *106*, 2893-2905.

135. Forrester, T. R.; Smith, W. *J. Chem. Soc., Faraday Trans.* **1997**, *17*, 3249-3257.

136. Demontis, P.; Kärger, J.; Suffritti, G. B.; Tilocca, A. *Phys. Chem. Chem. Phys.* **2000**, *2*, 1455-1463.

137. Clark, L. A.; Ye, G. T.; Snurr, R. Q. *Phys. Rev. Lett.* **2000**, *84*, 2893-2896.

138. Paschek, D.; Krishna, R. *Langmuir* **2001**, *17*, 247-254.

139. Blanco, C.; Saravanan, C.; Allen, M.; Auerbach, S. M. *J. Chem. Phys.* **2000**, *113*, 9778-9787.

140. Dukovski, I.; Machta, J.; Saravanan, C.; Auerbach, S. M. *J. Chem. Phys.* **2000**, *113*, 3697-3703.

141. Jobic, H.; Fitch, A. N.; Combet, J. *J. Phys. Chem.* **2000**, *104*, 8491-8497.

142. Barzkin, A. V.; Hashimoto, S. *J. Chem. Phys.* **2000**, *113*, 2841-2845.

143. Jousse, F.; Auerbach, S. M.; Vercauteren, D. P. *J. Chem. Phys.* **2000**, *112*, 1531-1540.

144. Favre, D. E.; Schaefer, D. J.; Auerback, S. M.; Chmelka, B. F. *Phys. Rev. Lett.* **1998**, *81*, 5852-5855.

145. Martens, L. R. M.; Grobet, P. J.; Jacobs, P. A. *Nature* **1985**, *315*, 568-570.

146. Harrison, M. R.; Edwards, P. P.; Klinowski, J.; Thomas, J. M. *J. Solid State Chem.* **1984**, *54*, 330-341.

147. Liu, X.; Thomas, J. K. *Chem. Phys. Lett.* **1992**, *192*, 555-559.

148. Edwards, P. P.; Woodal, L. J.; Anderson, P. A.; R., A. A.; Slaski, M. *Chem. Soc. Rev.* **1993**, *22*, 305-312.

149. Xu, B.; Kevan, L. *J. Phys. Chem.* **1992**, *96*, 2542-2645.

150. Shibata, W.; Seff, K. *J. Phys. Chem.* **1997**, *101*, 9022-9026.

151. Sun, T.; Seff, K. *J. Phys. Chem.* **1993**, *97*, 5213-5214.

152. Sun, T.; Seff, K.; Heo, N. H.; Petranovskii, V. P. *Science* **1993**, *259*, 495- 497.

153. Kim, Y.; Han, H. W.; Seff, K. *J. Phys. Chem.* **1993**, *97*, 12663-12664.

154. Armstrong, A. R.; Anderson, P. A.; Woodall, L. J.; Edwards, P. P. *J. Am. Chem. Soc.* **1995**, *117*, 9087-9088.

155. Thomas, J. K. *Chem. Rev.* **1993**, *93*, 301-320.

156. Zhang, G.; Liu, X.; Thomas, J. K. *Radiat. Phys. Chem.* **1998**, *51*, 135-152.

157. Nakano, T.; Ikemoto, T.; Nozue, Y. *Mol. Cryst. Liq. Cryst.* **2000**, *341*, 1265-1270.

158. Ikemoto, Y.; Nakano, T.; Kuno, M.; Nozue, Y. *Mol. Cryst. Liq. Cryst.* **2000**, *341*, 1257-1263.

159. Iu, K. K.; Thomas, J. K. *J. Phys. Chem.* **1991**, *95*, 506-509.

160. Liu, X.; Zhang, G.; Thomas, J. K. *J. Phys. Chem.* **1995**, *99*, 10024-10034.

161. Liu, X.; Thomas, J. K. *Langmuir* **1992**, *8*, 1750-1756.

162. Takatani, S.; Fukumura, H.; Masuhara, H.; Hashimoto, S. *J. Phys. Chem. B* **1997**, *101*, 3365-3369.

163. Liu, X.; Zhang, G.; Thomas, J. K. *J. Phys. Chem. B* **1997**, *101*, 2182-2194.

164. Ursenbach, C. P.; Madden, P. A.; Stich, I.; Payne, M. C. *J. Phys. Chem.* **1995**, *99*, 6697-6714.

165. O'Neill, M. In *Nanosecond Time-Resolved Diffuse Reflectance Studies of Reactive Carbocations and Charge Migration in Non-Acidic Zeolites*; Ph. D.; Dalhousie University: Halifax, Nova Scotia, 2001.

166. O'Neill, M. A.; Cozens, F. L.; Schepp, N. P. *Tetrahedron* **2000**, *56*, 6969-6977.

167. Cozens, F. L.; Ortiz, W.; Schepp, N. P. *J. Am. Chem. Soc.* **1998**, *120*, 13543-13544.

168. Jockusch, S.; Hirano, T.; Liu, Z.; Turro, N. J. *J. Phys. Chem. B* **2000**, *104*, 1212-1216.

169. Werst, D. W.; Tartakovsky, E. E.; Piocos, E. A.; Trifunac, A. D. *J. Phys. Chem.* **1994**, *98*, 10249-10257.

170. Cano, M. L.; Fornes, V.; Garcia, H.; Miranda, M. A.; Pérez-Prieto, J. *J. Chem. Soc., Chem. Commun.* **1995**, 2477-2478.

171. García, H.; García, S.; Pérez-Prieto, J.; Scaiano, J. C. *J. Phys. Chem.* **1996**, *100*, 18158-18164.

172. Fornés, V.; García, H.; Martí, V.; Fernández, L. *Tetrahedron* **1998**, *54*, 3827-3832.

173. Pitchumani, K.; Lakshminarasimhan, P. H.; Prevost, N.; Corbin, D. R.; Ramamurthy, V. *Chem. Commun.* **1997**, 181-182.

174. Fernández, L.; Martí, V.; García, H. *Phys. Chem. Chem. Phys.* **1999**, *1*, 3689-3695.

175. Caspar, J. V.; Ramamurthy, V.; Corbin, D. R. *J. Am. Chem. Soc.* **1991**, *113*, 600-610.

176. Chen, F. R.; Fripiat, J. J. *J. Phys. Chem.* **1992**, *96*, 819-823.

177. Rhodes, C. J. *Colloids Surf. A.* **1993**, *72*, 111-118.

178. Roduner, E.; Wu, L. M.; Crockett, R. *Catalysis Letters* **1992**, *14*, 373-379.

179. Ramamurthy, V.; Caspar, J. V.; Corbin, D. R. *J. Am. Chem. Soc.* **1991**, *113*, 594-600.

180. Cozens, F. L.; García, H.; Scaiano, J. C. *Langmuir* **1994**, *10*, 2246-2249.

181. Brede, O.; David, F.; Steenken, S. *J. Chem. Soc., Perkin Trans. 2* **1995**, 23-32.

182. Brede, O.; David, F.; Steenken, S. *J. Photochem. Photobiol. A: Chem.* **1996**, 127-131.

183. Rao, V. J.; Prevost, N.; Ramamurthy, V.; Kojima, M.; Johnston, L. J. *Chem. Commun.* **1997**, 2209-2210.

184. Mohr, M.; Marx, D.; Parrinello, M.; Zipse, H. *Chem. Eur. J.* **2000**, *6*, 4009-4015.

185. Johnston, L. J.; Schepp, N. P. *J. Am. Chem. Soc.* **1993**, *115*, 6564-6571.

186. Schepp, N. P.; Johnston, L. J. *J. Am. Chem. Soc.* **1994**, *116*, 6895-6903.

187. Beckwith, A. L.; Crich, D.; Duggan, P. I.; Yao, Q. *Chem. Rev.* **1997**, *97*, 3273-3312.

188. Mohr, M.; Zipse, H. *Chem. Eur. J.* **1999**, *5*, 3046-3054.

189. Robins, M. J.; Guo, Z. Q.; Samano, M. C.; Wnuk, S. F. *J. Am. Chem. Soc.* **1999**, *121*, 1425-1433.

190. Glatthar, R.; Spichty, M.; Gugger, A.; Batra, R.; Damm, W.; Mohr, M.; Zipse, H.; Giese, B. *Tetrahedron* **2000**, *56*, 4117-4128.

191. Giese, B.; Beyrich-Graf, X.; Burger, J.; Kesselheim, C.; Senn, M.; Schäfer, T. *Angew. Chem. Int. Ed. Engl.* **1993**, *32*, 1742-1743.

192. Giese, B.; Erdmann, P.; Giraud, L.; Göbel, T.; Petretta, M.; Schäfer, T. *Tetrahedron Lett.* **1994**, *35*, 2683-2686.

193. Stubbe, J.; Kozarich, J. W.; Wu, W.; Vanderwall, D. E. *Acc. Chem. Res.* **1996**, *29*, 322-330.

194. Müller, S. N.; Batra, R.; Senn, M.; Giese, B.; Kisel, M.; Shadyro, O. *J. Am. Chem. Soc.* **1997**, *119*, 2795-2803.

195. Scaiano, J. C.; Netto-Ferreira, J. C.; Wintgens, V. *J. Photochem. Photobiol. A: Chem.* **1991**, *59*, 265-268.

196. Koltzenburg, G.; Behrens, G.; Schulte-Frohlinde, D. *J. Am. Chem. Soc.* **1982**, *104*, 7311-7312.

197. Koltzenburg, G.; Bastian, E.; Steenken, S. *Angew. Chem. Int. Ed. Engl.* **1988**, *27*, 1066-1067.

198. Zipse, H. *Acc. Chem. Res.* **1999**, *32*, 571-578.

199. Zipse, H. *Angew. Chem. Int. Ed. Engl.* **1994**, *33*, 1985-1988.

200. Cozens, F. L.; O'Neill, M.; Bogdanova, R.; Schepp, N. *J. Am. Chem. Soc.* **1997**, *119*, 10652-10660.

201. Newcomb, M.; Miranda, N.; Huang, X.; Crich, D. *J. Am. Chem. Soc.* **2000**, *122*, 6128-6129.

202. Scaiano, J. C.; Barra, M.; Krzywinski, M.; Sinta, R.; Calabrese, G. *J. Am. Chem. Soc.* **1993**, *115*, 8340-8344.

203. Scaiano, J. C.; Barra, M.; Calabrese, G.; Sinta, R. *J. Chem. Soc., Chem. Commun.* **1992**, 1418-1419.

204. Choi, S. Y.; Crich, D.; Horner, J. H.; Huang, X.; Newcomb, M.; Whitted, P. O. *Tetrahedron* **1999**, *55*, 3317-3326.

205. Newcomb, M.; Horner, J. H.; Whitted, P. O.; Crich, D.; Huang, X.; Yao, Q.; Zipse, H. *J. Am. Chem. Soc.* **1999**, *121*, 10685-10694.

206. Barclay, L. R. C.; Lusztyk, J.; Ingold, K. U. *J. Am. Chem. Soc.* **1984**, *106*, 1793-1796.

207. Beckwith, A. L. J.; Duggan, P. J. *J. Am. Chem. Soc.* **1996**, *118*, 12838-12839.

208. Zipse, H. *J. Chem. Soc., Perkin Trans. 2* **1996**, 1797-1800.

209. Zipse, H. *J. Am. Chem. Soc.* **1997**, *119*, 1087-1093.

210. Zipse, H. *J. Am. Chem. Soc.* **1997**, *119*, 2889-2893.

211. Kevill, D. N. In *Advances in Quantitative Structure-Property Relationships*; JAI Press Inc., 1996; Vol. 1, pp 81-115.

212. Kamlet, M. J.; Taft, R. W. *J. Chem. Soc., Perkin Trans. 2* **1979**, 349-356.

213. Reichardt, C. *Chem. Rev.* **1994**, *94*, 2319-2358.

214. Bentley, T. W.; Llewellyn, G. *Prog. Phys. Org. Chem.* **1990**, *17*, 121-158.

215. Liu, K. T.; Chen, H. I. *J. Chem. Soc., Perkin Trans. 2* **2000**, *10*, 893-898.

216. Bentley, T. W.; Carter, G. E. *J. Org. Chem.* **1983**, *48*, 579-584.

217. Kevill, D. N.; Pinhas, A. R. *J. Org. Chem.* **1993**, *58*, 197-201.

218. Lowry, T. H.; Richardson, K. S. *Mechanism and Theory in Organic Chemistry*; 3rd ed.; Harper & Row: New York, 1987.

219. Bentley, T. W. *J. Am. Chem. Soc.* **1982**, *104*, 5741-5747.

220. Liu, K. T.; Chang, C. W.; Chen, H. I.; Chin, C. P.; Duann, Y. F. *J. Phys. Org. Chem.* **2000**, *13*, 203-207.

221. Kevill, D. N.; Abduljaber, M. H. *J. Org. Chem.* **2000**, *65*, 2548-2554.

222. Bentley, T. W.; Carter, G. E.; Roberts, K. *J. Org. Chem.* **1984**, *49*, 5183-5189.

223. Bentley, T. W.; Roberts, K. *J. Chem. Soc., Perkin Trans. 2* **1989**, 1055-1060.

224. Dvorko, G. F.; Pervishko, T. L.; Leunov, D. I.; Ponomareva, E. A. *Russ. J. Org. Chem.* **1999**, *35*, 1643-1647.

225. Schepp, N. P.; Johnston, L. J. *J. Am. Chem. Soc.* **1993**, *119*, 10652-10659.

226. March, J. *Advanced Organic Chemistry - Reactions, Mechanisms and Structure*; 4th. ed.; John Wiley & Sons: New York, 1992.

227. Carroll, F. A. *Perspectives on Structure and Mechanism in Organic Chemistry*; 1st ed.; Brooks/Cole Publishing Co.: Pacific Grove, CA, 1998.

228. Kyong, J. B.; Park, B. C.; Kim, C. B.; Kevill, D. N. *J. Org. Chem.* **2000**, *65*, 8051-8058.

229. Frost, A. A.; Pearson, R. G. *Kinetics and Mechanism*; 2nd ed.; John Wiley & Sons: New York, 1961.

230. Fujio, M.; Goto, M.; Susuki, T.; Akasaka, I.; Mishima, M.; Tsuno, Y. *Bull. Chem. Soc. Japan* **1990**, *63*, 1146-1153.

231. The loading level for these samples is one molecule in every five cavities as significantly weaker signals than for the chloro-substituted molecules were obtained.

232. Ramamurthy, V.; Caspar, J. V.; Eaton, D. F.; Kuo, E. W.; Corbin, D. R. *J. Am. Chem. Soc.* **1992**, *114*, 3882-3892.

233. Due to the extremely low laser intensities obtained with the 266nm YAG laser during the time period for these experiments, the laser beam was focused onto the sample thus increasing the probability of photoionization occuring.

234. Gehlen, M. H.; De Schryver, F. C. *Chem. Rev.* **1993**, *93*, 199-221.

235. Wagner, B. D.; Ware, W. R. *J. Phys. Chem.* **1990**, *94*, 3489-3494.

236. Maslak, P.; Asel, S. L. *J. Am. Chem. Soc.* **1988**, *110*, 8260-8261.

237. Popielarz, R.; Arnold, D. R. *J. Am. Chem. Soc.* **1990**, *112*, 3068-3082.

238. Cozens, F. L.; Schepp, N. P. *Unpublished results.*

239. Ellison, E. H. *J. Phys. Chem. B* **1999**, *103*, 9314-9320.

240. Inoue, Y.; Hakushi, T.; Liu, Y.; Tong, L. H.; Shen, B. J.; Jin, D. S. *J. Am. Chem. Soc.* **1993**, *115*, 475-481.

241. Tao, W.; Barra, M. *J. Chem. Soc., Perkin Trans. 2* **1998**, 1957-1960.

242. Rekharsky, M.; Inoue, Y. *J. Am. Chem. Soc.* **2000**, *122*, 10949-10955.

243. Qian, H.; Hopfield, J. J. *J. Chem. Phys.* **1996**, *105*, 9292-9298.

244. Cozens, F. L.; O'Neill, M.; Schepp, N. P. *J. Am. Chem. Soc.* **1997**, *119*, 7583-7584.

245. Adam, W.; Oestrich, R. S. *J. Am. Chem. Soc.* **1992**, *114*, 6031.

246. Banks, J. T.; Scaiano, J. C.; Adam, W.; Oestrich, R. S. *J. Am. Chem. Soc.* **1993**, *115*, 2473.

247. Bromberg, A.; Schmidt, K. H.; Meisel, D. *J. Am. Chem. Soc.* **1985**, *107*, 83.

248. Johnston, L. J. *Chem. Rev.* **1993**, *93*, 251-266.

249. Hirano, T.; Abrams, L.; Krusic, P. J.; Ottaviani, M. F.; Turro, N. J. *J. Org. Chem.* **2000**, *65*, 1319-1330.

250. Chen, F. R.; Fripiat, J. J. *J. Phys. Chem.* **1993**, *97*, 5796-5797.

251. Turro, N. J. *Pure & Appl. Chem.* **1986**, *58*, 1219-1228.

252. García-Garibay, M. A.; Lei, X. G.; Turro, N. J. *J. Am. Chem. Soc.* **1992**, *114*, 2749-2751.

253. García-Garibay, M. A.; Zhang, Z.; Turro, N. J. *J. Am. Chem. Soc.* **1991**, *113*, 6212-6218.

254. Warrier, M.; Turro, N. J.; Ramamurthy, V. *Tetrahedron Lett.* **2000**, *41*, 7163-7167.

255. Lem, G.; Turro, N. J. *Chem. Commun.* **2000**, 293-294.

256. Johnston, L. J.; de Mayo, P.; Wong, S. K. *J. Am. Chem. Soc.* **1982**, *104*, 307-309.

257. Lipson, M.; Noh, T.; Doubleday, C. E.; Zaleski, J. M.; Turro, N. J. *J. Phys. Chem.* **1994**, *98*, 8844-8850.

258. Läufer, M.; Dreeskamp, H. *J. Magn. Reson.* **1984**, *60*, 357-365.

259. Zhang, X.; Nau, W. M. *J. Phys. Org. Chem.* **2000**, *13*, 634-639.

260. Turro, N. J.; Kraeutler, B. *Acc. Chem. Res.* **1980**, *13*, 369.

261. Step, E. N.; Turro, N. J. *J. Photochem. Photobiol. A: Chem.* **1994**, *84*, 249-256.

262. Ramamurthy, V.; Corbin, D. R.; Eaton, D. F.; Turro, N. J. *Tetrahedron Lett.* **1989**, *30*, 5833-5836.

263. Turro, N. J.; Lei, X.; Li, W.; McDermott, A.; Abrams, L.; Ottavianai, M. F.; Beard, H. S. *Chem. Commun.* **1998**, *695-696*.

264. Turro, N. J.; Cheng, C. C.; Abrams, L.; Corbin, D. *J. Am. Chem. Soc.* **1987**, *109*, 2449-2456.

265. Turro, N. J.; Zhang, Z. *Tetrahedron Lett.* **1987**, *28*, 5637-5640.

266. Turro, N. J.; McDermott, A.; Lei, X.; Li, W.; Abrams, L.; Ottaviani, M. F.; Beard, H. S.; Houk, K. N.; Beno, B. R.; Lee, P. S. *Chem. Commun.* **1998**, 697-698.

267. Hirano, T.; Li, W.; Abrams, L.; Krusic, P. J.; Ottaviani, M. F.; Turro, N. J. *J. Am. Chem. Soc.* **1999**, *121*, 7170-7171.

268. Kelly, G.; Willsher, C. J.; Wilkinson, F.; Netto-Ferreira, J. C.; Olea, A.; Weir, D.; Johnston, L. J.; Scaiano, J. C. *Can. J. Chem.* **1990**, *68*, 812-819.

269. Johnston, L. J.; Scaiano, J. C.; Shi, J. L.; Siebrand, W.; Zerbetto, F. *J. Phys. Chem.* **1991**, *95*, 10018-10024.

270. Tung, C. H.; Ying, Y. M. *J. Chem. Soc., Perkin Trans. 2.* **1997**, 1319-1322.

271. Tung, C. H.; Ying, Y. M. *Res. Chem. Intermed.* **1998**, *24*, 15-23.

272. Vasenkov, S.; Frei, H. *J. Phys. Chem. A* **2000**, *104*, 4327-4332.

273. Meisel, D.; K., D. P.; Hug, G. L.; Bhattachryya, K.; Fessenden, R. W. *J. Am. Chem. Soc.* **1986**, *108*, 4706-4710.

274. Wilson, R. M.; Schnapp, K. A. *Chem. Rev.* **1993**, *93*, 223-249.

275. Chatgilialoglu, C. In *Handbook of Organic Photochemistry*; Scaiano, J. C., Ed.; CRC Press: Boca Raton, Fl., 1989; Vol. II, p 3.

276. Tokumura, K.; Ozaki, T.; Nosaka, H.; Saigusa, y.; Itoh, M. *J. Am. Chem. Soc.* **1991**, *113*, 4974-4980.

277. Hodgkins, J. E.; Megarity, E. D. *J. Am. Chem. Soc.* **1965**, *87*, 5322-5326.

278. Epling, G. A.; Lopes, A. *J. Am. Chem. Soc.* **1977**, *99*, 2700-2704.

279. Meiggs, T. O.; Grossweiner, L. I.; Miller, S. I. *J. Am. Chem. Soc.* **1972**, *94*, 7981-7986.

280. Meiggs, T. O.; Miller, S. I. *J. Am. Chem. Soc.* **1972**, *94*, 1989-1994.

281. Meiggs, T. O.; Grossweiner, L. I.; Miller, S. I. *J. Am. Chem. Soc.* **1972**, *94*, 7986-7991.

282. Xu, M.; Wan, P. *Chem. Commun.* **2000**, 2147-2148.

283. Ohno, T.; Fukumoto, T.; Hirashima, T.; Nishiguchi, I. *Chem. Lett.* **1991**, 1085-1088.

284. Yokoi, H.; Nakano, T.; Fujita, W.; Ishiguru, K.; Sawaki, Y. *J. Am. Chem. Soc.* **1998**, *120*, 12453-12458.

285. Cozens, F. L.; Cano, M. L.; García, H.; Schepp, N. P. *J. Am. Chem. Soc.* **1998**, *120*, 5667-5673.

286. Cozens, F. L.; Garcia, H.; Scaiano, J. C. *J. Am. Chem. Soc.* **1993**, *115*, 11134-11140.

287. Hilbom, J. W.; Pincock, J. A. *J. Am. Chem. Soc.* **1991**, *113*, 2683-2686.

288. Bockman, T. M.; Hubig, S. M.; Kochi, J. K. *J. Am. Chem. Soc.* **1996**, *118*, 4502-4503.

289. Bockman, T. M.; Hubig, S. M.; Kochi, J. K. *J. Org. Chem.* **1997**, *62*, 2210-2221.

290. Cozens, F. L.; Scaiano, J. C. *J. Am. Chem. Soc.* **1993**, *115*, 5204-5211.

291. Okamoto, K.; Hirota, N.; Terazima, M. *J. Phys. Chem. A* **1997**, *101*, 5269-5277.

292. Burkhart, R. D. *J. Phys. Chem.* **1969**, *73*, 2703-2706.

293. Oelkrug, D.; Honnen, W.; Wilkinson, F.; Willsher, C. J. *J. Chem. Soc., Faraday Trans. 2* **1987**, *83*, 2081-2095.

294. Dorfman, L. M.; Sujdak, R. J.; Bockrath, B. *Acc. Chem. Res.* **1976**, 352-357.

295. Fox, M. A. *Chem. Rev.* **1979**, *79*, 253-273.

296. Margerum, J. D. *J. Am. Chem. Soc.* **1965**, *87*, 3772-3773.

297. Frederick, B.; Johnston, L. J.; de Mayo, P.; Wong, S. K. *Can. J. Chem.* **1984**, *62*, 403-410.

298. Lei, X. G.; Turro, N. J. *J. Photochem. Photobiol. A: Chem.* **1992**, *69*, 53-56.

299. Zhang, J.; Krawietz, T. R.; Skloss, T. W.; Haw, J. F. *Chem. Commun.* **1997**, 685-686.

300. Kim, Y.; Lee, B. I.; Yoon, M. *Chem. Phys. Lett.* **1998**, *286*, 466-472.

301. Kim, Y.; Mallouk, T. E. *J. Phys. Chem.* **1992**, *96*, 2879-2885.

302. Commercial chlorine was used when available. Otherwise, Chlorine was generated by the action of concentrated hydrochloric acid upon $KMnO_4$ as described by Vogel, reference 310.

303. Varma, R. S.; Naicker, K. P. *Tetrahedron Lett.* **1998**, *39*, 7463-7466.

304. Fringelli, F.; Germani, R.; Pizzo, F.; Savelli, G. *Synth. Commun.* **1989**, *19*, 1939-1943.

305. Schröder, M. *Chem. Rev.* **1980**, *80*, 187-213.

306. DiCosimo, R.; Szabo, H. C. *J. Org. Chem.* **1988**, *53*, 1673-1679.

307. Delton, M. H.; Yuen, G. U. *J. Org. Chem.* **1968**, *33*, 2473-2477.

308. Dale, J. A.; Mosher, H. S. *J. Org. Chem.* **1970**, *35*, 4002-4003.

309. Ferraboschi, P.; Grisenti, P.; Manzocchi, A.; Santaniello, E. *J. Chem. Soc., Perkin Trans. 1* **1990**, 2469-2474.

310. Vogel, A. I. *Textbook of Practical Organic Chemistry*; 5th ed.; Longman Scientific & Technical: New York, 1989.

311. Akashi, K.; Palermo, R. E.; Sharpless, K. B. *J. Org. Chem.* **1978**, *43*, 2063-2066.

312. Jönsson, Å. *Acta Chem. Scand.* **1954**, *8*, 1210-1216.

313. Pipette amounts of reaction mixture were diluted with DCM, washed and dried (MgSO₄) before transfer to GC vials.

314. Scaiano, J. C. *Acc. Chem. Res.* **1983**, *16*, 234.

315. Hadel, L. M. In *Handbook of Organic Photochemistry*; Scaiano, J. C., Ed.; CRC Press: Boca Raton, Fl., 1989; Vol. I, p 279.

316. Wilkinson, F.; Kelly, G. In *Handbook of Organic Photochemistry*; Scaiano, J. C., Ed.; CRC Press: Boca Raton, Fl., 1989; Vol. I, p 293.

317. Wilkinson, F. *J. Chem. Soc., Faraday Trans. 2* **1986**, *82*, 2073-2081.